Simulations of Zero Boiloff, Densification, and Solidification in a Large-Scale Liquid Hydrogen Tank

By

Colin Philip Mahony

A Dissertation
Submitted to the Faculty of
University of Memphis
in Partial Fulfillment of the Requirements
for the Degree of Doctor of Philosophy
in Mechanical Engineering
in the Department of Mechanical Engineering

Memphis, Tennessee

December 2023

Simulations of Zero Boiloff, Densification, and Solidification in a Large-Scale Liquid Hydrogen Tank

By

Colin Philip Mahony

Approved:

_____
Jeffrey Marchetta
(Major Professor)

_____
John Hochstein
(Committee Member)

_____
Daniel Foti
(Committee Member)

_____
Sabri
(Committee Member)

_____
Headley
(Committee Member)

_____
Ranga
(Graduate Coordinator)

_____
Dean's Name
Dean
College's Name

Name: Colin Philip Mahony

Date of Degree: December 1, 2023

Institution: University of Memphis

Major Field: Mechanical Engineering

Select Appropriate Title: Add the name(s) of the person(s) heading your committee.

Title of Study: Simulations of Zero Boiloff, Densification, and Solidification in a Large-Scale Liquid Hydrogen Tank

Pages in Study **Error! Bookmark not defined.**

Candidate for Degree of Doctor of Philosophy

The current research utilizes an Energy of Fluid (EOF) approach to develop a finite volume-based Computation Fluid Dynamic (CFD) model to create a benchmark simulation of the densification of liquid hydrogen (LH2) in an experimental Integrated Refrigeration and Storage (IRAS) tank at the Kennedy Space Center (KSC). The computational code will incorporate the FLUENT pressure-based model with User Defined Functions (UDF) to implement the EOF model. The enhanced model will solve the energy equation in terms of internal energy and provide temperature and pressure calculations for a given tank geometry. Specifically, a convection term will be added to an already existing code for a more accurate simulation of LH2 densification. However, currently the research focuses on utilizing User Defined Scalars (UDS) with FLUENT to show the built-in solvers are as accurate as the written UDS. This will reduce the computational time down significantly by utilizing an already built in solver for the momentum equation. A custom UDF has been written to solve transient and steady state conduction, and results obtained using the UDF agree with results obtained using the built-in FLUENT solver. Currently, a convection UDF is being added and will be verified

using known solutions for solidification and validated with the experimental results from the Cryogenics Test Laboratory (CTL) at KSC for the IRAS densification process.

DEDICATION

As an optional page, the author may choose to add a Dedication page as a means to recognize individual people, groups, and/or organizations that supported/inspired the author. If a dedication is not used, but you are planning on having an "ACKNOWLEDGEMENTS", simply change the word "DEDICTATION" to "ACKNOWLEDGEMENTS and delete the following acknowledgements section. If neither a dedication or acknowledgements are desired, delete both sections and set the page number on the first page of the Table of Contents to start at "ii"

ACKNOWLEDGEMENTS

As an optional page, the author may choose to add an Acknowledgements page to recognize any special contributors that helped make the work possible. If an acknowledgements is used, it immediately follows the dedication (if applicable, otherwise after the abstract) and continues page numbering (or if there is not a Dedication, then the Acknowledgements is numbered with a lowercase Roman numeral "ii"). If an acknowledgements section is not desired, simply delete this section.

TABLE OF CONTENTS

LIST OF TABLES

LIST OF FIGURES

CHAPTER I

INTRODUCTION AND BACKGROUND

1.1 Overview of Cryogenic Storage

The word cryogenics is synonymous with very low temperatures, and the National Bureau of Standards at Boulder, Colorado defined the field of cryogenics as any system involving temperatures below -150°C or -240°F. The reason this temperature was chosen as the standard was due to the boiling point of the permanent gases such as nitrogen, oxygen, hydrogen, etc. are below the value of -150°C. Cryogenics has applications in many different fields of study including MRI's in the medical industry, food processing, high energy physics applications, and most notably the space industry. The field of cryogenic engineering focuses on the development and improvement of low temperature practices, procedures, and equipment. Cryogenic engineering develops real-world utilization of the low temperature phenomena, by familiarization with engineering principles in order to better design experiments and cryogenic devices [1].

From NASA's Gemini, Apollo, and Shuttle missions to the modern SpaceX and Blue Origin companies, the space industry utilized cryogenic fluids as the main source of propellants for the ascending rockets and space craft that took man to the moon and eventually further into space. The main reason cryogenic fluids are used as rocket propellants is the amount of potential energy stored in these fluids. One of the leading issues discovered early in the field of cryogenics and in space applications is the storage

of the cryogenic fluid, and subsequently the transportation of commodities. Cryogenic fluids are normally stored at/near the normal boiling point (NBP) in well-insulated tanks such as in Figure 1.1 which is the liquid hydrogen (LH2) tank at Launch Complex 39B at the Kennedy Space Center (KSC) [2].

Figure 1.1 Liquid hydrogen tank (LH2) tank at LC-39B at KSC

Often gases such as oxygen, hydrogen, nitrogen, etc. are transported in the liquid state at cryogenic temperatures. When cryogenic fluids expand from a liquid to a vapor, and the density increases from standard temperature and pressure (STP) gas to normal boiling liquid, the expansion rate is approximately:

1. Hydrogen → 865:1
2. Oxygen → 877:1
3. Natural Gas → 600:1

Therefore, without pressure control measures the pressure can increase quickly in an enclosed container with a rapidly expanding cryogenic fluid and could become hazardous in the case of material failure.

Due to the rapid expansion behavior of cryogenic fluids, experimental work determined the storage capabilities of tanks to reduce the possibility of rupture due to material failure. When a cryogenic fluid vaporizes inside an enclosed space, a pressure rise could be characterized, i.e., tank self-pressurization. This tank self-pressurization had been the focus of numerous experimental studies beginning mainly in the early days of NASA, to transport humans safely into space utilizing cryogenic fluid as the propellant the pressure rise rate inside a tank had to be properly characterized. The ability to control the pressure rise rate presented unique research topic, and to accomplish this one must reduce the thermal stratification of the fluid [3–5].

During the Apollo era, the Saturn V vehicle required roughly 1.74M liters of LOX and 1.25M liters of LH2 on-board at lift-off, and the spherical storage tanks at Launch Complex 39 were approximately 3.41M liters for LH2 and 3.22M liters for LOX [Adam's 3]. NASA lost roughly 50% of the LH2 purchased during the Space Shuttle program due to tank heat leak, transport, and other losses. Table 1.1 shows the normal boiling point and critical temperature as well as the cost per liter of different cryogenic fluids [6].

Table 1.1 Characteristics of different cryogenic fluids

Fluid	NBP	Critical Temperature	Density	Heat of vaporization	Cost
	K	K	kg/m^3	kJ/kg	$/L
Methane (LNG)	111.7	190.6	0.42	510.8	~0.39
Oxygen	90.2	154.6	1.14	213.1	~0.15
Argon	87.3	150.7	1.40	161.1	~1.4
Nitrogen	77.4	126.2	0.81	199.2	~0.08
Hydrogen	20.4	33.1	0.07	448.7	~0.50
Helium	4.2	5.2	0.12	20.8	~15

Further investigation into tank self-pressurization led to mathematical and computational research [7]. The limitation of the experimental works limited the computational verification, and more extensive experimental work is necessary. However, limited data is not the only issue faced in computational work, the phase-change process which drives tank self-pressurization created difficulties. The phase-change process, whether solidification/melting or evaporation/condensation, creates large discontinuities in the fluid properties. Therefore, many researchers have developed methods to simulate the phase-change process considering these discontinuities. Hochstein, Aydelott, and Hasan developed some of the early models of tank self-pressurization in cryogenic tanks [20-22, 25-26].

The three types of models that have been used in modeling cryogenic phase change include Lumped Node/Thermodynamic, Volume of Fluid (VOF)/Enthalpy, and the Energy of Fluid (EOF)/Internal Energy methods. The Lumped Node method broke the ullage and liquid domains into separate thermodynamic nodes, which required the

energy equation to be solved for the separate nodes. This method showed good results, however the phase change problem caused issues in the communication between the nodes [references]. Mattick developed a multi-node lumped parameter approach for the multiphase problem utilizing a hybrid sharp interface procedure. The multi-node procedure broke the ullage and the liquid into two separate nodes whose mass and energy equations were solved given the pressure and temperature data. The sharp hybrid interface procedure solved the equations for the liquid and ullage independently while an internal boundary allowed for mass and heat transfer across. The method showed slight improvement in pressure predictions compared to similar computations [40].

Barsi developed a multi-zone model in which the ullage, liquid, and surrounding tank were considered as separate zones. Bulk conservation equations were solved in the liquid and ullage and coupled to the heat conduction through the tank wall and the mass transfer. The zonal model was compared to a homogeneous thermodynamic model and the experimental data presented before in "Investigation of Tank Pressurization and Pressure Control-Part I: Experimental Study" [42]. The thermodynamic lumped model under predicted the experimental results due in part by the homogeneity assumption which restricts the ullage, liquid, and tank to be at saturation temperature. Thermodynamic lumped model did not accurately predict tank pressurization, however as a design tool uncovered trends in the pressurization behavior. When compared with 1-g experimental data, the zonal model reasonably predicted the pressurization. At high mixing jet velocities, the zonal model presented similar results to experimental data, however at low jet speeds the buoyancy and convective forces adversely effected the jet.

Since each bulk phase in the zonal model were assumed spatially uniform then the buoyancy interaction could not be accurately represented [43].

The VOF method has been researched by several authors for the use of cryogenic fluid study. [52], [53]. Stewart utilized VOF for studies and found issues at the interface such as: velocities not converging at the interface, surface tension, and uncertainty in the saturation pressure [54]. To aid in the issues at the interface, Stewart utilized VOF with an added sub-grid model at the interface. A fine grid at the interface could produce more accurate results, however would be computationally expensive [55].

Shyy showed the phase change process created temperature gradients in the liquid while gravitational forces produced buoyancy induced convection. The enthalpy based model implemented Darcy's Law into the momentum equation to account for a mushy zone, and the inclusion of an unsteady term enhanced numerical stability and the contributions of the implicit terms [56], [57]. Wei Shyy compared multiple schemes for approximating the convection terms in the transport equation in scenarios where high Peclet number, skewness of numerical grid lines, and accuracy of numerical approximations set by boundary conditions and by the presence of a source term. The different schemes studied include first-order upwind, skew upwind, second order upwind, second-order central differencing, and QUICK (Quadratic Upstream Interpolation for Convective Kinematics). The first order upwind failed to produce accurate approximations, and the same is true of the skew upwind method in the presence of a source term. QUICK and second-order central differencing are of the same order of accuracy as the second-order upwind, however the second-order upwind gave the most satisfactory results when compared to the other four schemes [58]. Shyy [59][60] also

developed a computational method to predict the two-phase fluid flow and heat transfer with a reservoir with a capillary-pumped-loop. The model is based on an enthalpy formulation of the energy equation. “The enthalpy formulation instead of temperature formulation has been employed wherein the different phases are differentiated based on the local temperature at each nodal point, thus a unified set of governing equations can be written for both phases. The enthalpy formulation alleviates the need to explicitly tracking the phase boundaries, but introduces extra source terms arising from the release of latent heat which can make the computation more difficult to converge [61].” The reservoir remained at a constant thermodynamic pressure and subjected to 1-g and 0-g conditions. Three different modes of convection were identified as thermocapillary buoyancy, and rapid expansion, and both showed dependence upon the heat input, gravity level, and reservoir orientation. At 0-g and high heat input evaporation rates were higher and caused the wick to be engulfed in vapor, and in the absence of gravity rapid expansion was the only mode of convection. Under low heat and 1-g the liquid evaporated however over time buoyancy forces created a more uniform temperature and began converting vapor back into liquid, but at higher heat input the liquid boiled off too quickly for any buoyancy forces to impact the fluid [61]. Cherkasov created a model that calculated the temperature stratification in a cryogenic fuel tank based on equation for free convection boundary layer in the integral form. The calculated results compared closely with numerical solution as well as experimental data [62]. Panzarella demonstrated that buoyancy and natural convection effected the pressurization and thermal stratification of large tanks [80], [81].

The Enthalpy method allowed for a single fluid domain with the ease of communication between the liquid and ullage domains via the VOF which distinguished the phase in a cell with a temperature difference in order to smear the fluid properties across the interfaces. However, solving the energy equation for the phase change problem in terms of enthalpy created discontinuities in the fluid properties as well as a transient pressure term [references]. Winter et al. proposed using the Energy of Fluid (EOF) approach for modeling constant volume cryogenic evaporation/condensation. This method utilized an internal energy formulation of the energy equation rather than an enthalpy formulation and was derived from Anghaie and Ding's formulation. According to Winter, one of the main drawbacks to the enthalpy formulation included a transient pressure term which added complexity to the problem, whereas the EOF model does not. A commercially available model solved the mass and momentum equations and the energy equation was solve sequentially and separately after pressure and velocity terms were obtained from the Enthalpy-based solvers [76]. The results showed more work was needed to optimize the relaxation factor for temperature and vapor pressure; due to the face that the saturation temperature is derived from these and any changes would greatly affect the solution. The EOF method solved the energy equation in terms of the internal energy of the fluid, and therefore derived the energy equation without the transient pressure term allowing for a simpler computation. The EOF also smeared the properties across the phases, however with an internal energy difference rather than a temperature difference, which allowed the phase change to occur at one temperature [Marchetta, Winters, Gasmen] [71]–[75].[77]..

These three methods aided in the experimental process, but more experimental work is required to identify and better understand the heat input to the tanks creating the self-pressurization problem. Heat leaks can be slowed down, but never eliminated in these large-scale tanks which leads to boiloff of the commodities. Counteracting or controlling the self-pressurization behaviors via passive (insulation) and active (refrigeration) technologies produced many experimental discoveries.

NASA has developed another heavy lift launch vehicle termed the Space Launch System (SLS) which would require 46% more propellant [Adam's 5]. The new heavy lift rocket strained the LC-39 storage systems; therefore, a larger spherical tank was commissioned of approximately 4.73M liters of LH2 [Adam's 6]. Ways to eliminate losses and recuperate cost of this large-scale tanks is to counteract the heat leak with the newly developed passive and active technologies e.g., insulation or Integrated Refrigeration and Storage (IRAS) [Adam's Thesis]

1.2 Cryogenic Storage and Refrigeration at NASA KSC

Some of the earliest work on cryogenic refrigerators and liquefiers was conducted at the National Bureau of Standards (NBS) Cryogenics Engineering Laboratory [Adam's 8-10]. However more recent studies showed that for long duration missions, the ability to store cryogenics in a ZBO system was of the utmost importance [Adam's 11, 12].

Upon the retirement of the Shuttle program and driven by the LH2 losses presented previously, NASA decided to capitalize on the next generation of cryogenic storage technologies. Passive cryogenic technologies included multilayer insulation (MLI) and vapor cooled shields whereas active technologies required some power input. For example, a cryogenic refrigerator, a cryocooler, were both created to actively

maintain the low temperatures. Examples of the active cryogenic cooling application included the reverse Turbo-Brayton cycle, Stirling, and Pulse-Tube coolers. Integrated active and passive cryogenic technologies formed a hybrid system that minimized the launch mass and proved to efficient in long duration missions [8–13]. Hastings stated the Zero-Boiloff (ZBO) involved thermal systems of both passive and active technologies. A cryocooler and radiator system intercepted and rejected the heat leak into the cryogenic storage system [14]. The MLI maintained heat leak from the cooler, and a mixer ensured temperature destratification and pressure control independent of the ullage position. The ZBO system allowed for tank venting to be eliminated. In a gravitational environment in which the ullage would be at the top of the tank, a cryocooler cold head could be positioned in the ullage to control the tank pressure without the use of a mixer [14]. Plachta developed a ZBO system consisting of an insulated tank, cryogenic heat pipe, radiator, and cryocooler. The system removed approximately 7 Watts of heat from the tank at75K and 150 Watts of power input [15], [16].

The Integrated Refrigeration and Storage (IRAS) considered a hybrid system consisted of a storage tank with a cryogenic refrigerator via an internal heat exchanger distributed throughout the bulk fluid volume. There are five unique capabilities of an IRAS system which are:

1. Zero-loss tank chill down from ambient temperature
2. Zero-loss tanker off-loading of cryogenic liquid
3. Zero boiloff (ZBO)
4. Liquefaction
5. Densification

IRAS capabilities one through four have economic benefits, whereas five was considered a more advanced technological capability that would effect on both launch vehicles and launch pad infrastructure and operations [Adam's 7]. For a properly designed IRAS system, the entire bulk volume of cryogenic liquid could be conditioned anywhere along the saturation curve for the given fluid, from the maximum allowable pressure rating of the vessel to the triple point, an impossible feat without the use of active refrigeration. Figure 1.2 presented an example of the IRAS system compared to the traditional large-scale cryogenic storage tank.

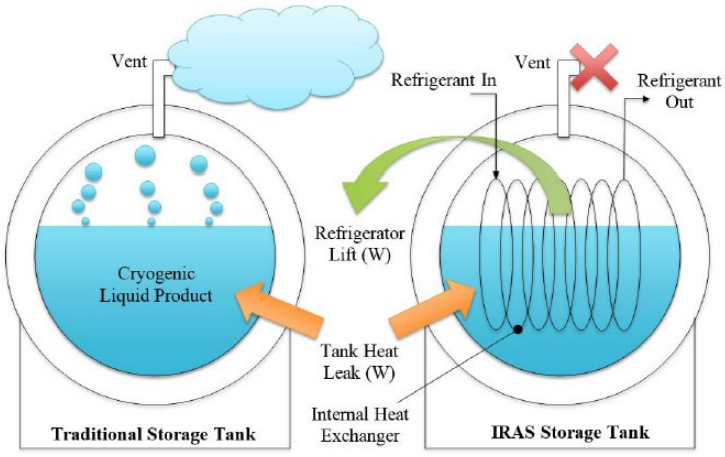

Figure 1.2 Comparison of traditional storage tank and an IRAS tank

The IRAS system is novel in that it chills the cryogenic liquid directly, reducing the thermal resistance between the refrigerant and the cryogen while utilizing only free convection. There are several advantageous characteristics of the IRAS system when compared to past systems. For instance, cooling the liquid directly enables the control of the bulk temperature of the cryogen as opposed controlling the pressure in the ullage. The system also allows for conditioning or densification of the cryogenic fluid and facilitates greater thermal response during transient operations. Forced convection methods require

active components that add heat from a pumping system, however exploiting free convection the heat input is significantly reduced.

Notardonato et. al. demonstrated hydrogen liquefaction from a gaseous supply inside a 180 L vessel and showed the ability of ZBO and densification [Adam's 13]. Also, a 400 L IRAS ZBO cryostat with a liquid nitrogen heat exchanger stored liquid oxygen. The height of the was varied to determine the effect on the refrigerator lift [Adam's 14]. These works led to the design and development of the Ground Operations and Demonstration Unit for Liquid Hydrogen (GODU-LH2).

The GODU-LH2 tank was originally constructed in 1991 for the Titan-Centaur program. The tank is a horizontal-cylindrical configuration with 2:1 elliptical heads. This vacuum-jacketed tank could store a maximum of 125,000 L of LH2 at NBP. The outer jacket measures roughly 23 m long and 3.4 m in diameter, while the inner tank length and diameter are 21.8 m and 2.9 m respectively. Figure 1.3 shows the tank being lowered into position to be modified with the IRAS system.

Figure 1.3 GODU-LH2 tank (Photo: NASA)

The modifications to the GODU tank consisted of the development of an internal heat exchanger. The IRAS heat exchanger consisted of approximately 290 m of stainless steel with Helium inlet (lower) and exit (upper) manifolds made of 25 mm diameter tubing. Connecting these manifolds were forty 6.4 mm diameter tubes, evenly spaced, and bent into a 3-dimensional shape that followed the curvature of the tank wall. Total heat transfer area of the heat exchanger was roughly 8 m^2 [Adam's thesis and 18-20]. All twenty-four temperature sensors inside the tank were silicon diodes, Scientific Instruments model Si-410 with group AA calibration (±0.5 K from 450 K to 25 K, and ±0.1 K from 25 K to 1.5 K). Figure 1.4 presented the CAD model of the GODU-LH2 tank with the IRAS modifications.

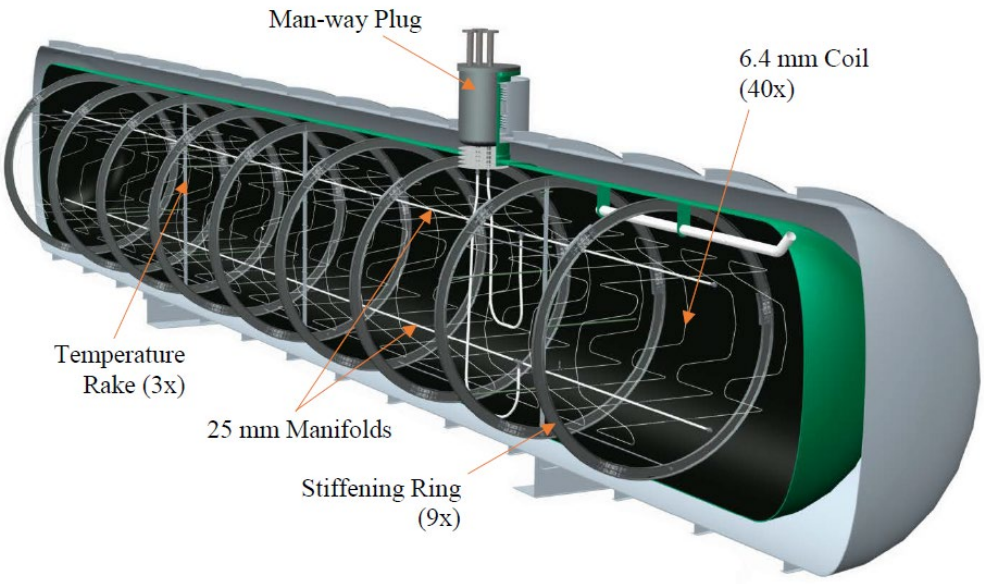

Figure 1.4 Cut-away of GODU-LH2 with IRAS modifications

The GODU-LH2 project confirmed the ability to control a full-scale LH2 tank, however the understanding of the free convection during these processes were not fully understood. Numerous mathematical models and simulations have been developed to predict other cryogenic tanks during of ZBO and densification. Swanger developed a Lumped Node analysis model for the GODU-LH2 system which concentrates on a section of Densification testing for the LH_2 fill levels of 100% and 67%.

1.3 Current Research

The current research is to develop a Computational Fluid Dynamic (CFD) model to simulate a LH_2 cryogenic tank for quasi-steady state, ZBO, densification, and solidification processes. The model will be validated with other models and then verified with experimental data from the GODU-LH2 tank experiments.

The objectives of this research include:

1. Develop Internal Energy and commercially available Enthalpy model for conduction, convection, and phase change heat transfer.
2. Validate the models with other models for conduction, convection, and solidification.
3. Compare the Internal Energy and Enthalpy models to a Lumped node analysis and experimental results for the GODU-LH2 tank ZBO, densification, and solidification processes.

Simulation of cryogenic tanks has been characterized by numerous researchers and in several methods, namely a lumped homogenous thermodynamic (lumped node) method, Enthalpy method, and Internal Energy model. The lumped thermodynamic model coupled the ullage with the transport equations in the liquid, and at the interface a mass balance accounted for the phase change on a cell-by-cell basis. This demonstrated the disadvantages in modeling the liquid/vapor interface. Most thermodynamic models assume the heat conduction within the lump portion is much greater than the convection, and convection was neglected. However, the Enthalpy method's main advantage over the thermodynamic model was the ullage and liquid are now not separate entities, and the interface was defined by the ratio of fluid to liquid in a computational cell. The major difference between the current, Internal Energy model, and the Enthalpy method is the interface is defined by the internal energy in the computational cell rather than a temperature window as in the Enthalpy method.

In essence, the evaporation/condensation simulation is slightly more difficult than solidification because the pressure changes much more quickly. During solidification, the pressure changes very slowly which mean changes in temperature have the most

significant influence on changes in internal energy, enthalpy, and density. Further modeling solidification in cryogenics has become important now with the concept of cryocoolers and IRAS systems that can go below the freezing point of certain cryogens. This research work takes all the previous computational work done with the more the complex evaporation/condensation and adapts it for use for high fidelity solidification modeling. This allows for the use of experiments to validate the EOF model with conduction, convection, and solidification phase change.

The current research will utilize the previously described EOF model to create an internal energy-based solution to the buoyancy driven flow problem occurring inside the GODU-LH2 experimental tank during quasi-steady state, ZBO, densification, and solidification. This model will be validated for conduction and convection during phase change. The model will be verified with the experimental temperature and pressure results for the GODU-LH2 tank and compared to a commercially available enthalpy-based solver and a lumped node analysis given by Swanger.

CHAPTER II

ENERGY EQUATION FORMULATION

2.1 Mathematical Formulation

2.1.1 Governing Equation

For a closed system the First Law of Thermodynamics is expressed as

$$\delta Q = dE + \delta W \tag{2.1}$$

where Q is the heat transfer, E is the internal energy, and W is the work. In the phase change process being investigated the system is rigid enclosure with a constant volume where no mechanical work (i.e., pumping or jet mixing) is present. Therefore, the first law reduces to

$$\delta Q = dE = dH - VdP \tag{2.2}$$

where H is the enthalpy, V is volume, and P is the pressure. Equation 2.2 states that the heat exchange is equal to the change internal energy, which is equal to the difference between the change in enthalpy and the volume multiplied by the change in pressure. Thus, the latent heat associated with phase change induces changes in enthalpy, pressure, and internal energy.

2.1.2 Enthalpy Formulation

The Navier-Stokes equations with an enthalpy formulation of the energy equation for a two-phase system can be written as

$$\frac{\partial \rho}{\partial t} + \nabla \cdot (\rho \vec{v}) = 0 \tag{2.3}$$

$$\frac{\partial \rho v_x}{\partial t} + \nabla \cdot (\rho \vec{v} v_x) = -\frac{\partial p}{\partial x} + \nabla \cdot (\mu \nabla v_x) + S_x \tag{2.4}$$

$$\frac{\partial \rho v_y}{\partial t} + \nabla \cdot \left(\rho \vec{v} v_y\right) = -\frac{\partial p}{\partial y} + \nabla \cdot \left(\mu \nabla v_y\right) - g(\rho - \rho_0) + S_y \tag{2.5}$$

$$\frac{\partial \rho v_z}{\partial t} + \nabla \cdot (\rho \vec{v} v_z) = -\frac{\partial p}{\partial z} + \nabla \cdot (\mu \nabla v_z) + S_z \tag{2.6}$$

Given the enthalpy, H, the energy equation becomes

$$H = h + \Delta H = h + \beta L \tag{2.7}$$

$$\frac{\partial \rho h}{\partial t} + \nabla \cdot (\rho \vec{v} h) = \nabla \cdot (k \nabla T) + -\Delta H \frac{\partial (\rho \beta)}{\partial t} - \Delta H \nabla \cdot \left(\rho \vec{V} \beta\right) \tag{2.8}$$

where

$$\beta = \begin{cases} 0, & T < T_{solidus} \\ \frac{T - T_{solidus}}{T_{liquidus} - T_{solidus}}, & T_{solidus} < T < T_{liquidus} \\ 1, & T_{liquidus} < T \end{cases} \tag{2.9}$$

where P is the pressure, v is velocity vector, T is temperature, k is thermal conductivity, ρ is the density, ΔH is the latent heat, and S are source terms. A Boussinesq approximation is utilized in the y-momentum equation where $\rho_0$represented the reference density, g was the gravitational force, and ρ is the density. The enthalpy formulation of the phase change energy equation requires a Liquid Fraction, β. The Liquid fraction is the ratio of liquid to solid in a computational cell and is defined by a temperature window. While the computational cell is within the temperature window, between and, the cell is considered to be in a mushy zone. Then the source terms applied to the x-, y-, and z-momentum equations utilize the Darcy Law of flow through a porous material and were given as:

$$S_x = -C\frac{(1-\beta)^2}{\beta^3+0.001}u \tag{2.3}$$

$$S_y = -C\frac{(1-\beta)^2}{\beta^3+0.001}v \tag{2.4}$$

$$S_z = -C\frac{(1-\beta)^2}{\beta^3+0.001}w \tag{2.5}$$

where u, v, and w were the velocity component in the x-, y-, and z-direction, β is the Liquid Fraction, and C was a large enough constant to force the velocities to go to zero, 1E8. As the cell solidifies or as the phase fraction goes to zero, the source term becomes larger which effectively reduces the velocities in the cell. Once the fluid in the cell is completely solidified, the source term is maximized, and the velocities go to zero.

2.1.3 Internal Energy Formulation

For the current study an internal energy-based formulation of the energy equation which is utilized for hydrogen densification and solidification phase change. The internal energy formulation, EOF model, of the mass; x-, y-, z-momentum; and energy conservations can be written as

$$\frac{\partial\rho}{\partial t} + \nabla\cdot\left(\rho\vec{V}\right) = 0 \tag{2.13}$$

$$\frac{\partial\rho u}{\partial t} + \nabla\cdot\left(\rho\vec{V}u\right) = -\frac{\partial p}{\partial x} + \nabla\cdot(\mu\nabla u) + S_x \tag{2.14}$$

$$\frac{\partial\rho v}{\partial t} + \nabla\cdot\left(\rho\vec{V}v\right) = -\frac{\partial p}{\partial y} + \nabla\cdot(\mu\nabla v) - \rho g + S_y \tag{2.15}$$

$$\frac{\partial\rho w}{\partial t} + \nabla\cdot\left(\rho\vec{V}w\right) = -\frac{\partial p}{\partial z} + \nabla\cdot(\mu\nabla w) + S_z \tag{2.16}$$

$$\frac{\partial\rho E}{\partial t} + \nabla\cdot\left(\rho\vec{V}E\right) = \nabla\cdot(k\nabla T) - \Delta e\frac{\partial(\rho f)}{\partial t} - \Delta e\nabla\cdot\left(\rho\vec{V}f\right) \tag{2.6}$$

where E is the internal energy may be expressed, Δe is the latent heat of fusion, and f is the EOF phase fraction defined as

$$E = e + f\Delta e \tag{2.18}$$

$$f = \begin{cases} 0, & E < e_s \\ \frac{E - e_s}{e_l - e_s}, & e_s < E < e_l \\ 1, & e_l < E \end{cases} \tag{2.19}$$

The subscript l represents liquid, and s represents the solid. If the phase fraction goes to one then the fluid inside the computational cell is liquid, and if the ratio goes to zero then the cell is solid.

To model natural convection, a buoyancy force term is added the momentum equation to account for the fluid motion occurring in the presence of density changes in a gravitational field. A Boussinesq approximation replaced the density times gravity term in the momentum equation:

$$\rho g = g(\rho - \rho_0) \tag{2.70}$$

where the subscript 0 represented the reference density, g was the gravitational force, and ρ was the averaged density that accurately reconstructed the static pressure gradient in the fluid domain [107 – 109]. Source terms were added to the momentum equations for the Darcy Law similar to Equations 2.12 – 2.14, however the Liquid Fraction, β, is replaced with the EOF phase fraction, f, given in Equations 2.22 – 2.24.

$$S_x = -C\frac{(1-f)^2}{f^3+0.001}u \tag{2.8}$$

$$S_y = -C\frac{(1-f)^2}{f^3+0.001}v \tag{2.9}$$

$$S_z = -C\frac{(1-f)^2}{f^3+0.001}w \tag{2.10}$$

2.2 Model Implementation

For the complex geometries, both the Enthalpy and Internal Energy methods utilize a finite volume method with upwind differencing to discretize the governing differential equations into linear algebraic equations and solving these equations with the algebraic multigrid (AMG) method. The current simulations employed a pressure-based solver with a pressure-velocity coupling utilizing a semi-implicit-method-for-pressure-linked-equations (SIMPLE). In the software pressure-staggered-option (PRESTO) method evaluated the pressure, a Second Order Upwind method for momentum, energy, and transport scalar, and a First Order Implicit marched forward through time. All the subroutines and code modifications were written in C language.

2.2.1 Scalar Transport Equation

In addition to utilizing the built-in enthalpy implementation of the energy equation for the current study, a User Defined Function (UDF) is developed and implemented to solve the energy equation in terms of internal energy. The UDF utilizes the User Defined Scalar (UDS) transport theory [83], which solves the scalar transport equation in terms of an arbitrary scalar, ϕ_k

$$\frac{\partial \rho \phi_k}{\partial t} + \frac{\partial}{\partial x_i}\left(\rho u_i \phi_k + \Gamma_k \frac{\partial \phi_k}{\partial x_i}\right) = S_{\phi_k} \quad k = 0, \dots, N \tag{2.11}$$

where Γ_k and S_{ϕ_k} are the diffusion coefficient and source term for the N number of scalar equations. The first term on the left-hand side is the transient term. In the second term on the left-hand side, the first term inside the partial derivative is the convective flux term, and the second term is the conductive diffusive term. Source terms were added in

momentum and energy equations to include the buoyancy force and the phase fraction terms.

$$\phi_k = E \tag{2.12}$$

$$\Gamma_k = k \tag{2.13}$$

$$S_k = -\Delta e \frac{\partial(\rho f)}{\partial t} - \Delta e \nabla \cdot \left(\rho \vec{V} f\right) \tag{2.14}$$

With some substitution and manipulation, Equation 2.20, can be written in terms of internal energy to match Equation 2.19 shown in Equation 2.24.

$$\frac{\partial \rho E}{\partial t} + \frac{\partial}{\partial x_i}(\rho u_i E) - \nabla \cdot (k \nabla T) = -\Delta e \frac{\partial(\rho f)}{\partial t} - \Delta e \nabla \cdot \left(\rho \vec{V} f\right) \tag{2.15}$$

2.2.2 Material Properties

Hydrogen has a normal boiling point, NBP, of approximately 20.27 K and 101.35 kPa, and a triple point of 13.8 K and 7.04 kPa given in the phase diagram in Figure 2.1.

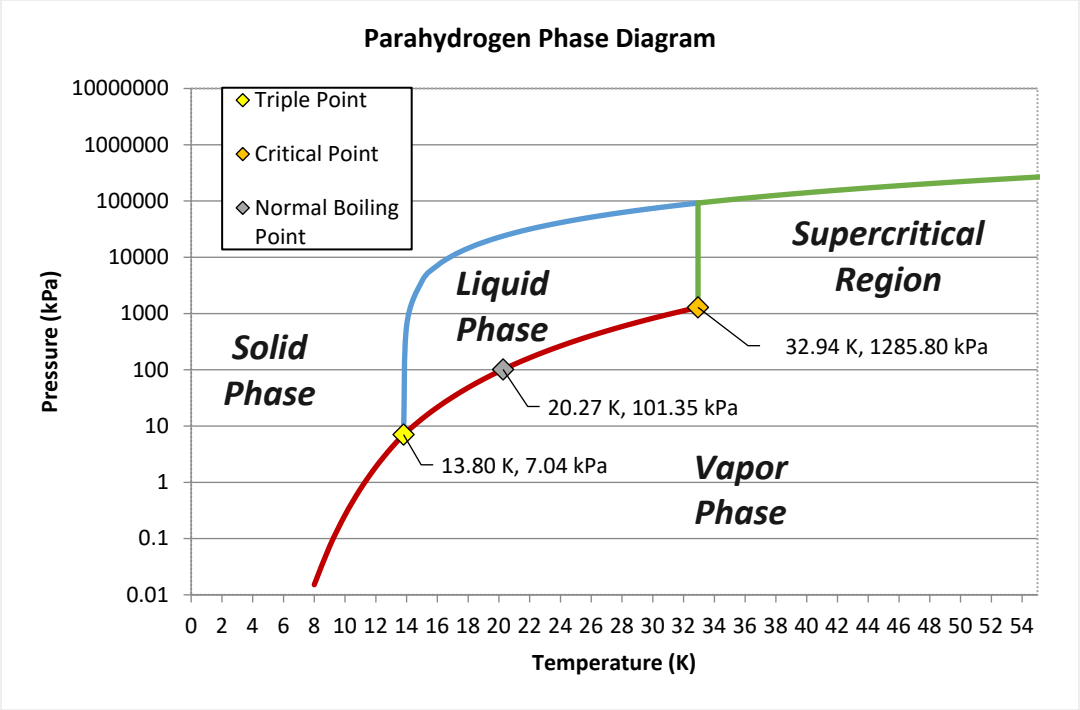

Figure 2.1 Parahydrogen Phase Change Diagram

The thermophysical properties of parahydrogen are utilized for the LH_2 inside the GODU tank under the assumption that most of the hydrogen contained within the tank has transformed from ortho- to parahydrogen. Another assumption for the model is that the hydrogen inside GODU tank is saturated for all fill levels. Therefore, during the initialization of the quasi-steady state analysis of the system the thermophysical properties were calculated with polynomials created from the saturated tables given by NIST for the initial given pressure as a function of temperature.

After the first timestep in the steady state analysis and for all subsequent simulations, a combination of previously studied methods are utilized in calculating the properties of the hydrogen with a basis in the Maxwell relations. The Benedict-Webb-Rubin equation of state utilizes 32-terms to calculate the pressure as a function of both density and temperature. From the equations of state, sets of coefficients, data curve fits,

and integrations accurately predict some of the properties of hydrogen [102 – 103]. The author, Younglove, developed a curve fit the density of hydrogen as a function of the saturated temperature of the fluid [104]. For the saturation temperature and pressure ranges in this study, the dynamic viscosity and thermal conductivity of the fluid do not change significantly. Therefore, a property look-up table is created with data from NIST given saturation temperature and pressure as the axes [105]. The properties are calculated utilizing sets of linear interpolations between the saturation property data points.

As the temperature and pressure approached the triple point of hydrogen, the saturation relations do not predict the thermophysical properties once solidification begins. The properties for solid hydrogen are tabulated by authors McCarty, Hord, and Roder [106]. The values are presented as a function of temperature and a curve fit function was created to predict the property as the temperature in a computational cell dropped to 13.8 K and below.

For the mixed phase computational cells or cells that contain both solid and liquid hydrogen, a phase fraction volume-weighted average method is used to calculate the material properties. This linear interpolation scheme calculates the cell-centered properties for all computational cells in the phase change interface. Equation 2.28 presented such a scheme for a general cell-centered property, θ , where the subscripts l and s denote the values of liquid and solid, respectively.

$$\theta = a\theta_l + (1 - a)\theta_s \tag{2.16}$$

where a is either the Enthalpy model Liquid Fraction or the Internal Energy method EOF phase fraction.

CHAPTER III

INTERNAL ENERGY (EOF) MODEL CODE VERIFICATION

3.1 Conduction Heat Transfer

Conduction heat transfer is the most significant mode of heat transfer within solid objects. To verify the implementation of the conduction term in the internal energy (EOF) model, simulation results are compared to analytical solutions for conduction heat transfer with constant temperature and constant heat flux boundary conditions. Both cases are setup using a 0.1 x 0.1 m two-dimensional square geometry with a 100 x 100 cell mesh, a flow time of 600 seconds, and a time step size of 1 second. The governing equation for a one-dimensional unsteady conduction is:

$$\rho c_v \frac{\partial T}{\partial t} = k \frac{\partial^2 T}{\partial y^2} \tag{3.1}$$

with the material properties presented in Table 3.1 for water at a pressure of 101.325 kPa and a temperature of 300 K.

Table 3.1 Material properties of water at 101.325 kPa and 300 K

Density	Thermal Conductivity	Specific Heat	Thermal Diffusivity
$\rho\ (kg/m^3)$	$k\ (W/m*K)$	$c_v\ (J/kg*K)$	$\alpha\ \left(\frac{m^2}{s}\right)$
996.5	0.6102	4130.0	1.465E-7

3.1.1 Unsteady Conduction Heat Transfer

The first case consists of temperature boundaries on the top and bottom of the square cavity with adiabatic walls on the left and right sides shown in Figure 3.1(a). The temperature on the bottom of the cavity is the hot wall at 325 K, and the bottom wall is the cold boundary at 300 K. The initial temperature of the water inside the cavity is 300 K. The analytical solution provided by Meyer for the temperature at a distance y for a region of $0 < y < L$ where $y = \begin{cases} 0, & T = T_O = 325K \\ L, & T = T_L = 300K \end{cases}$ and for time, t, is presented in Equation 3.2 [86].

$$T(y,t) = T_O - (T_O - T_L)\frac{y}{L} - \frac{2}{\pi}(T_O - T_L)\sum_{n=1}^{\infty}\left[\sin\left(\frac{n\pi y}{L}\right)\exp\left(-\frac{n^2\pi^2\alpha t}{L^2}\right)\right] \quad (3.2)$$

The result from the internal energy model (EOF) as well as the built-in Fluent enthalpy model show good agreement, as reflected in the Residual Sum of the Squares (RSS)

$$RSS = \sum_{i=1}^{n}(y_i - f(x_i))^2 \quad (3.3)$$

which is the difference in the analytical solution, y_i, and the simulation, $f(x_i)$, at a time of 600 seconds, presented in Figure 3.1(b) and (c).

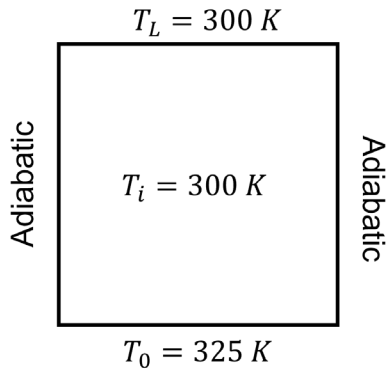
$T_L = 300\ K$
Adiabatic
$T_i = 300\ K$
Adiabatic
$T_0 = 325\ K$

(a)

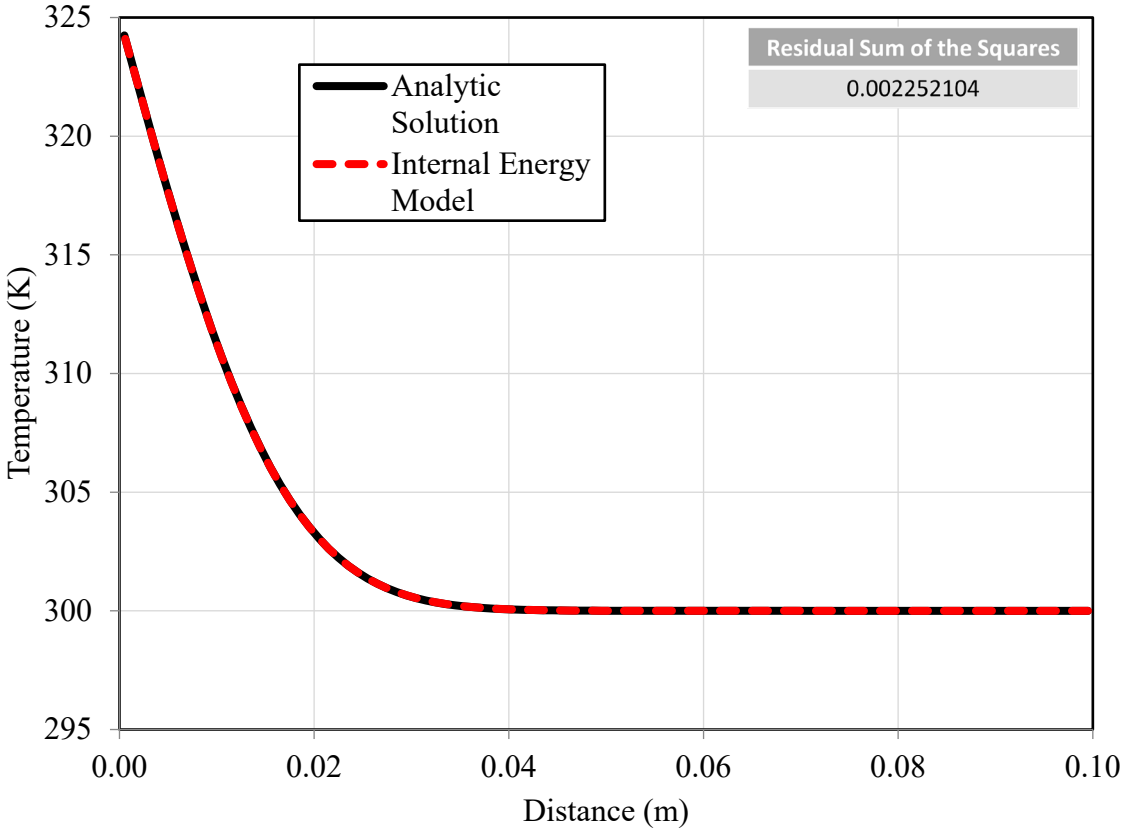
Residual Sum of the Squares
0.002252104
Analytic Solution
Internal Energy Model
Temperature (K)
325
320
315
310
305
300
295
0.00
0.02
0.04
0.06
0.08
0.10
Distance (m)

(b)

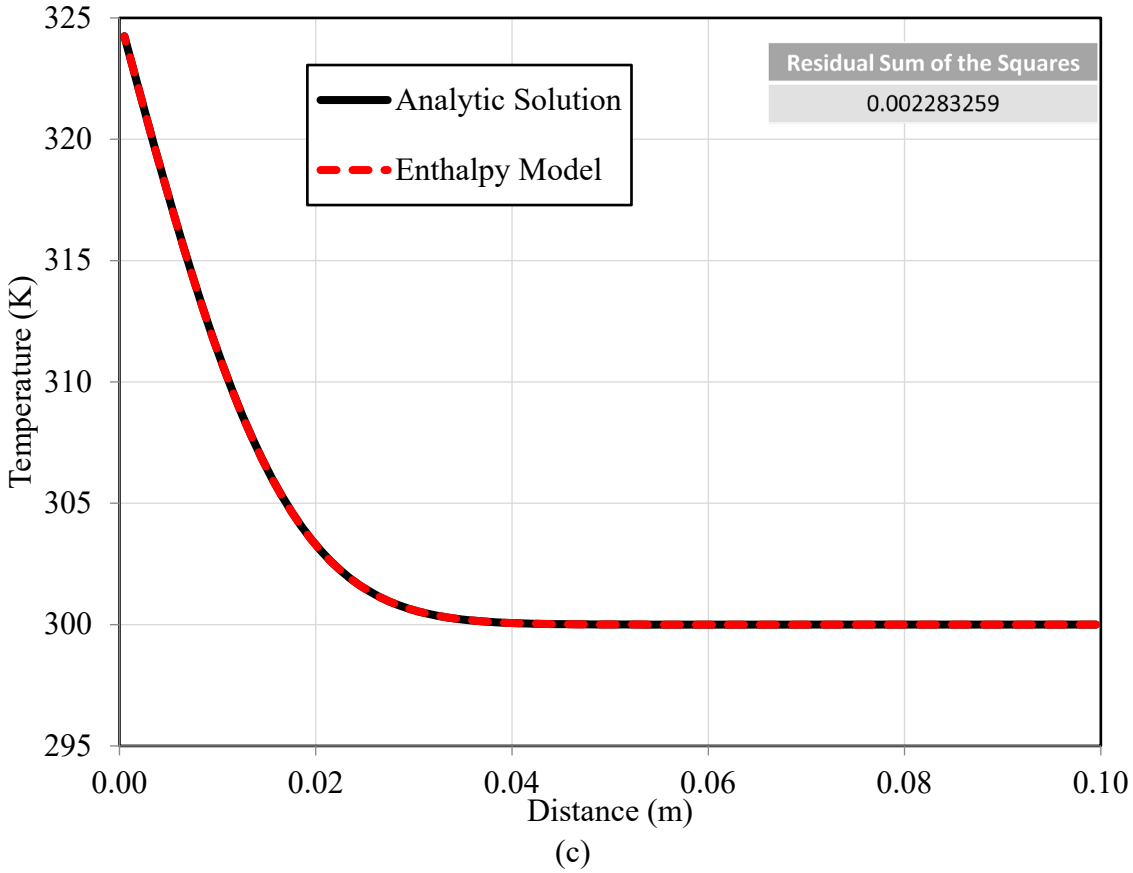

(c)

Figure 3.1 Temperature boundary case: (a) boundary and initial conditions and (b) Internal Energy Model results at 600 seconds (c) Enthalpy Model results at 600 seconds compared to Meyers analytical solution.

The second verification case for heat conduction utilizes the same geometry as the temperature boundary condition case except for the second case instead of two temperature boundaries, there were three adiabatic boundaries on the left, right, and bottom of the square cavity. The heat flux boundary condition of $200\ W/m^2$ was applied to the top wall of the cavity as shown in Figure 3.1(a). The initial temperature of the fluid was the same as in the first case, $T_i = 300\ K$. Carslaw provided an analytical solution for the specified heat flux boundary given by Equation 3.3 [84].

$$T(y,t) = T_i + \frac{2q(\alpha t)^{1/2}}{k}\sum_{n=0}^{\infty}\left[ierfc\frac{(2n+1)(L-y)}{2(\alpha t)^{1/2}} + ierfc\frac{(2n+1)(L+y)}{2(\alpha t)^{1/2}}\right] \quad (3.4)$$

$$ierfc(x) = \frac{1}{\sqrt{\pi}} e^{-x^2} - x[ierfc(x)] \tag{3.5}$$

. Figure 3.2(b) and (c) shows the results of the internal energy model EOF and Enthalpy model when compared to the analytical solution. The sum of the squares of the residuals comparing the internal energy EOF model and enthalpy model predictions to the analytic solution are 1.66591E-05 and 2.03914E-05, respectively, which demonstrates both models are in excellent agreement with analytic solution at 600 seconds of flow time.

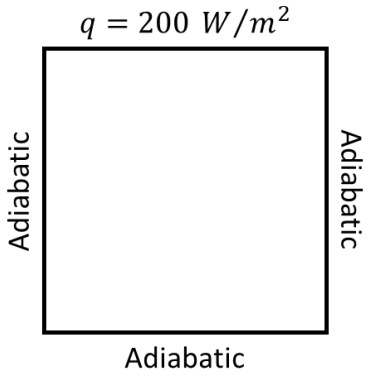
$q = 200\ W/m^2$
Adiabatic
Adiabatic
Adiabatic

(a)

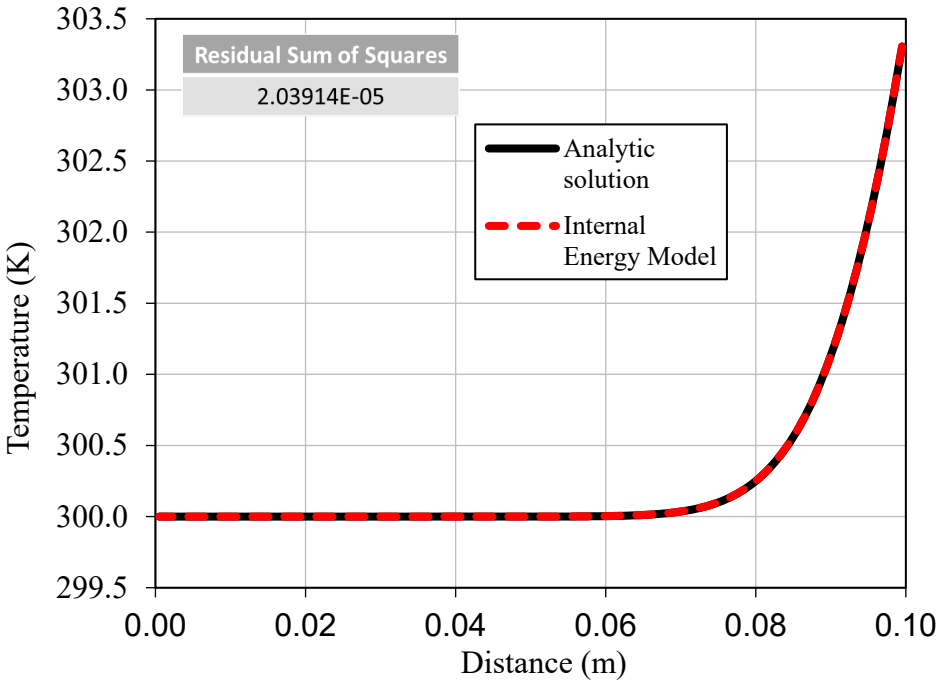
Residual Sum of Squares
2.03914E-05
Analytic solution
Internal Energy Model
Temperature (K)
303.5
303.0
302.5
302.0
301.5
301.0
300.5
300.0
299.5
0.00
0.02
0.04
0.06
0.08
0.10
Distance (m)

(b)

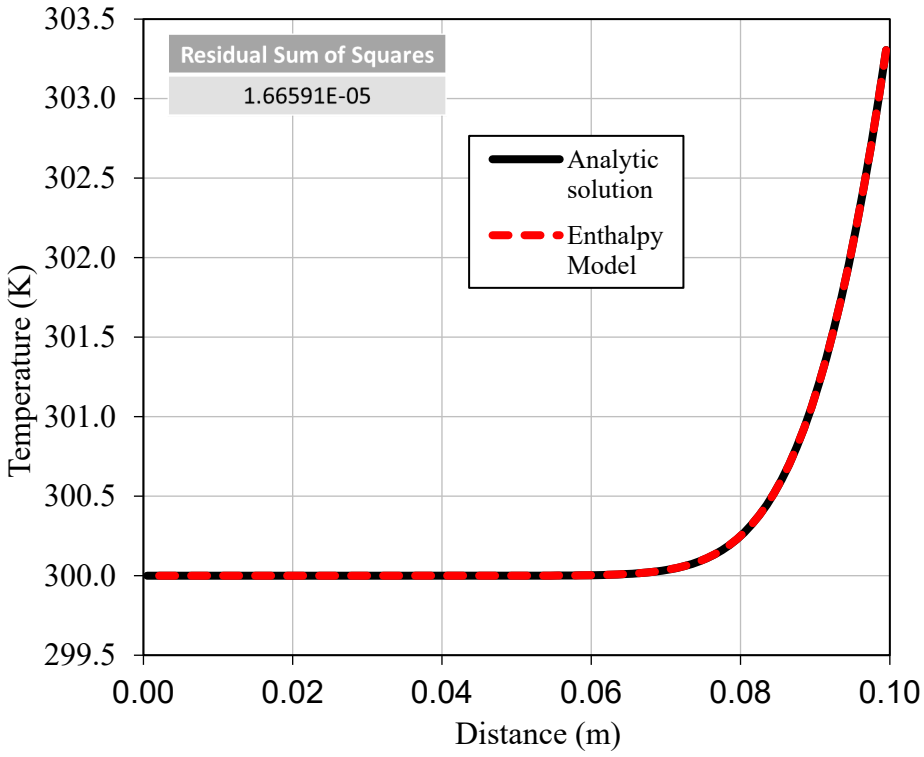

Figure 3.2 Heat flux boundary case: (a) boundary and initial conditions and (b) Internal Energy Model results at 600 seconds (c) Enthalpy Model results at 600 seconds compared to Carslaw analytical solution.

3.1.2 Conduction Heat Transfer with Phase Change

The simplest approach to verify the capability of EOF UDF to model phase change is to consider the case of conduction and solidification in one dimension. The governing equation for one-dimensional conduction phase change is

$$\rho c_v \frac{\partial T}{\partial t} = k \frac{\partial^2 T}{\partial y^2} - \rho \Delta e \frac{\partial f}{\partial y} \tag{3.6}$$

Carslaw introduced an analytical solution for pure conduction solidification in one dimension for an area initial temperature at T_i for all y, and at $y = 0$ for time, $t > 0$, the surface is maintained at T_0 [84]. The phase front, Y, is calculated for time, t, as shown in

Equation 3.6, where the root, $\lambda = 0.079$, is given in a data table presented in Carslaw and α is the thermal diffusivity for the material.

$$Y = 2\lambda\sqrt{\alpha t} \tag{3.7}$$

The two-dimensional region for $0 < y < L$, where $L = 0.1m$, the initial temperature is $T_i = 275.15K$ with the boundary conditions shown in Figure 3.1. The phase change temperature for the fluid is $T_m = 273.15K$, and the boundaries at the top and bottom are maintained at $T_{top} = 275.15K \; or \; T_{bottom} = 271.15K$. The two-dimensional geometry has the dimensions of $x = 0.0025m$ and $y = 0.1m$, so that the heat transfer is only acting in the y-direction, and the fluid will solidify in the +y-direction. The pressure is initialized and held constant at 101.325 kPa, and the material properties of water are used and listed in Table 3.2, and with a latent heat of fusion of $\Delta e = 334.944 \frac{kJ}{kg}$.

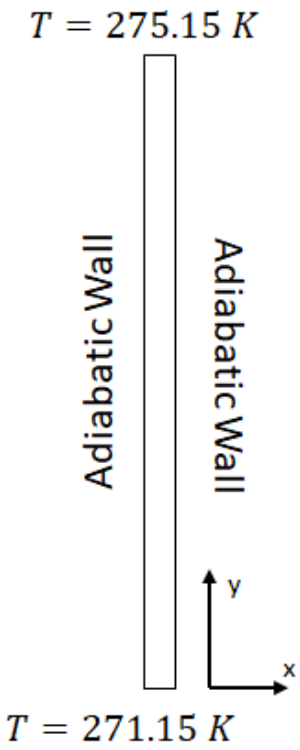

Figure 3.3 Boundary conditions for pure conduction solidification case.

Table 3.2 Material properties of water at 101.325 kPa.

Liquid at 275.15 K		Solid at 273.15 K	
$k\ (W/m*K)$	0.6029	$k\ (W/m*K)$	2.2190
$\rho\ (kg/m^3)$	1000.0	$\rho\ (kg/m^3)$	920.0
$\alpha\ (m^2/s)$	1.4400E-7	$\alpha\ (m^2/s)$	1.1476E-6
$C_p\ (J/kg*K)$	4186.8	$C_p\ (J/kg*K)$	2101.77
$C_v\ (J/kg*K)$	4186.8	$C_v\ (J/kg*K)$	2101.77

Simulations of the pure conduction solidification case are performed for a flow time of 600 seconds with a time step of 1 second using both the EOF model and enthalpy model. The location of the liquid solid interface was calculated utilized an interpolation scheme presented in Equation 3.7

$$Y = y_{cell} + (0.5 - f)\Delta y \tag{3.8}$$

where the phase front Y was a function of the y-coordinate of the cell centroid, y_{cell}, the phase fraction,f , and the vertical length of the uniform computational cell,Δy. The sharpness of the solid-liquid interface when using the enthalpy and internal energy models employed for this study will only improve when the mesh density at the interface is increased. e. Therefore, a mesh convergence study was conducted for both the EOF, and Fluent solidification model presented in Figures 3.4 and 3.5 respectively.

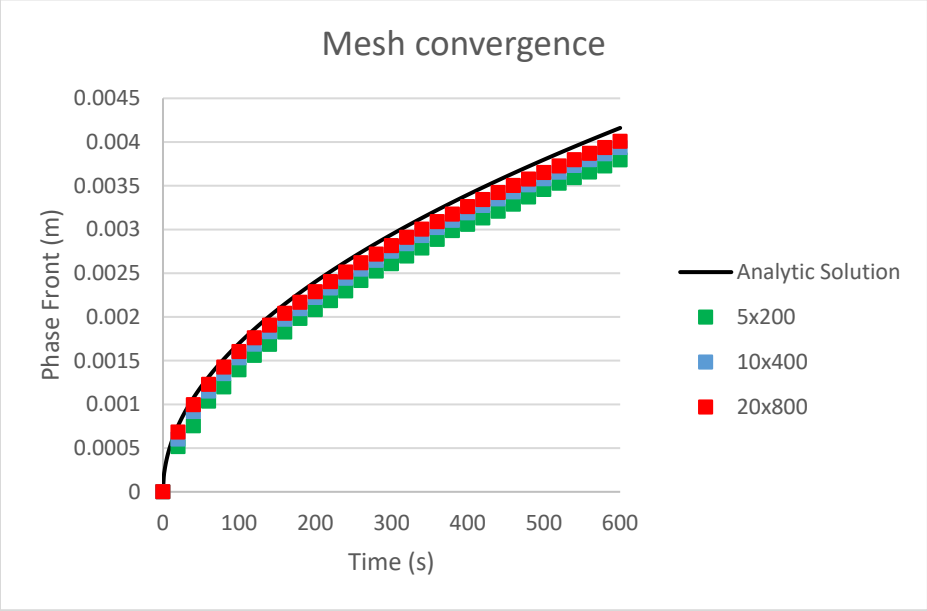

Figure 3.4 Conduction phase change: Internal Energy phase front mesh sensitivity results

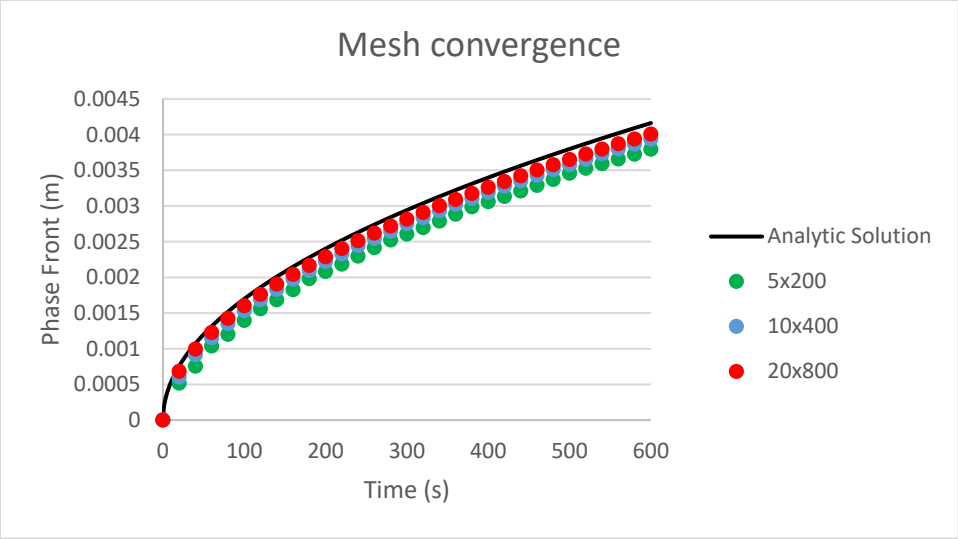

Figure 3.5 Conduction phase change: Enthalpy phase front mesh sensitivity results

From Table 3.3, as the Coefficient of Determination approaches one the more accurate the simulations. The Coefficient of Determination, or r^2, is the ratio of the disparity in the predicted value from the analytical solution shown in Equations 3.8 and 3.9.

$$Coefficient\ of\ Determination = CoD = \sqrt{\frac{TSS - RSS}{TSS}} \tag{3.8}$$

where RSS is the Residual Sum of the Squares, described in previous sections, and Total Sum of the Squares, TSS, is

$$TSS = \sum_{i=1}^{n}(y_{i-} - \bar{y})^2 \tag{3.9}$$

Given y_i is the predicted value, and $\bar{y}$ is the mean of the of the data set.

As the mesh density for the conduction phase change models was increased the Coefficient of Determination approached one, therefore the simulations are considered to be in excellent agreement with the analytic solution.

Table 3.3 Coefficient of Determination for the Internal energy (EOF) model and the Fluent Enthalpy Solidification model when compared to the analytical model

Mesh	Coefficient of Determination	
	Internal Energy	Enthalpy
5X200 cells	0.917160	0.912481
10X400 cells	0.961901	0.966120
20X800 cells	0.976120	0.977105

3.2 Convection Heat Transfer

Convection heat transfer is the energy transfer caused by bulk fluid motion, and this mode of heat transfer is present in fluid systems with a temperature differential. When there is no force acting upon the fluid other than the temperature differential, then in most cases the temperature difference gives rise to buoyancy forces caused by the density differences. The higher temperature usually causes a density reduction which gives rise to fluid motion in the presence of a gravitational field, this is referred to as natural convection.

In addition to conduction, convection is a common mode of heat transfer in real world fluid thermal system problems which can have an influence on formation and shape of a two-phase interface. Several computational methods have been developed to model real world phase change and experiments have been performed for the purposes of validating the models. Most numerical simulations showed slight differences with the experimental results at the interface and the ice front shape [19], [66]–[68]. Another phase change study by Voller and Prakash developed an enthalpy-based formulation for a fixed grid methodology to solve convection-diffusion mushy zone phase-change problem. The authors created a rectangular thermal cavity with hot and cold boundary conditions.

A mushy region was introduced in this simulation and modeled using Darcy's Law for flow in a porous media, where the enthalpy is the controlling variable. One of the main issues with the fixed grid enthalpy-based solvers is the zero-velocity condition in the solid region. The results presented showed similar results to other simulations of a similar setup [69]. Michalek simulated water freezing in a differentially heated cavity and included free convection. Ansys Fluent implemented the enthalpy-porosity method to simulate the phase change via forced convection in water. The enthalpy-porosity method solved the enthalpy-based energy equation; however, the phase front is modeled as a porous media as the dendrites of solid material are created. The authors mentioned freezing water simulations required fine meshes and reduced timestep size [70].

Kowalewski and Rebow experimented with freezing water a rectangular cavity that was differentially heated. Temperature and velocity measurements were taken and validated with a Finite Element Model (FEM) developed by the authors that uses the enthalpy formulation of the energy equation. Tracer crystals and a camera captured the velocity inside the cavity and showed comparable results to the numerical analysis [19]. Banaszek also developed a Finite Element Model (FEM) based on an enthalpy approach for the energy conservation for steady-state and phase change. Michalek developed a finite volume approach utilizing Enthalpy model for the steady-state and an enthalpy-porosity method for solidification.

3.2.1 Convection Heat Transfer: Buoyancy Driven Flow

For the first case of natural convection in a two-dimensional heated square cavity of water with a height, $H = 38\ mm$; the top wall was adiabatic while the right and left walls were isothermal at temperatures, $T_C = 273\ K$ and $T_H = 283\ K$, presented in Figure

3.6. The initial fluid temperature was $T_i = 278\ K$. This first convection case considered is the quasi-steady solution at a flow time of 2000 seconds presented by Banaszek, Kowalewski, and Rebow [19], [68-70].

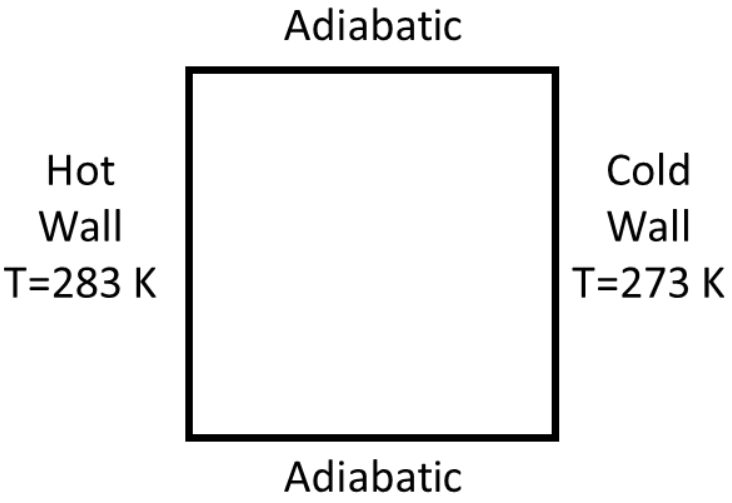

Figure 3.6 Convection boundary conditions for first 2000 seconds

The governing equations derived by the author, Michalek, for the two-dimensional system which include the enthalpy formulation of the energy equation are as follows

$$\frac{\partial u}{\partial x} + \frac{\partial v}{\partial y} = 0 \tag{3.9}$$

$$\rho \frac{\partial u}{\partial t} + \rho u \frac{\partial u}{\partial x} + \rho v \frac{\partial u}{\partial y} = -\frac{\partial P}{\partial x} + \mu \Delta u \tag{3.10}$$

$$\rho \frac{\partial v}{\partial t} + \rho u \frac{\partial v}{\partial x} + \rho v \frac{\partial v}{\partial y} = -\frac{\partial P}{\partial y} + \mu \Delta v - g[\rho(T) - \rho] \tag{3.11}$$

$$\frac{\partial \rho c_p T}{\partial t} + \nabla \cdot \left(\rho \vec{V} c_p T\right) = \nabla \cdot (k \nabla T) \tag{3.12}$$

where u, v P,g, T, and α denote the horizontal and vertical velocities, pressure gravitational acceleration, temperature, and thermal diffusivity, respectively. Michalek,

Kowalewski, and Rebow present a fourth order polynomial for the density as a function of temperature:

$$\rho(T) = 999.8 + 0.0673T - 0.0089T^2 + 8.785E(-5)T^3 - 6.621E(-7)T^4 \quad (3.3)$$

Table 3.4 Properties of water presented by Michalek

Material Properties of liquid water		Value	Units
ρ	density of water	999.8	kg/m^3
μ	dynamic viscosity	0.001003	kg/ms
$v = \mu/\rho$	kinematic viscosity	1.0032E(-6)	m^2/s
k	thermal conductivity	0.6	W/mK
c_{liquid}	specific heat	4182	J/kgK
g	gravitational acceleration	9.81	m/s^2
$\alpha = k/\rho c_p$	thermal diffusivity	1.435E(-7)	$m^2 s$
β	thermal expansion coefficient	6.734E(-5)	$1/K$
$Ra = g\beta(T_H - T_C)L^3/\alpha v$	Rayleigh number	2.518E(6)	n/a
$Pr = v/\alpha$	Prandtl number	6.99	n/a

A 76 x 76 cell uniform mesh is utilized for the 38 x 38 mm square computation domain. and a simulation time of 2000 seconds is specified. Banaszek's finite element model, Michalek's enthalpy model, and the EOF internal energy model are all compared to the experimental results obtained by Kowalewski and Banaszek. As the simulation advances in time, water in contact with the cold wall flows in the direction of gravity as the water density increases due to the lower temperature. Water along the hot wall rises along the wall in the opposite the direction of gravity as the density of the water decreases due to the higher wall temperature. A large area of clockwise circulation due to the natural convection forms. A small area of counterclockwise circulation forms in the bottom right corner of the cavity consistent with the experimental results as time progressed until 2000 seconds is reached. Figure 3.7 shows the model predictions and

experimental results depicting the two areas of circulation. The complex experimental flow pattern presented in Figure 3.7 was achieved with suspended thermochromic liquid crystals and digital particle image velocimetry.

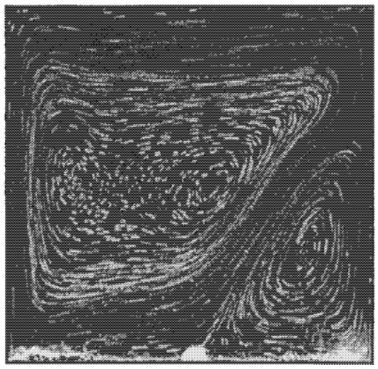

Figure 3.7 Complex experimental flow pattern presented in Banaszek

The simulations reach a quasi-steady state when these positive and negative buoyant forces are balanced across the domain. The temperature profiles for the Enthalpy model, finite element model (Banaszek), and the Internal Energy model are shown in Figure 3.8 (a), (b), and (c) respectively.

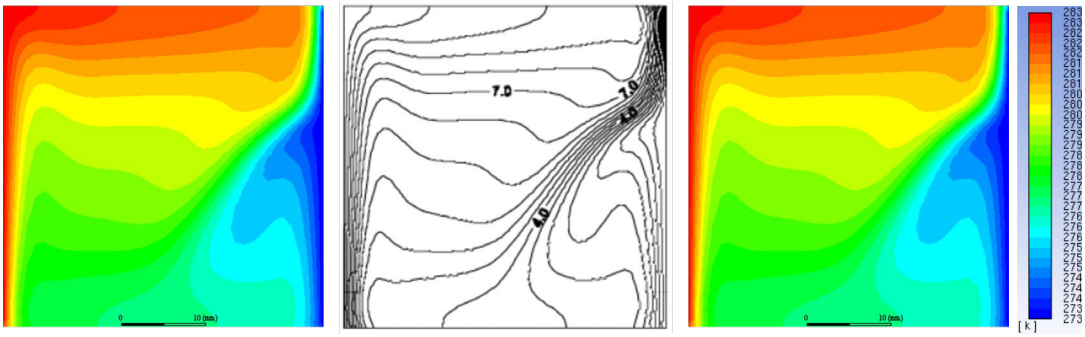

(a) (b) (c)

Figure 3.8 Temperature Contours for: (a) Enthalpy model, (b) Banaszek enthalpy finite element model, and (c) EOF Internal Energy model

The simulations are further validated by comparing the local vertical velocity components in the $+Y$ direction along three dimensionless height ratios, $Y/H = 0.25, 0.50, and\ 0.75$. Figure 3.9 (a-c) presents the y-component of the velocities of the models and the experimental results. All the simulations predictions are in good agreement with the experimental results.

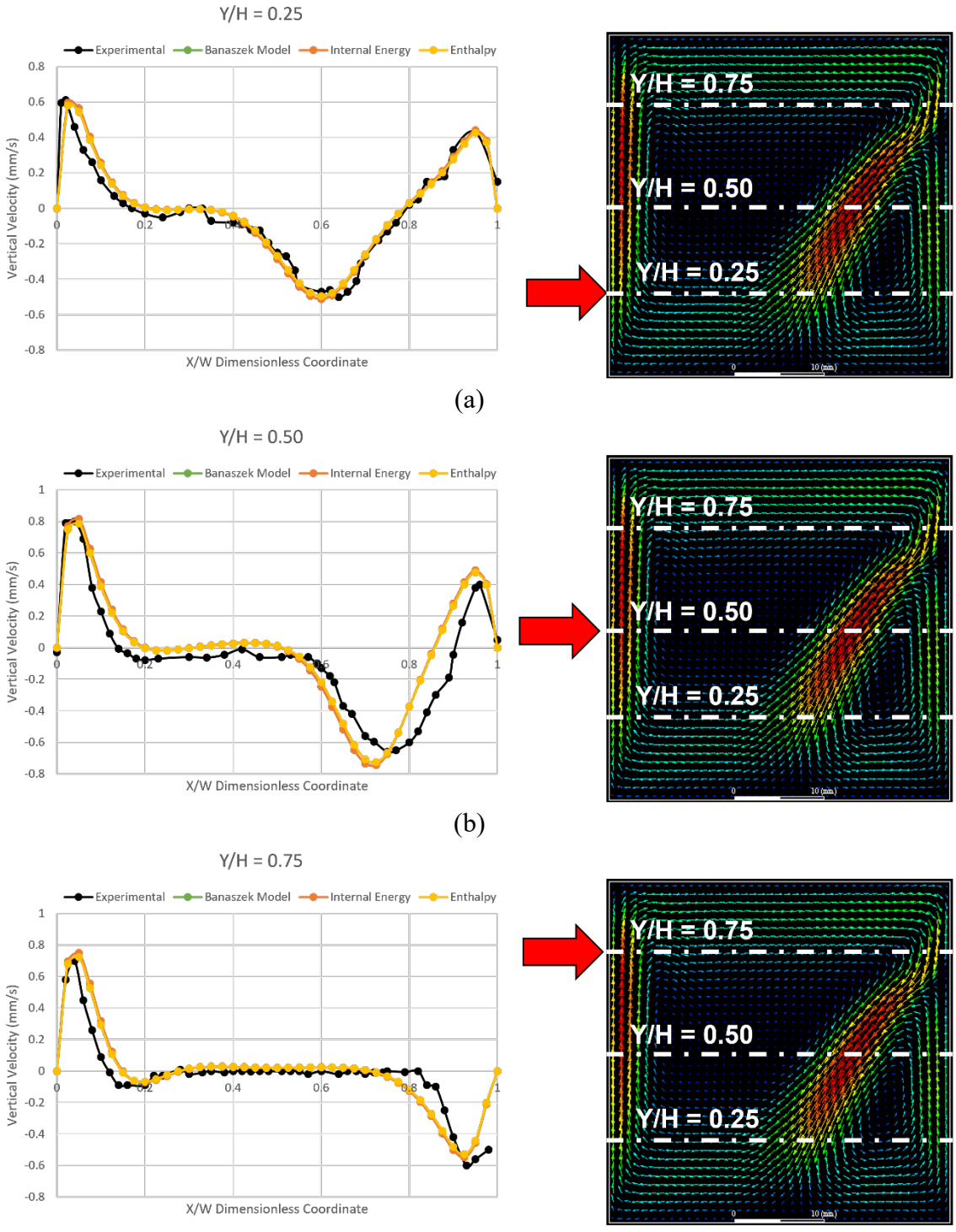

Figure 3.9 Y-velocity component at flow time of 2000 seconds and at locations: (a) Y/H = 0.25 and (b) Y/H = 0.50 and (c) Y/H = 0.75

Table 3.5 Coefficient of Determination for the Banaszek, Internal energy (EOF) model, and the Enthalpy convection model when compared to the experimental data

Height ratio, Y/H	Coefficient of Determination		
	Banaszek Model	Internal Energy	Enthalpy
0.25	0.770988	0.976251	0.977473
0.50	0.937200	0.868572	0.879739
0.75	0.968183	0.875747	0.883220

3.2.2 Convection Phase Change: Buoyancy Driven Flow

The second case for validation of convection is a continuation of the previous case with the inclusion of phase change or solidification of the water inside the cavity. Kowalewski presents the enthalpy formulation of the energy equation for solidification phase change as

$$\frac{\partial \rho c_p T}{\partial t} + \nabla \cdot \left(\rho \vec{V} c_p T\right) = \nabla \cdot (k \nabla T) - \lambda \frac{\partial (\rho f)}{\partial t} \tag{3.14}$$

where λ is the latent heat of fusion and f is the phase fraction. Source terms are added to the momentum equations (Equations 3.9 and 3.10 above) to suppress the velocities as the fluid solidifies. Darcy's law for flow in a porous media is utilized for the source terms which is a function of the phase fraction and the velocity component at the cell center as shown in Equation 3.14.

$$S_{\vec{v}} = -C \frac{(1-f)^2}{f^3 + 0.001} \vec{v} \tag{3.15}$$

The constant in the Darcy source term is $C = 10^8$ and $\vec{v}$ is the velocity vector. The phase fraction is equal to one in the liquid phase, and as the liquid undergoes solidification the phase fraction will change from to a value less than 1 and greater than or equal to zero. .. Therefore, as the cell solidifies the source term decreases the cell velocity until the

velocity equals zero when the phase fraction equals zero. Equations 2.6 – 2.11 from the previous section are utilized for the internal energy (EOF) model with the addition of the Darcy source terms.

The thermo-physical properties of the ice or the solid phase are assumed to be constant and given as $k_{solid} = 2.2\,W/mK$, $c_{solid} = 2116\ J/kgK$, $\rho_{solid} = 920\,kg/m^3$, $\Delta e = 335\,kJ/kg$ for the thermal conductivity, specific heat, density and the latent heat.

The quasi-steady simulation results from the previous validation case at 2000 seconds are used as the initial conditions for the solidification case. The temperature of the cold wall is instantaneously decreased 273 K to 263 K, which is 10 degrees below the freezing point temperature for water. Figure 3.10 shows the boundary conditions for the given case.

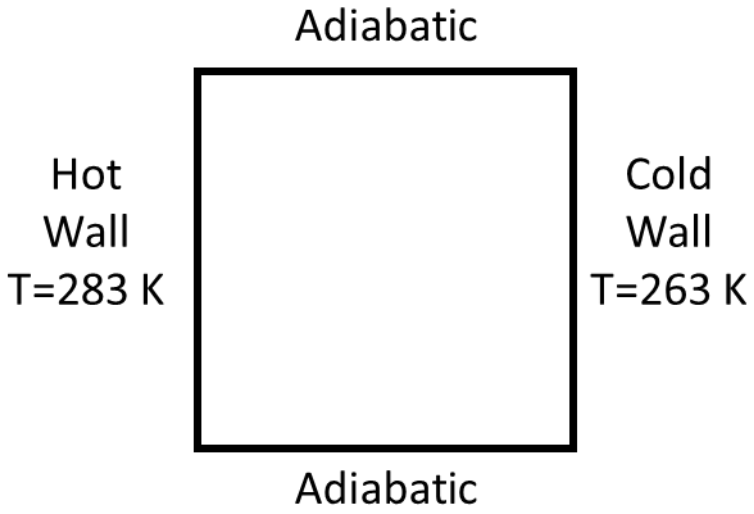

Figure 3.10 Convection boundary conditions beginning at 2000 seconds and running for another 3000 seconds

This solidification simulation is setup with a computational time of 3000 seconds. As the simulation progresses ice begins to form along the cold wall forcing the competing

vortices to shift toward the hot wall. Figure 3.11 shows the experimental results with the suspended crystals to indicate flow patterns in the cavity and the solid section of ice forming along the cold wall. The two vortices were visible in the experiment images with the lower counterclockwise rotation being smaller in size than the clockwise rotation formed from the flow of the water from the hot wall towards the cold wall. This had an impact on the ice formation shown in the figures, as the ice was much thicker along the bottom of the cavity whereas the warmer water from the hot wall reduces the rate of ice formation.

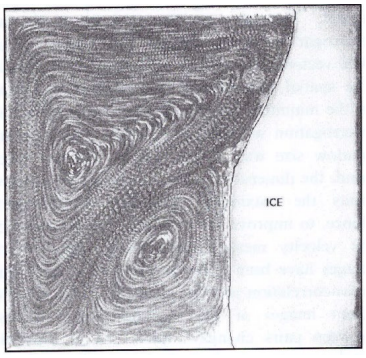

Figure 3.11 Kowalewski and Rebow experimental results for velocity and ice formation in a differentially heated cube [reference]

Banaszek's FEM enthalpy model predictions of ice formation and the velocity field, shown in the Figure 3.12 are in good agreement with the experiment results presented in Figure 3.11. Figure 3.13 shows the phase fraction predictions using internal energy (EOF) model and the enthalpy model Both models are in excellent agreement.

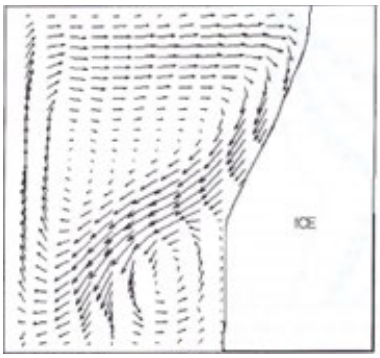

Figure 3.12 Banaszek numerical results for velocity and ice formation in a differentially heated cube

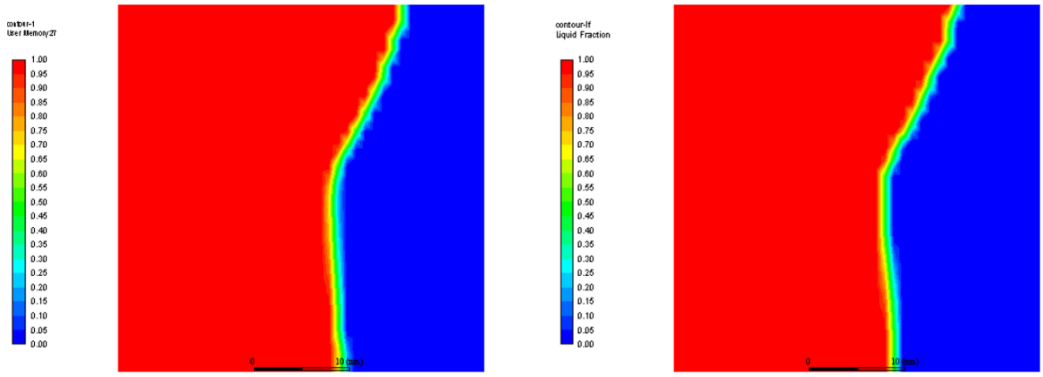

(a) (b)

Figure 3.13 Phase fraction results after 3000 seconds for (a) Internal Energy (EOF) model and (b) Enthalpy model

The velocity profiles presented in Figure 3.14 (a) and (b) for the internal energy (EOF) model and enthalpy model shows that the two vortices are similar to the experimental results. The internal energy model shows a slightly higher upward velocity in the lower vortex along the interface.

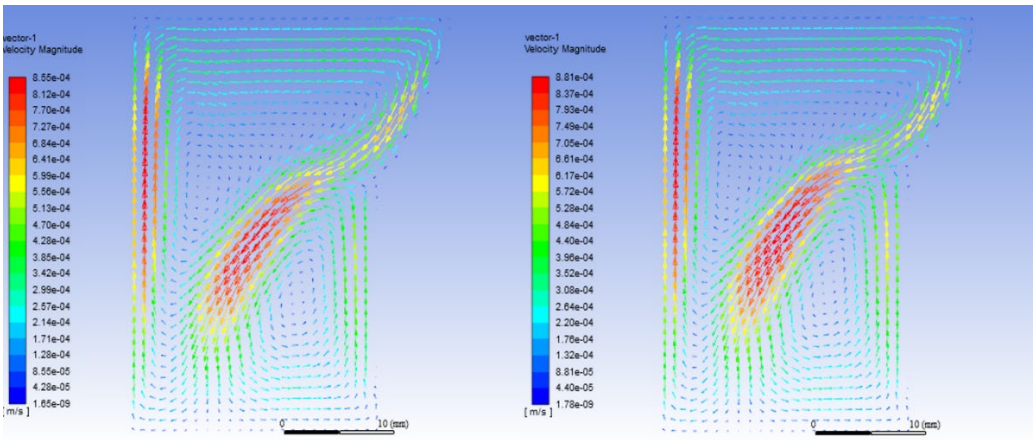

(a) (b)

Figure 3.14 Velocity profiles after 3000 seconds for (a) Internal energy (EOF) model and (b) Enthalpy model

The temperature contours, shown in Figure 3.15, for the different models are also in excellent agreement. Conduction can be observed through the ice formed in the cavity while natural convection dominates liquid flow field along warm wall boundary.

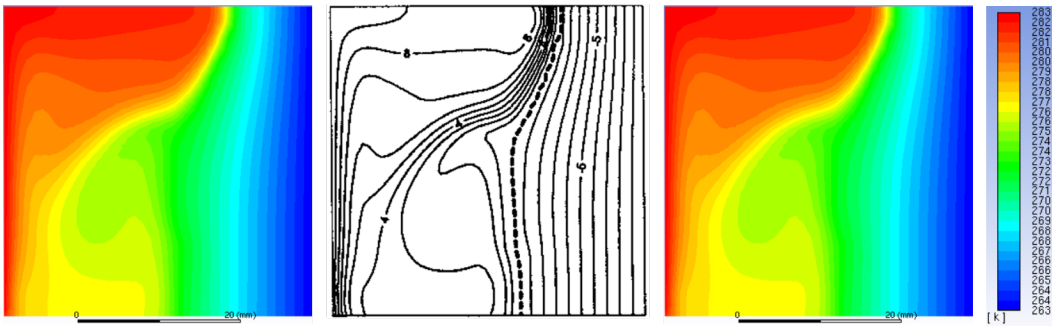

(a) (b) (c)

Figure 3.15 Temperature Contours for: (a) Enthalpy, (b) Banaszek enthalpy finite element model, and (c) internal energy (EOF) model

As in the previous case, the simulations are quantitatively compared using local vertical velocity components along three dimensionless coordinates, $Y/H = 0.25,\ 0.50,$ and , 0.75. Figure 3.16 (a-c) presents the y-component of the velocities for all the models

and the experimental results. As illustrated in the figures, the vertical velocity components are zero in the ice near the cold boundary. It is also apparent in the figures that the models all differ from the experimental results slightly. The greatest difference can be observed in the recirculation zone near the phase front which was larger in size in all of the models as compared to the experiment results. Even with this difference, the previous authors concluded their model predictions were in reasonable agreement with the experimental results. For the purposes of this study, it should be noted the internal energy model predictions are consistent with the predictions obtained using the enthalpy model.

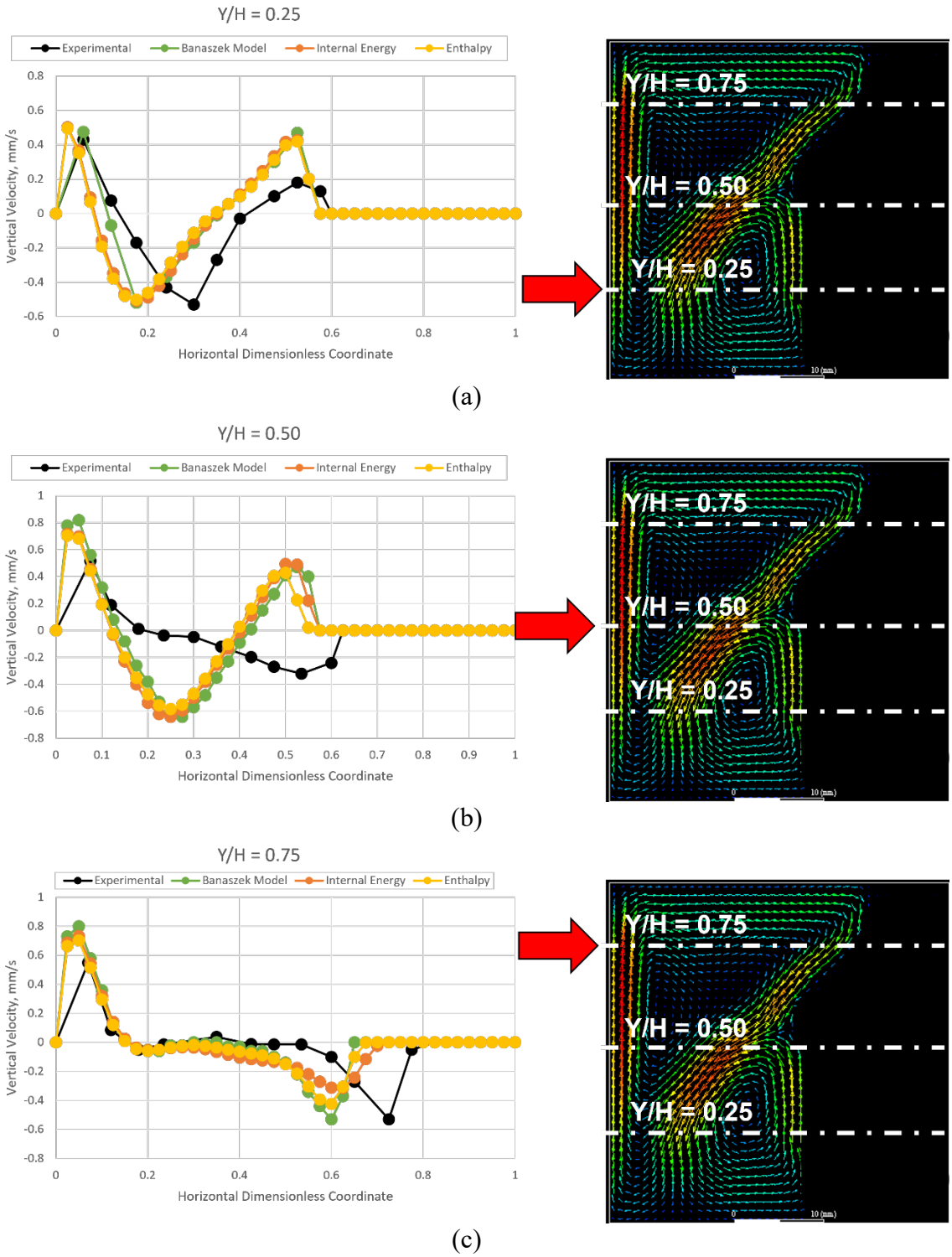

Figure 3.16 Y-velocity component after 3000 seconds and at locations: (a) Y/H = 0.25 and (b) Y/H = 0.50 and (c) Y/H = 0.75

Table 3.6 Coefficient of Determination for the Banaszek, Internal energy (EOF) model, and the Enthalpy solidification model when compared to the experimental data

Height ratio, Y/H	Coefficient of Determination		
	Banaszek Model	Internal Energy	Enthalpy
0.25	0.979952	0.954509	0.961564
0.50	0.871964	0.894995	0.862422
0.75	0.935754	0.934603	0.935564

Code verification of the internal energy approach (EOF) demonstrated the model produced accurate results when compared to other enthalpy models and experimental results for water contained in a differential heated cavity for a steady state and phase change simulations.

CHAPTER IV

RESULTS

The ability to validate computer models or codes depends on the availability of valuable experimental results, without useful data, assumptions would have to be made in the models which could lead to unacceptable simulation results. “Validation is the assessment of the accuracy of a computer model with experimental or real world data [85].” The GODU-LH2 IRAS tank described in previous section was well instrumented with temperature and pressure sensors with locations presented in Table 4.1. This is the only large-scale tank to accomplish LH2 densification and solidification. Figure 4.1 shows the GODU-LH2 tank with the refrigerant coils in different views. In Figure 4.1 (c) the top view shows the refrigerant coils. For the simulations, the computational domain consists of a three-dimensional section of a tank which contains a segment of the asymmetric refrigeration coil. Ignoring the effects of the endcaps of the GODU-LH2 IRAS tank, the tank segment used for the simulation includes the asymmetric refrigeration coil and is repeatable along the length of the tank as shown in Figure 4.2. A periodic permeable boundary condition is applied along the two plane surfaces of the computational domain. A no-slip wall boundary condition is specified along the cylindrical tank wall.

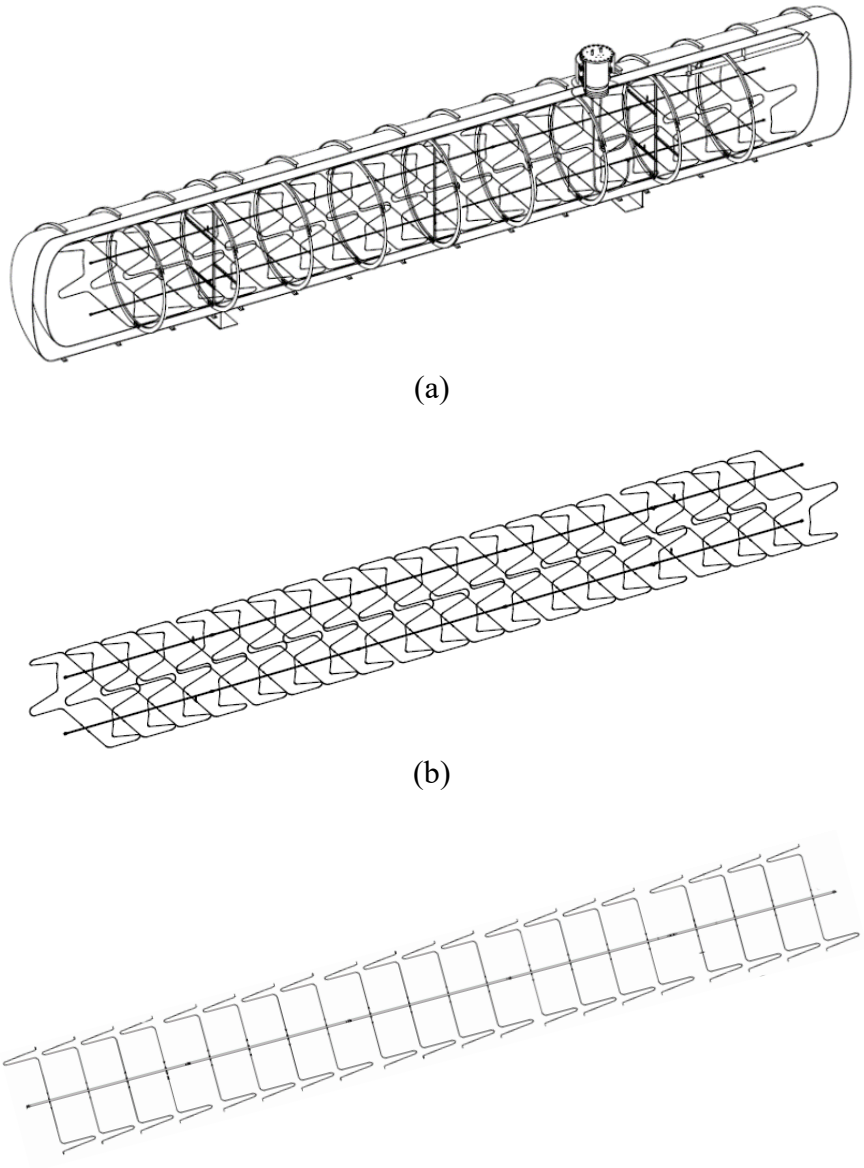

Figure 4.1 GODU-LH2 tank and heat exchanger: (a) isometric view of tank and heat exchanger, (b) isometric view of heat exchanger, (c) top view of heat exchanger

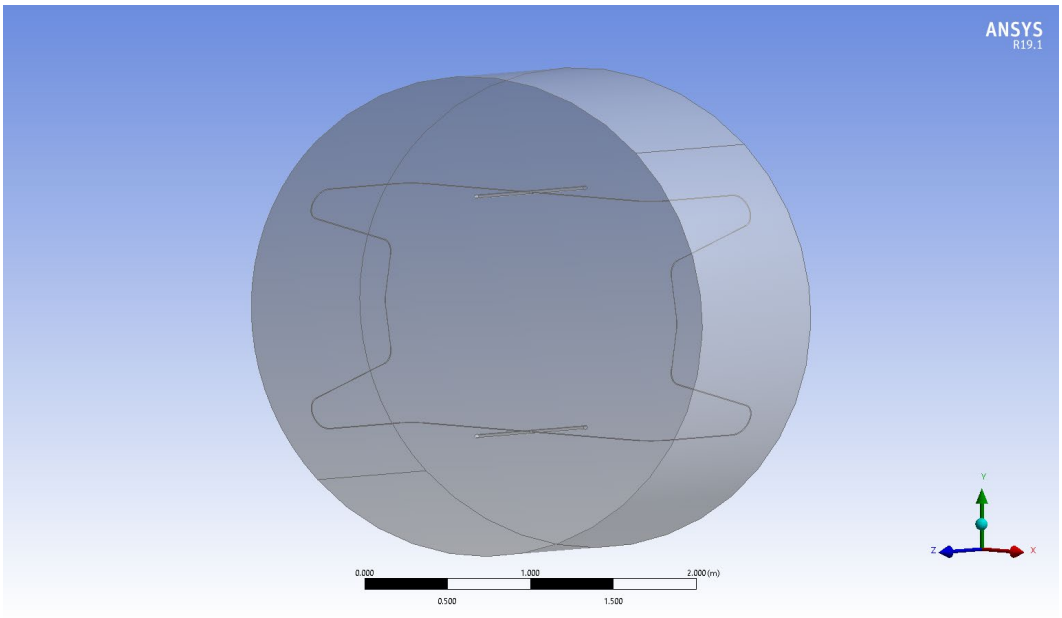

Figure 4.2 Tank computational domain with single refrigerant coil

The GODU-LH2 IRAS tank is configured with thermocouples to measure the temperature at various locations inside the tank and to gauge the liquid fill level. The positions of all the thermocouples within the tank are presented in Table 4.1. Most of the thermocouples in Table 4.1 are positioned along the same horizontal planes to assess whether the expected stratification of temperatures of LH2 within the tank are relatively consistent along a horizontal plane of the tank. The refrigerant coil boundary condition specified in the simulation was based on the measurements obtained from thermocouples, TT23 and TT24, which were inserted into the helium refrigerant coil. The thermocouples TT3, TT4, TT9, TT10, TT15, and TT16 are attached vertically to a mount inside the tank to measure the temperature of hydrogen. A “100% fill level” corresponds to maximum allowable liquid fill volume which is 90% of the total tank volume. Conversely, 10% of the total tank volume is allocated for the ullage. The maximum allowable fill volume for the 100% fill level of LH2 is 125,000 L of LH2 at NBP. As shown in Figure 4.3, at a

100% fill level, thermocouples TT3 – TT16 are submerged in the liquid hydrogen. For a 67% fill level, TT15 and TT16 measure the temperature of the ullage space while TT3, TT4, TT9, and TT10 are measuring temperature in the liquid. In both cases, the specified fill level is not a percentage of the total tank volume, but a percentage of the maximum allowable liquid fill volume.

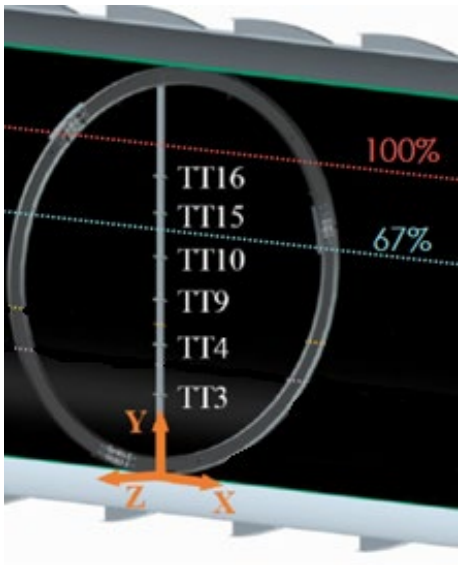

Figure 4.3 Tank fill levels and thermocouple locations

Table 4.1 Temperature sensor coordinates inside the GODU-LH2 IRAS tank

Sensor #	Distance (m)			Sensor #	Distance (m)		
	X-dir	Y-dir	Z-dir		X-dir	Y-dir	Z-dir
TT1	-4.11	0.57	0.16	TT11	-4.11	1.24	0.00
TT2	-4.11	0.57	-0.99	TT12	-4.11	1.24	1.27
TT3	0.12	0.57	0.08	TT13	-4.11	2.12	0.00
TT4	0.12	0.92	0.08	TT14	-4.11	1.85	0.08
TT5	6.27	0.57	0.00	TT15	0.12	1.85	0.08
TT6	6.27	0.57	1.15	TT16	0.12	2.12	0.08
TT7	6.27	1.24	0.16	TT17	6.27	2.12	0.00
TT8	6.27	1.24	-1.10	TT18	6.27	1.85	1.39
TT9	0.12	1.24	0.08	TT19	6.27	2.72	0.00
TT10	0.12	1.54	0.08	TT20	-4.11	2.72	0.00

*Note: Directions correspond to the coordinate system in Figure 4.3

The temperature and pressure measurements obtained during the 100% and 67% fill level experiments are presented in Figures 4.4 and 4.5 which show the various phases for each experiment at both the fill levels. The liquid was loaded during the tanker off load portion, and then the boiloff testing began for both fill levels. Several ZBO experiments were conducted such as: Duty Cycling (ZBO-DC), Pressure Controlled (ZBO-PC), and Temperature Controlled (ZBO-TC). For the ZBO-DC, the helium refrigerator was turned on and off running at full power creating temperature and pressure cycles in the IRAS tank. In the ZBO-PC phase, the refrigerator output heater was controlled using the IRAS tank pressure as the control point, and if the tank pressure increases above the set point, the heater power is reduced, thus increasing the refrigeration capacity delivered to the tank. In the ZBO-TC portion the temperature of the helium supply was controlled with a refrigerator command and software. The final section of experimentation consists of the densification phase, which also includes solidification once the LH2 reached the triple point. The 100% fill experiment was halted before the triple point was reached due to the impending project close-out, coupled with a shut-down caused by hurricane Matthew that made landfall at KSC in October 2016; however, the 67% fill test was maintained at the triple point for approximately 30 hours which suggests that's a portion of the LH2 solidified.

From Figures 4.4 and 4.5, diodes TT21 – TT24 were inserted in the helium flow stream at the top and bottom of two heat exchanger coils to measurer the inlet and outlet temperatures of the helium refrigerant in the refrigeration coils. Pressure transducer, or PT 2, was used to measure the tank pressure.

Both fill level experiments had periods designated for Boiloff Testing. Data collected during the Boiloff Testing period, which is presented in Table 4.2, is utilized to calculate of the heat leaks into the tank for each fill level test. The heat fluxes shown in Table 4.2 are used to specify a thermal boundary condition at the tank wall in simulations.

The Lumped Node Analysis performed by A. M. Swanger, from Section 1.2, focuses on a segment of Densification testing region in Figure 4.4. The Lumped Node analysis segment occurs over a period of 150 hours with initial conditions of pressure at 52.0 kPa and temperature at 18.2 K. The 67% fill case Lumped Node analysis initial conditions were given at a pressure of 71.7 kPa and temperature of 19.2 K.

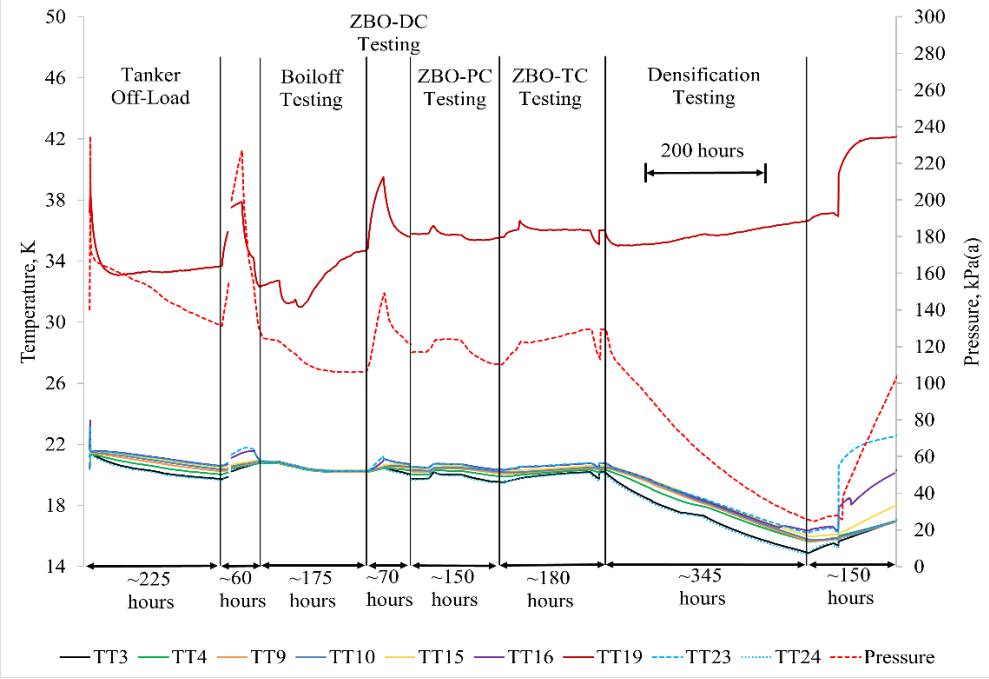

Figure 4.4 100% fill data for the experimental study period with Steady State and Densification analysis for the lumped node model regions highlighted.

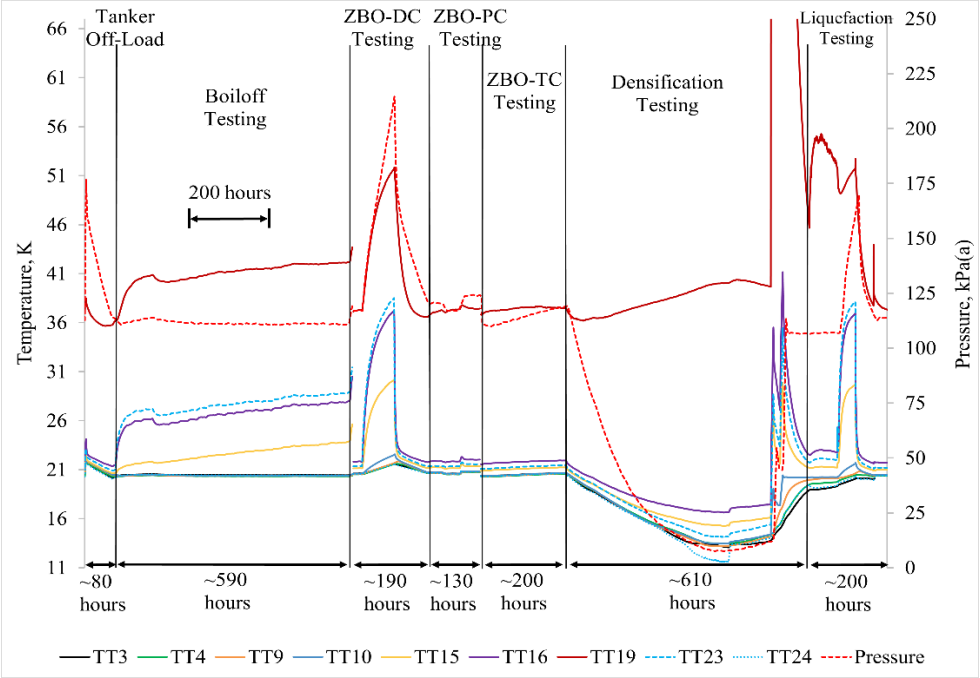

Figure 4.5 67% fill data for the experimental study period with Steady State and Densification analysis for the lumped node model regions highlighted

Table 4.2 GODU-LH2 boiloff heat leak results

Fill Level	Boiloff Flow Rate (slpm)	Tank Pressure (kPa)	Avg. Liquid Temp (K)	TT19 Reading (K)	Liquid Heat Load (W)	Ullage Heat Load (W)	Total Heat Load (W)	Total Heat Flux† (W/m^2)
67%	295	117.2	20.4	41.3	196	100	296	1.28
100%	351	109.6	20.3	34.5	234	81	315	1.36

†Based on log-mean area between the outside of the inner shell and the inside of the outer shell

4.2 Steady State Operation: Zero Boiloff Analysis

For a LH_2 tank without an active system to prevent tank self-pressurization, as heat leaks into the system, the boiloff gases must be vented. Thus, the mass flow rate of vented boiloff vapor can be measured. The mass flow rate is a function of the heat leak, and the temperature as it exits the system. In a pure ZBO system, the refrigerator lift

capacity equals the heat leak. For the study the ZBO operation of the GODU-LH2 IRAS tank, the system is maintained at a constant pressure and consequently, the temperatures remain relatively unchanged. The ZBO analysis region was taken from the ZBO-PC portion of the experimentation, due to the comparatively steady nature of the pressure and temperature inside the tank. From Table 4.2 the calculated heat leak into the tank is applied as the outer wall boundary condition, and the refrigerator coil boundary is based on temperature recorded by the diodes TT21 – 24 as shown in the ZBO-PC experiments presented in Figures 4.4 and 4.5. The initial conditions for the 100% fill case for tank pressure and temperature were 124.125 kPa and 20.4 K, respectively. For the 67% fill case, the initial conditions are 117.225 kPa and 20.4 K for tank pressure and temperature. Both fill cases reached a quasi-steady state at approximately 100 hours of flow time when the changes in temperatures, pressure, and velocities and are negligible. After quasi-steady state was reached in all cases, the ZBO simulations began.

4.2.1 100% Fill Level

For the 100% fill level case simulations, an eighteen-hour period during the ZBO-PC phase was analyzed. The simulations for the 100% fill level steady-state were performed using three polyhedral meshes an example of which is shown in Figure 4.6.

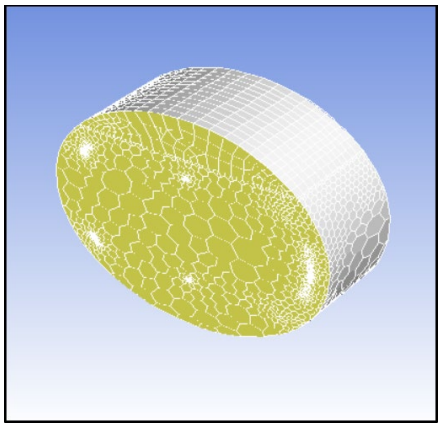

Figure 4.6 Example of the 100% fill level polyhedral mesh

The cell count for the 100% fill level polyhedral meshes are approximately: 200K cells, 350K cells, and 500K cells

A time series of temperature profiles for the Enthalpy and Internal Energy models for a plane inside the IRAS tank are shown in Figures 4.7 (a – c) and Figure 4.9 (a – c), respectively. It is apparent from the time series of temperature profiles; the ullage stratifies more quickly to a quasi-steady state than the liquid. This is due in part to the relatively larger increase in velocities over time in the ullage space. Figure 4.8 (a – c) and Figure 4.10 (a – c) show the velocity magnitudes inside the tank along a centralized plane for the Enthalpy and the Internal Energy models, respectively. It is apparent from the velocity magnitudes for both models, the liquid density increases when the liquid is in contact with the refrigeration coil which results in the flow of the liquid towards the tank wall in the same direction as gravity. As a result of the heat flux into the tank through the tank walls the liquid density decreases when the liquid is in contact with the tank wall which results in the flow of the fluid in the opposite direction of gravity along the side of the walls. The liquid flow is turned in towards the center of the tank due to the liquid vapor interface such that the net effect is the formation of recirculation regions.

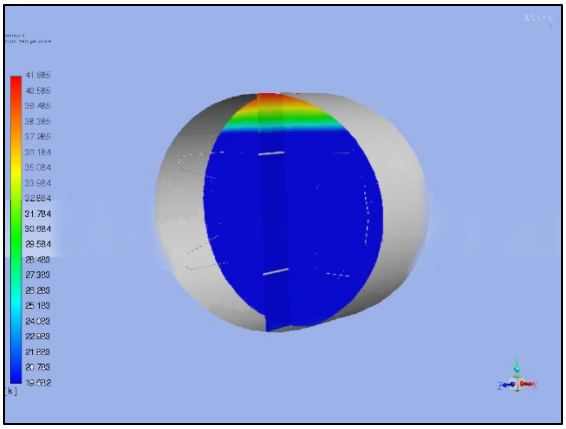

(a)

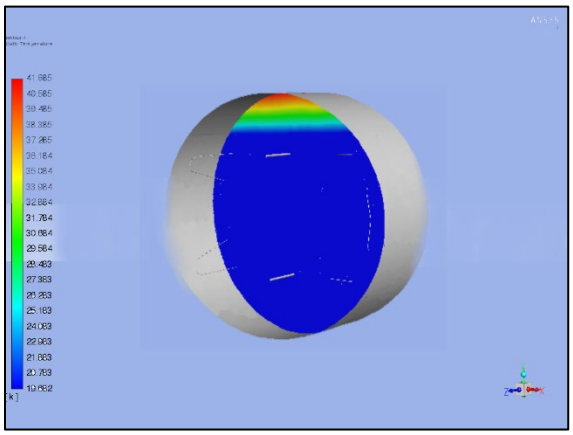

(b)

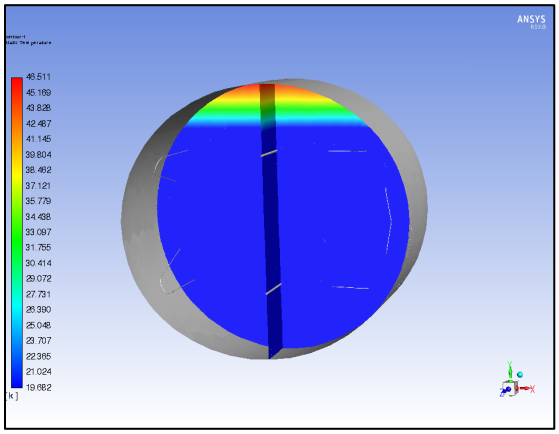

(c)

Figure 4.7 Temperature profiles for the Enthalpy method at (a) 15 minutes, (b) 60 hours, (c) 120 hours; and for the Internal Energy method at (a) 15 minutes, (b) 60 hours, (c) 120 hours

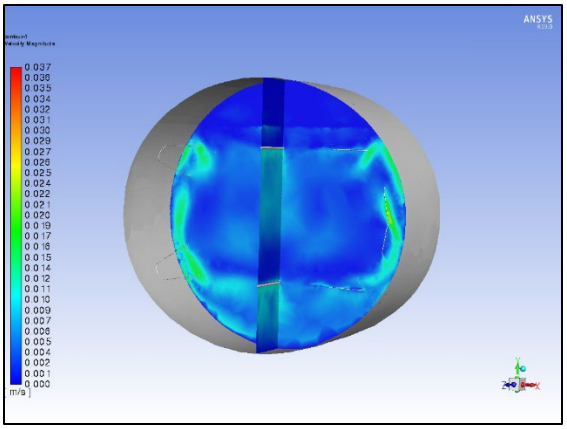

(a)

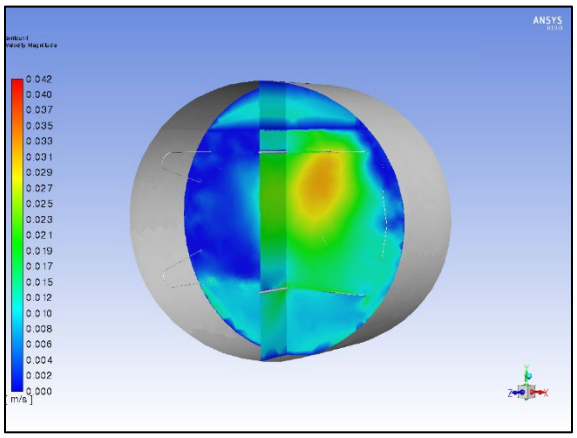

(b)

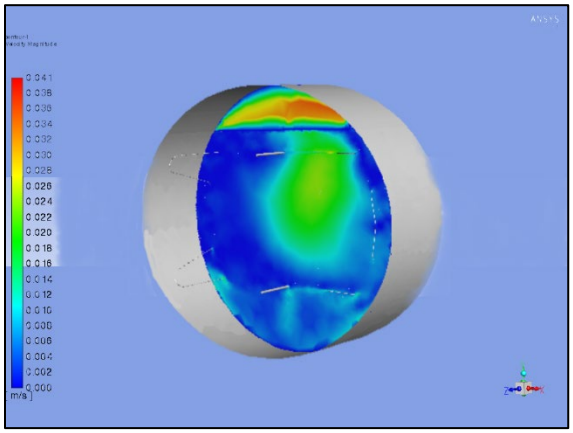

(c)

Figure 4.8 Velocity profiles for the Enthalpy method at (a) 15 minutes, (b) 60 hours, (c) 120 hours; and for the Internal Energy method at (a) 15 minutes, (b) 60 hours, (c) 120 hours

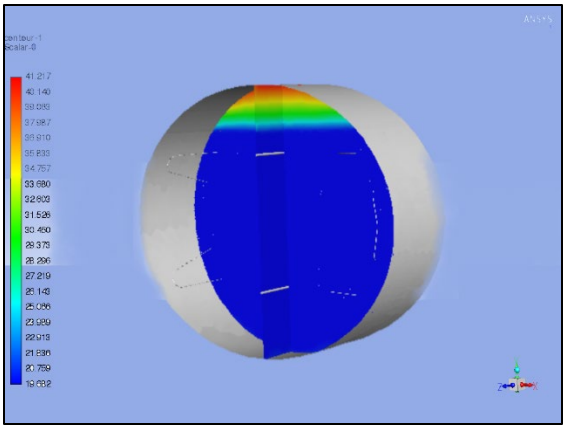

(a)

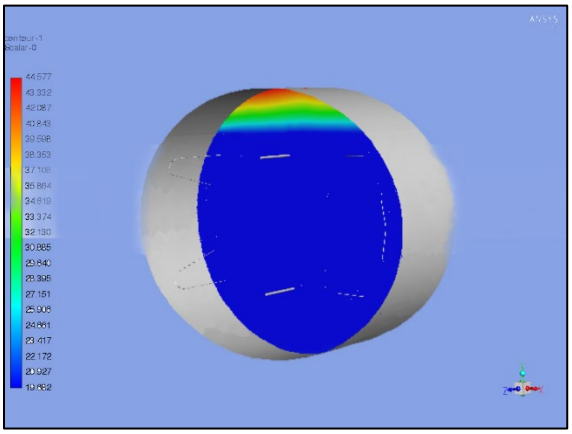

(b)

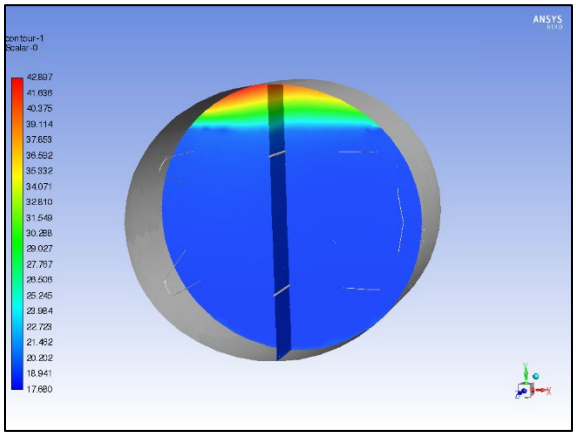

(c)

Figure 4.9 Temperature profiles for the Internal Energy method: (a) 15 minutes from beginning of simulation, (b) 60 hours through simulation, (c) final simulation time of 120 hours

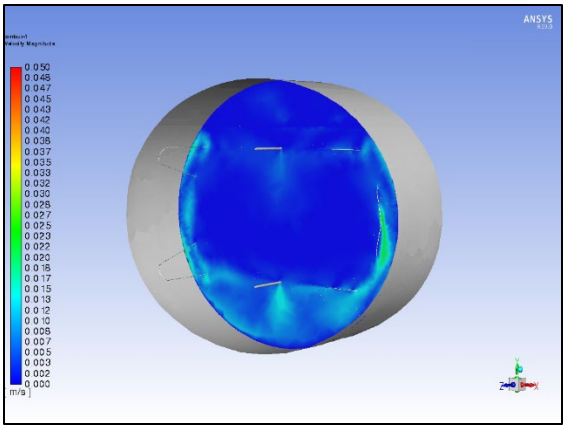

(a)

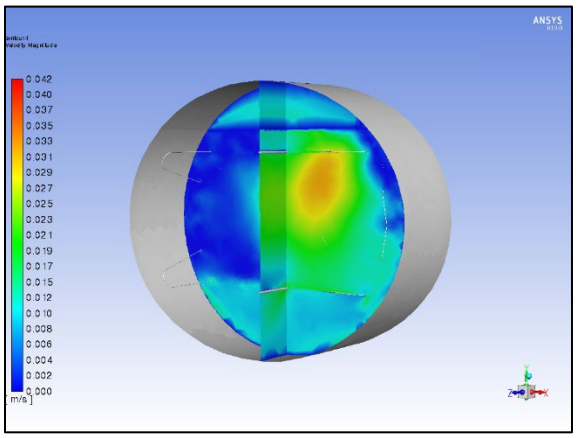

(b)

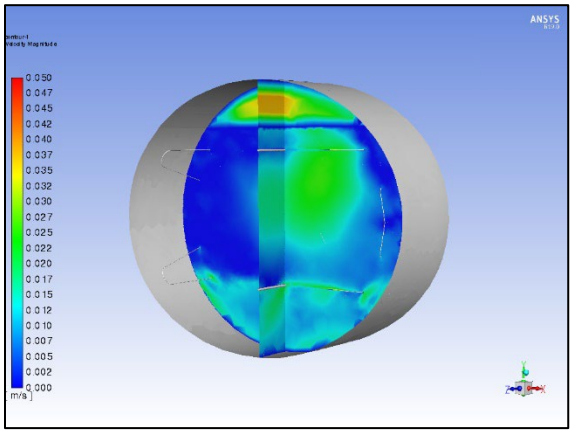

(c)

Figure 4.10 Velocity profiles for the Internal Energy method: (a) 15 minutes from beginning of simulation, (b) 60 hours through simulation, (c) final simulation time of 120 hours

Figure 4.11 shows the experimental data and color-coded thermocouple and pressure data. Thermocouples TT3, TT4, TT9, TT10, TT15, and TT16 are submerged in the LH2 whereas TT19 is located in the ullage space shown in Figure 4.11.

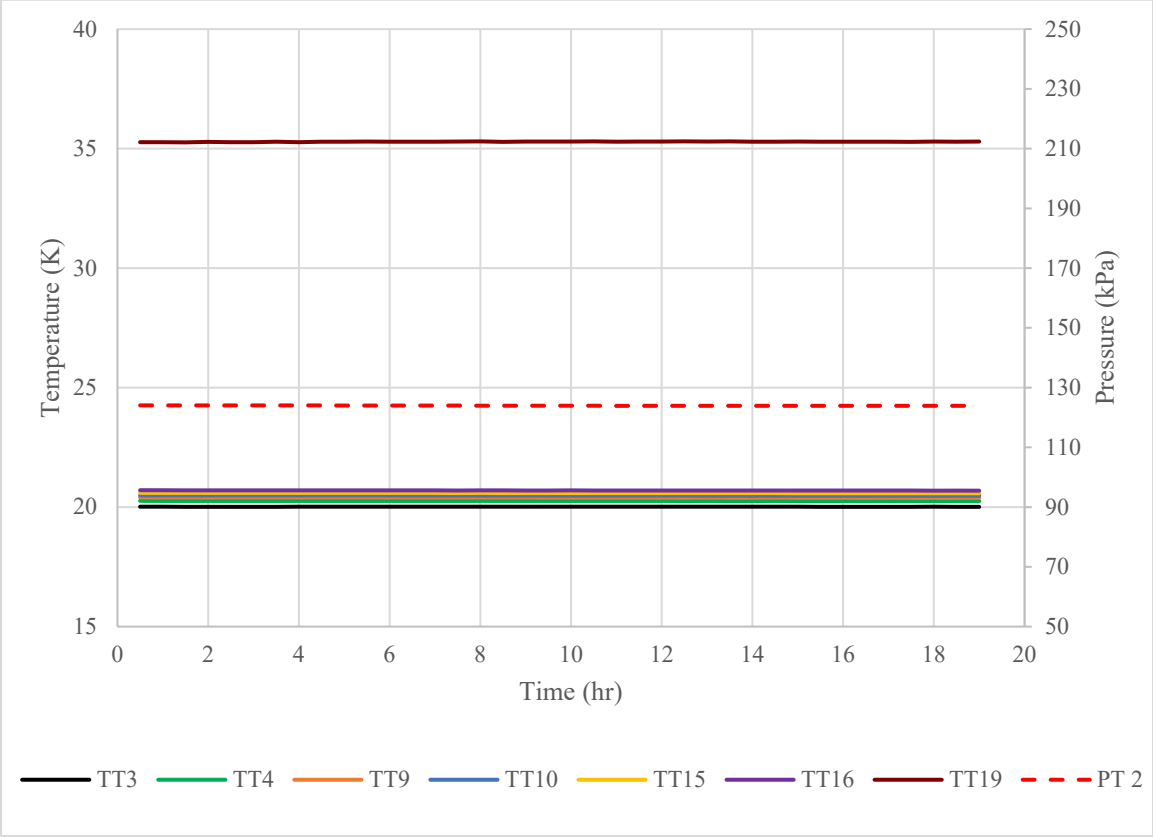

Figure 4.11 100% fill experimental data for the steady state analysis

Figures 4.12 and 4.13 show simulation predictions at the lowest mesh density of 200K cells using the enthalpy model and the internal energy model, respectively. Simulation predictions for both models using the 350K cell mesh are shown in Figures 4.14 and 4.15, respectively. For the highest density mesh of 500K cells, the simulation predictions for both models are compared to the experimental results in Figures 4.16 and 4.17.

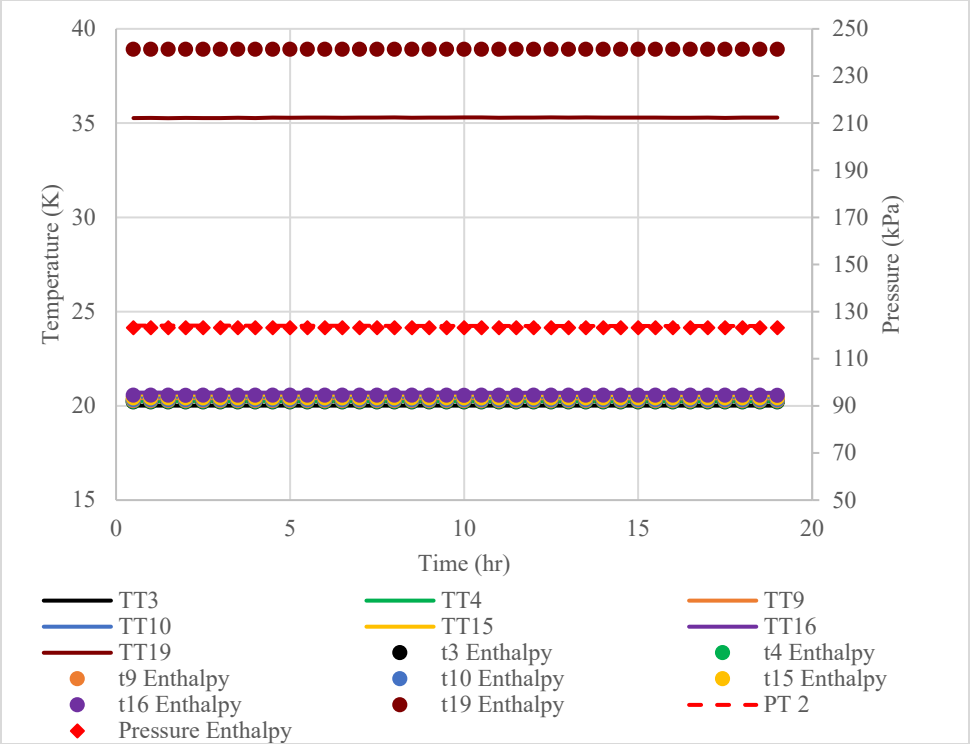

Figure 4.12 100% fill 200k mesh Enthalpy model compared to experimental results

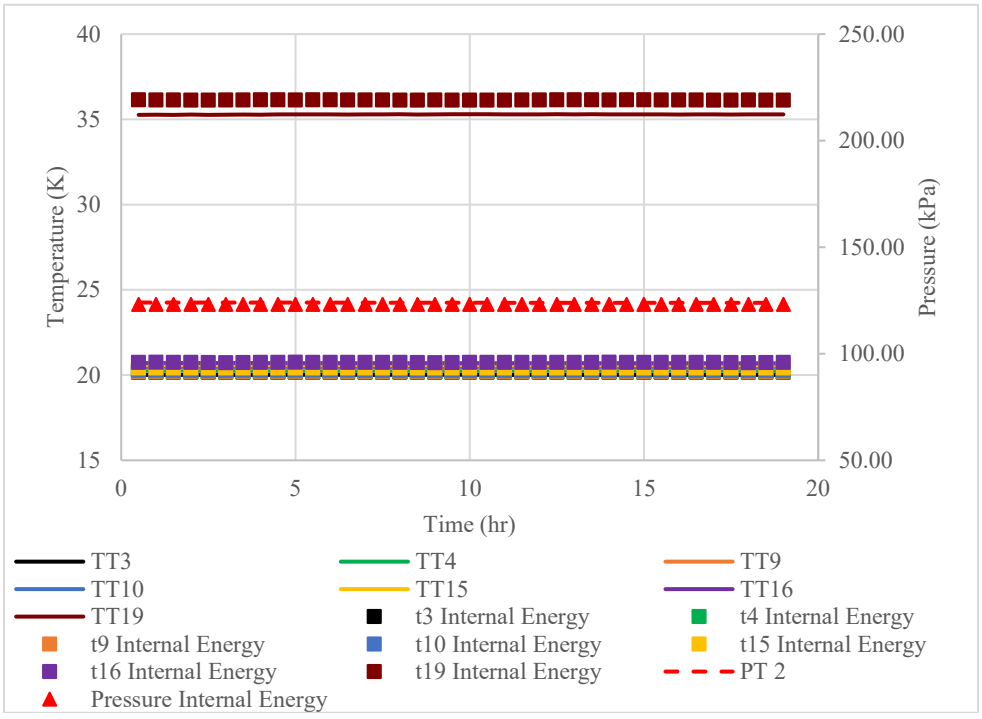

Figure 4.13 100% fill 200k mesh Internal Energy model compared to experimental results

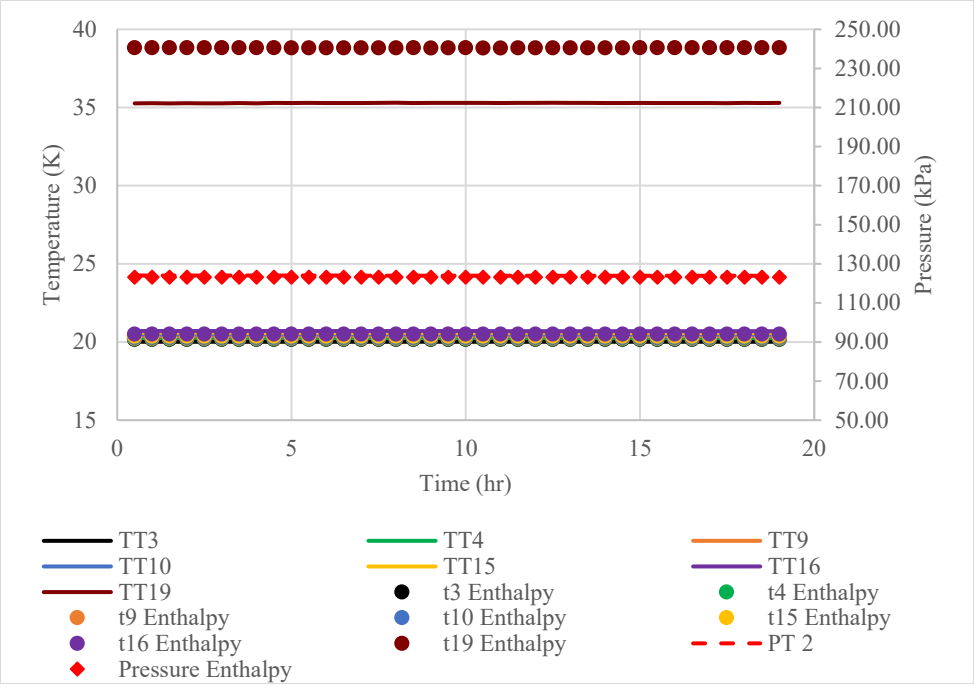

Figure 4.14 100% fill 350k mesh Enthalpy model compared to experimental results

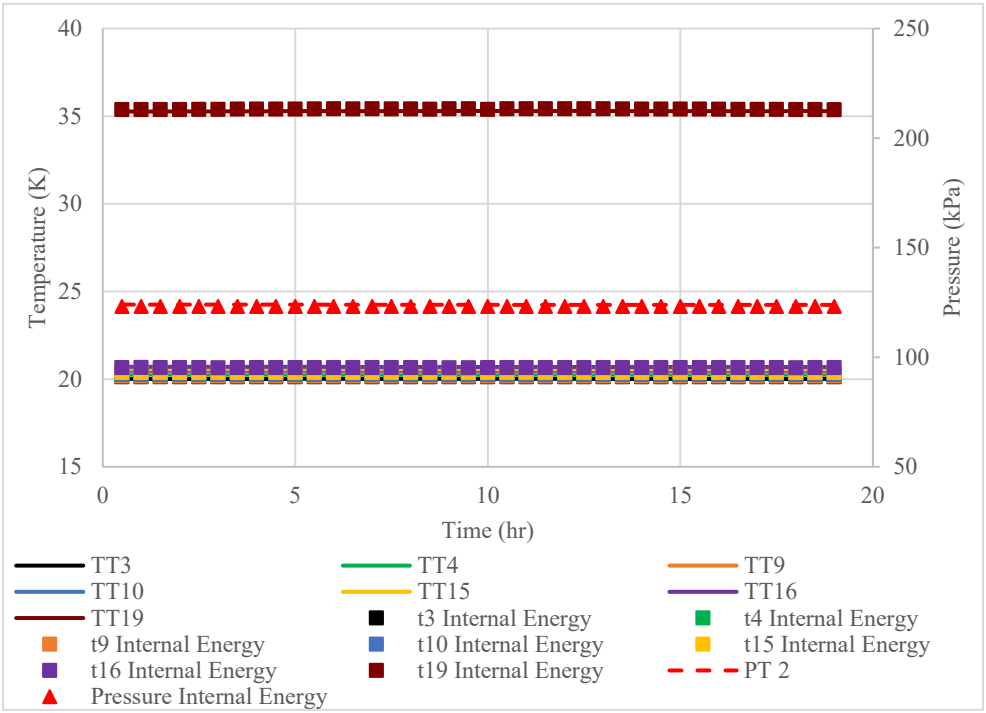

Figure 4.15 100% fill 350k mesh internal energy Internal Energy model compared to experimental results

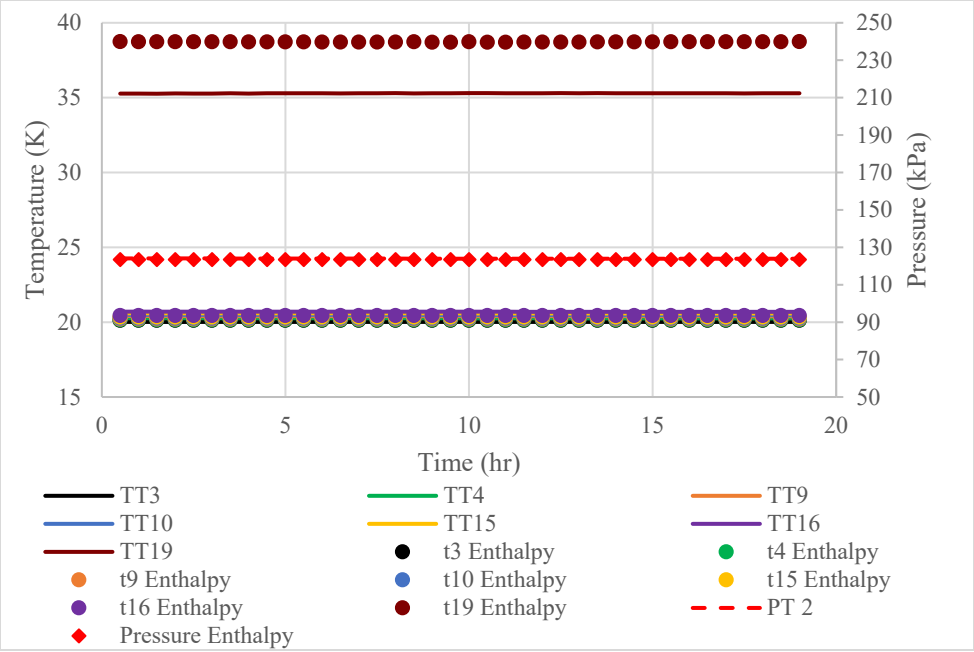

Figure 4.16 100% fill 500k mesh Enthalpy model compared to experimental results

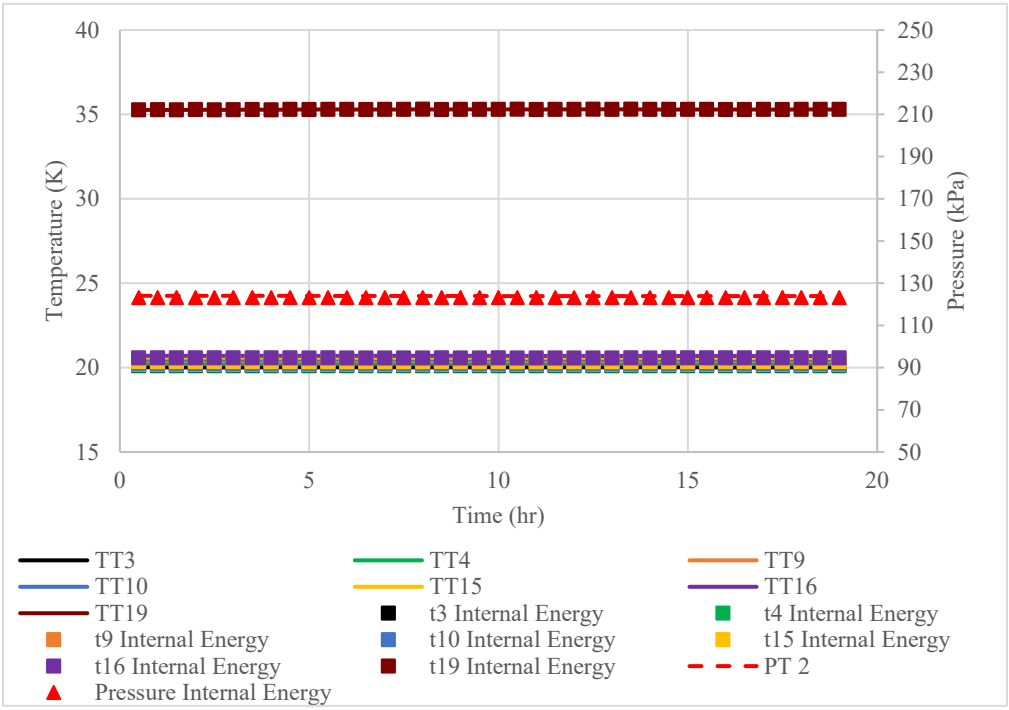

Figure 4.17 100% fill 500k mesh Internal Energy model compared to experimental results

To quantify the differences in temperatures between the simulation predictions and the experiment measurements, the percent errors, given by Equation 4.1, were calculated and the maximum for each of the different cases is presented in Table 4.3.

$$\%error = \left|\frac{T_{experimental} - T_{predicted}}{T_{predicted}}\right| * 100 \quad (4.1)$$

Table 4.3 Coefficient of Determination and maximum percent error for 100% fill ZBO between simulation predictions using three meshes and experimental results.

Steady-State				
100% fill level				
	Enthalpy		Internal Energy	
Mesh	Coefficient of Determination, Pressure	Maximum Percent Error in Temperature, Diode	Coefficient of Determination, Pressure	Maximum Percent Error in Temperature, Diode
200k	0.998055	9.385%, TT19	0.997427	2.423%, TT19
350k	0.998833	9.174%, TT19	0.998056	1.959%, TT19
500k	0.999412	8.962%, TT19	0.998597	1.311%, TT19

From Table 4.3 the largest differences between the thermocouple measurements and the simulation predictions, are in the ullage domain. Also, the table shows the Coefficient of Determination which compares pressure predictions for the two models to the experiment pressure data. For comparison, a Coefficient of Determination closer to one in this study represents a more accurate prediction of pressure when compared to the experiment. As the mesh density increases, the Coefficient of Determination will approach unity. Since the Coefficient of Determination is greater than 0.99 for all three mesh and with both models and that the change in the Coefficient of Determination is

relatively small as the mesh density increases, it is concluded that mesh convergence is achieved using the 500K cell mesh.

4.2.2 67% Fill Level

Like the 100% fill level case, an eighteen-hour segment during the ZBO-PC phase of the experiment is described as the ZBO analysis for the 67 % fill case. Three polyhedral meshes, an example of which shown in Figure 4.18, are used to simulate the 67% fill case.

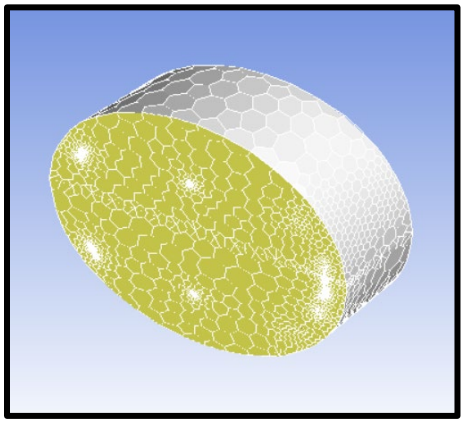

Figure 4.18 Example of the 67% fill level polyhedral mesh

The cell count for the 67% fill level polyhedral meshes are approximately: 320K cells, 430K cells, and 660K cells.

The temperature profile found at a center plane inside the IRAS tank for the Enthalpy and Internal Energy models are shown in Figures 4.19 (a – c) and Figures 4.21 (a – c). The different timesteps in the figures show how the temperature stratification occurred inside the IRAS tank. In Figure 4.19 (a) and Figure 4.21 (a) at approximately 15 minutes into the simulation, the highest temperatures occurred at the top of the tank,

however as time continued, the temperature stratified through the tank shown in Figures 4.19 (b – c) and Figures 4.21 (b – c).

Figure 4.20 (a – c) and Figure 4.22 (a – c) present the velocity profile of the Enthalpy model and Internal Energy model. Figure 4.20 (a) and Figure 4.22 (a) show the velocity profile after 15 minutes of experiment time as the cool denser liquid drops from the coil and the warmer liquid climbed the side wall to create recirculation zones at the interface. Also, in Figure 4.20 (a – c) and Figure 4.22 (a – c), at the beginning of the simulation, the velocity magnitude is higher in the liquid space, however at the end of the simulations the velocity magnitude in the ullage space is higher. A large recirculation zone is created in the ullage space for both models.

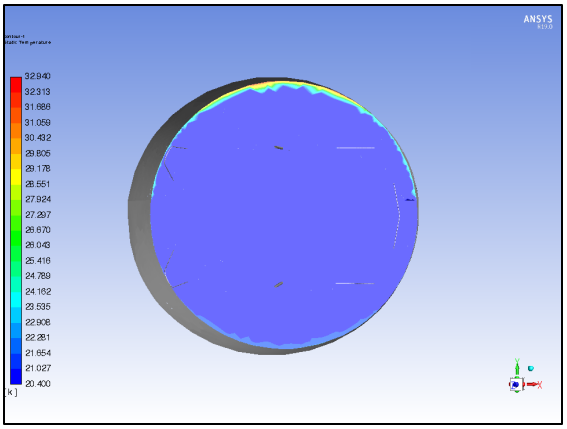

(a)

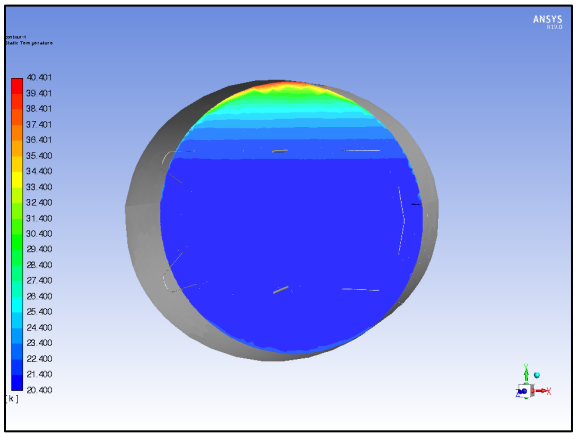

(b)

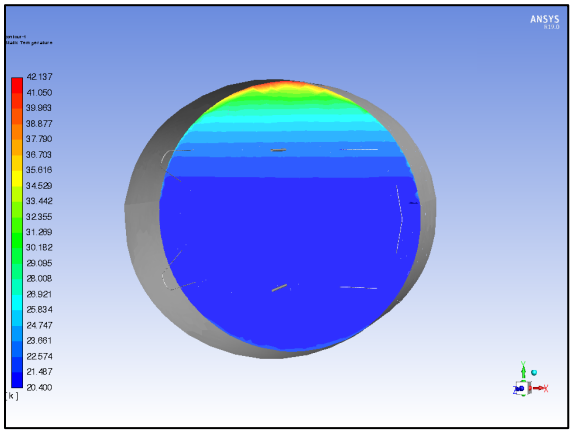

(c)

Figure 4.19 Temperature profiles for the Enthalpy method: (a) 15 minutes from beginning of simulation, (b) 60 hours through simulation, (c) final simulation time of 120 hours

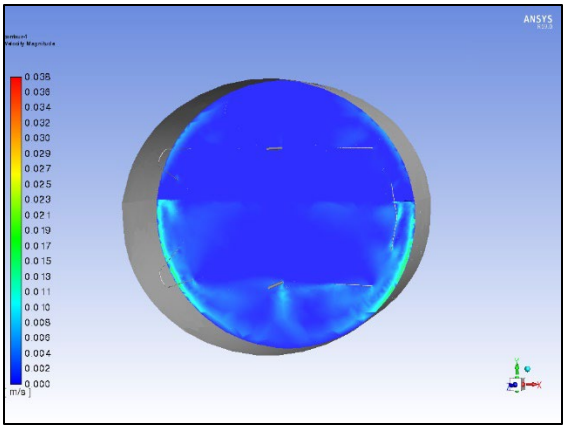

(a)

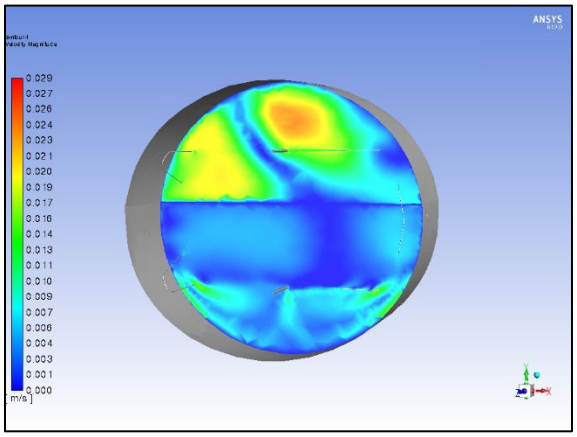

(b)

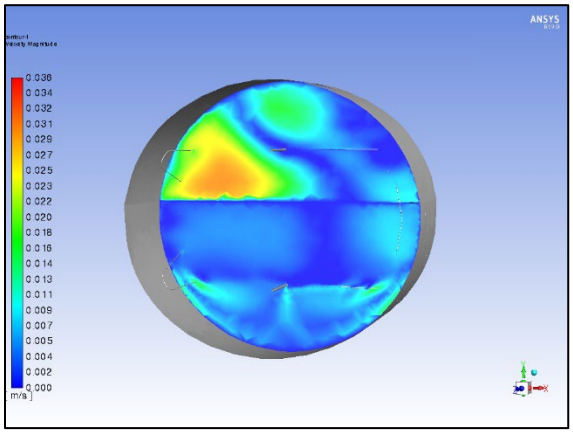

(c)

Figure 4.20 Velocity profiles for the Enthalpy method: (a) 15 minutes from beginning of simulation, (b) 60 hours through simulation, (c) final simulation time of 120 hours

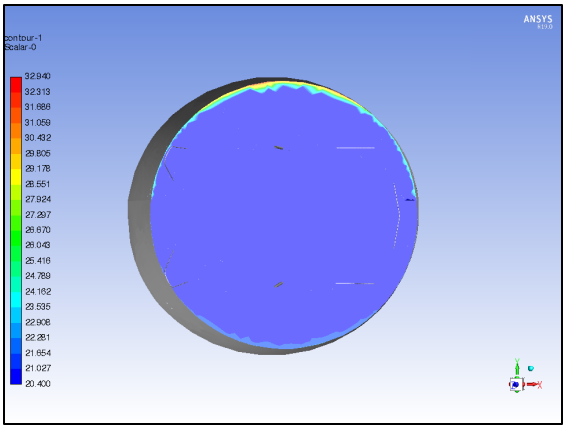

(a)

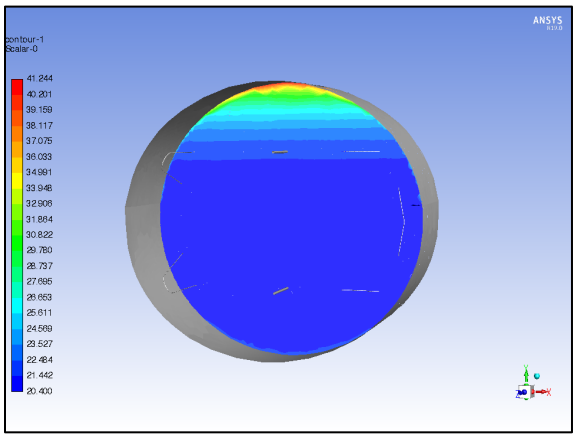

(b)

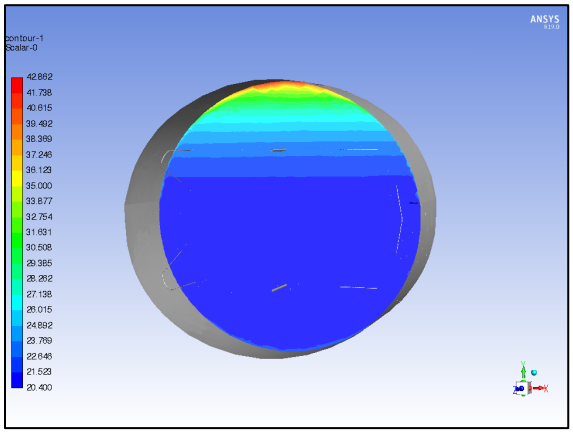

(c)

Figure 4.21 Temperature profiles for the Internal Energy method: (a) 15 minutes from beginning of simulation, (b) 60 hours through simulation, (c) final simulation time of 120 hours

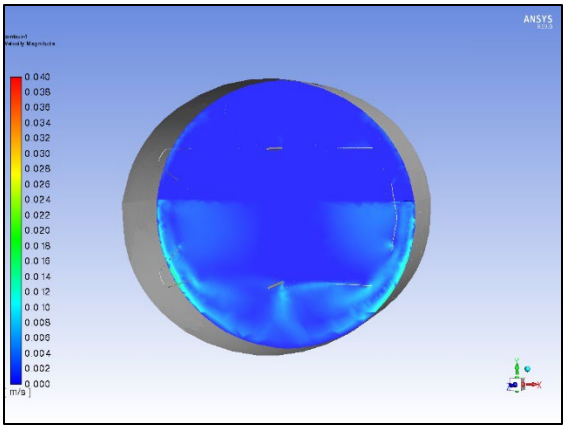

(a)

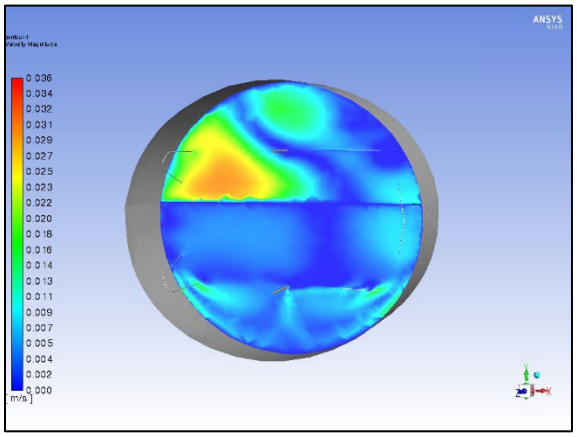

(b)

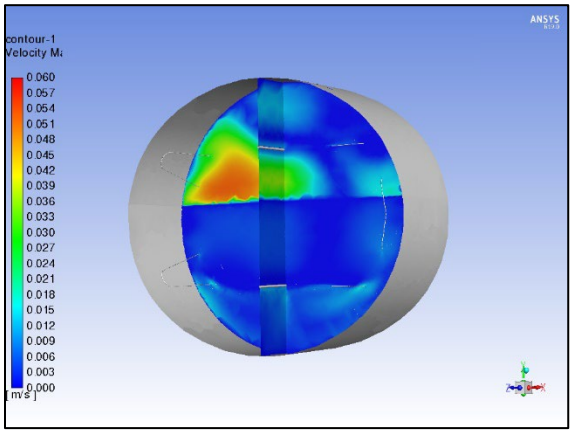

(c)

Figure 4.22 Velocity profiles for the Internal Energy method: (a) 15 minutes from beginning of simulation, (b) 60 hours through simulation, (c) final simulation time of 120 hours

The experimental temperature and pressure data for the 67% fill level ZBO analysis are shown in Figure 4.23. Thermocouples TT3, TT4, TT9, and TT10 are submerged in the LH_2 whereas TT15, TT16, and TT19 are in the ullage space.

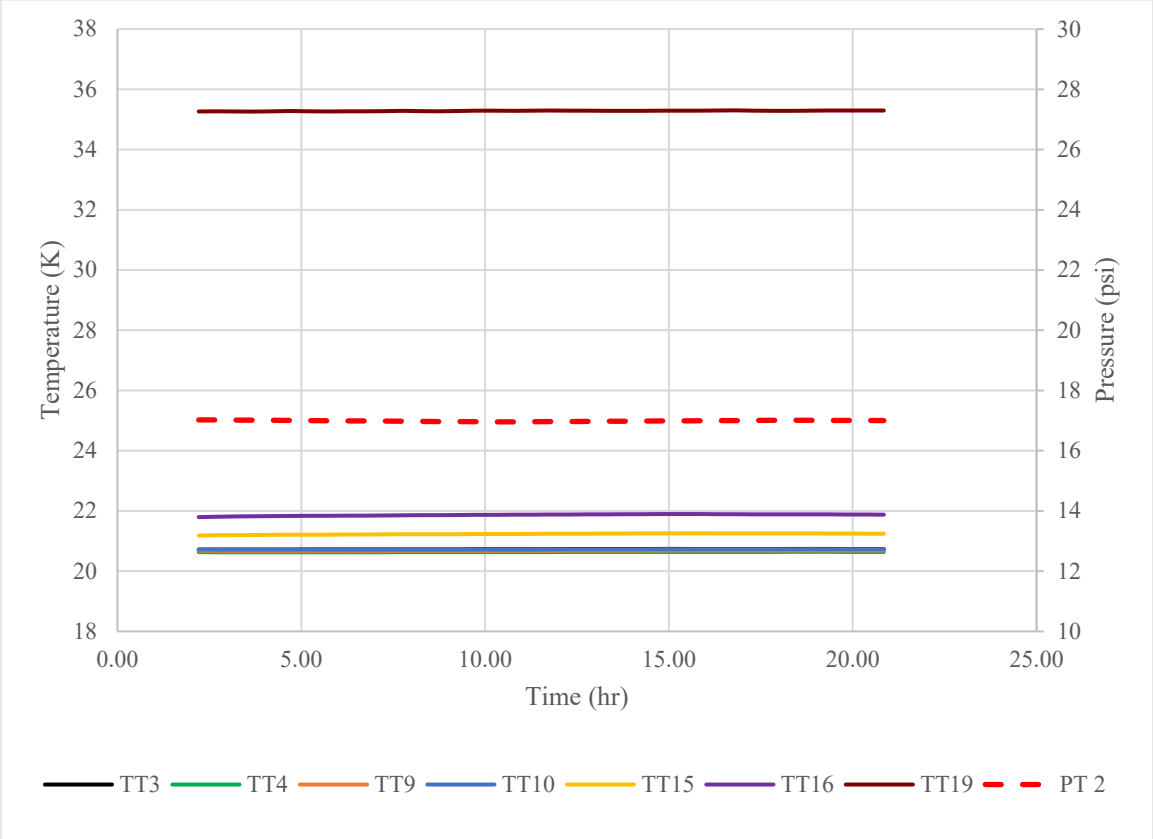

Figure 4.23 67% fill experimental data for the steady state analysis

Figures 4.24 and 4.25 show the Enthalpy model and Internal Energy model compared to the experimental results for the pressure and temperature for the lowest density mesh, 320K computational cells. Results for the 430K cell mesh are presented in Figures 4.26 and 4.27. For the highest density mesh, 660K cells, the model results were compared to the experimental results in Figures 4.28 and 4.29.

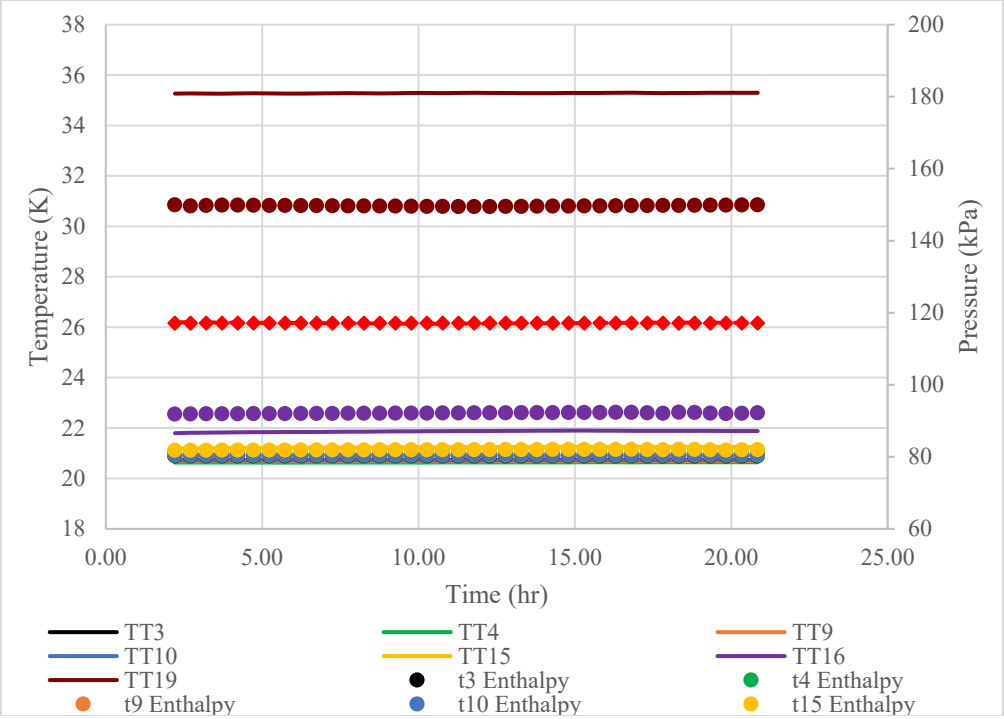

Figure 4.24 67% fill 320k mesh Enthalpy model compared to experimental results

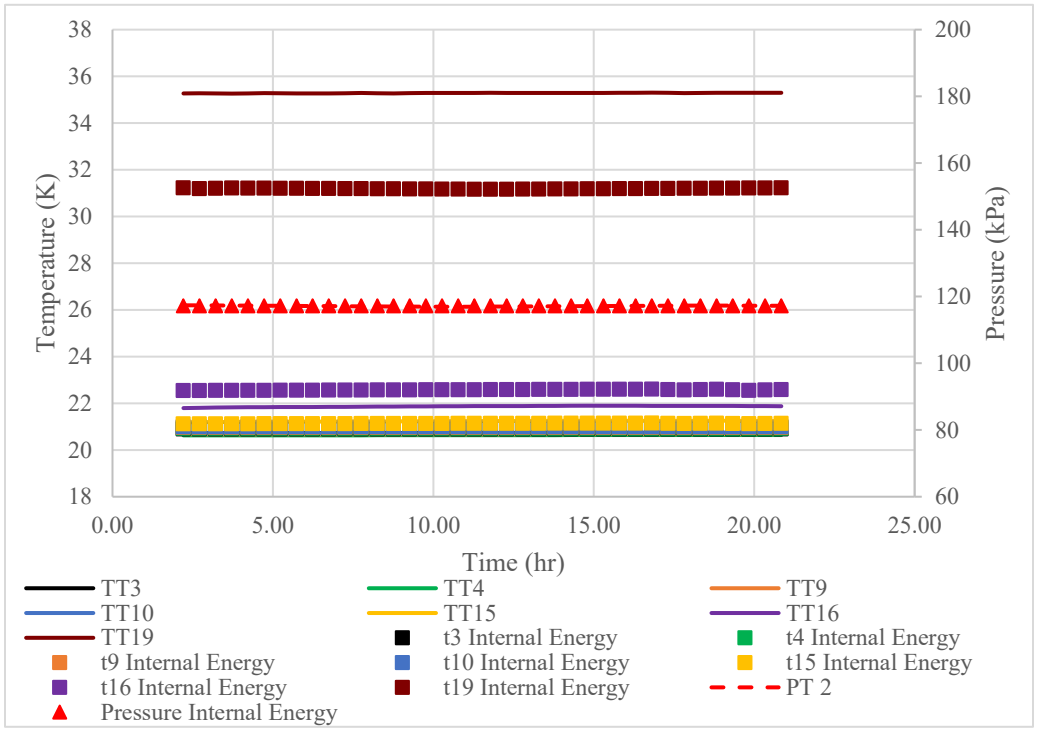

Figure 4.25 67% fill 320k mesh Internal Energy model compared to experimental results

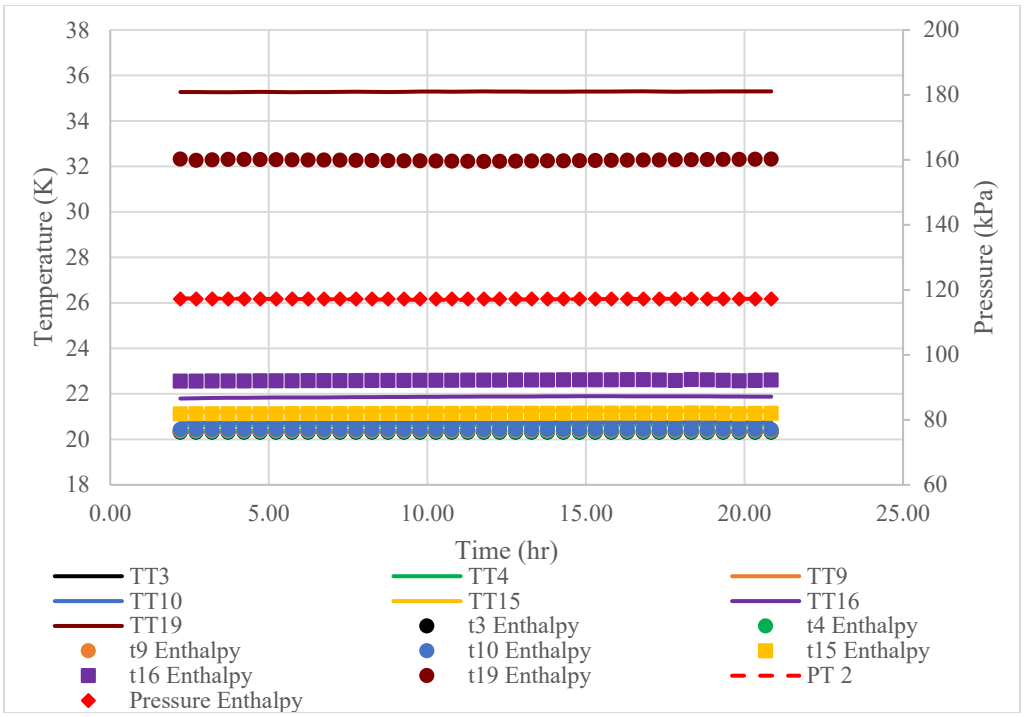

Figure 4.26 67% fill 430k mesh Enthalpy model compared to experimental results

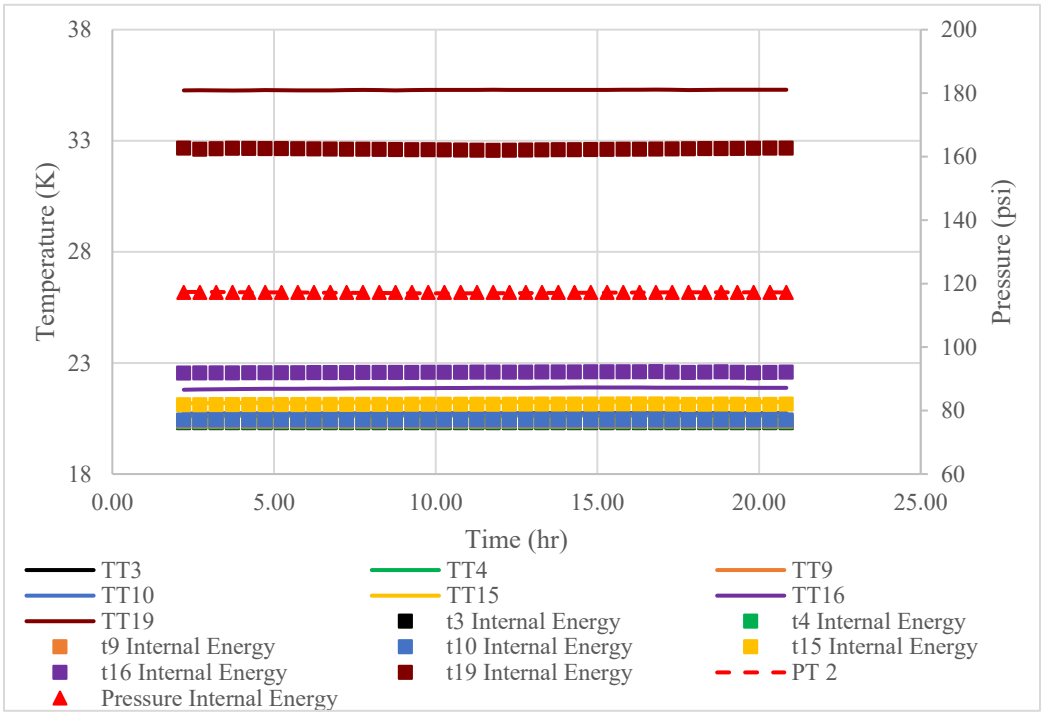

Figure 4.27 67% fill 430k mesh Internal Energy model compared to experimental results

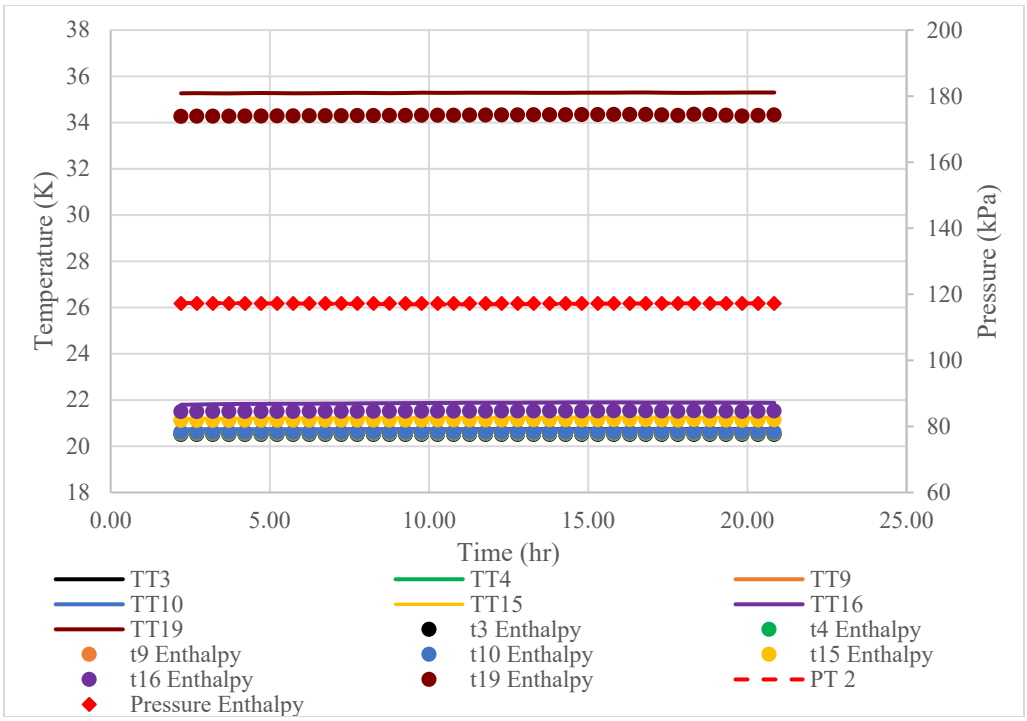

Figure 4.28 67% fill 660k mesh Enthalpy model compared to experimental results

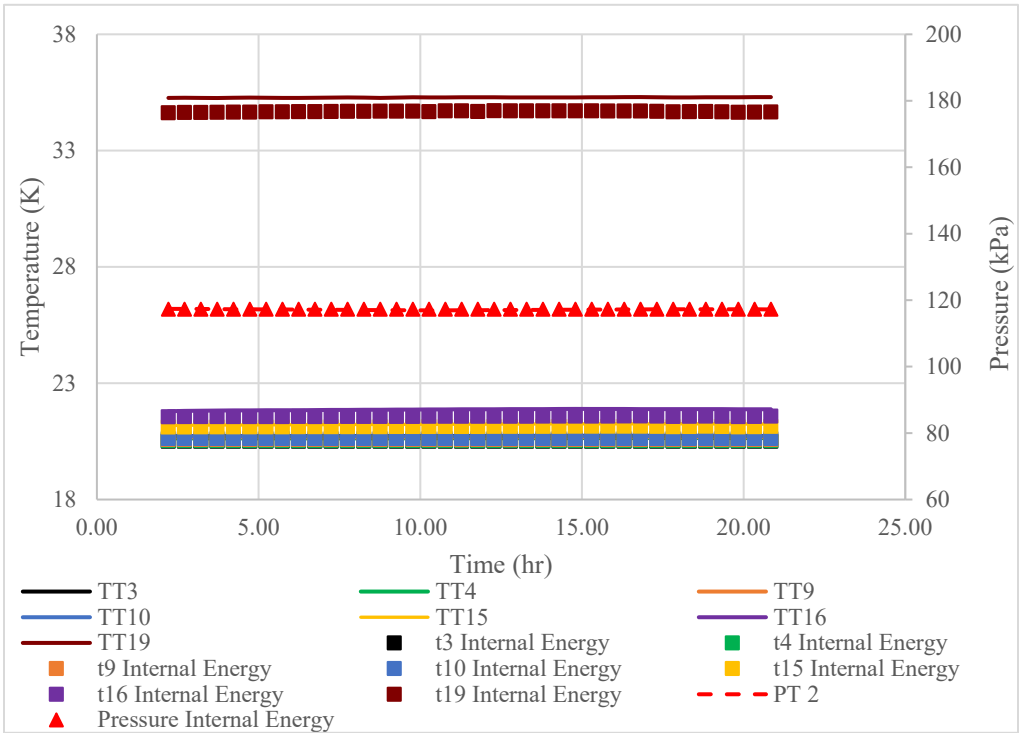

Figure 4.29 67% fill 660k mesh Internal Energy model compared to experimental results

From Figures 4.24 – 4.29, the pressure and temperatures for both models show good agreement with the experiment measurements, however, to better quantify the fit of the different models the Coefficient of Determination was calculated for each model and mesh. The Coefficient of Determination for the pressure and maximum percent errors for the temperature data are given in Table 4.4. As the mesh density increases the Coefficient of Determination is very close to one. It can be concluded that the pressure prediction is less dependent on the mesh density. The higher temperature errors, which are less than 10%, are found in the ullage space of the models when compared to the experimental temperature results. The percent errors decrease as the mesh density increases, indicating a more accurate simulation in terms of temperature as the number of computational cells increases.

Table 4.4 Coefficient of Determination and maximum percent error for 67% fill ZBO between simulation predictions using three meshes and experimental results.

Steady-State				
67% fill level				
	Enthalpy		Internal Energy	
Mesh	Coefficient of Determination, Pressure	Maximum Percent Error in Temperature, Diode	Coefficient of Determination, Pressure	Maximum Percent Error in Temperature, Diode
320k	0.999948	14.67%, TT19	0.999922	13.28%, TT19
430k	0.999959	12.06%, TT19	0.999937	10.77%, TT19
660k	0.999962	9.56%, TT19	0.999948	8.38%, TT19

4.2.3 Discussion of Steady State Results

Both the Enthalpy and the Internal Energy model demonstrate good agreement when compared to the experimental results for the GODU-LH2 tank. The simulations are

performed using three different meshes and at two fill levels. The lowest calculated maximum temperature error, which occurs in the ullage, is achieved in the highest mesh density for both models and both fill levels. However, the Internal Energy model is approximately 1% more accurate in predicting the ullage temperature than the Enthalpy model. Since the maximum errors in the simulation predictions decrease for both fill levels as the mesh sized increases then the simulations show better agreement using the higher mesh densities as expected. s. Also, the 67% fill simulation predictions have slightly higher errors in the diodes than the 100% fill simulation predictions, which could be a result of the differing mesh densities used between the two fill levels.

As in the temperature results, the pressure calculations show that with increased mesh density the simulation predictions are in slightly better agreement with the experimental data. This is corroborated in Tables 4.3 and 4.4 with the Coefficient of Determination calculations. Since the Coefficient of Determination values are all very close to 1 for all three meshes, it can be concluded the pressure is not significantly sensitive to mesh density. As an aggregate, the results suggest the simulation predictions at the highest mesh densities have the best agreement with the experimental results.

4.3 Transient Densification Analysis

As discussed in Chapter 1, a mission enabling capability of the IRAS technology is the capacity to densify large quantities of stored cryogens. The tank is a sealed system during densification operations; therefore, the pressure decreases as heat is removed from the LH2 by the refrigerator coils. The pressure will eventually fall below atmospheric, effectively converting the tank into a vacuum chamber. Given the added complexity in an

IRAS system during densification, it is of particular interest to develop predictive models that can accurately predict pressure and temperature drop inside the IRAS tank.

Results from the Densification phase of the experiments are shown in Figures 4.4 and 4.5 for the 100% and 67% fill levels. The Enthalpy and Internal Energy models are compared to the experimental data. The initial conditions used for the Densification simulations are the temperature, pressure, velocity, and phase fraction fields from last timestep of the ZBO analysis. As in the ZBO analysis, the heat leaks into the system are set as the wall boundary conditions, and the refrigerator boundary conditions are based on the diodes TT21 – TT24. The 100% densification runs approximately 210 hours before the experimental data was stopped for the GODU tank. The 67% fill case ran for 315 hours, before the triple point of hydrogen was reached which will be discussed later in this chapter. The full processes were simulated with the Enthalpy and Internal Energy models. Swanger's Lumped Node Analysis model has been utilized to predict densification of LH2 in the GODU-LH2

The Lumped Node Analysis model defines the liquid and vapor regions as different nodes and assumes the hydrogen in the system is at saturation where the properties were calculated from Refprop [101]. Results obtained using the Lumped Node Analysis are compared to the Enthalpy model and Internal Energy model predictions for tank densification. The hydrogen properties used in the Enthalpy model and Internal Energy model are also interpolated from Refprop and the hydrogen is also assumed to be in a saturated state. The initial conditions for the Lumped Node Analysis for the 100% fill case are a pressure of 52.0 kPa and a temperature of 18.2, and for the 67% case a pressure of 71.7 kPa and temperature of 19.2. The experiment times simulated using the Lumped

Node Analysis are 100 hours for the 100% fill case and 150 hours for the 67% fill case. The simplifying assumption that the system is saturated at the given pressure during densification is represented in Figure 4.28 along with the heat leaks into the ullage and liquid and the heat removed by the refrigerator.

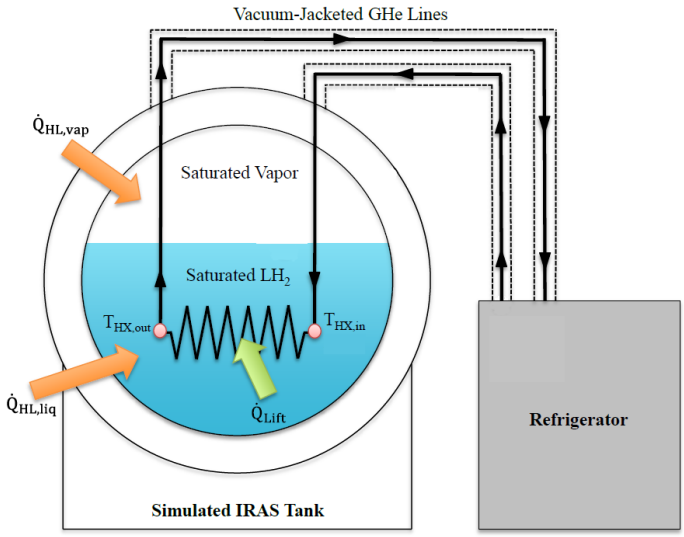

Figure 4.30 Simplified Saturated Model Setup

4.3.1 100% Fill Level

As mentioned previously for the 66% fill level case, the initial conditions used for the Densification simulations are the temperature, pressure, velocity, and phase fraction fields from last timestep of the ZBO analysis. The simulations are performed on the same meshes discussed in Section 4.1.2. The densification process for the 100% fill level experiment ran for approximately 210 hours. The simulations are setup with a total time of 210 hours and a timestep size of 3 seconds. A time sequence of temperature profiles inside the tank for the 500k mesh for the Enthalpy model and Internal Energy model are shown in Figure 4.31 (a – c), and Figure 4.33 (a – c), respectively. The corresponding

time sequence of velocity profiles inside the tank are shown in Figure 4.32 (a – c) and Figure 4.34 (a – c) for the Enthalpy model and Internal Energy model, respectively.

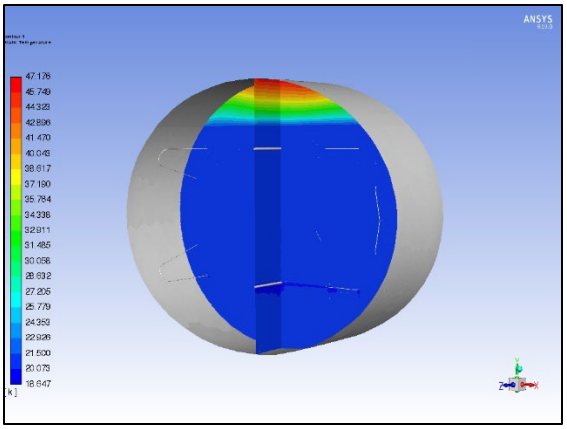

(a)

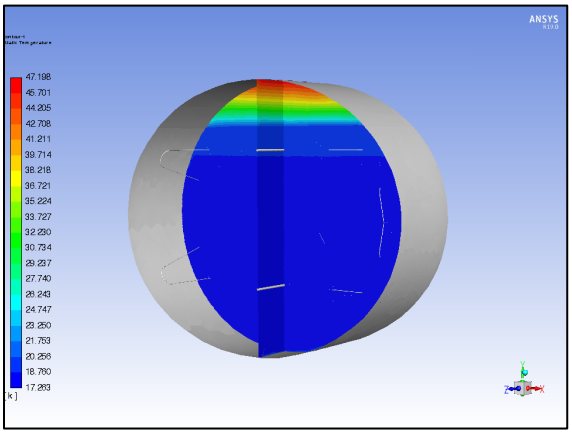

(b)

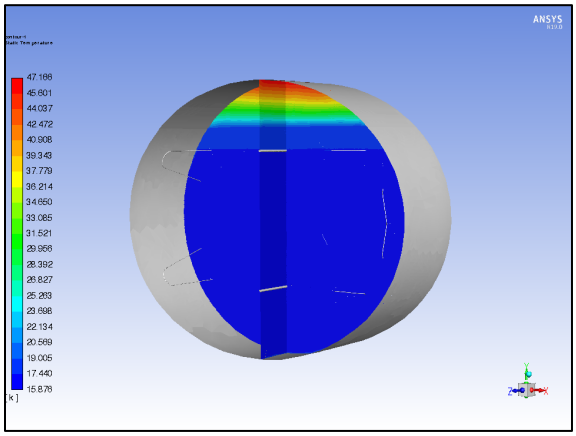

(c)

Figure 4.31 Temperature profiles for the Enthalpy method: (a) 15 minutes from beginning of simulation, (b) 105 hours through simulation, (c) final simulation time of 210 hours

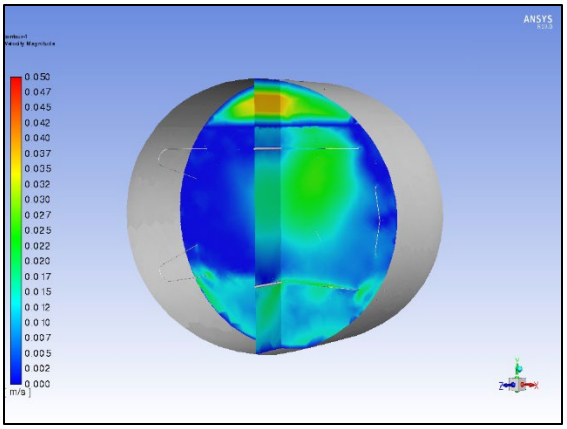

(a)

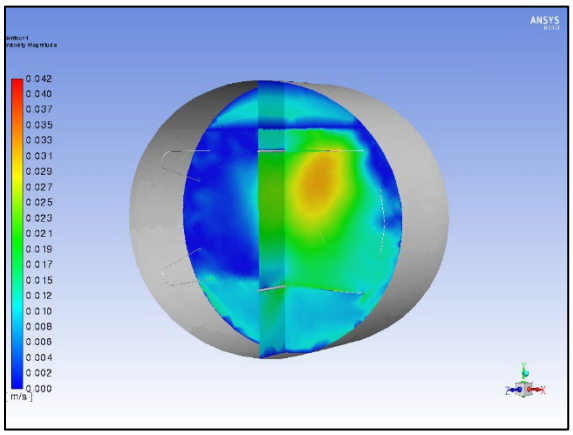

(b)

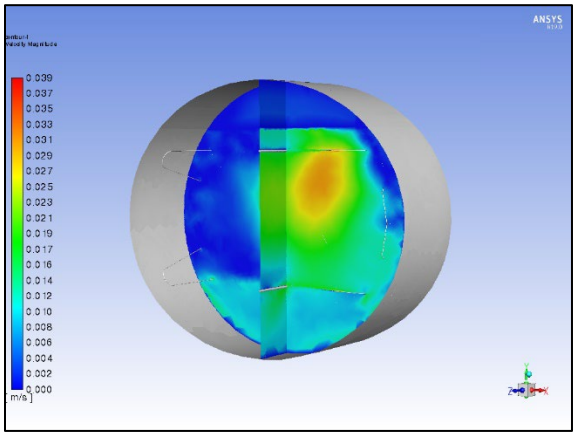

(c)

Figure 4.32 Velocity profiles for the Enthalpy method: (a) 15 minutes from beginning of simulation, (b) 105 hours through simulation, (c) final simulation time of 210 hours

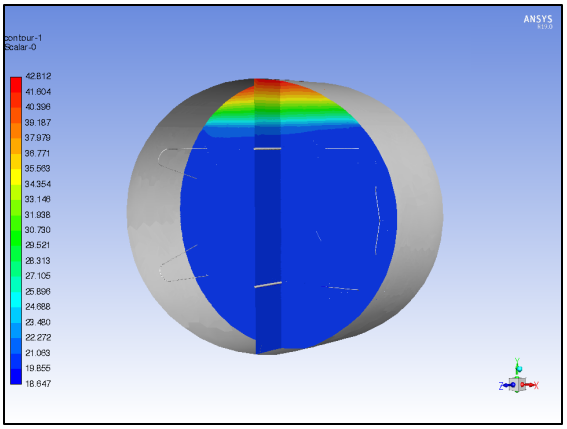

(a)

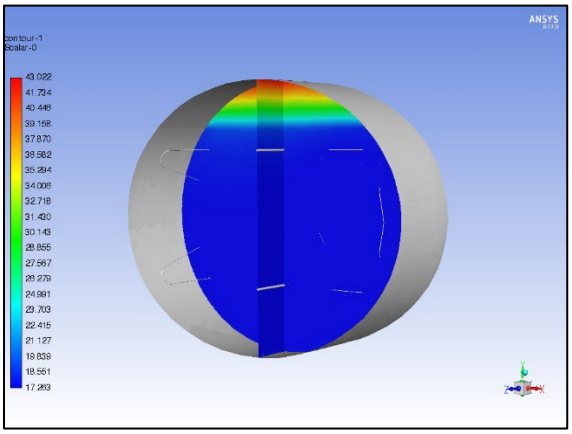

(b)

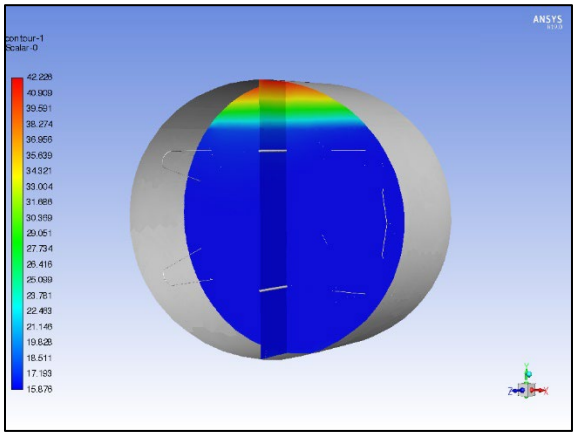

(c)

Figure 4.33 Temperature profiles for the Internal Energy method: (a) 15 minutes from beginning of simulation, (b) 105 hours through simulation, (c) final simulation time of 210 hours

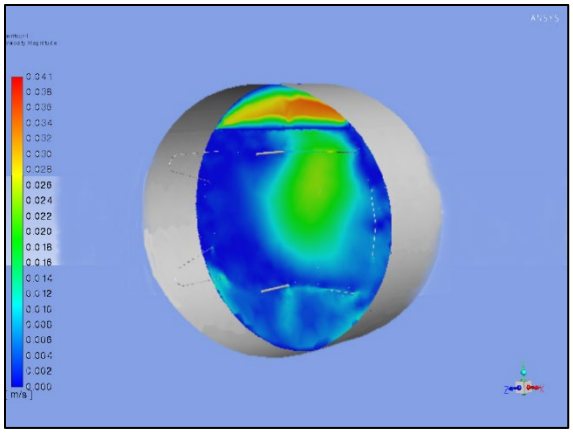

(a)

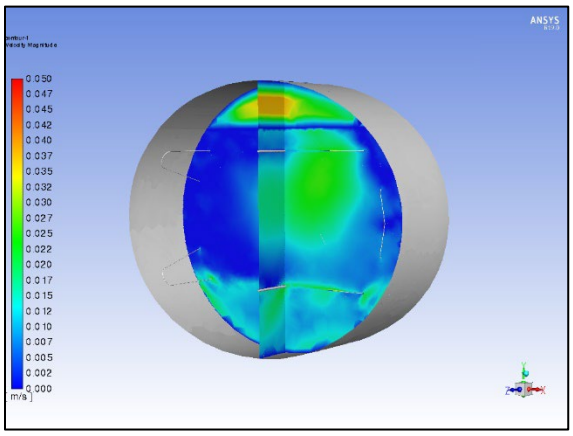

(b)

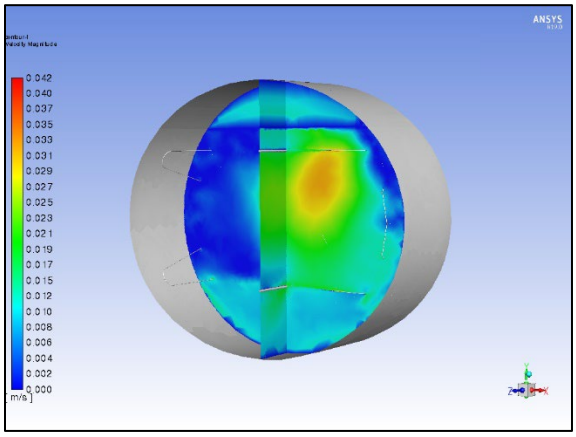

(c)

Figure 4.34 Velocity profiles for the Internal Energy method: (a) 15 minutes from beginning of simulation, (b) 105 hours through simulation, (c) final simulation time of 210 hours

The temperature profiles shown in Figures 4.31 (a – c) and 4.33 (a – c) indicate the hydrogen remains thermally stratified over the time of the experiment. The velocity profiles after 15 minutes as presented in Figures 4.32 and 4.34 indicate the velocities are higher in the ullage space than in the liquid space. However, as densification of the fluid continues over the time of experiment, the temperatures of the liquid began to decrease as the velocities in the increase which culminates in the formation of a recirculation zone near the center of the fluid domain.

The experimental results for temperature and pressure are presented in Figure 4.35. Again, the same color scheme is used for the thermocouple temperatures and pressure as presented in the steady state analysis. Figures 4.36 and 4.37 show the experiment pressure and temperature data compared to the predictions obtained using the Enthalpy and Internal Energy models at the lowest mesh density. Figures 4.38 and 4.39 present the Enthalpy and Internal Energy model predictions using the medium density mesh, and Figures 4.40 – 4.41 present the Enthalpy and Internal Energy predictions using the highest density mesh.

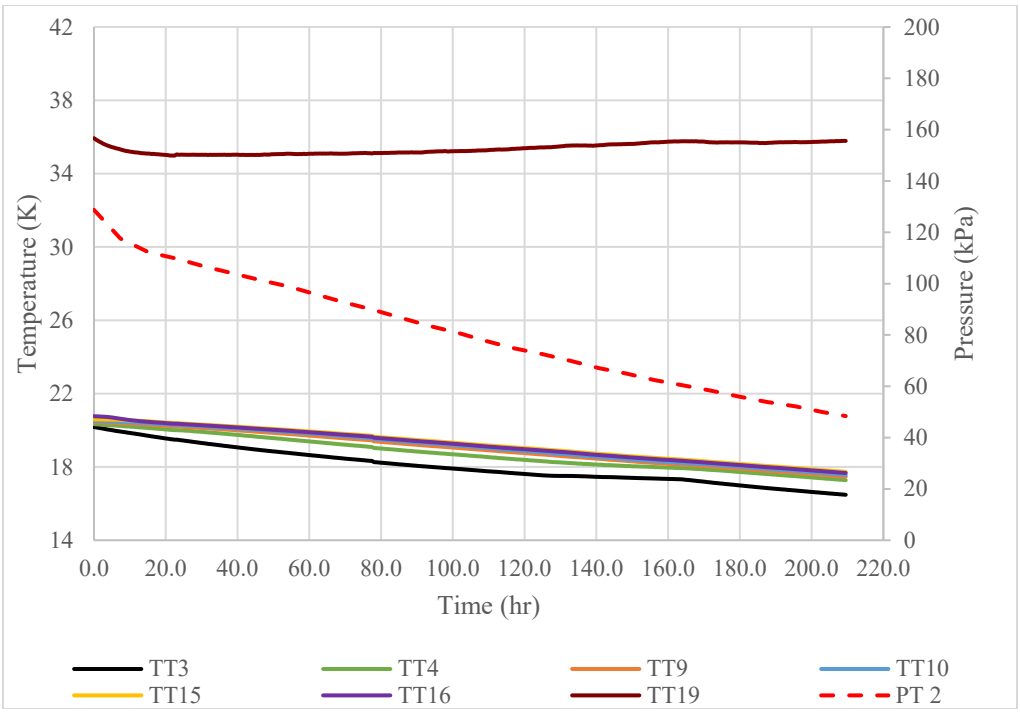

Figure 4.35 100% tank fill experimental temperatures and pressure densification data

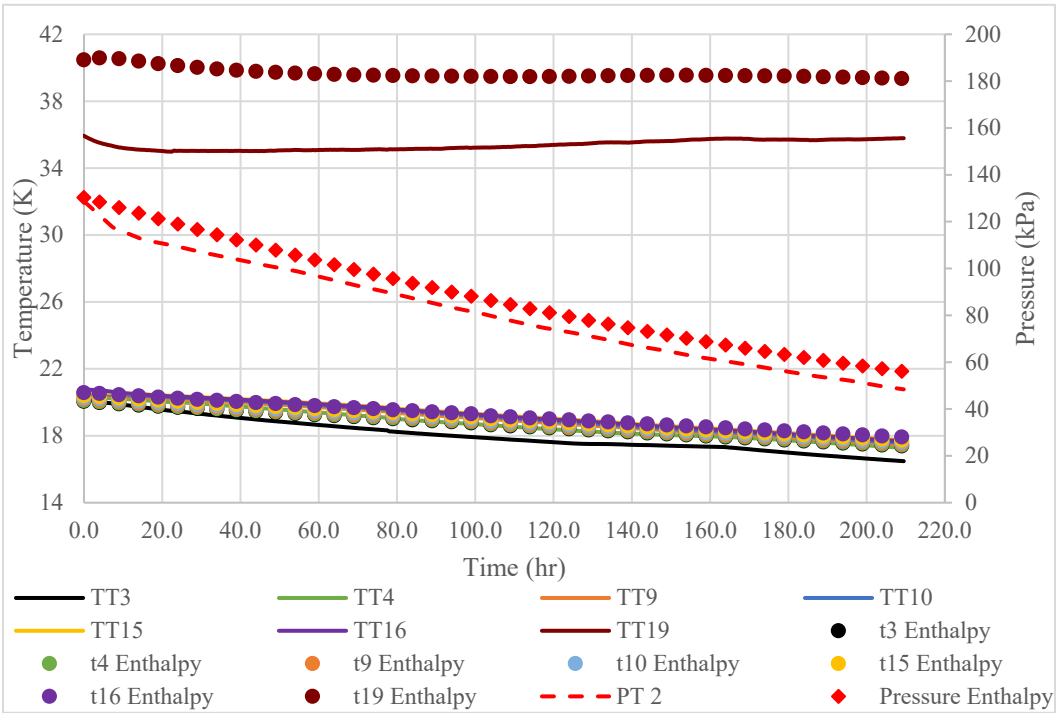

Figure 4.36 100% tank fill experimental temperatures compared to the 200k mesh Enthalpy model

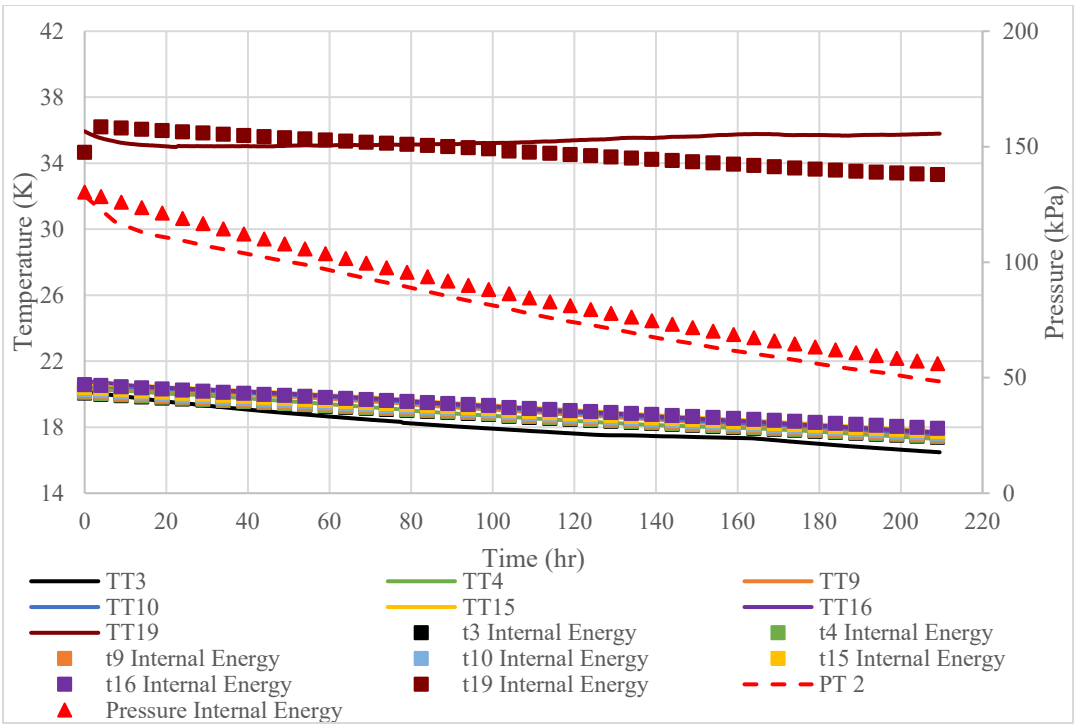

Figure 4.37 100% tank fill experimental temperatures compared to the 200k mesh Internal Energy model

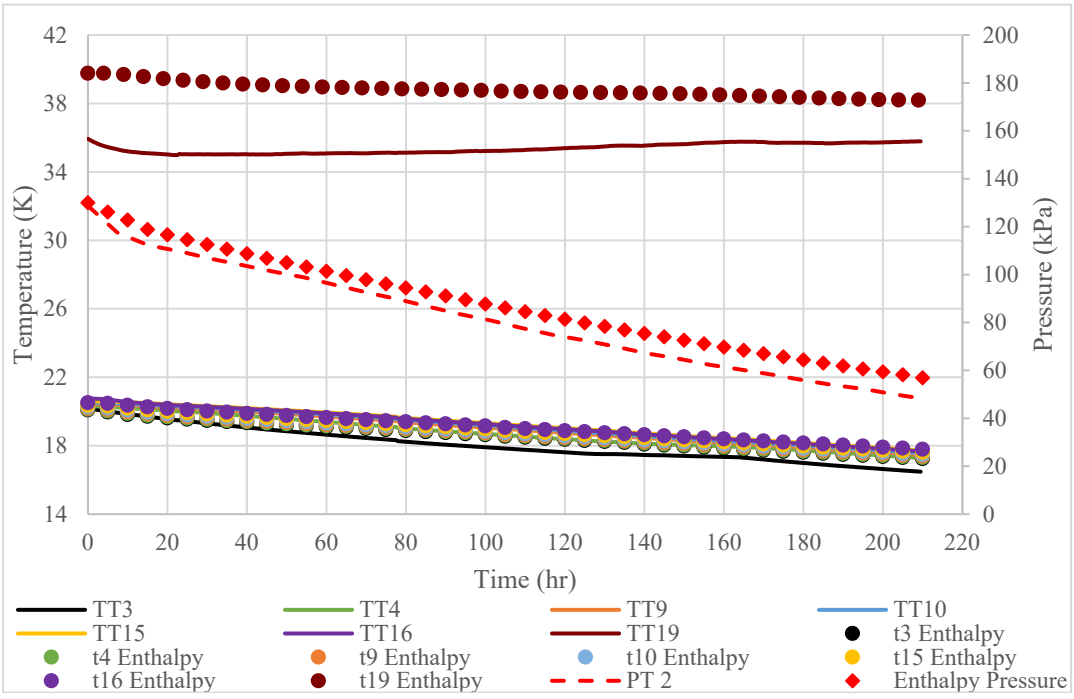

Figure 4.38 100% tank fill experimental temperatures compared to the 350k mesh Enthalpy model

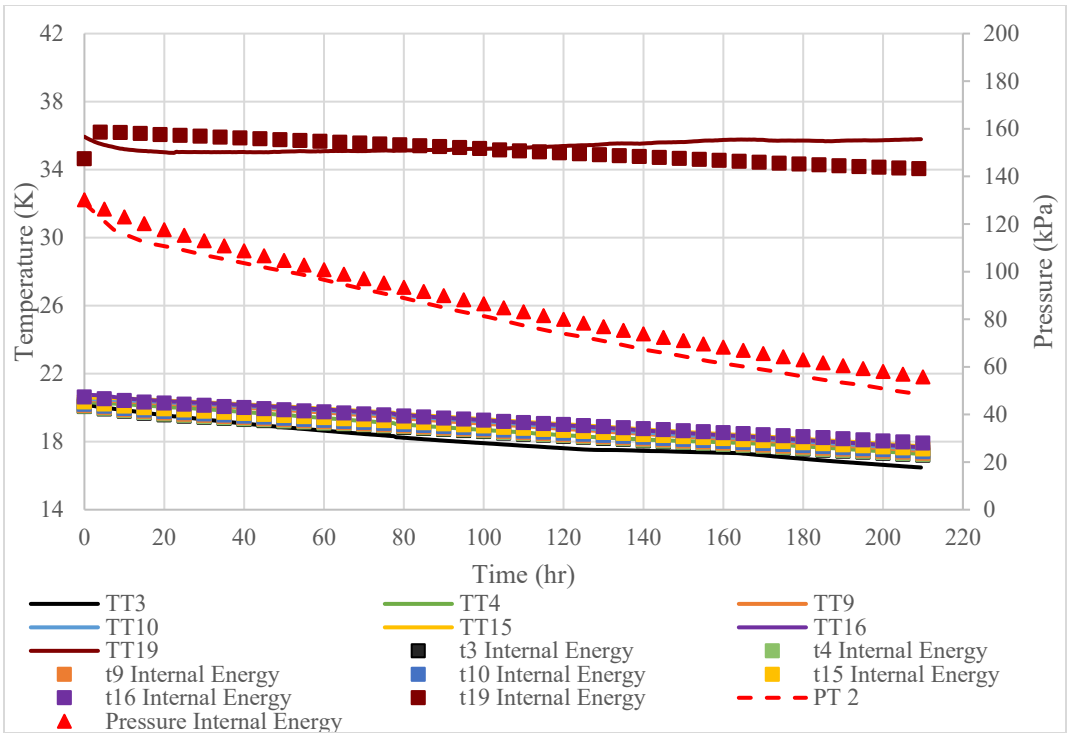

Figure 4.39 100% tank fill experimental temperatures compared to the 350k mesh Internal Energy model

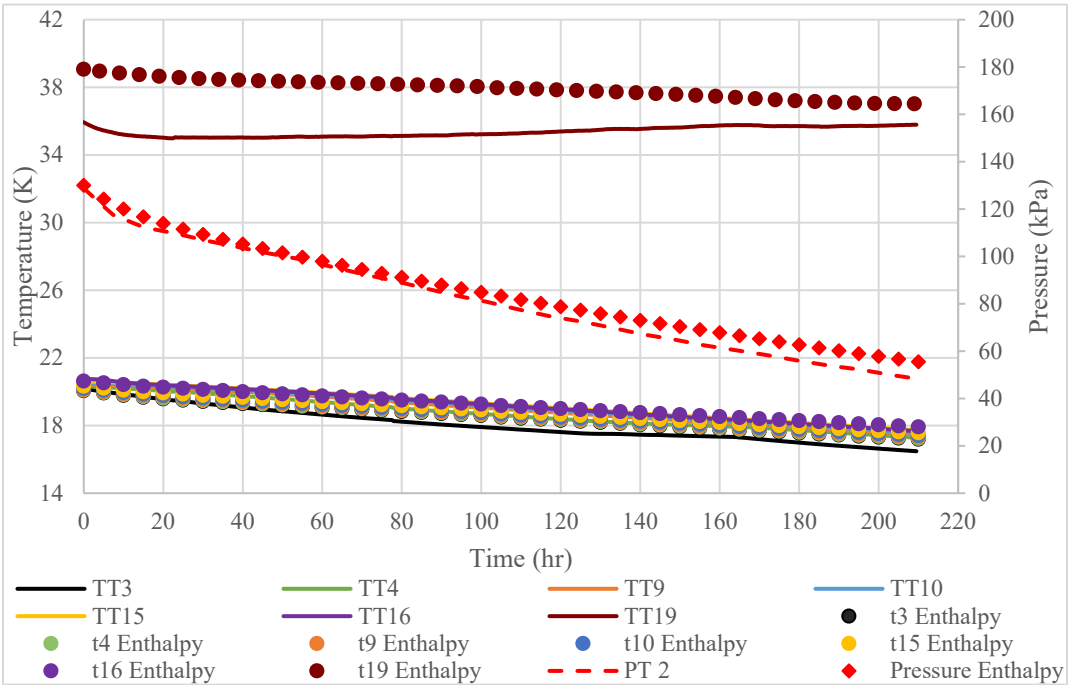

Figure 4.40 100% tank fill experimental temperatures compared to the 500k mesh Enthalpy model

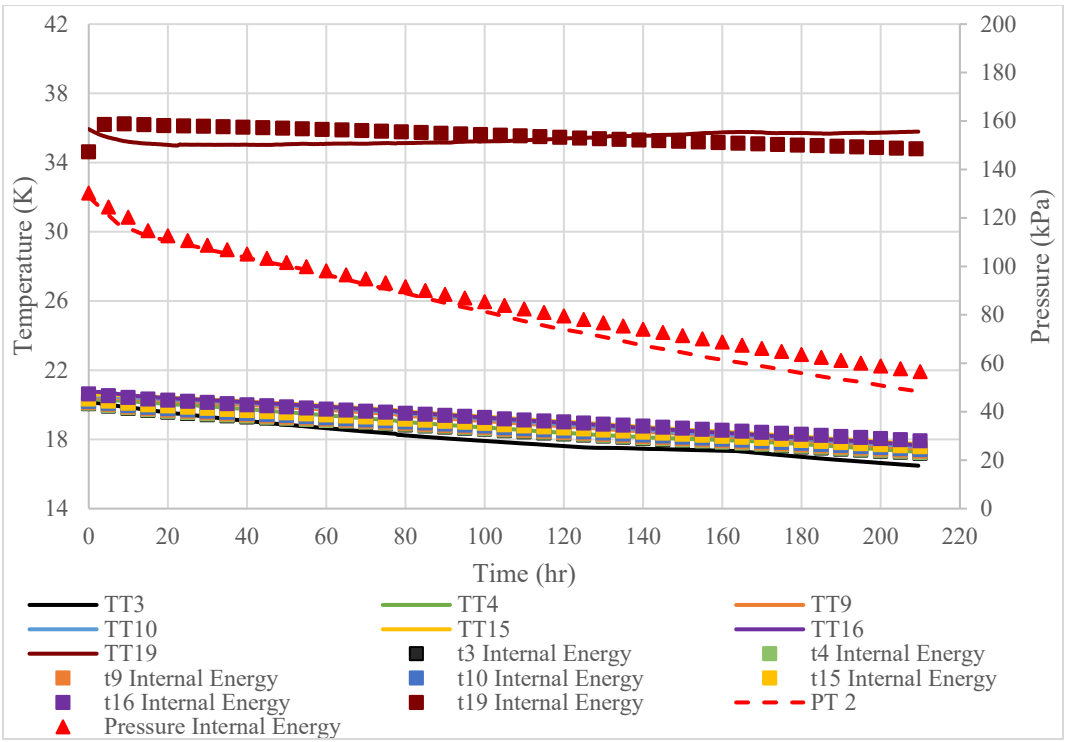

Figure 4.41 100% tank fill experimental temperatures compared to the 500k mesh Internal Energy model

The temperature predictions for both models show agreement with the experimental data for all meshes. The temperature predictions presented in Figures 4.36 – 4.41 show the hydrogen is thermally stratified, however the diodes submerged in the liquid were decreasing with time. The tank pressure also decreased with the removal of heat following the saturation curve the hydrogen.

The pressure data presented above shows that as the mesh density increases the predicted pressure becomes more accurate as compared to the experiment. Table 4.6 presents the Correlation Coefficient calculations for the two different models and the different meshes. For both models, a Correlation Coefficient of 0.99 for the pressure prediction is achieved using the 500k mesh. The maximum Percent Error of the

temperature in the ullage is less than 10% for both models using the 500k mesh which indicates good agreement between the simulations and experiment.

Table 4.5 Coefficient of Determination and maximum percent error for 100% fill Densification between simulation predictions using three meshes and experimental results.

Densification				
100% fill level				
	Enthalpy		Internal Energy	
Mesh	Coefficient of Determination, Pressure	Maximum Percent Error in Temperature, Diode	Coefficient of Determination, Pressure	Maximum Percent Error in Temperature, Diode
200k	0.901544	13.171%, TT19	0.913999	4.448%, TT19
350k	0.960740	11.314%, TT19	0.964108	3.992%, TT19
500k	0.991469	9.420%, TT19	0.991429	3.627%, TT19

The Internal Energy and Enthalpy models are compared in Figure 4.42 to the Lump Node Analysis predictions reported by Swanger for the densification process. For this study, the bulk temperatures reported hereafter represent the average of the submerged thermocouple temperature measurements. The initial pressure and temperature for the Lumped Node Analysis are 52.0 kPa and 18.2K, respectively. Therefore, the Enthalpy and Internal Energy model predictions are compared to the Lump Node Analysis prediction for the 100-hour period of experiment time after the tank pressure 52.0 kPa is reached.

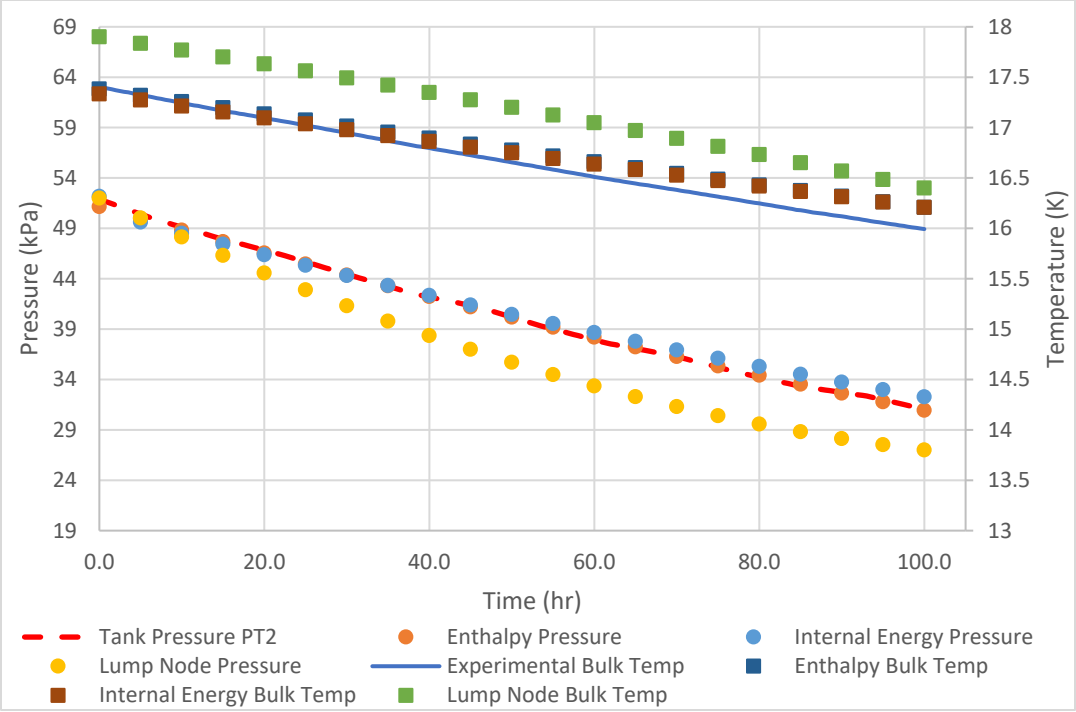

Figure 4.42 100% tank fill experimental pressures and bulk temperatures compared to the Internal Energy, Enthalpy, and Lump Node models

As shown in Figure 4.42, all three model predictions are in good agreement with the experimental data. All models present a good fit for the 100% fill case when comparing the Coefficient of Determination calculated for the temperature and pressure. Shown in Table 4.6, all models have a value of 0.99 or higher for both pressure and temperature results. The Coefficient of Determination is found to be the closest to one in the Enthalpy model for the pressure, and the best fit for the temperature was the Internal Energy model given in Table 4.6.

Table 4.6 Coefficient of Determination for 100% fill Densification between the three simulation predictions and experimental results.

Densification		
100% fill level		
Model	Coefficient of Determination, Pressure	Coefficient of Determination, Temperature
Lumped Node	0.994952	0.999555
Enthalpy	0.999981	0.999968
Internal Energy	0.999854	0.999975

4.3.2 67% Fill Level

As in the 100% fill case, the initial conditions used for the Densification simulations are the temperature, pressure, velocity, and phase fraction fields from last timestep of the steady state simulation. The densification phase of the 67% fill level experiment was conducted over approximately 315 hours. Simulations of the densification phase are performed with a total time of 315 hours, consistent with the experiment time, and with a time step of 3 seconds. The simulations are performed using the same meshes used in the steady state analysis. The temperature distribution predictions inside the tank obtained using the Internal energy and Enthalpy models using and the 660k mesh are shown in Figures 4.43 and 4.45, respectively. Figures 4.44 and 4.46 presents the predicted velocity profiles at different time intervals: 15 minutes, 195 hours, and 315 hours.

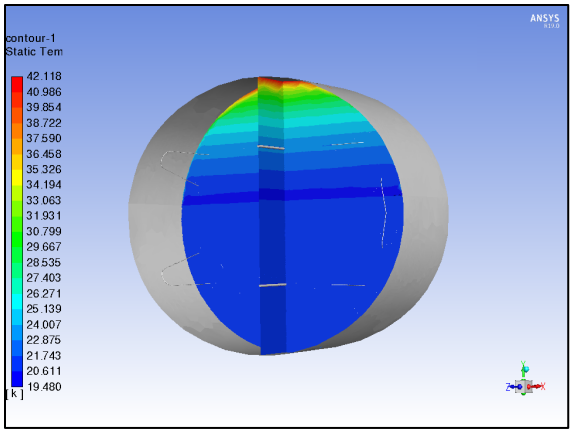

(a)

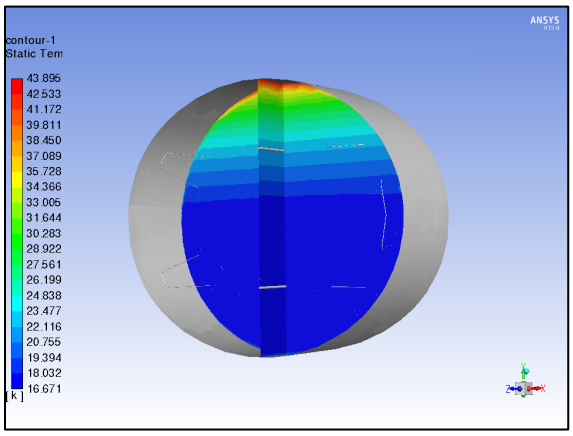

(b)

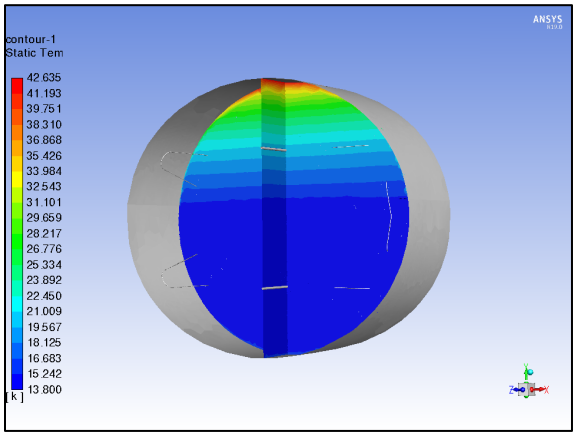

(c)

Figure 4.43 Temperature profiles for the Enthalpy method: (a) 15 minutes from beginning of simulation, (b) 105 hours through simulation, (c) final simulation time of 210 hours

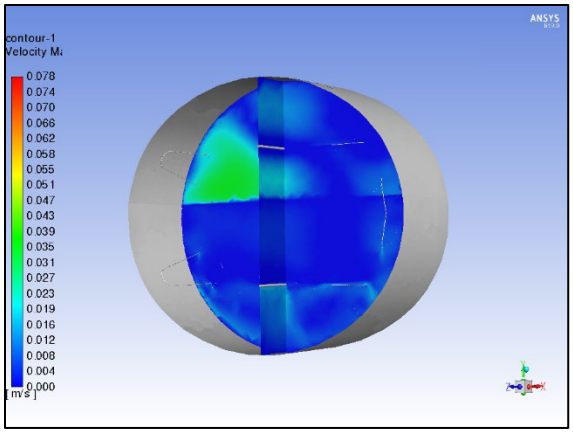

(a)

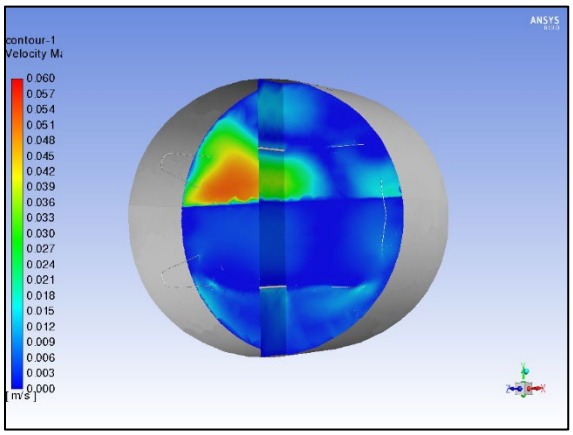

(b)

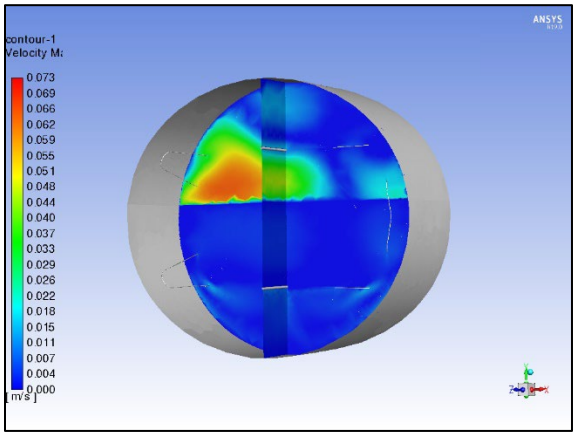

(c)

Figure 4.44 Velocity profiles for the Enthalpy method: (a) 15 minutes from beginning of simulation, (b) 105 hours through simulation, (c) final simulation time of 210 hours

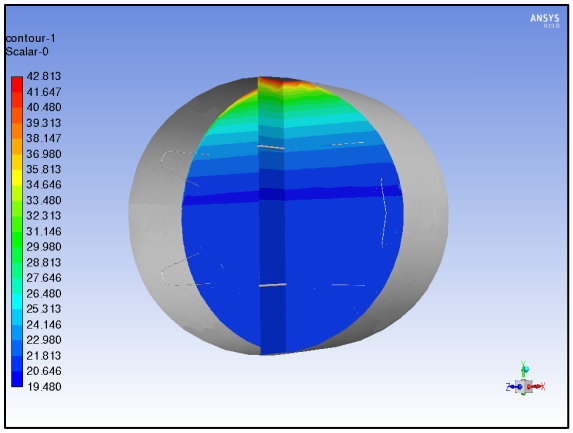

(a)

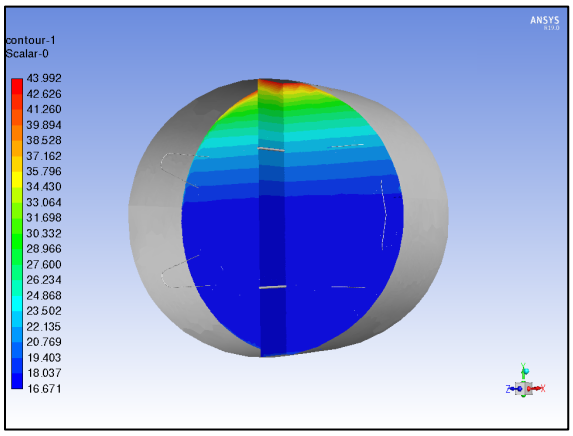

(b)

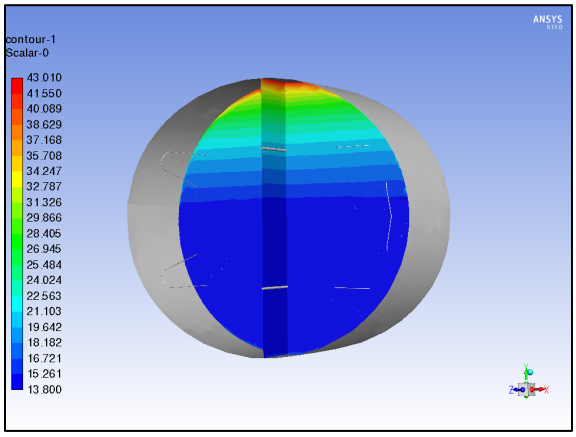

(c)

Figure 4.45 Temperature profiles for the Internal Energy method: (a) 15 minutes from beginning of simulation, (b) 105 hours through simulation, (c) final simulation time of 210 hours

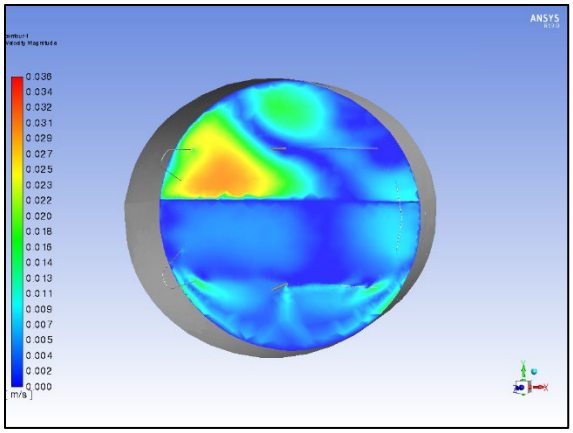

(a)

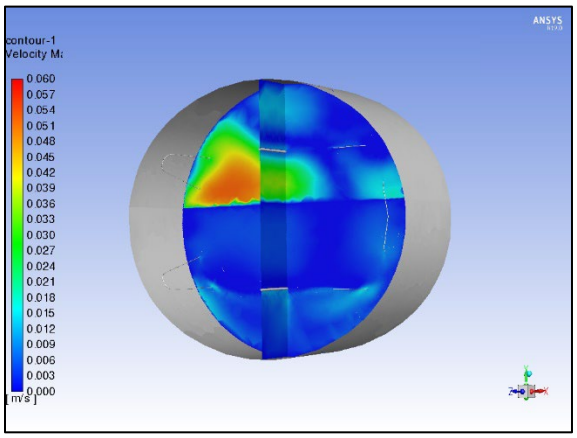

(b)

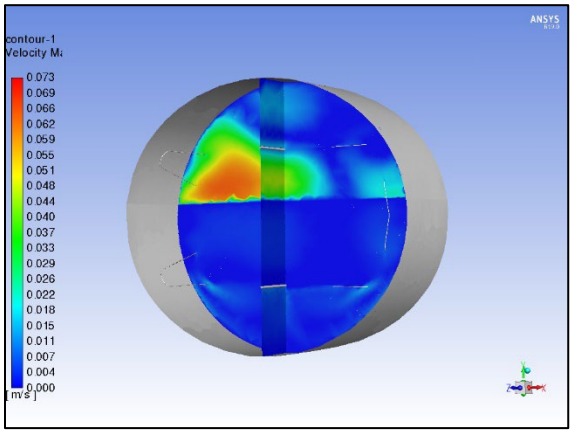

(c)

Figure 4.46 Velocity profiles for the Internal Energy method: (a) 15 minutes from beginning of simulation, (b) 105 hours through simulation, (c) final simulation time of 210 hours

It is apparent from the temperature profiles in the simulation that as the temperature decreases over time, the temperature in the tank remains stratified particularly in the ullage region. The velocity profiles indicate that a recirculation zone behind the coil remained, but then the velocities in the recirculation zone the coil began to decrease in the liquid space over time. The velocity decrease is due to the temperature approaching the freezing point of LH_2.

Figure 4.47 shows the experimental temperature and pressure data for the densification process, and Figures 4.48 and 4.49 show the Enthalpy and Internal Energy model predictions using the lowest mesh density, approximately 320k. Figures 4.50 and 4.51 show the experiment temperature and pressure measurements, and the Enthalpy and Internal Energy model predictions using the medium mesh density, approximately 430k. Finally, Figures 4.52 and 4.53 show the experiment temperature and pressure measurements, and the Enthalpy and Internal Energy model predictions for the highest mesh density, approximately 660k.

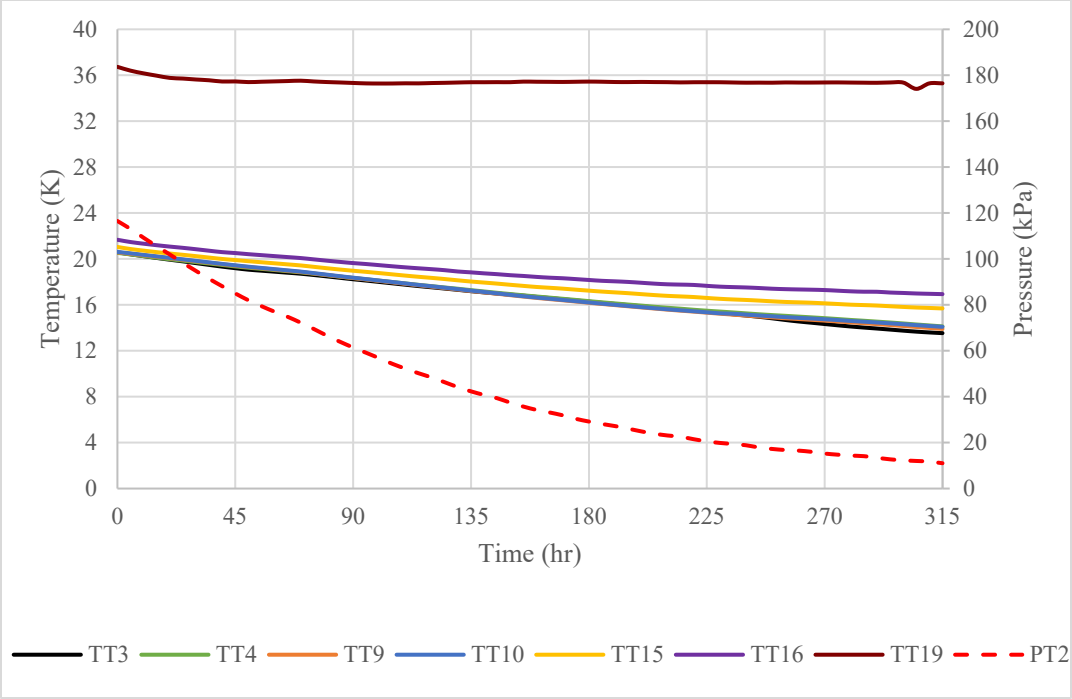

Figure 4.47 67% tank fill experimental temperatures and pressure densification data

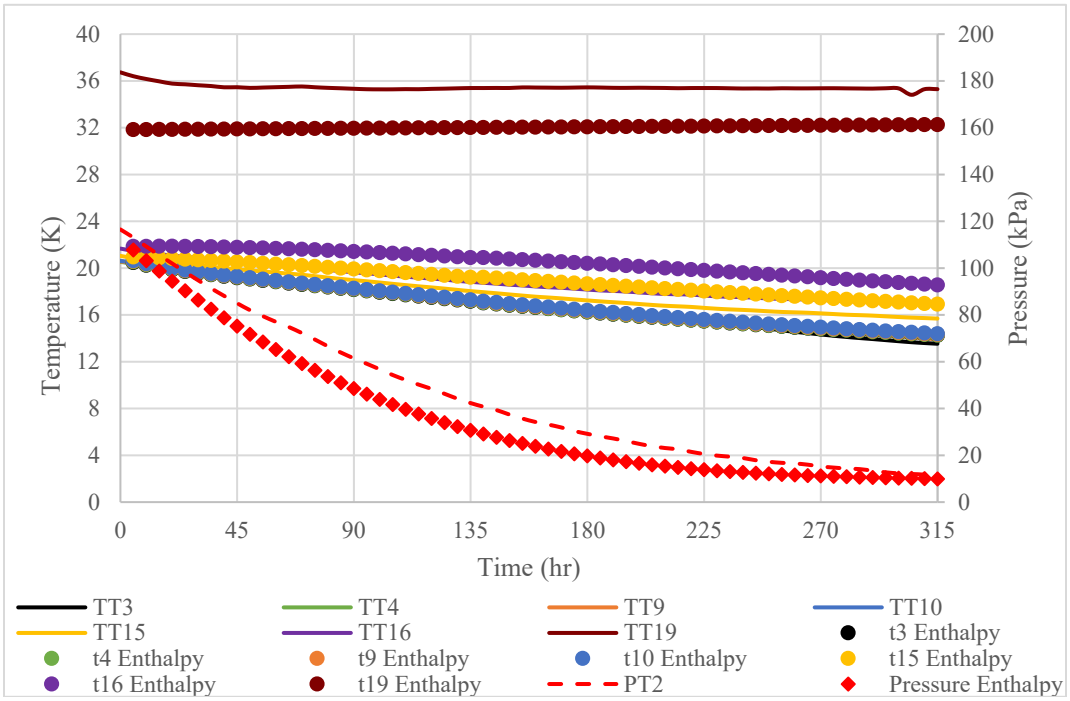

Figure 4.48 67% tank fill experimental temperatures compared to the 320k mesh Enthalpy model

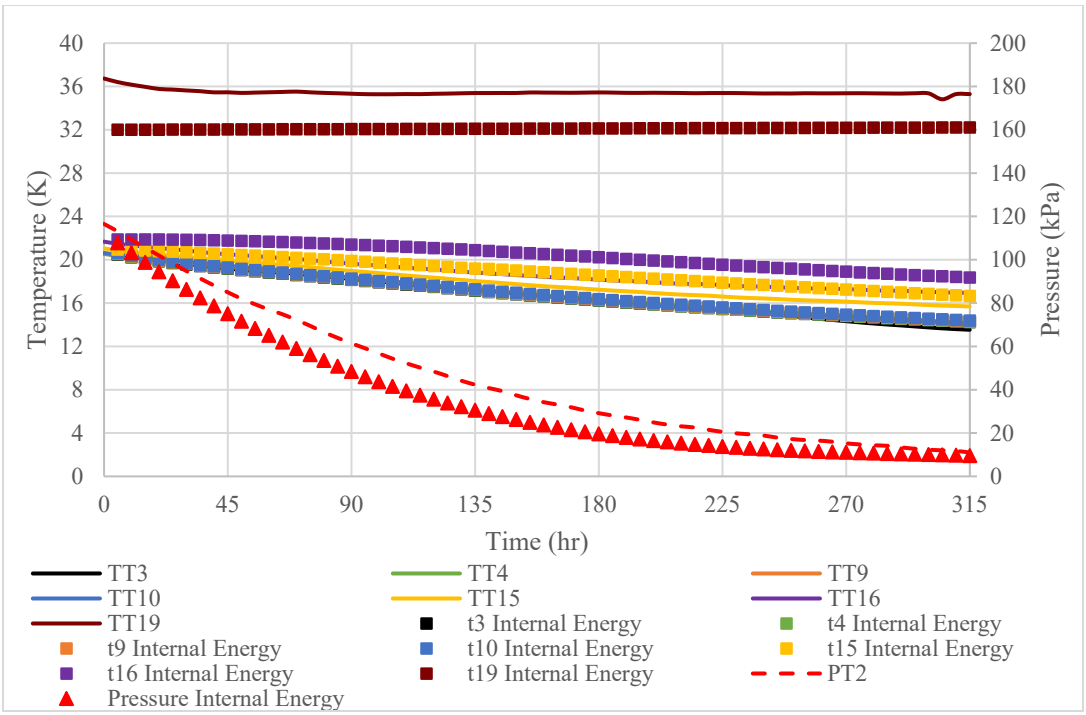

Figure 4.49 67% tank fill experimental temperatures compared to the 320k mesh Internal Energy model

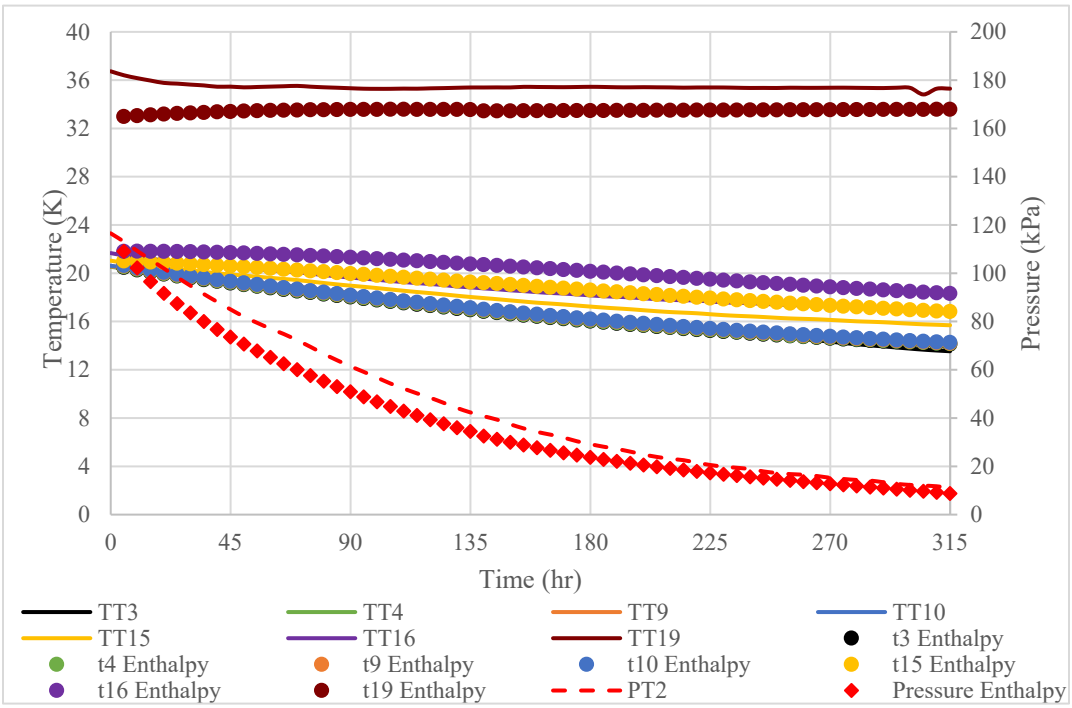

Figure 4.50 67% tank fill experimental temperatures compared to the 430k mesh Enthalpy model

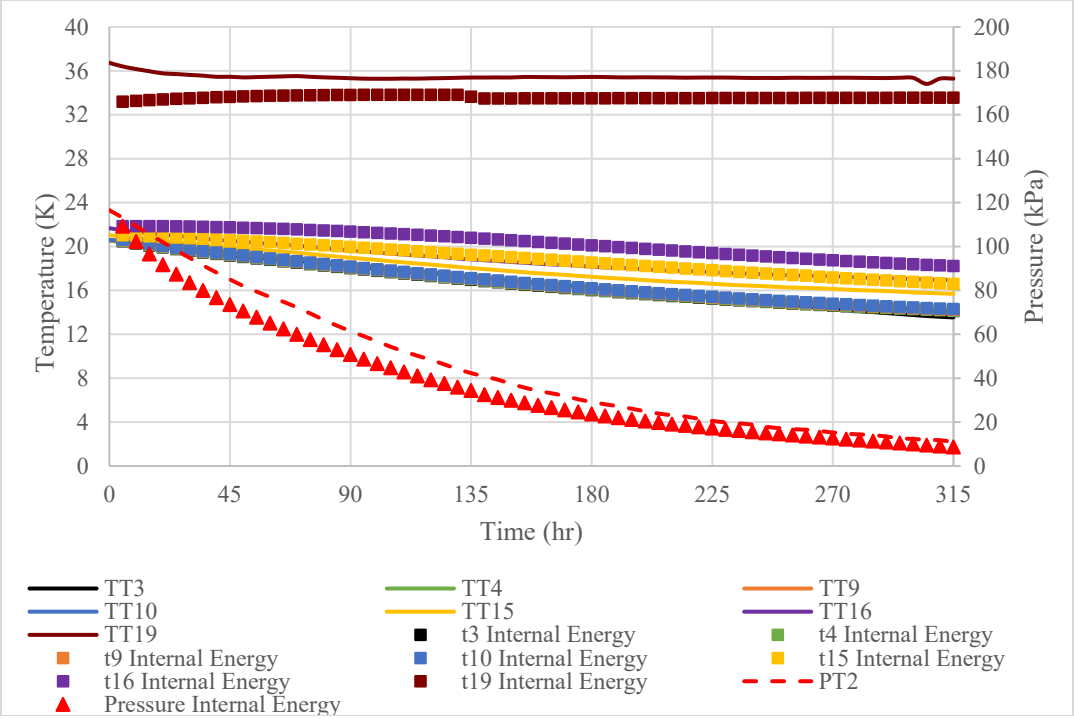

Figure 4.51 67% tank fill experimental temperatures compared to the 430k mesh Internal Energy model

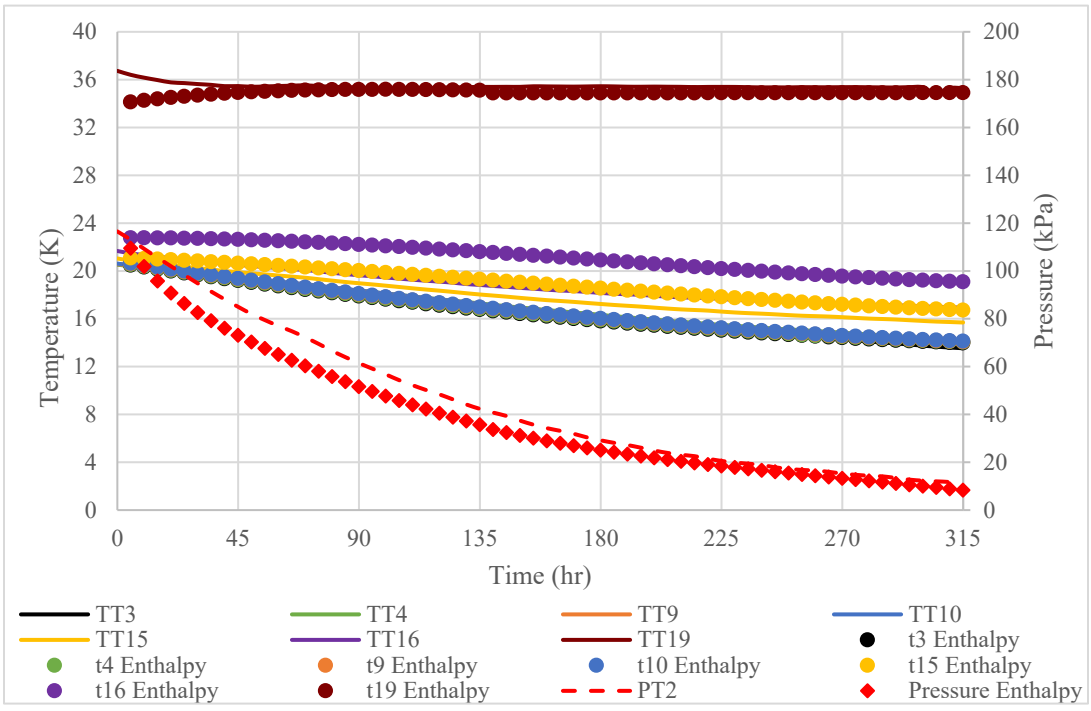

Figure 4.52 67% tank fill experimental temperatures compared to the 660k mesh Enthalpy model

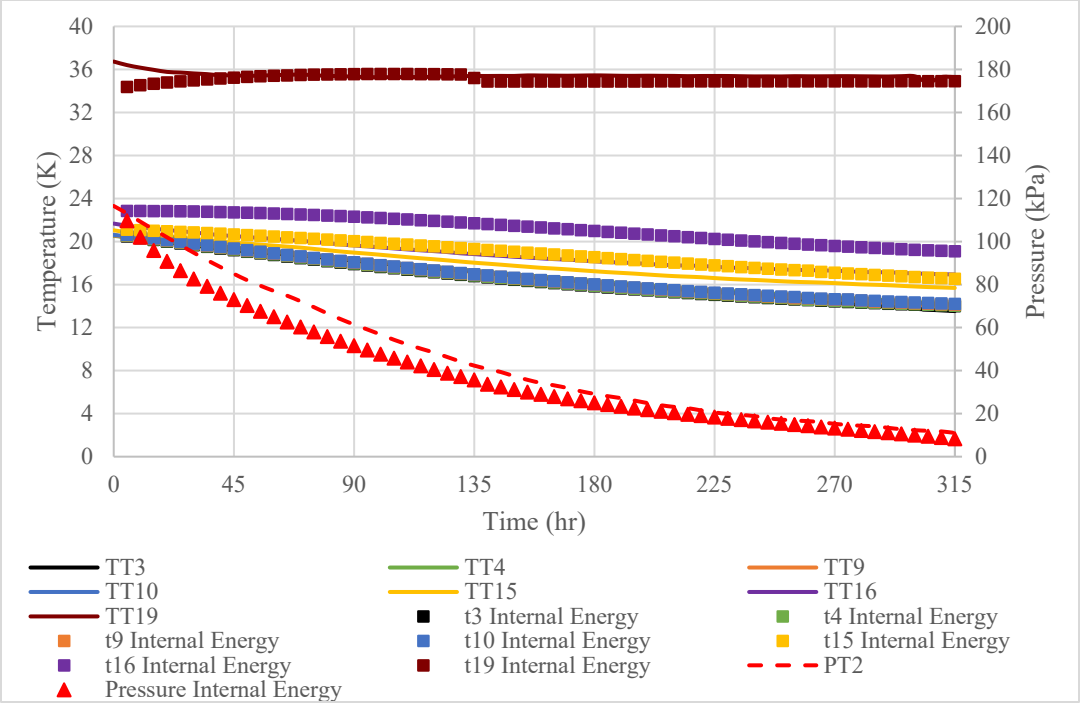

Figure 4.53 67% tank fill experimental temperatures compared to the 660k mesh Internal Energy model

The temperature predictions for the thermocouples in the ullage space, TT15 and TT16, presented in Figures 4.48 – 4.53 are slightly higher for both the Enthalpy and Internal Energy models when compared to the experimental results. Whereas the temperature predictions for TT19 are lower than temperatures recorded during the experiment. Although it is difficult to discern from the Figures, the temperature predictions for the thermocouples submerged in LH2; TT3, TT4, TT9, and TT10, show good agreement with the experimental results in all the simulations. The maximum errors between the temperature predictions and experiments results are presented in Table 4.6. The liquid temperature distribution is remains stratified as the heat is removed from the tank, however toward the end of the densification phase, both the simulations and the experiment temperatures converging upon temperature of 13.8 K.

The pressure predictions for both models show good agreement with the experimental results. As the number of computational cells increases, the pressure predictions approach the experimental results for both Enthalpy and Internal Energy models. From the above figures, both models underpredict the pressure using all three meshes. As shown in Table 4.6 a Correlation Coefficient of 0.99 for the pressure prediction is achieved using the 660k mesh for both models. The maximum Percent Error of the temperature in the ullage is less than 12% for both models using the 660k mesh which indicates acceptable agreement between the simulations and experiment.

Table 4.7 Coefficient of Determination and maximum percent error for 67% fill Densification between simulation predictions using three meshes and experimental results.

Densification				
67% fill level				
	Enthalpy		Internal Energy	
Mesh	Coefficient of Determination, Pressure	Maximum Percent Error in Temperature, Diode	Coefficient of Determination, Pressure	Maximum Percent Error in Temperature, Diode
320k	0.991661	15.431%, TT19	0.991921	14.799%, TT19
430k	0.995529	13.142%, TT19	0.995455	13.471%, TT19
660k	0.995619	11.912%, TT19	0.995495	11.236%, TT19

The models are compared to the lump node analysis performed by Swanger for the 67% fill and presented in Figure 4.54. The initial conditions for the lump node analysis were 71.7 kPa for tank pressure and 19.2 K for the temperature. The comparison of pressure and bulk temperature between the Lump Node Analysis, the Internal Energy model, the Enthalpy model, and experiment is made over the 150-hour period once the simulations reach 71.7 kPa.

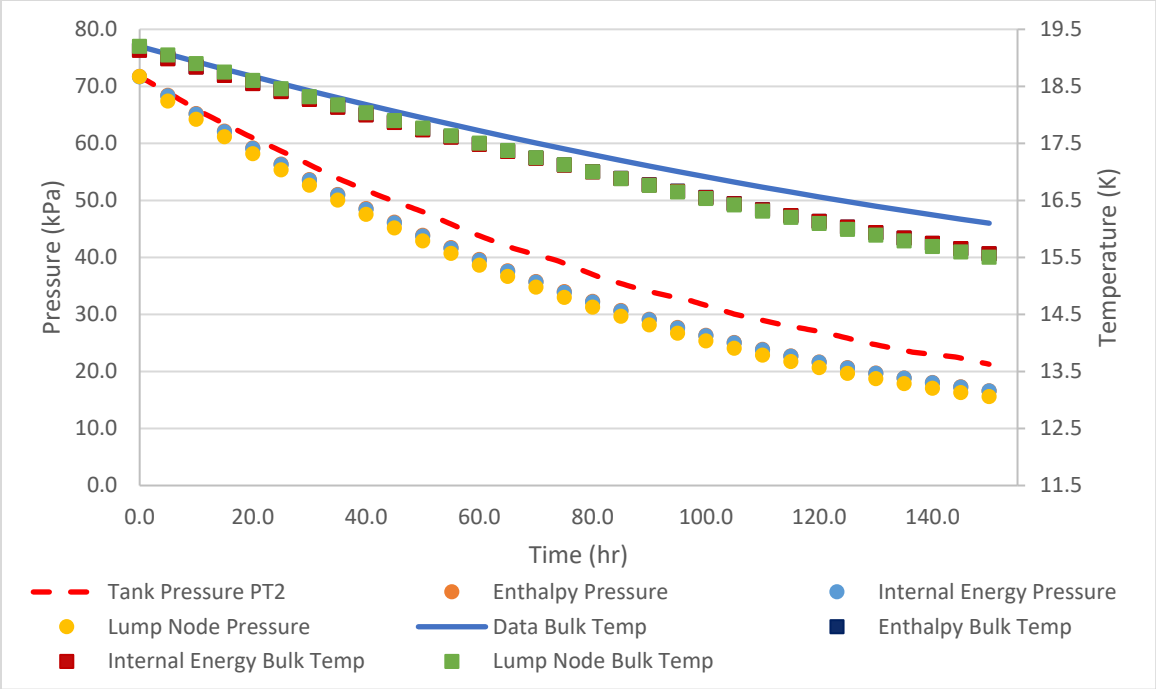

Figure 4.54 67% tank fill experimental pressures and bulk temperatures compared to the Internal Energy, Enthalpy, and Lump Node models

The temperatures recorded by the diodes are averaged to get a bulk liquid temperature for the experiment, Enthalpy model, and Internal Energy model. The results from the 660k mesh were used to calculate the bulk temperatures and pressures. For the Lump Node analysis, Enthalpy, and Internal Energy showed good agreement with the experimental result for the 150-hour run time. All models present a good fit when comparing their respective calculated Coefficient of Determination. From Table 4.8, all models have a value of 0.98 or higher for both pressure and temperature results. The Coefficient of Determination is found to be the closest to one in the Enthalpy model for both the pressure and temperature.

Table 4.8 Coefficient of Determination for 67% fill Densification between the three simulation predictions and experimental results.

Densification		
67% fill level		
Model	Coefficient of Determination, Pressure	Coefficient of Determination, Temperature
Lumped Node	0.989306	0.999590
Enthalpy	0.993191	0.999628
Internal Energy	0.992859	0.999622

4.3.3 Discussion of the Densification Results

In the 100% fill densification simulation, both the Enthalpy and the Internal Energy models show good agreement when compared to the experimental results, using the highest density meshes. As heat is removed by the refrigerator coil, the temperature inside the tank decreases, but the fluid temperature distribution does remain stratified as shown in Figures 4.36 – 4.41. A nearly centralized recirculation zone in the liquid domain becomes the dominant for both models as shown in Figures 4.32 and 4.34. The 0.99 Coefficient of Determination for the pressure predictions of the 100% fill level case indicate excellent agreement with the experiment data. The Enthalpy and Internal Energy model predictions are compared to a lump node analysis previously conducted on the GODU-LH2 tank. All three models' predictions when compared to the experimental results showed similar results. The temperature predictions using the Enthalpy and Internal Energy method are more accurate than the lump node analysis in the 100% fill case, and similarly for the pressure data presented in Figure 4.42 and quantified in Table 4.7.

The densification temperature predictions for the 67% fill cases using the Enthalpy and Internal Energy models, presented in Figures 4.48 – 4.53, show good agreement with for the thermocouple temperature data obtained during the experiment. Figures 4.43 and 4.45 show that the temperature decreases inside the tank over time and of that the temperature distribution remains stratified throughout the densification phase. . A recirculation zone develops behind the top bend in the refrigerator coil as predicted by both models, and the velocity decreases in the liquid domain as the temperature approached the triple point as shown in Figures 4.44 and 4.46. The Coefficients of Determination using the highest density meshes for the pressure predictions of the 67% fill case quantitatively show that the simulations are accurately modeling the experiment., For the 67%, the model predictions are also compared to the predictions obtained using a lumped node analysis, as presented in Figure 4.54. The comparison shows that both the Enthalpy and Internal Energy models are more accurate at predicting the temperatures and pressures measured during experiments than the Lumped Node Analysis

4.4 Solidification of Hydrogen on a Large Scale

The solidification phase of the experiment begins as the refrigeration coil surface temperature reaches the triple point temperature of 13.8K and the pressure in the tank is 7.042kPa. A mentioned previously, the triple point temperature was not reached for the 100% fill experiment. Thus, the study of large scale LH2 solidification is limited to the 67% fill level experiment. For the previous phases, of the experiment, the solidification source terms are already included in both the Enthalpy and Internal Energy models, but the terms are zero until the hydrogen reaches the triple point temperature. In addition, the properties for all three phases of hydrogen are also included in the codes for both models

as a User Defined Function (UDF). Thus, the Enthalpy and Internal Energy model predictions for the solidification phase of the 67% fill level experiment are simply a continuation of the densification simulations when the refrigeration coil drops below the triple point temperature. From the mesh convergence study conducted during the densification phase, the solidification results are presented for the highest density mesh, 660k mesh. Figures 4.55 and 4.58 present the temperature stratification occurring inside the ullage and liquid domains, while Figures 4.56 and 4.59 show the velocity profiles. Figure 4.57 presents the Liquid Fraction of hydrogen for the Enthalpy method, and Figure 4.60 shows the EOF fraction (shown in red) for the Internal Energy method. It should be noted that the EOF fraction represents the liquid fraction in the Internal Energy model. Figures 4.61 and 4.62 show the experimental temperatures and pressures compared to the predictions obtained using both the Internal Energy and Enthalpy models.

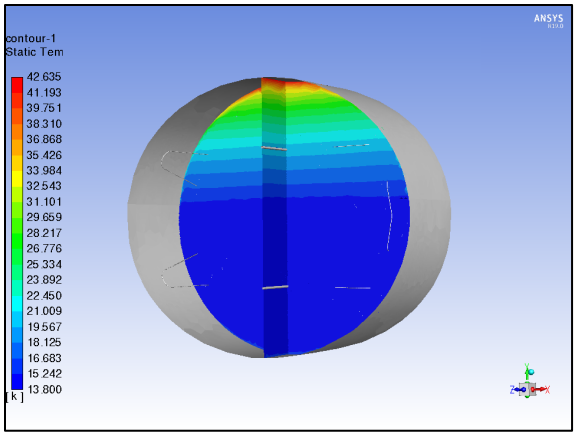

(a)

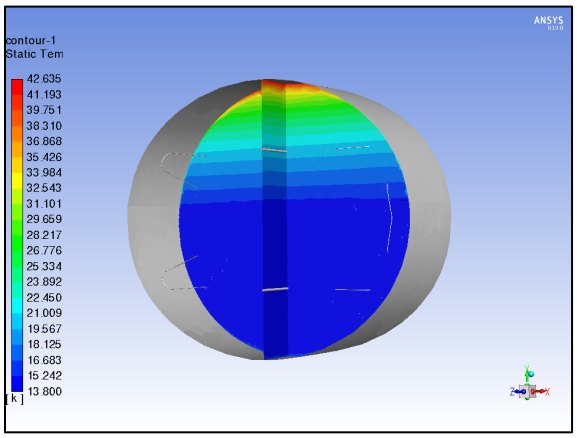

(b)

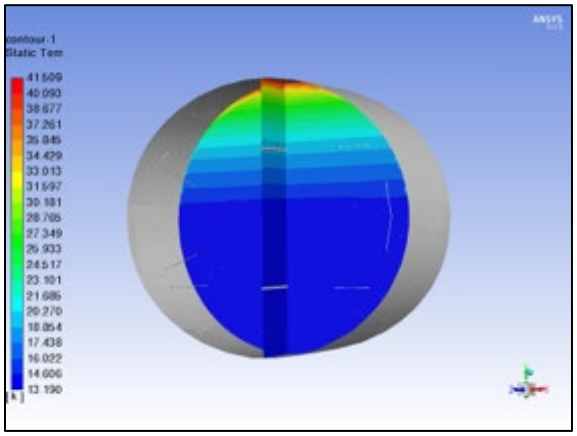

(c)

Figure 4.55 Temperature profiles for the Enthalpy method: (a) onset of visible solidification, (b) 15 hours of solidification, (c) approximately 30 hours of solidification

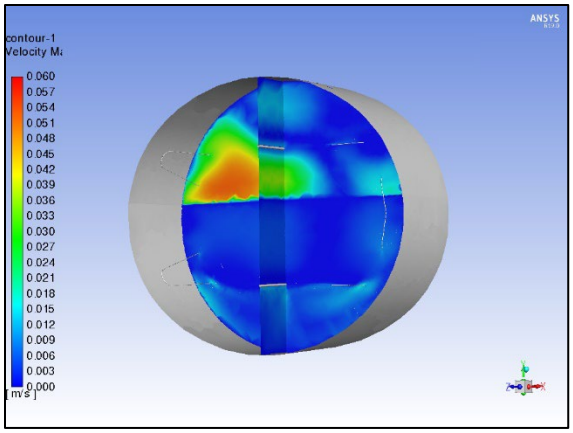

(a)

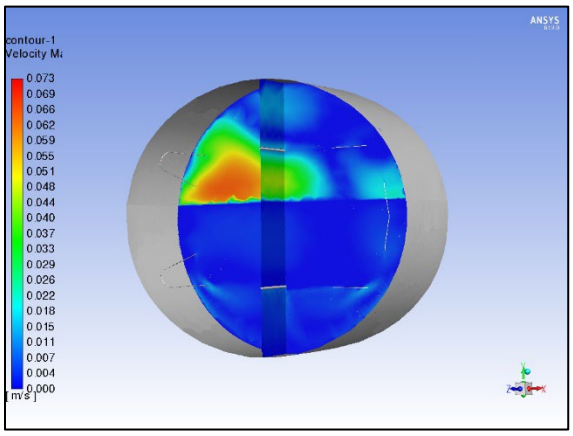

(b)

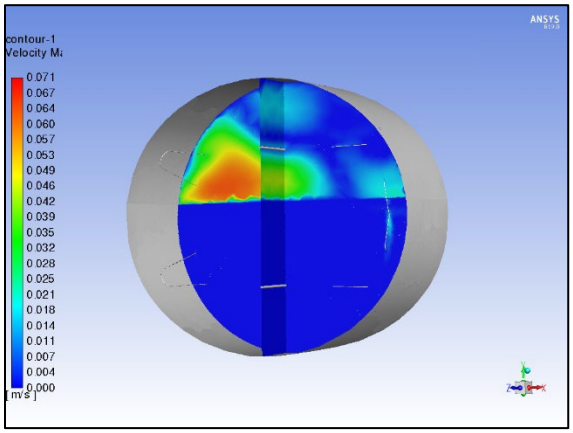

(c)

Figure 4.56 Velocity profiles for the Enthalpy method: (a) onset of visible solidification, (b) 15 hours of solidification, (c) approximately 30 hours of solidification

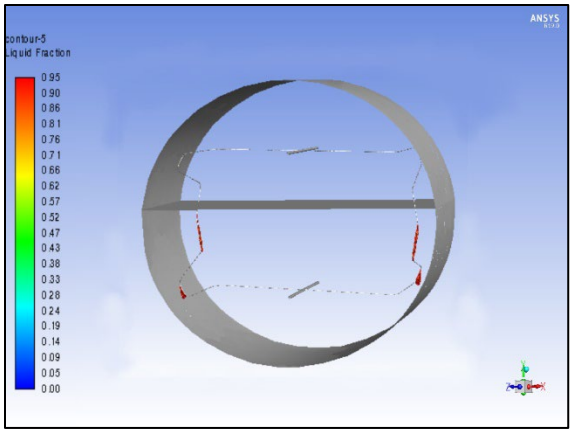

(a)

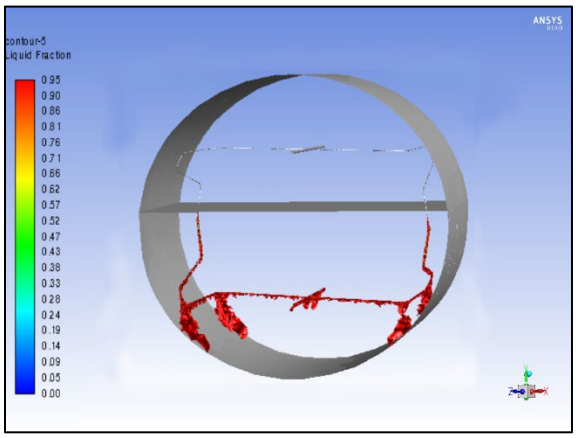

(b)

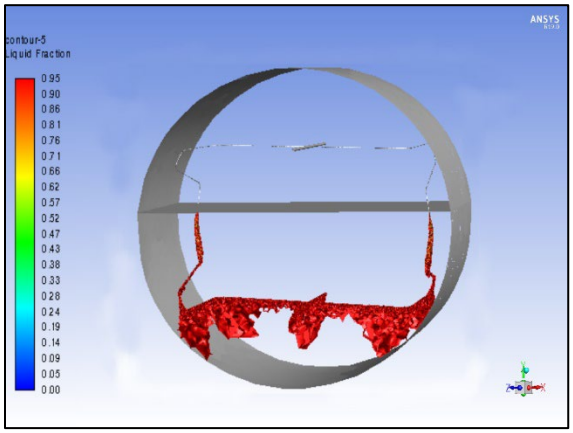

(c)

Figure 4.57 Liquid Fraction for the Enthalpy method: (a) onset of visible solidification, (b) 15 hours of solidification, (c) approximately 30 hours of solidification

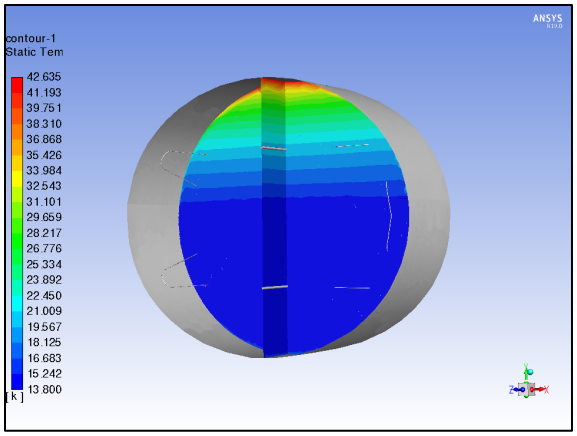

(a)

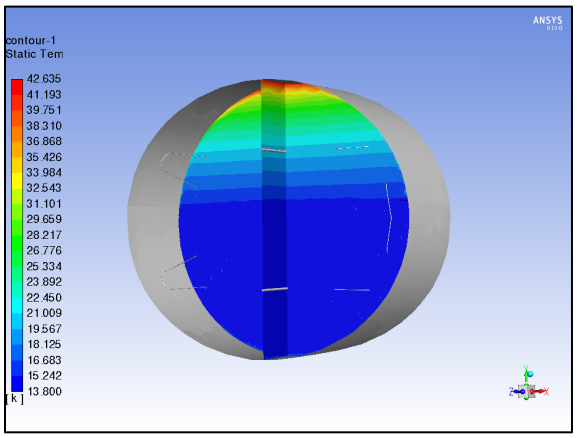

(b)

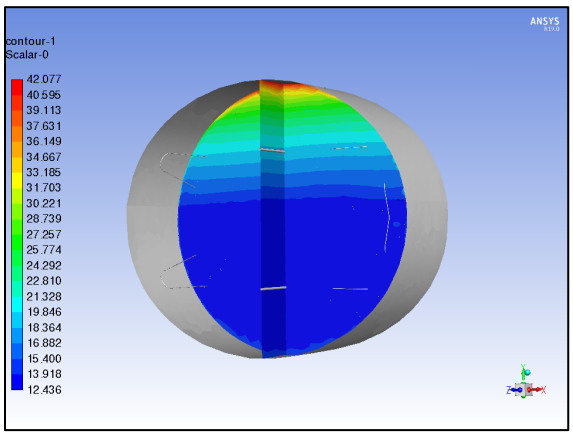

(c)

Figure 4.58 Temperature profiles for the Internal Energy method: (a) onset of visible solidification, (b) 15 hours of solidification, (c) approximately 30 hours of solidification

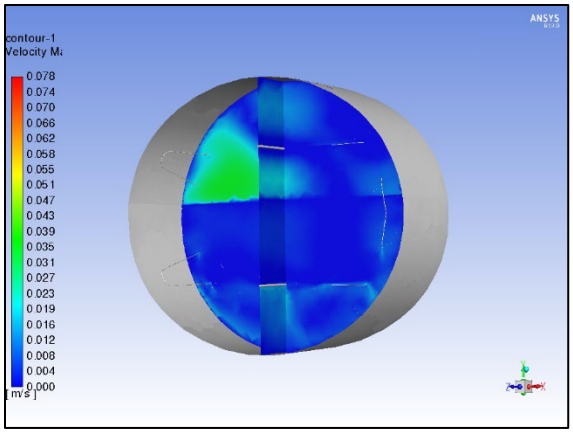

(a)

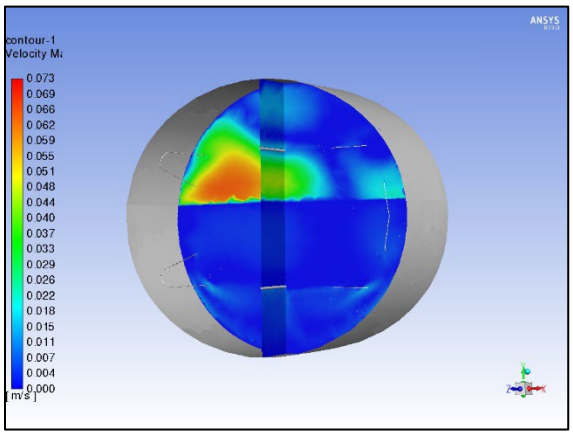

(b)

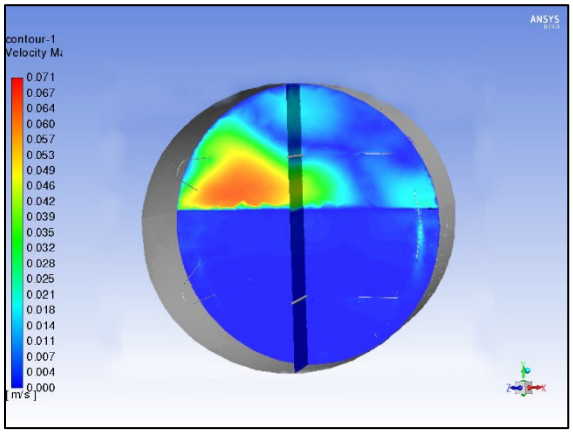

(c)

Figure 4.59 Velocity profiles for the Internal Energy method: (a) onset of visible solidification, (b) 15 hours of solidification, (c) approximately 30 hours of solidification

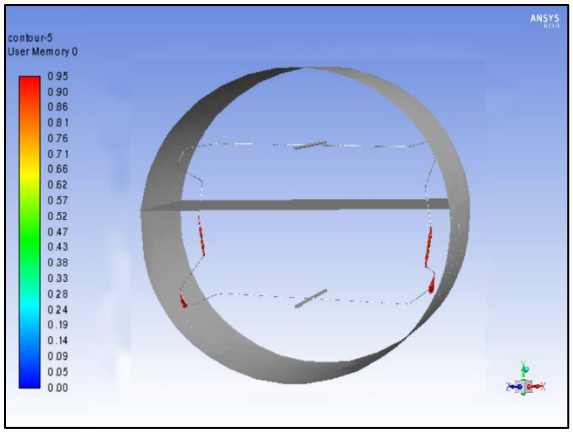

(a)

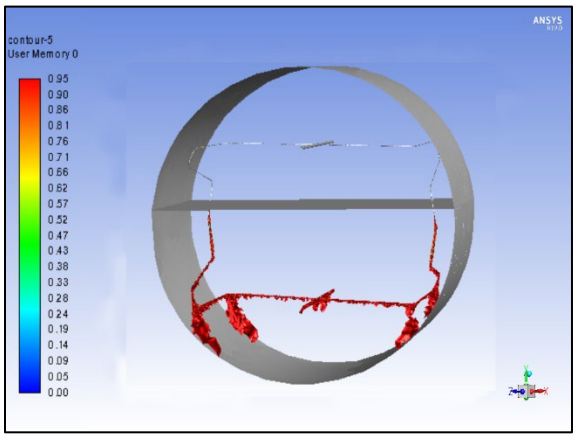

(b)

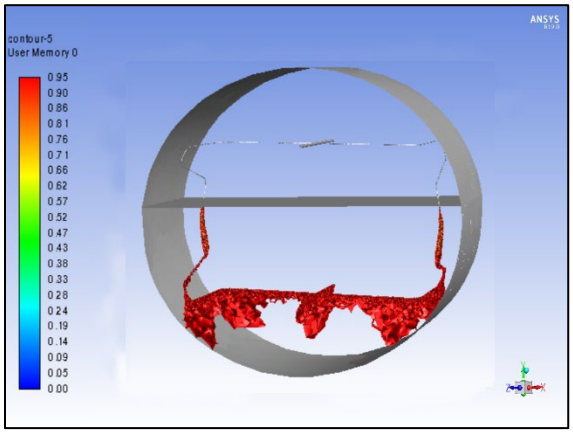

(c)

Figure 4.60 Energy of Fluid for the Internal Energy method: (a) onset of visible solidification, (b) 15 hours of solidification, (c) approximately 30 hours of solidification

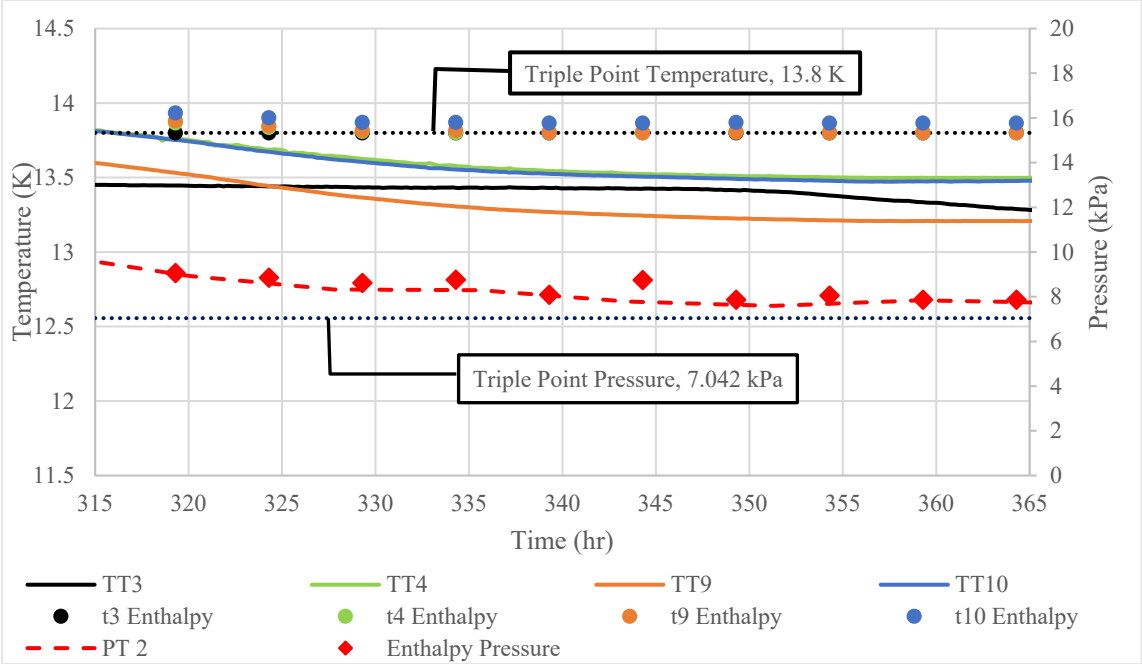

Figure 4.61 67% tank fill experimental pressure and temperature compared to the Enthalpy model

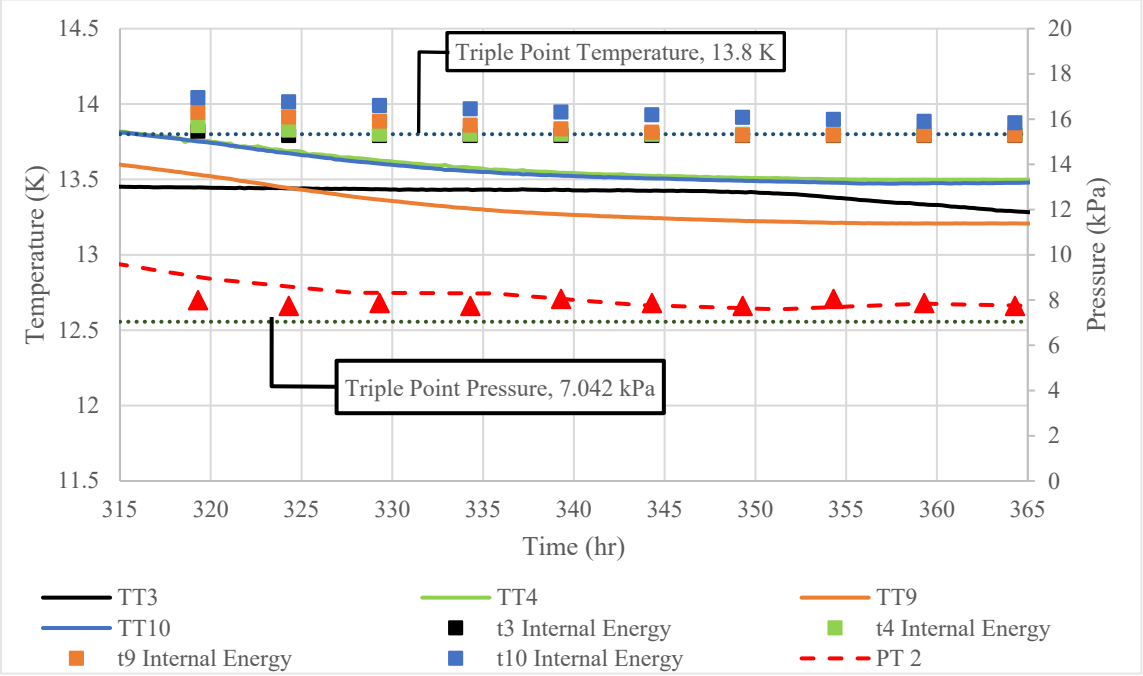

Figure 4.62 67% tank fill experimental pressure and temperature compared to the Internal Energy model

From Figures 4.61 and 4.62, the pressure and temperature predictions for both models qualitatively show good agreement with the experiment, however, to better quantify the accuracy of the different models to the experiment results, the Coefficient of Determination is calculated for the pressure. The Coefficient of Determination for the pressure and maximum percent errors for the temperature data are given in Table 4.7. The 0.99 Coefficient of Determination for the pressure predictions and maximum percent error in temperature of less than 10% in the 67% fill level during the solidification phase indicate excellent agreement with the experiment data

Table 4.9 Coefficient of Determination and maximum percent error for 67% fill Solidification between simulation predictions using experimental results.

Solidification				
67% fill level				
	Enthalpy		Internal Energy	
Mesh	Coefficient of Determination, Pressure	Maximum Percent Error in Temperature, Diode	Coefficient of Determination, Pressure	Maximum Percent Error in Temperature, Diode
660k	0.998004	7.14%, TT16	0.996559	6.93%, TT16

One of the objectives in the effort to develop the Internal Energy model for modeling cryogenic three phase system is to reduce the time required to complete simulations when compared to using the more well-established Enthalpy model. Therefore, it is desirable to use models which are accurate and efficient. As mentioned in previous chapters, the major difference between the Enthalpy and Internal Energy methods is the transient pressure term which is in the Enthalpy model. The transient pressure term is a consequence of the coupling of internal energy, pressure, and density in the combined property of enthalpy. This coupling creates a stiffness in the solution of the

enthalpy formulation of the energy equation which necessitates the use of a small-time step to achieve convergence in systems which experiences large pressure changes over short periods of time (i.e., cryogenic tank self-pressurization). The increase in computational efficiency of the Internal Energy model as compared to the Enthalpy model was previously demonstrated by Anghaie and Ding.,. Unlike cryogenic tank self-pressurization, the pressure changes in the GODU-LH2 experiments gradually decrease over a relatively long period of time due to the gradual decrease in temperature of the refrigeration coil during the densification and solidification phases. Thus, it is expected that the time efficiency of obtaining solutions using both the Internal Energy and Enthalpy model will be similar. A time efficiency comparison using the Wall time per iteration as a benchmark is shown in Table 4.10, the two models on the 660K mesh.

Table 4.10 Wall time per iteration for the Enthalpy and Internal Energy models

Mesh	Enthalpy (s)	Internal Energy (s)	Percent Difference
660k	0.617	0.579	6.16%

From the table for the 660k mesh, the time per iteration for the Internal Energy model took less time to converge compared to the Enthalpy method. The Internal Energy model for the 660 mesh was 6.16% faster in terms of Wall time per iteration than the Enthalpy model. It is anticipated that the Internal Energy model will be more efficient than the Enthalpy model when the Internal Energy model is further developed to simulate cryogenic tank self-pressurization.

4.4.2 Discussion of the Solidification Results

The solidification phase of the experiment is simulated using the Enthalpy and the Internal Energy models s once the temperature and pressure during the densification phase decrease below the triple point in the ullage space, the temperature of the fluid remains stratified as shown in Figures 4.55 and 4.58 for the Enthalpy and Internal Energy predictions. Figures 4.56 and 4.59 show that the recirculation zone created during the densification phase behind the bend in the coil remains throughout the solidification process, while the velocity in the liquid domain reduces to near zero once the hydrogen begins to solidify. Figure 4.57 presents the Liquid Fraction predictions obtained using the Enthalpy method at onset of visible solidification, after 15 hours of solidification, and after approximately 30 hours of solidification. Figure 4.60 shows the EOF predictions at the same points in time. For both models, the ice begins to form along the long vertical tubes and then on the horizontal coils in the liquid domain. The hydrogen then solidifies downward from the refrigeration coil forming larger areas of solid hydrogen similar to the formation of water into icicles. The largest areas of solid hydrogen formation appear directly under the larger manifold pipe and in the bent sections of the refrigerator coils. The 0.99 Coefficient of Determination for the pressure predictions and maximum percent error in temperature of less than 10% in the 67% fill level during the solidification phase indicate both models are reasonably accurate in modeling experiment. From Table 4.7 for 660k, the percentage difference in Wall time per iteration is calculated for both models. The Internal Energy model is approximately 6.159% faster in simulating solidification than the Enthalpy model.

CHAPTER V

SUMMARY AND CONCLUSIONS

The Ground Operations and Demonstration Unit for Liquid Hydrogen (GODU-LH2) successfully demonstrated the IRAS technology capabilities such as zero boiloff, liquid densification, and hydrogen solidification. Due to the possibilities of IRAS implemented storage tanks for cryogens, significant effort was expended in developing efficient models that can predict the performance of the IRAS system for both steady state and transient operations and validating the models with GODU-LH2 experimental data.

In the development process the Enthalpy and Internal energy models had to be verified by comparing models in literature for conduction, convection, and phase change. Both models accurately simulated conduction heat transfer and phase change based on comparisons with analytical solutions. For the buoyancy driven flow (natural convection) problem, both model predictions showed excellent agreement with the literature values and the experimental values presented. The model results differed slightly for the convection phase change case, however, both models predicted results similar to the tabulated values in the literature.

The ZBO steady state analysis focused on the comparison of the model predictions to the experimental data for a constant pressure process in which the refrigerator lift equaled the heat transfer into the system. The pressure predictions were

more accurate as the mesh density increased as substantiated by the Coefficient of Determination. The temperature predictions for all the meshes showed agreement with the experimental data. The temperature percent errors were calculated for each of the different thermocouples in the tank across the three meshes and for both fill levels. These results revealed the Internal Energy method produced more accurate results than the Enthalpy method. The lowest percent errors were tabulated in the 100% fill level in the Internal Energy method, however there was an increase in error in the 67% fill ullage domain predictions. The models predicted a lower temperature at the top of the tank than the experimental data, however the errors for the highest density mesh were within 10%. The 67% fill simulations had higher errors in the thermocouples than the 100% fill simulations, possibly due to differing mesh densities in the ullage domain between the two fill levels. The ullage space in the 67% fill was more sparsely populated to reduce mesh size and increase simulation speed.

The ZBO, steady state, analysis results were utilized as the initial conditions in the densification phase. The densification analysis really concentrated on the ability of the models to accurately predict the tank depressurization rate and temperature drop and focused on the comparison of the Enthalpy model, Internal Energy model, and a lump node analysis to the experiment data for the 100% fill and 67% fill cases. All models were assumed to be at saturation pressure at any given bulk fluid temperature. The Enthalpy and Internal Energy models showed good agreement when compared to the experimental results supported by the calculation of the Coefficient of Determinations. The lumped node analysis over-predicted the depressurization rate more so than Enthalpy and Internal energy models when compared to the experimental results for the 100% fill

study. Also, for the 100% case, all the models under-predicted the temperature drop for the study period. The lumped node analysis predictions were the least accurate of three model in simulating the experiment. For the 67% fill simulations, the Enthalpy and Internal Energy models predicted results which were in good agreement with the experimental work. All models over-predicted the depressurization and temperature decrease, and all models resulted in relatively similar predictions for the depressurization and temperature decrease.

At the end of the densification process for the 67% fill case, the temperature and pressure remained relatively constant indicating the beginning of solidification phase change. The simulation pressure predictions approached the triple point pressure. While the simulation temperature predictions converged onto the triple point temperature indicating solidification, the experimental temperatures continued to decrease until converging on a temperature lower than the triple point signifying phase change in the experimental data. The Liquid Fraction predictions for the Enthalpy method and the Energy of Fluid (EOF) fractions for the Internal Energy model predicted initial freezing points in the connecting corners of a coil and the manifold at the bottom and along the long vertical shaft of the coil. This is likely due to the cold fluid falling down the cold vertical coil, which results in a more rapid temperature decrease to the triple point. The velocity of the fluid decreases as it falls along the vertical coil as the temperature decreases which increases the rate of solid hydrogen formation. Next, solid hydrogen forms for quickly in the curved region due to the proximity of the two cooling bodies. Shortly thereafter, the entire coil becomes encompassed in the solid hydrogen. The temperature and pressure predictions showed good agreement with the experimental data

during the solidification phase. In addition, the Internal Energy and Enthalpy model efficiencies were compared for the solidification simulations. During the simulation of the solidification phase the Internal Energy model was roughly 6% faster than the Enthalpy method, which saved approximately two weeks in Wall time.

The choice for which method to use depends on a researchers end use, the level of detail, and timeframe required to complete an individual project. If the researcher desired a simulation that could predict results within the error bounds of the experimental results without the fluid dynamics details, then the lumped node analysis may be a good choice. The Enthalpy method produced results that corresponded to the experimental results and had fluid motion details. Therefore, if the researcher wanted to accurately resolve thermal fluid flow details and was less time constrained, then the Enthalpy method might be the better choice. However, if the researcher wanted to accurately resolve thermal fluid flow details and was time constrained, then the Internal Energy might be the better choice.

The clear takeaway was that developing a simulation capable of modeling of the various phases of the GODU-LH2 IRAS tank experiments was computationally challenging., The validation effort presented herein provides a solid foundation to build upon. For active cryogenic propellant management systems which are intended to control the pressure, the models presented can be used to guide future and potentially more complex designs. Future research can continue the development of the Internal energy model for simulating cryogenic tank self-pressurization and nucleate pool boiling. Extending the. Nevertheless, it is felt as though this work achieved its primary goal of creating an accurate and efficient model that can lead to a practical engineering understanding of large-scale IRAS systems and their capabilities.

REFERENCES

[1] R. F. Barron, *Cryogenic Systems*, 2nd ed. New York: Oxford University Press, 1985.

[2] B. Birmingham, Brown, E., Class, C. and Schmidt, A., Vessels for the storage and transport of liquid hydrogen. Journal of Research of the National Bureau of Standards, 58(5), pp.243-253, 1957.

[3] J. C Aydelott, "Normal gravity self-pressurization of 9-inch- (23 CM) diameter spherical liquid hydrogen tankage.," 1967.

[4] J. C. Aydelott, "Effect of Gravity on Self-Pressurization of Spherical Liquid Hydrogen Tankage," 1967.

[5] W. D. Ward, *et al.*, "Evaluation of AS-203 Low Gravity Orbital Experiment," *NASA Tech. Rep. HSM-R421-67*, vol. Fluid Mech, no. Huntsville, AL, pp. 1–203, 1967.

[6] J. K. Partridge, "Fractional consumption of liquid hydrogen and liquid oxygen during the space shuttle program". Advances in Cryogenic Engineering, AIP Conference Proceedings, Vol.1434, pp.1765-1770, 2012.

[5] L. J. Poth and J. R. Van Hook, "Control of Thermodynamic State of Space Stored Cryogens by Jet Mixing," *J. Spacecr.*, vol. 9, no. 5, pp. 332–336, 1972.

[6] J. C. Aydelott, "Axial Jet Mixing of Ethanol in Cylindrical Containers During Weightlessness," *NASA Tech. Pap. 1487, Lewis Res. Center, Cleveland, OH*, 1979.

[7] J. C. Aydelott, "Modeling of Space Vehicle Propellant Mixing," *NASA Tech. Pap. 2107, Lewis Res. Center, Cleveland, OH*, pp. 1–30, 1983.

[8] S. A. Manatt, "The Evolution of Cryogenic Storage Systems Toward Advanced Spacecraft Missions," *SAE Tech. Pap. Ser.*, vol. 1, 1967.

[9] L. J. Salerno and P. Kittel, "Cryogenics and the Human Exploration of Mars," *Cryogenics (Guildf).*, vol. 39, no. 4, pp. 381–388, 1999.

[10] P. Kittel, L. J. Salerno, and D. W. Plachta, "Cryocoolers for Human and Robotic Missions to Mars," *Cryocoolers 10*, pp. 815–821, 1999.

[11] P. Kittel, “Propellant preservation using re-liquefiers,” *Cryogenics (Guildf).*, vol. 41, no. 11–12, pp. 841–844, 2001.

[12] D. Plachta and P. Kittel, “An Update to Zero Boil-Off Cryogenic Propellant Storage Analysis Applied to Upper Stages or Depots in a LEO Environment,” in *38th Joint Propulsion Conference and Exhibit*, 2002, no. NASA/TM-2003-211691, pp. 1–8.

[13] M. S. Haberbusch, C. T. Nguyen, R. J. Stochl, and T. Y. Hui, “Development of no-vent^{TM} liquid hydrogen storage system for space applications,” *Cryogenics (Guildf).*, vol. 50, no. 9, pp. 541–548, 2010.

[14] L. J. Hastings, D. W. Plachta, L. Salerno, and P. Kittel, “An overview of NASA efforts on zero boiloff storage of cryogenic propellants,” *Cryogenics (Guildf).*, vol. 41, no. 11–12, pp. 833–839, 2001.

[15] D. Plachta, “Results of an Advanced Development Zero Boil-Off Cryogenic Propellant Storage Test,” in *40th Joint Propulsion Conference and Exhibit*, 2004, no. NASA/TM-2004-213390, pp. 1–7.

[16] D. W. Plachta, R. J. Christie, J. M. Jurns, and P. Kittel, “Passive ZBO storage of liquid hydrogen and liquid oxygen applied to space science mission concepts,” *Cryogenics (Guildf).*, vol. 46, no. 2–3, pp. 89–97, 2006.

[17] R. F. Barron and G. F. Nellis, *Cryogenic Heat Transfer*, 2nd ed. Boca Raton, FL: CRC Press, Taylor & Rancis Group, 2016.

[18] C. Benard, D. Gobin, and F. Martinez, “Melting in Rectangular Enclosures: Experiments and Numerical Simulations,” *J. Heat Transfer*, vol. 107, pp. 794–803, 1985.

[19] T. A. Kowalewski and M. Rebow, “Freezing of Water in Differentially Heated Cubic Cavity,” *Int. J. Comput. Fluid Dyn.*, vol. 11, pp. 193–210, 1999.

[20] J. HOCHSTEIN, P. GERHART, and J. AYDELOTT, “Computational modeling of jet induced mixing of cryogenic propellants in low-G,” in *AIAA Twentieth Joint Propulsion Conference*, 1984, pp. 7–20.

[21] J. I. HOCHSTEIN, H.-C. JI, and J. C. AYDELOTT, “Prediction of self-pressurization rate of cryogenic propellant tankage,” *J. Propuls. Power*, vol. 6, no. 1, pp. 11–17, 1990.

[22] J. Hochstein, J. G. Marchetta, and R. Thornton, “Microgravity geyser and flow field prediction,” *J. P*, vol. 24, no. 1, 2008.

[23] J. Marchetta and R. Benedetti, “Three Dimensional Modeling of Jet-Induced Geysers in Low Gravity,” in *45th AIAA Aerospace Sciences Meeting and Exhibit,*

Reno, NV, 2007.

[24] J. G. Marchetta and R. H. Benedetti, “Simulation of jet-induced geysers in reduced gravity,” *Microgravity Sci. Technol.*, vol. 22, no. 1, pp. 7–16, 2010.

[25] M. HASAN and C.-S. LIN, “Buoyancy effects on the vapor condensation rate on a horizontal liquid surface,” in *AIAA 28th Aerospace Sciences Meeting*, 1990, p. Reno,Nevada.

[26] G. SASMAL, J. HOCHSTEIN, M. WENDL, and T. HARDY, “Computational modeling of the pressurization process in a NASP vehicle propellant tank experimental simulation,” in *AIAA 27th Joint Propulsion Conference*, 1991.

[27] G. SASMAL, J. HOCHSTEIN, and T. HARDY, “Influence of heat transfer rates on pressurization of liquid/slush hydrogen propellant tanks,” in *31st Aerospace Sciences Meeting and Exhibit*, 1993, pp. 1–7.

[28] C. S. Lin, N. T. Van Dresar, and M. M. Hasan, “A Pressure Control Analysis of Cryogenic Storage Systems,” *NASA Tech. Memo. 104409*, vol. Prepared f, no. AIAA, 1991.

[29] C. S. Lin, N. T. Van Dresar, and M. M. Hasan, “Pressure Control Analysis of Cryogenic Storage Systems,” *J. Propuls. Power*, vol. 20, no. 3, pp. 480–485, 2004.

[30] J. Thornton and J. I. Hochstein, “Microgravity Propellant Tank Geyser Analysis and Prediction,” *Am. Inst. Aeronatics Astronaut.*, vol. AIAA-01-11, pp. 1–12, 2000.

[31] C. H. Panzarella and M. Kassemi, “On the validity of purely thermodynamic descriptions of two-phase cryogenic fluid storage,” *J. Fluid Mech.*, vol. 484, no. 484, pp. 41–68, 2003.

[32] S. Barsi and M. Kassemi, “A Numerical Study of Tank Pressure Control in Reduced Gravity,” in *44th Aerospace Sciences Meeting and Exhibit, 9-12 January 2006, Reno,NV A*, 2004, pp. 9–12.

[33] S. Barsi, C. Panzarella, and M. Kassemi, “An Active Vapor Approach to Modeling Pressurization in Cryogenic Storage Tanks,” in *43rd AIAA/ASME/SAE/ASEE Joint Propulsion Conference & Exhibit 8 - 11 July 2007, Cincinnati, OH*, 2007, no. July, pp. 1–17.

[34] M. Rahman and S. Mukka, “Computation of Fluid Circulation in a Cryogenic Storage Vessel,” in *2nd International Energy Conversion Engineering Conference 16 - 19 August 2004, Providence, Rhode Island*, 2004, pp. 1–9.

[35] J. I. Hochstein, H. . Ji, and J. C. Aydelott, “Effect of subcooling on the on orbit pressuriztion rate of cryogenic propellant tankage,” in *AIAA/ASME 4th Joint*

Thermophysics and Heat Transfer Conference, pp. 1–10.

[36] M. Lacroix, "Computation of heat transfer during melting of pure substance isothermal wall," *Numer. Heat Transf. Part B*, vol. 15, pp. 191–210, 1989.

[37] J. Sim, C.-K. Kuan, and W. Shyy, "Simulation of Spacecraft Fuel Tank Self-Pressurization Using Eulerian-Lagrangian Method," in *49th AIAA Aerospace Sciences Meeting including the New Horizons Forum and Aerospace Exposition, Orlando, Florida*, 2011, pp. 1–20.

[38] C. Kuan, J. Sim, and W. Shyy, "Parallel, Adaptive Grid Computing of Multiphase Flows in Spacecraft Fuel Tanks," no. January, pp. 1–21, 2014.

[39] C. Lin and M. Hasan, "Self-pressurization of a spherical liquid hydrogen storage tank in amicrogravity environment," in *30th Aerospace Sciences Meeting and Exhibit, AIAA*, 1992, pp. 1–9.

[40] S. Mattick, C. Lee, A. Hosangadi, and V. Ahuja, "Progress in Modeling Pressurization in Propellant Tanks," in *46th AIAA/ASME/SAE/ASEE Joint Propulsion Conference & Exhibit, Nashville, TN*, 2010, pp. 1–13.

[41] M. Seo and S. Jeong, "Analysis of self-pressurization phenomenon of cryogenic fluid storage tank with thermal diffusion model," *Cryogenics (Guildf).*, vol. 50, no. 9, pp. 549–555, 2010.

[42] S. Barsi and M. Kassemi, "Investigation of Tank Pressurization and Pressure Control—Part I: Experimental Study," *J. Therm. Sci. Eng. Appl.*, vol. 5, no. 4, p. 041005, 2013.

[43] S. Barsi and M. Kassemi, "Investigation of Tank Pressurization and Pressure Control—Part II: Numerical Modeling," *J. Therm. Sci. Eng. Appl.*, vol. 5, no. 4, p. 041006, 2013.

[44] J. J. Ren, J. Y. Shi, P. Liu, M. S. Bi, and K. Jia, "Simulation on thermal stratification and de-stratification in liquefied gas tanks," *Int. J. Hydrogen Energy*, vol. 38, no. 10, pp. 4017–4023, 2013.

[45] L. Wang, Y. Li, C. Li, and Z. Zhao, "CFD investigation of thermal and pressurization performance in LH 2 tank during discharge," *Cryogenics (Guildf).*, vol. 57, pp. 63–73, 2013.

[46] W. Lei, L. Yanzhong, Z. Kang, and J. Yonghua, "Comparison of three computational models for predicting pressurization characteristics of cryogenic tank during discharge," *Cryogenics (Guildf).*, vol. 65, pp. 16–25, 2015.

[47] W. Lei, L. Yanzhong, L. Zhan, and Z. Kang, "Numerical investigation of thermal distribution and pressurization behavior in helium pressurized cryogenic tank by

introducing a multi-component model," *Phys. Procedia*, vol. 67, pp. 392–397, 2015.

[48] M. Kassemi and O. Kartuzova, "Effect of interfacial turbulence and accommodation coefficient on CFD predictions of pressurization and pressure control in cryogenic storage tank," *Cryogenics (Guildf).*, vol. 74, pp. 138–153, 2016.

[49] M. Kassemi, O. Kartuzova, and S. Hylton, "Validation of two-phase CFD models for propellant tank self-pressurization: Crossing fluid types, scales, and gravity levels," *Cryogenics (Guildf).*, vol. 89, no. July 2017, pp. 1–15, 2018.

[50] J. U. Brackbill, D. B. Kothe, and C. Zemach, "A Continuum Method for Modeling Surface Tension," *J. Comput. Phys.*, vol. 100, pp. 335–354, 1992.

[51] L. A. Moiseeva and S. G. Cherkasov, "Theoretical Investigation of the Effect of the Thermal Conductivity of a Wall on the Processes of Free-Convective Heat Transfer in a Vertical Cylindrical Tank," vol. 40, no. 3, pp. 485–493, 2002.

[52] V. R. Gopala and B. G. M. van Wachem, "Volume of fluid methods for immiscible-fluid and free-surface flows," *Chem. Eng. J.*, vol. 141, no. 1–3, pp. 204–221, 2008.

[53] S. P. Kumar, B. V. S. S. S. Prasad, G. Venkatarathnam, K. Ramamurthi, and S. S. Murthy, "Influence of surface evaporation on stratification in liquid hydrogen tanks of different aspect ratios," *Int. J. Hydrogen Energy*, vol. 32, no. 12, pp. 1954–1960, 2007.

[54] M. Stewart and J. P. Moder, "Self-Pressurization of a Flightweight, Liquid Hydrogen Tank: Simulation and Comparison with Experiments," in *52nd AIAA/SAE/ASEE Joint Propulsion Conference, Salt Lake City, UT*, 2016, pp. 1–14.

[55] M. Stewart, "Pressurization of a Flightweight, Liquid Hydrogen Tank: Evaporation & Condensation at the Liquid/Vapor Interface," in *53rd AIAA/SAE/ASEE Joint Propulsion Conference*, 2017, no. July, pp. 1–13.

[56] W. Shyy and M.-H. Chen, "Steady State Natural Convection with Phase Change," *Int. Jounal Heat Mass Transf.*, vol. 33, no. 13, pp. 2545–2563, 1990.

[57] W. Shyy and M. Chen, "Computation of double diffusive convection with solidification in an enclosure," in *AIAA/ASME 5th Joint Thermophysics and Heat Transfer Conference*, 1990, p. Seattle, WA.

[58] W. Shyy, "A Study of Finite Difference Approximations to Steady-State, Convection-Dominated Flow Problems," *J. Comput. Phys.*, vol. 57, pp. 415–438, 1985.

[59] W. Shyy, “Elements of Pressure -Based Computational Algorithms for Complex Fluid Flow and Heat Transfer,” *Adv. Heat Transf.*, vol. 24, pp. 191–275, 1994.

[60] W. Shyy and M. M. Rao, “Enthalpy Based Formulations for Phase Change Problems with Application to g-jitter,” *Microgravity Sci. Technol.*, vol. 7, no. 1, 1994.

[61] W. Shyy, “Modelling of Transient Two-Phase Heat Transfer for Spacecraft Thermal Management,” *Microgravity Sci. Technol.*, vol. 7, no. 3, pp. 219–227, 1994.

[62] S. G. Cherkasov, “Natural Convection and Temperature Stratification in a Cryogenic Fuel Tank in Microgravity,” *Fluid Dyn.*, vol. 29, no. 5, pp. 710–716, 1994.

[63] S. Venkat and S. Sherif, “Self-Pressurization and Thermal Stratification in a Liquid Hydrogen Tank Under Varying Gravity Conditions,” in *2nd AIAA Aerospace Sciences Meeting and Exhibit 5 - 8 January 2004, Reno, Nevada*, 2004, pp. 1–11.

[64] G. Grayson, A. Lopez, F. Chandler, L. Hastings, and S. Tucker, “Cryogenic Tank Modeling for the Saturn AS-203 Experiment,” *42nd AIAA/ASME/SAE/ASEE Jt. Propuls. Conf. Exhib. 2006, Sacramento, Calif.*, pp. 1–7, 2006.

[65] D. Sauter, J. Hochstein, and L. Fite, “Computational Modeling of Cryogenic Propellant Resupply,” in *44th AIAA Aerospace Sciences Meeting and Exhibit 2006, Reno, Nevada*, 2006, pp. 1–16.

[66] M. Costa, A. Oliva, and C. D. Perez-Segarra, “Three-Dimensional Numerical Study of Melting Inside an Isothermal Horizontal Cylinder,” *Numer. Heat Transf. Part A Appl.*, vol. 32, no. 5, pp. 531–553, 1997.

[67] B. Binet and M. Lacroix, “Numerical study of natural-convection-dominated melting inside uniformly and discretely heated rectangular cavities,” *Numer. Heat Transf. Part A Appl.*, vol. 33, no. 2, pp. 207–224, 1998.

[68] J. Banaszek, Y. Jaluria, T. A. Kowalewski, and M. Rebow, “Semi-implicit FEM analysis of natural convection in freezing water,” *Numer. Heat Transf. Part A Appl.*, vol. 36, no. 5, pp. 449–472, 1999.

[69] V. R. Voller and C. Prakash, “A Fixed grid numerical modelling methodology for convection diffusion mushy region phase change problems,” *Int. Jounal Heat Mass Transf.*, vol. 30, no. 8, pp. 1709–1719, 1987.

[70] T. Michałek and T. A. Kowalewski, “Simulations of the Water Freezing Process – Numerical Benchmarks,” *Task Q.*, vol. 7, no. 3, pp. 389–408, 2003.

[71] Z. Ding and S. Anghaie, “Numerical Modelling of Conduction-Driven Bulk Evaporation and Condensation Processes with Constant Volume,” *Int. J. Numer. Methods Eng.*, vol. 39, no. August 1994, pp. 219–233, 1996.

[72] S. Anghaie and Z. Ding, “Thermal Hydraulic Analysis of Bulk Evaporation and Condensation in Multiphase Nuclear Fuel Cell,” *Heat Transf. Fluid Flow*, vol. 120, no. 1, pp. 57–69, 1997.

[73] Z. Ding and S. Anghaie, “A Numerical Study of Bulk Evaporation and Condensation Problem,” *Proc. ASME/JSME Internaltional Conf. Nucl. Eng.*, vol. 1, no. Part B, pp. 719–726, 1996.

[74] S. Anghaie and Z. Ding, “Modeling of Thermal Performance of Multiphase Nuclear Fuel Cell Under Variable Gravity Conditions,” *NASA Contract. Rep. 198391*, pp. 1–68, 1996.

[75] S. Anghaie, G. Chen, and S. Kim, “An Energy Based Pressure Correction Method For Diabatic Two-Phase Flow with Phase Change,” in *Trends in Numerical and Physical Modeling for Industrial Multiphase Flows*, 2000, pp. 1–10.

[76] A. Winter and J. Marchetta, “An Energy of Fluid (EOF) Approach to Modeling Self Pressurization in Propellant Tanks,” in *47th AIAA Aerospace Sciences Meeting Including The New Horizons Forum and Aerospace Exposition, Orlando, Florida*, 2009, pp. 1–7.

[77] A. Winter and J. Marchetta, “Simulating Self-Pressurization in Propellant Tanks,” in *48th AIAA Aerospace Sciences Meeting Including the New Horizons Forum and Aerospace Exposition, Orlando, Florida*, 2010, pp. 1–11.

[78] A. P. Winter, “Simulating Self Pressurization in Propellant Tanks Using and Energy of Fluid Approach,” University of Memphis, 2014.

[79] V. S. Yuferev, E. N. Kolesnikova, Y. A. Polovko, A. M. Sveshnikov, and A. I. Zhmakin, “Effect of the Coriolis Force on Thermal Convection under Microgravity,” *Theor. Comput. Fluid Dyn.*, vol. 12, no. 1, pp. 53–70, 2002.

[80] C. Panzarella, D. Plachta, and M. Kassemi, “Pressure control of large cryogenic tanks in microgravity,” *Cryogenics (Guildf).*, vol. 44, no. 6–8, pp. 475–483, 2004.

[81] C. H. Panzarella and M. Kassemi, “Self-Pressurization of Large Spherical Cryogenic Tanks in Space,” *J. Spacecr. Rockets*, vol. 42, no. 2, pp. 299–308, 2005.

[82] ANSYS INC, “Heat Transfer Theory,” *ANSYS Fluent Theory Guide*. 2013.

[83] ANSYS INC, “UDS Theory,” *ANSYS FLUENT 12.0 User’s Guide*. 2014.

[84] H. S. Carslaw and J. C. Jaeger, *Conduction of Heat in Solids*, 2nd ed. London:

Oxford University Press, 1959.

[85] D. Chato, J. Hochstein, M. Kassemi, and J. Marchetta, “Approaches to Validation of Models for Low Gravity Fluid Behavior,” *42nd Aerosp. Sci. Meet. Exhib. Spons. by Am. Inst. Aeronaut. Astronaut. Reno, Nevada, January 5–8, 2004*, vol. NASA/TM—20, no. AIAA–2004–1150, pp. 1–14, 2004.

[86] G. E. Myers, Analytical Methods in Conduction Heat Transfer, 2 ed., Madison, WI: AMCHT Publications, 1998, p. 135.

[87] Notardonato W, Johnson W, Swanger A M, and Tomsik T 2015 Ground operations demonstration unit for liquid hydrogen initial test results, Advances in Cryogenic Engineering, IOP Conference Series: Materials Science and Engineering 101

[88] Notardonato W, Swanger A, Fesmire J, Jumper K, Johnson W, and Tomsik T 2017 Final test results for the ground operations demonstration unit for liquid hydrogen. Cryogenics, Vol. 88, pp.147-155.

[89] Swanger A M, Notardonato W U, Fesmire J E, Jumper K M, Johnson W L, and Tomsik T M 2017 Large scale production of densified hydrogen to the triple point and below, Advances in Cryogenic Engineering, IOP Conference Series: Materials Science and Engineering 101

[90] Notardonato W U, Swanger A M, Fesmire J E, Jumper K M, Johnson W L, and Tomsik T M 2017 Zero boiloff methods for large scale liquid hydrogen tanks using integrated refrigeration and storage, Advances in Cryogenic Engineering, IOP Conference Series: Materials Science and Engineering 101

[91] Swanger A M, Jumper K M, Fesmire J E, and Notardonato W U 2015 Modification of a Liquid Hydrogen Tank for Integrated Refrigeration and Storage, Advances in Cryogenic Engineering, IOP Conference Series: Materials Science and Engineering 101

[92] Swanger A M, Notardonato W U, and Jumper K M 2015 ASME Section VIII Recertification of a 33,000 Gallon Vacuum-Jacketed LH2 Storage Vessel for Densified Hydrogen Testing at NASA Kennedy Space Center, ASME Pressure Vessels and Piping Conference, Massachusetts, Boston

[93] Fesmire J E, Tomsik T M, Bonner T, Oliveira J M, Conyers H J, Johnson W L, and Notardonato W U 2014 Integrated heat exchanger design for a cryogenic storage tank, Advances in Cryogenic Engineering, AIP Conference. Proceedings, Vol. 1573, pp.1365-1372

[94] Plachta D, Johnson W and Feller J 2016 Zero boiloff system testing. Cryogenics, Vol. 74, pp.88-94

[95] Notardonato W U, Baik J H and McIntosh G E 2004 Operational testing of densified hydrogen using G-M refrigeration, Advances in Cryogenic Engineering, AIP Conference Proceedings, Vol. 49, pp.64-74

[96] Al Ghafri S Z, Swanger A, Jusko V, Siahvashi A, Perez F, Johns M, May E 2022 Modelling of Liquid Hydrogen Boil-Off, Energies, Vol. 15, 1149

[97] Greene W, Knowles T, and Tomsik T 1999 Propellant densification for launch vehicles - Simulation and testing, 35th Joint Propulsion Conference and Exhibit

[98] Greene W, Vaughan D 1998 Simulation and testing of in-tank propellant densification for launch vehicles, 34th AIAA/ASME/SAE/ASEE Joint Propulsion Conference and Exhibit

[99] Tomsik T 1997 Performance Tests of a Liquid Hydrogen Propellant Densification Ground System for the X33/RLV, Joint Propulsion Conference and Exhibit, Seattle, Washington.

[100] Lak T, Lozano M, Tomsik T 1996 Advancement in cryogenic propulsion system performance through propellant densification, Joint Propulsion Conference and Exhibit, Buena Vista, Florida.

[101] Swanger A M, 2018 Large Scale Cryogenic Storage with Active Refrigeration, University of Central Florida

[102] Reynolds, W. C., Thermodynamic Properties in SI, Stanford, CA: Stanford Univeristy Department of Mechanical Engineering, 1979, pp. 122-125,139.

[103] Cengel, Y. A., and Boles, M. A., "Thermodynamic Property Relations," in Thermodynamics: An Engineering Approach, 8th ed., New York, McGraw-Hill Education, 2015, pp. 661-668.

[104] Younglove, B. A., "Thermophysical properties of fluids. I. Argon, ethylene, parahydrogen, nitrogen, nitrogen trifluoride, and oxygen," Journal of Physical and Chemical Reference Data, vol. 11, 1982.

[105] Lemmon, E. (2018). Reference Fluid Thermodynamic and Transport Properties Database (REFPROP). [online] NIST. Available at: https://www.nist.gov/programs- projects/reference-fluid-thermodynamic-and-transport-properties-database- refprop [Accessed 5 Feb. 2018].

[106] McCarty, R D, Hord, J, and Roder, H M. Selected properties of hydrogen (engineering design data). United States: N. p., 1981.

[107] ANSYS Fluent 19.1, 2018. [Online].

[108] ANSYS Fluent 19.1, "User's Guide," 2021. [Online].

[109] ANSYS Fluent 19.1, "Customization Manual," 2021. [Online].

APPENDIX A

GODU-LH2 SIMULATION RESULTS

A.1 Zero Boiloff Results

A.1.1 100% Fill Diodes TT3 – TT16

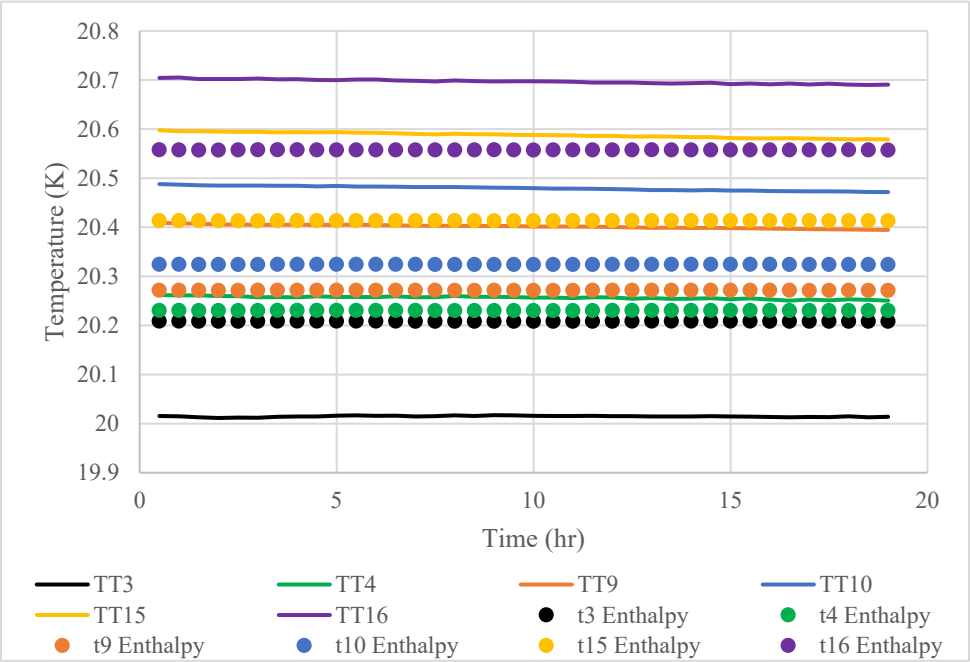

Figure A.1 200K Enthalpy Temperature Diodes

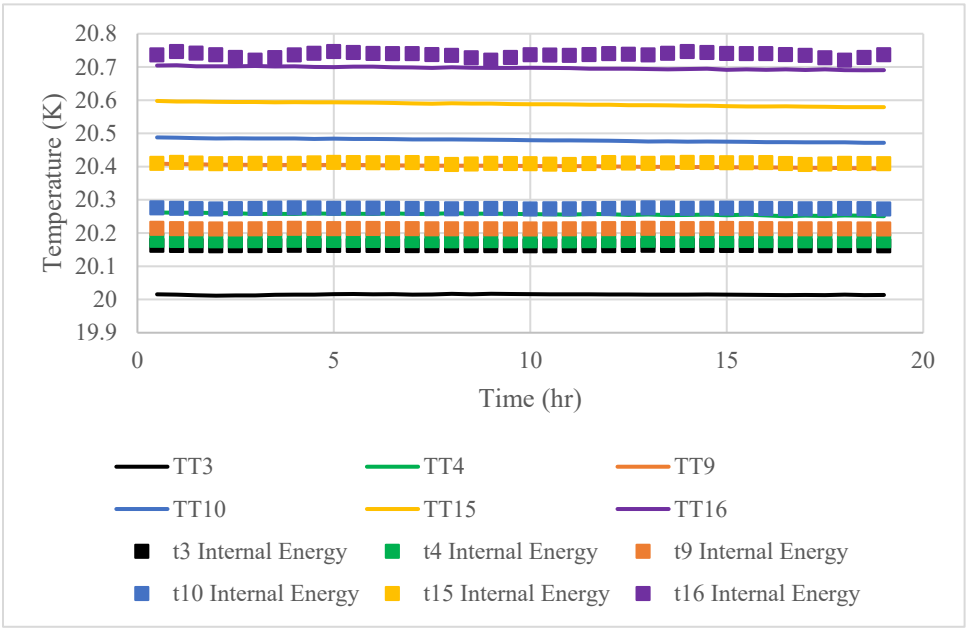

Figure A.2 200K Internal Energy Temperature Diodes

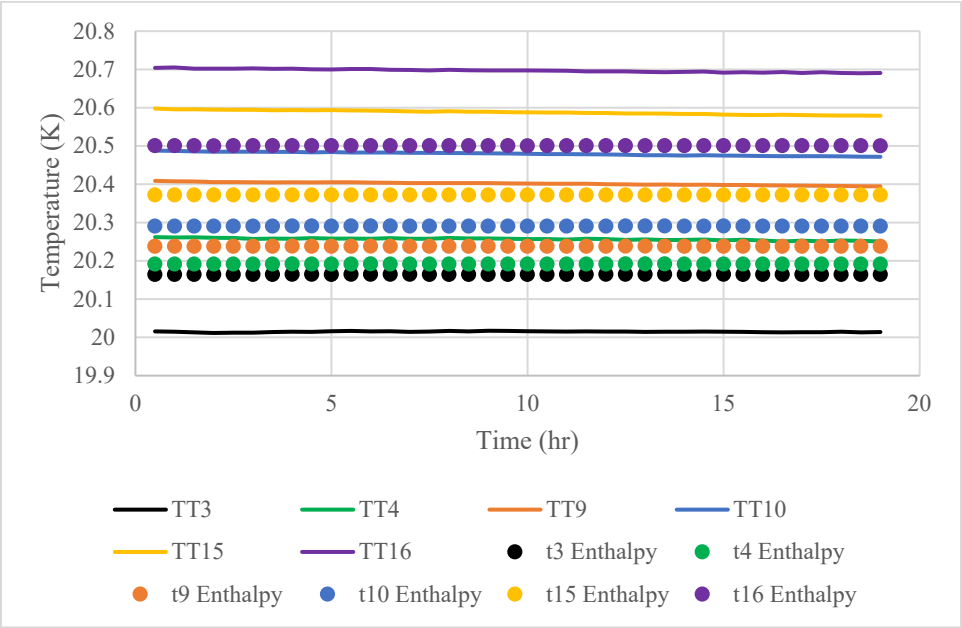

Figure A.3 350K Enthalpy Temperature Diodes

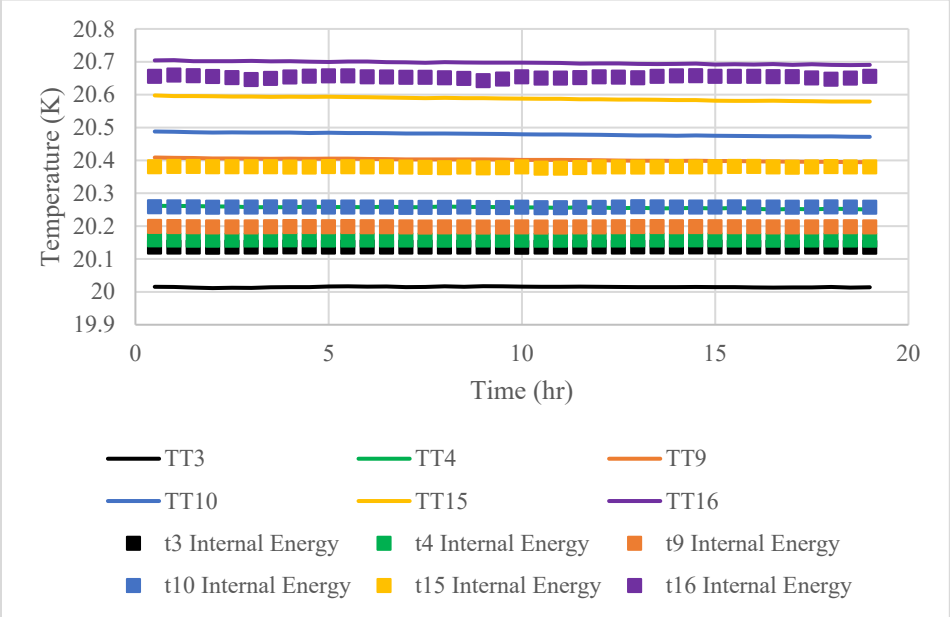

Figure A.4 350K Internal Energy Temperature Diodes

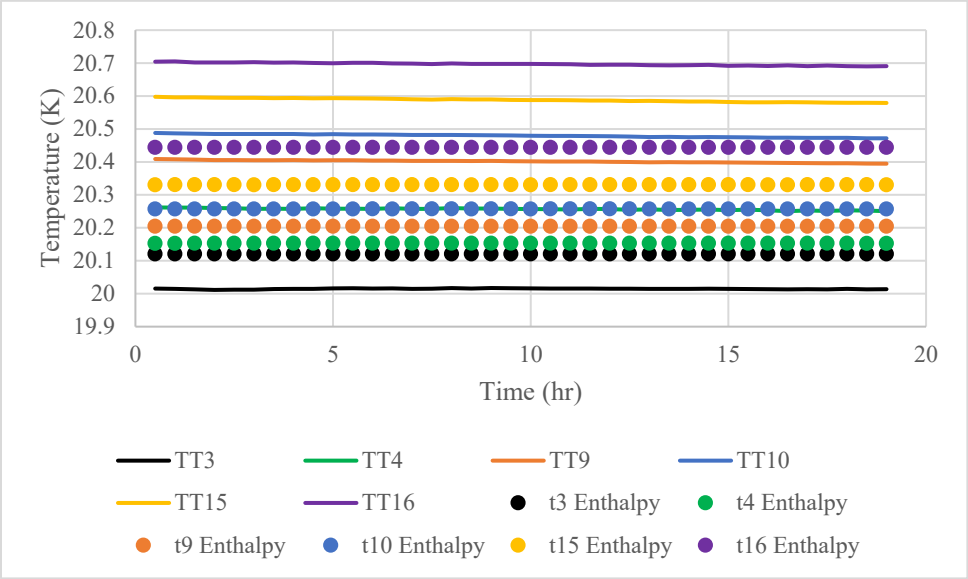

Figure A.5 500K Enthalpy Temperature Diodes

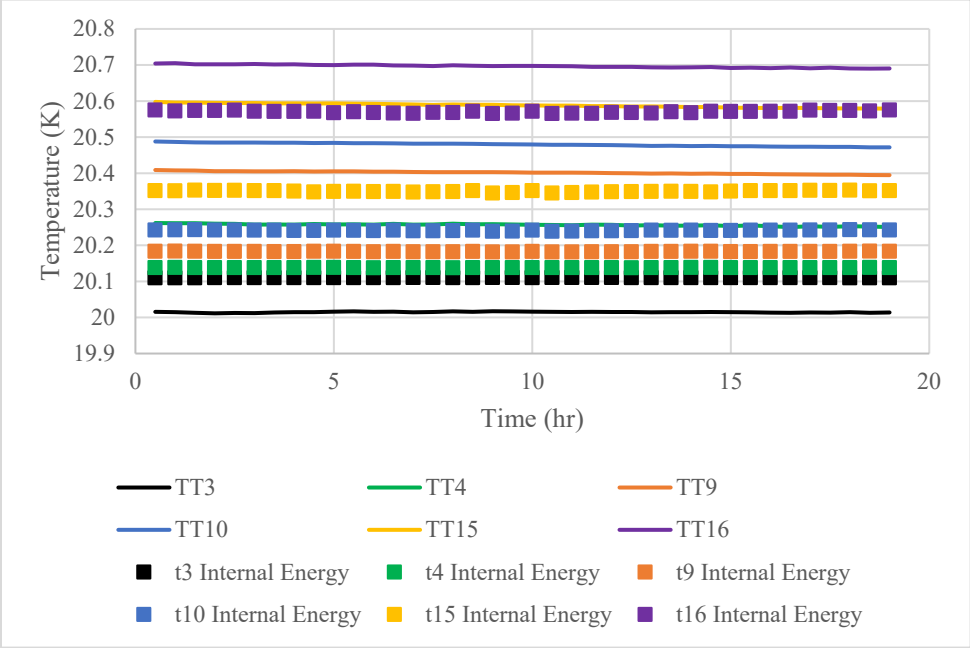

Figure A.6 500K Internal Energy Temperature Diodes

A.1.2 67% Fill Diodes TT3 – TT16

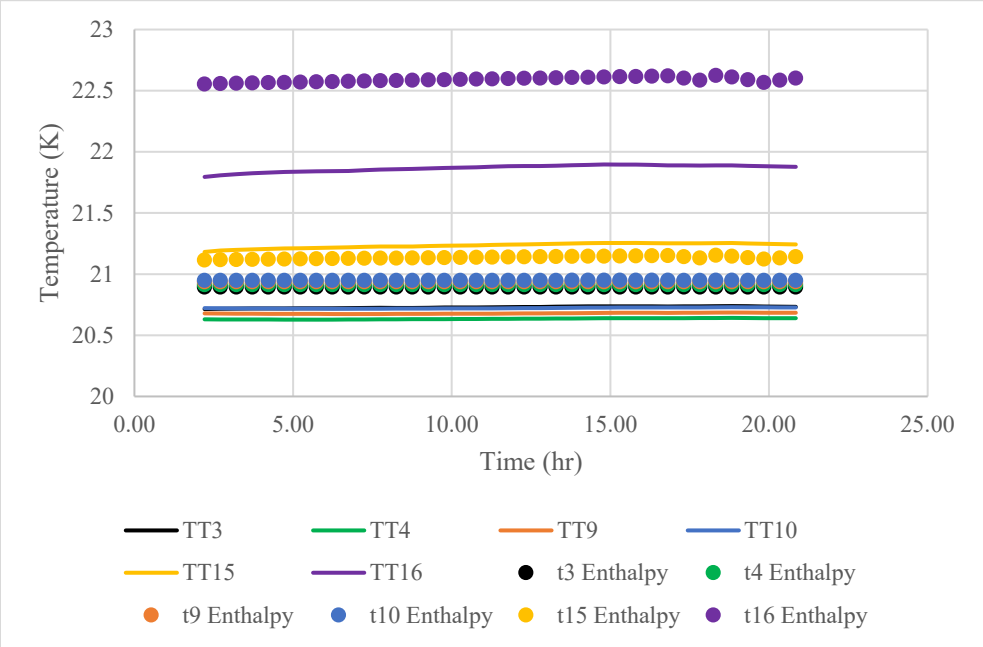

Figure A.7 320K Enthalpy Temperature Diodes

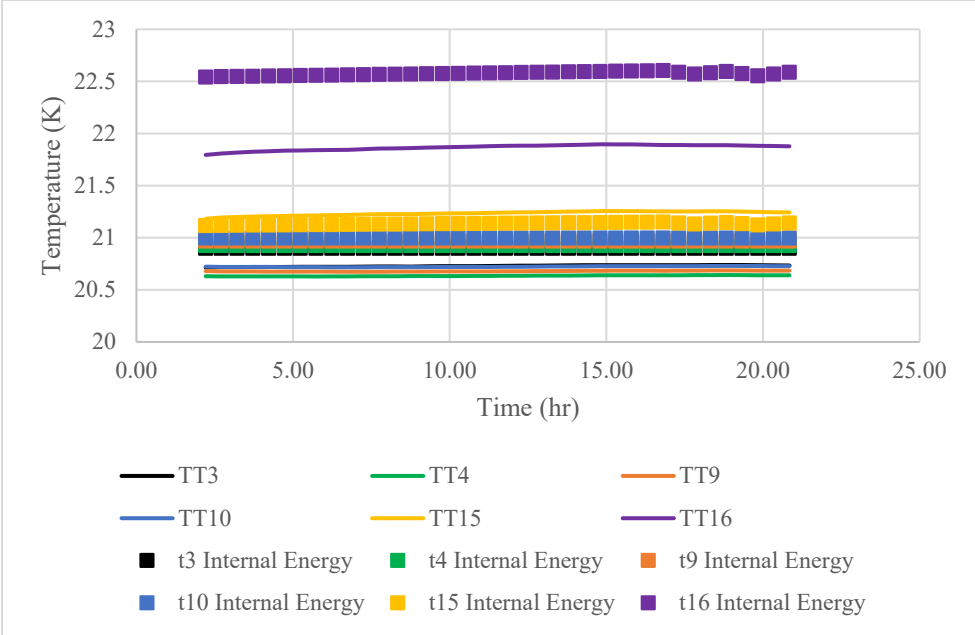

Figure A.8 320K Internal Energy Temperature Diodes

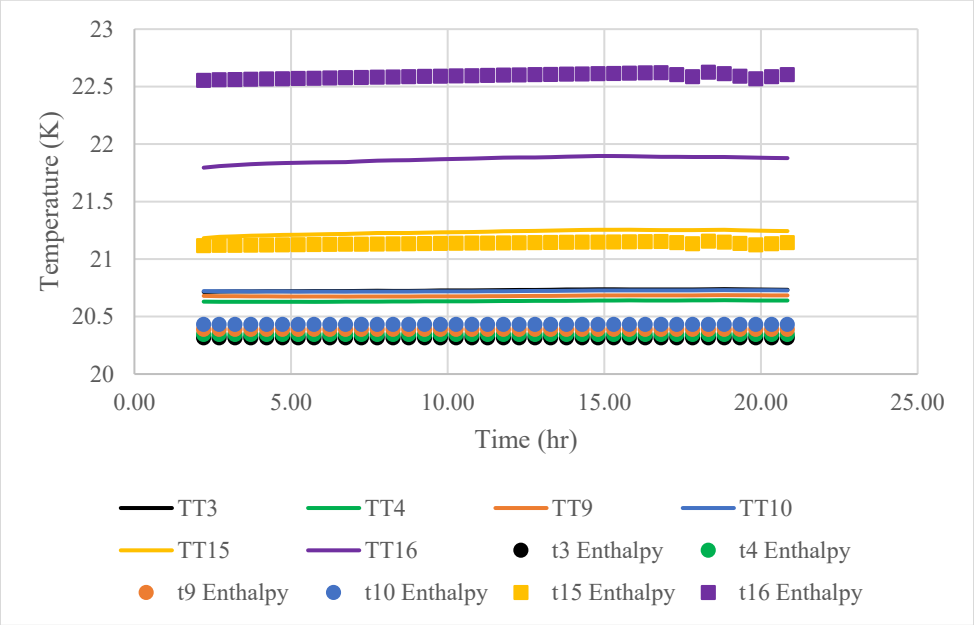

Figure A.9 430K Enthalpy Temperature Diodes

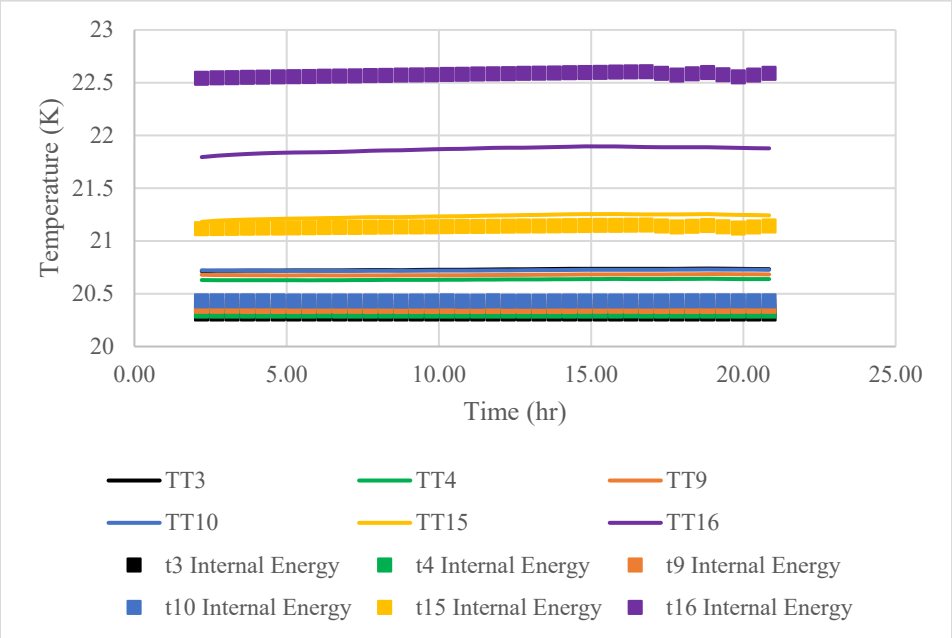

Figure A.10 430K Internal Energy Temperature Diodes

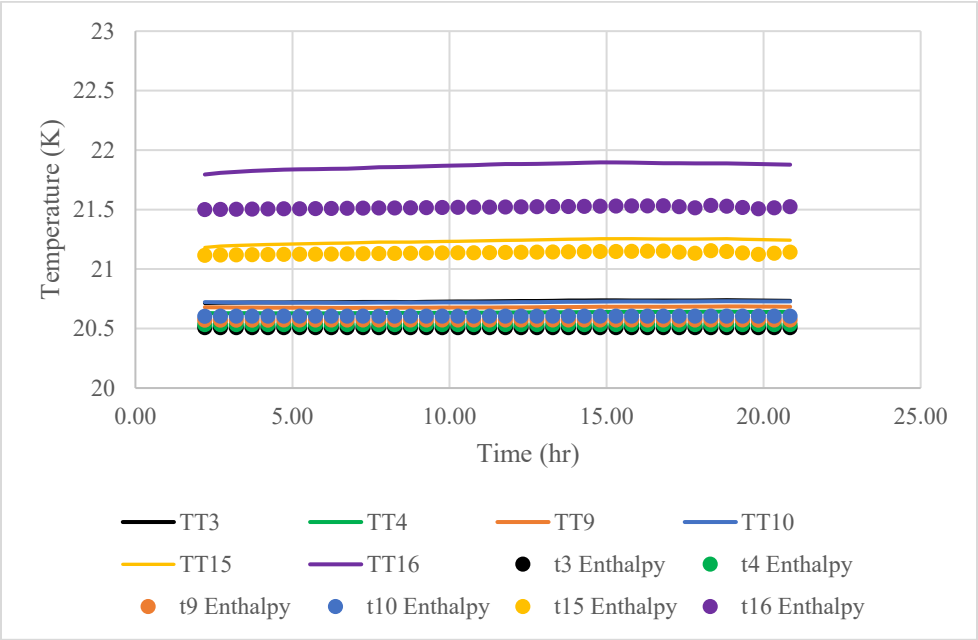

Figure A.11 660K Enthalpy Temperature Diodes

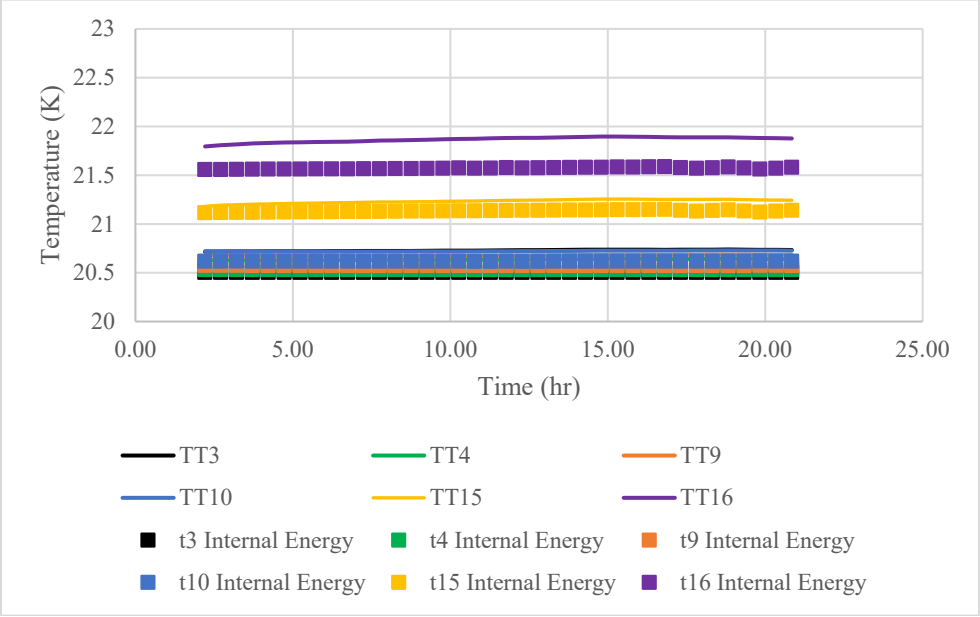

Figure A.12 660K Internal Energy Temperature Diodes

A.2 Densification Results

A.2.1 100% Fill Diodes TT3 – TT16

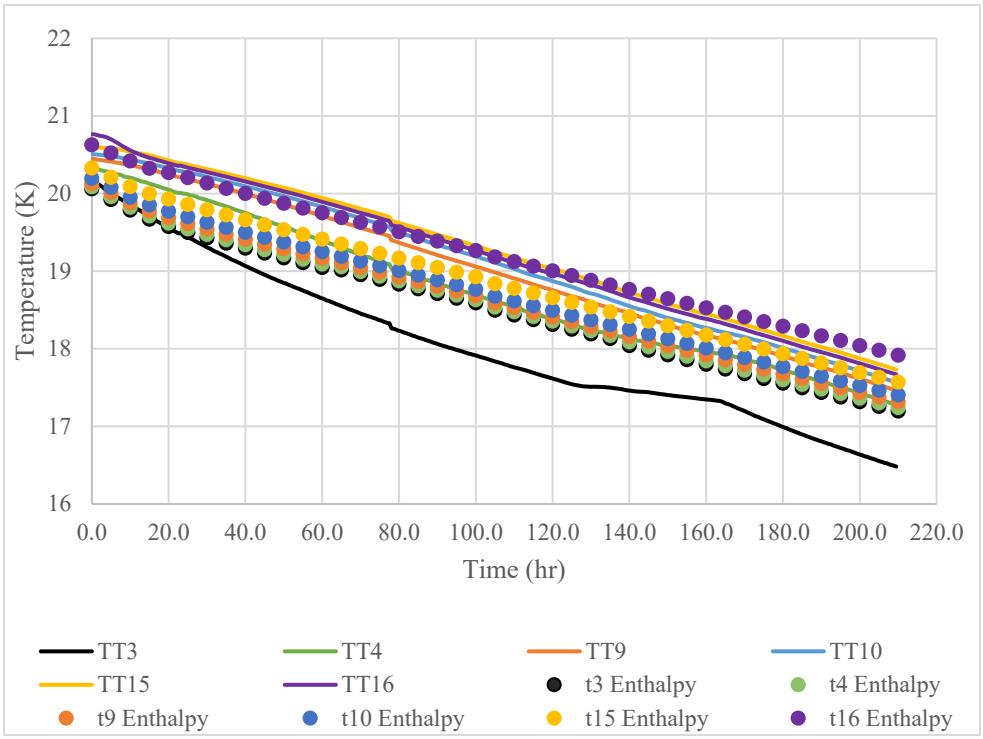

Figure A.13 200K Enthalpy Temperature Diodes

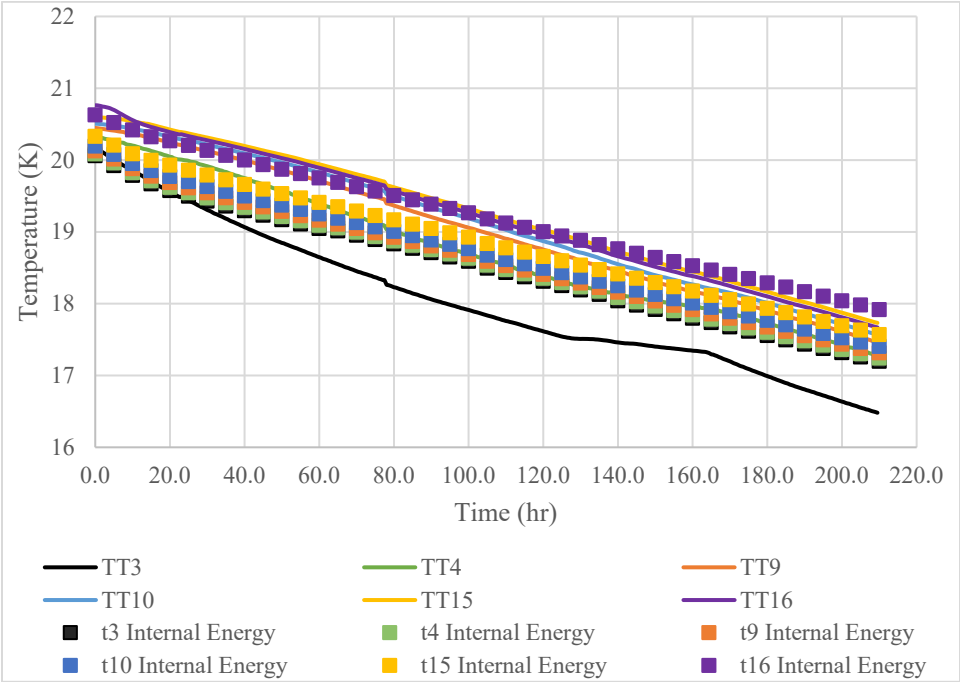

Figure A.14 200K Internal Energy Temperature Diodes

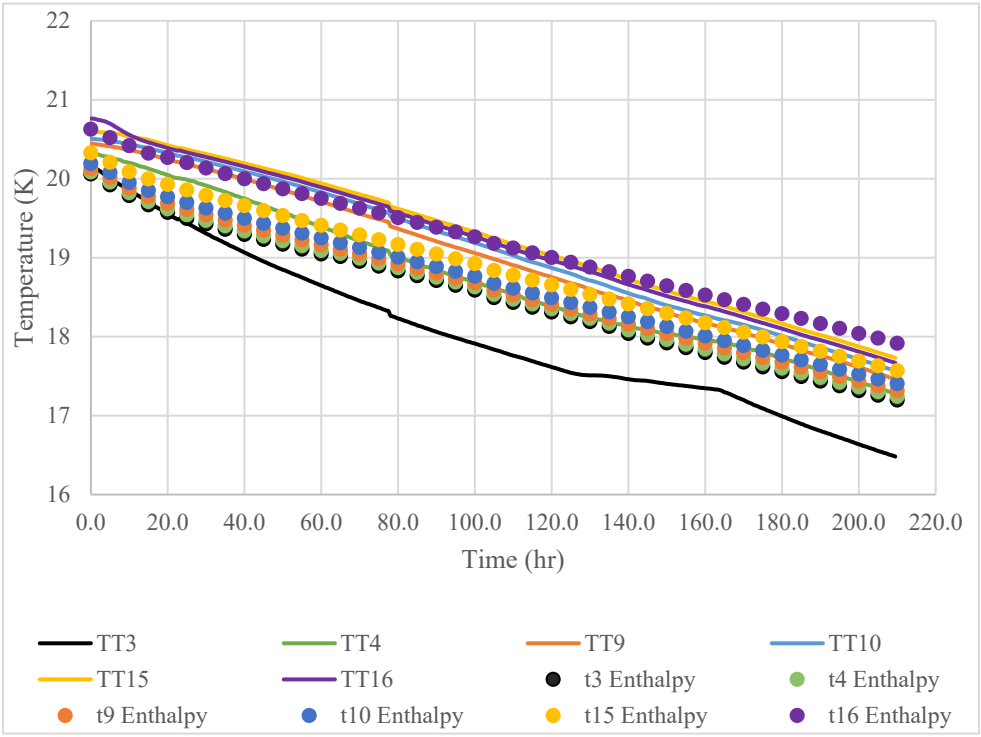

Figure A.15 350K Enthalpy Temperature Diodes

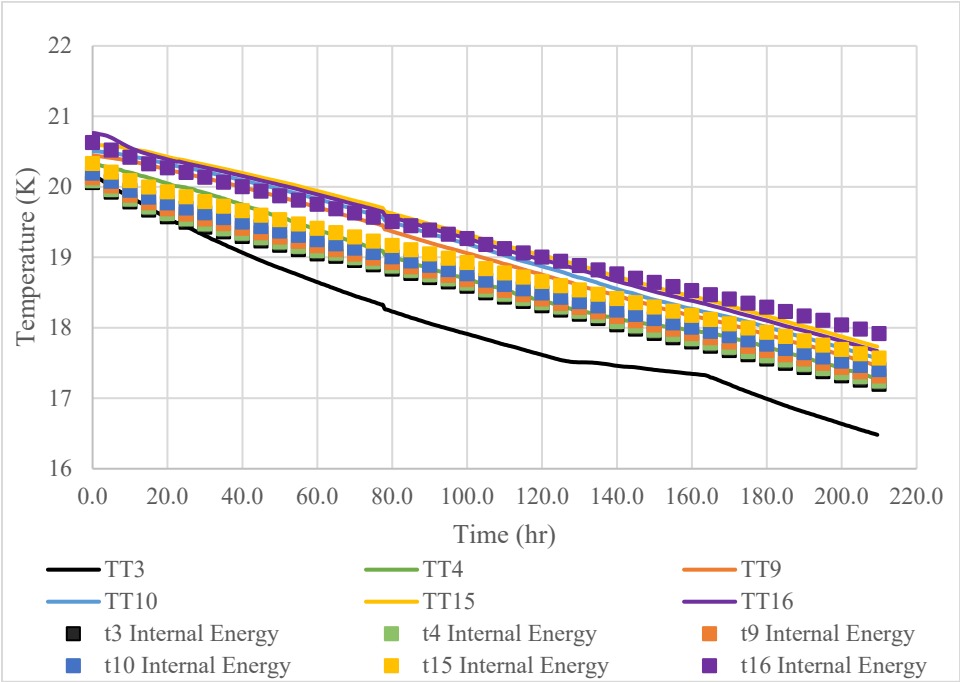

Figure A.16 350K Internal Energy Temperature Diodes

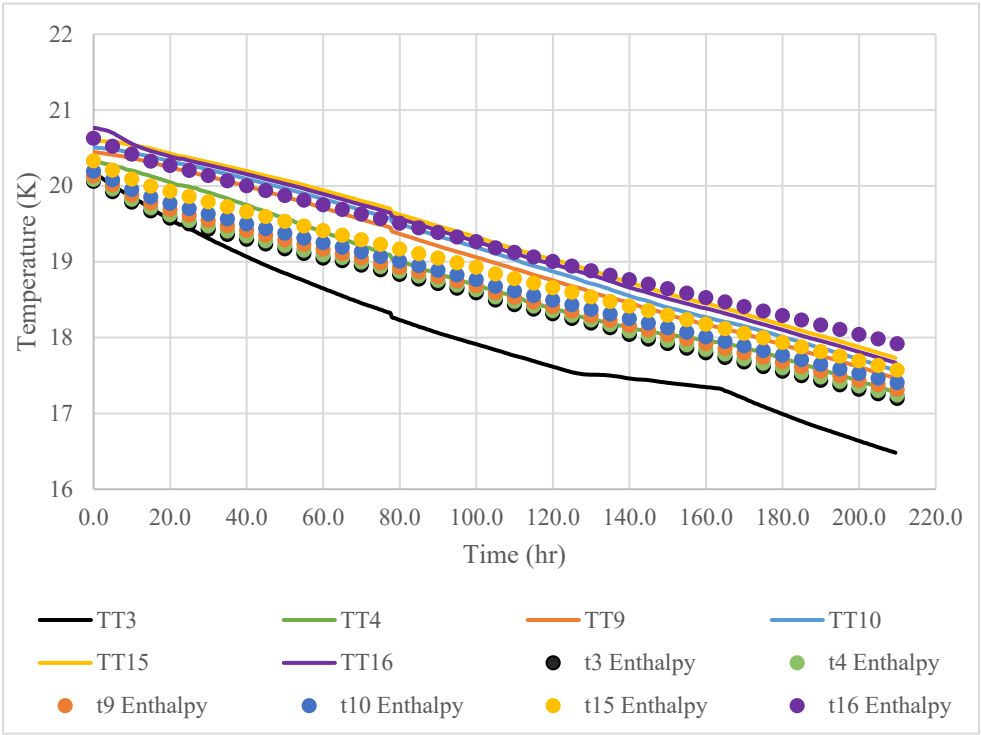

Figure A.17 500K Enthalpy Temperature Diodes

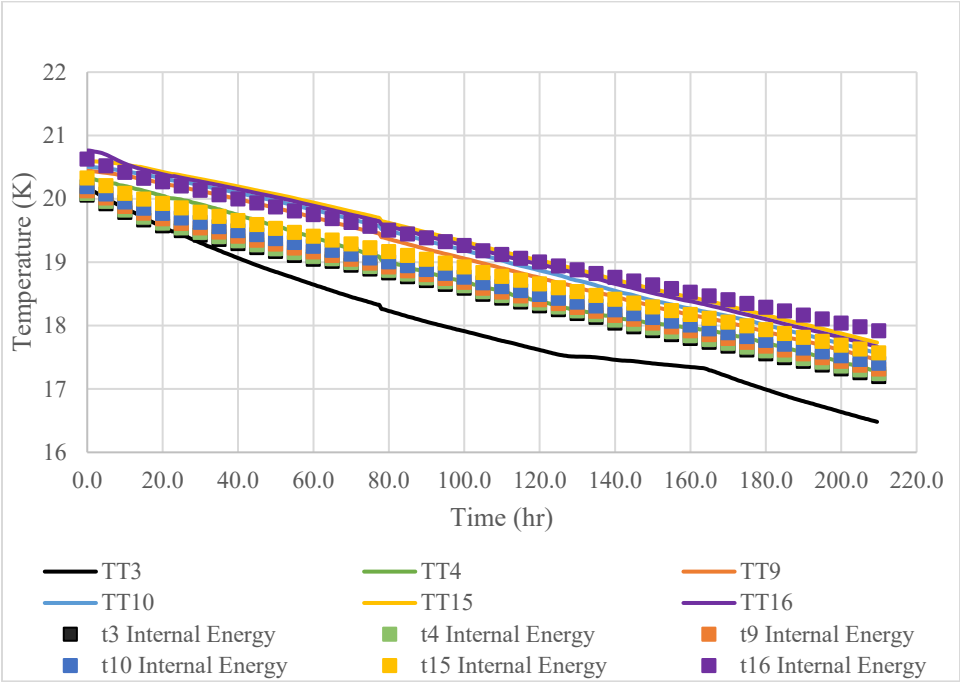

Figure A.18 500K Internal Energy Temperature Diodes

A.2.2 67% Fill Diodes TT3 – TT16

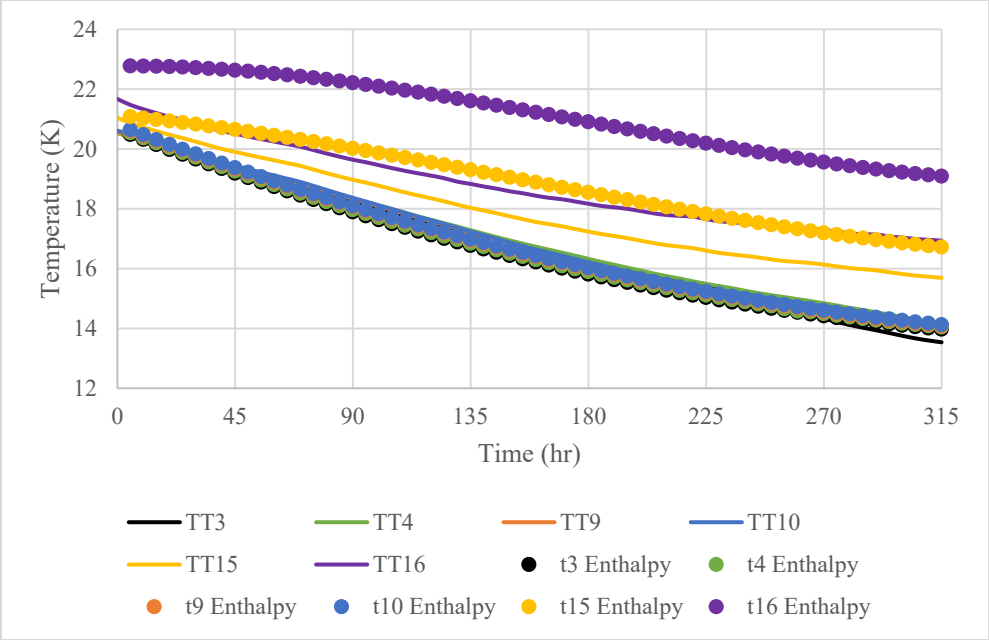

Figure A.19 320K Enthalpy Temperature Diodes

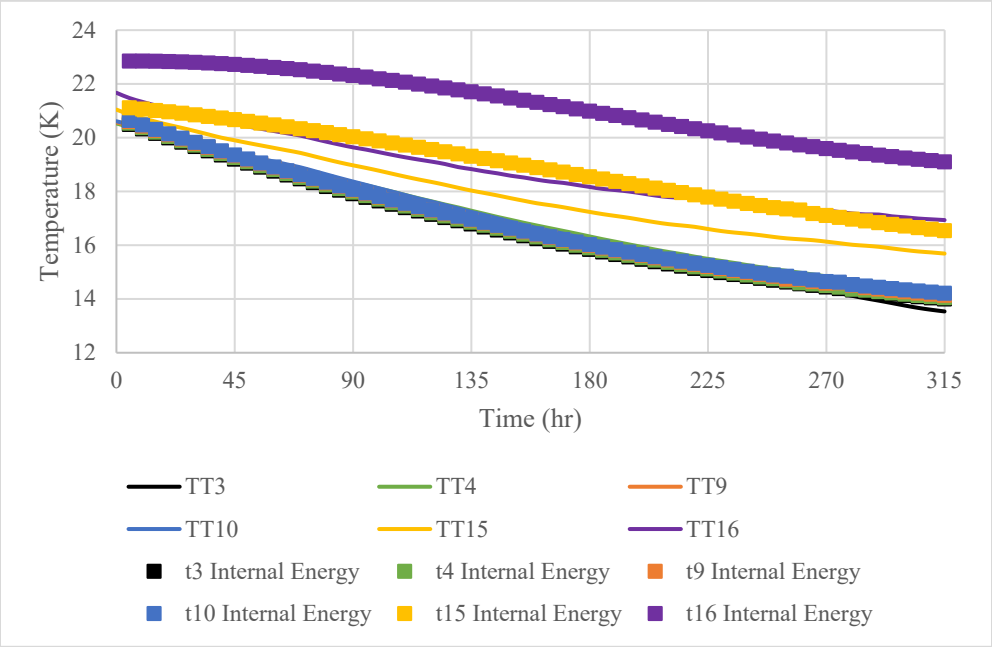

Figure A.20 320K Internal Energy Temperature Diodes

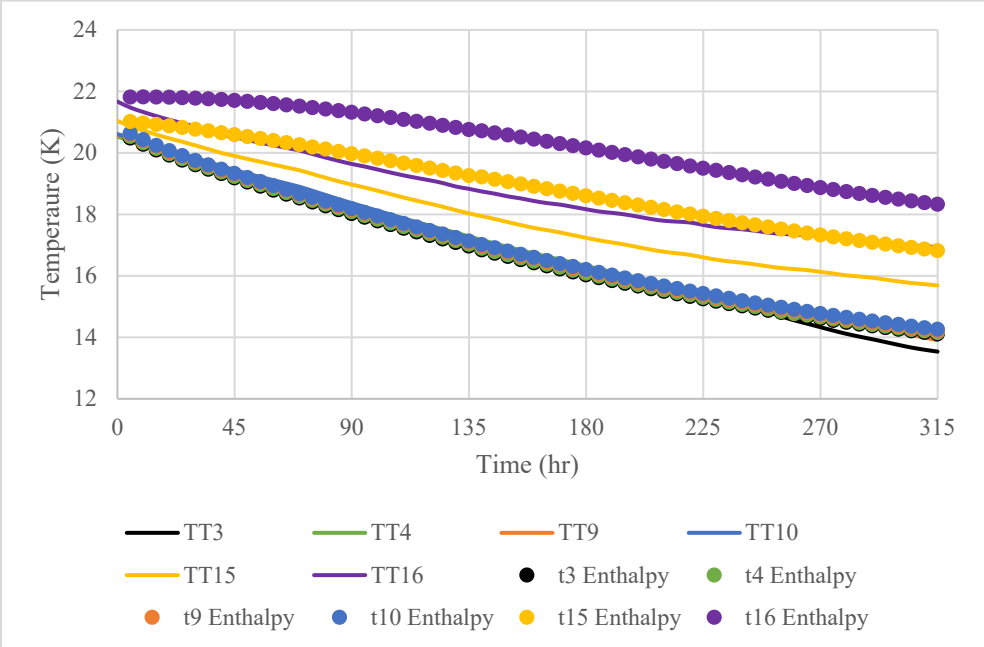

Figure A.21 430K Enthalpy Temperature Diodes

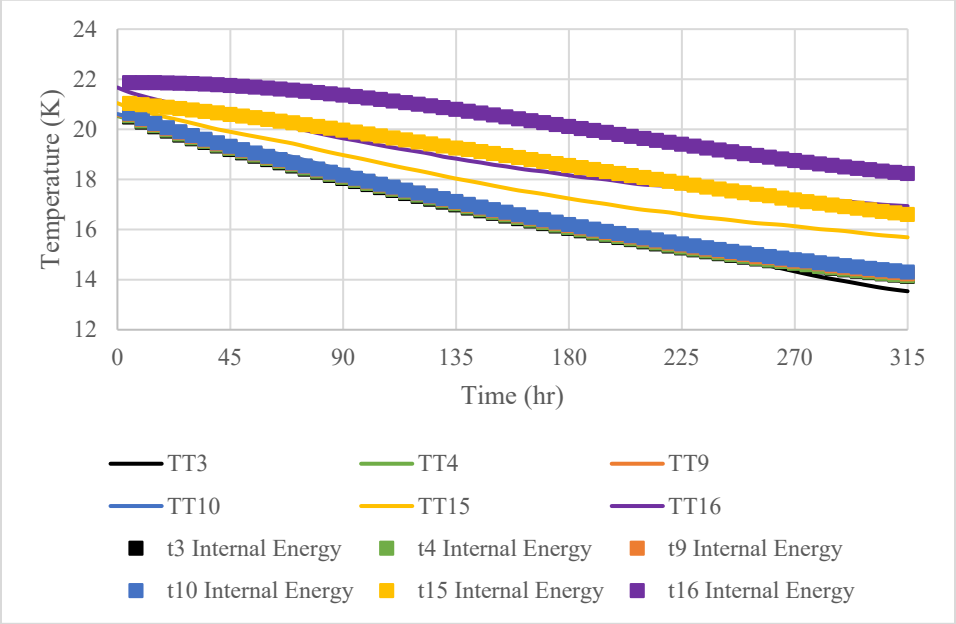

Figure A.22 430K Internal Energy Temperature Diodes

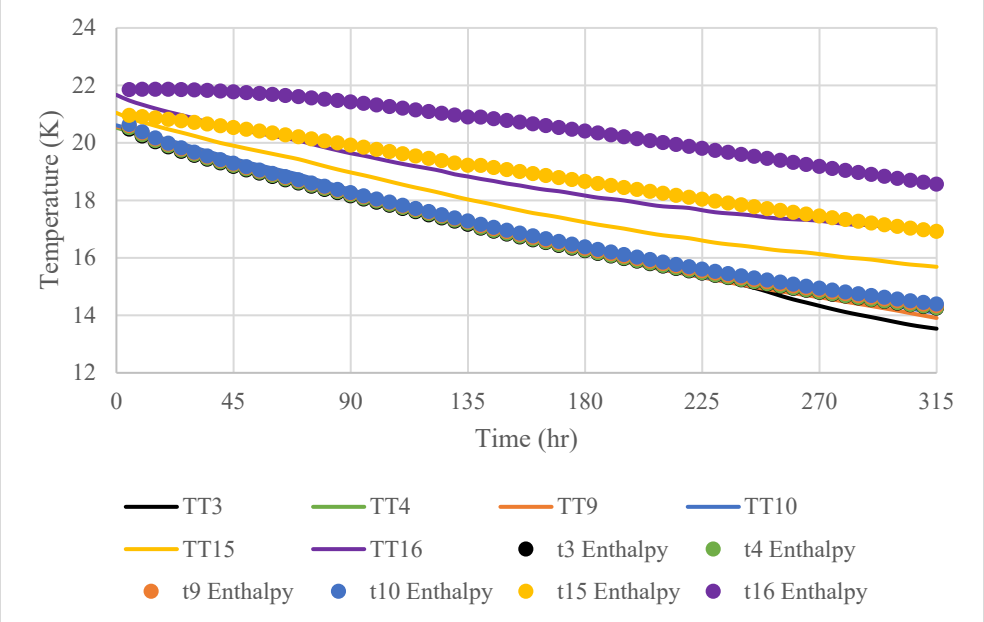

Figure A.23 660K Enthalpy Temperature Diodes

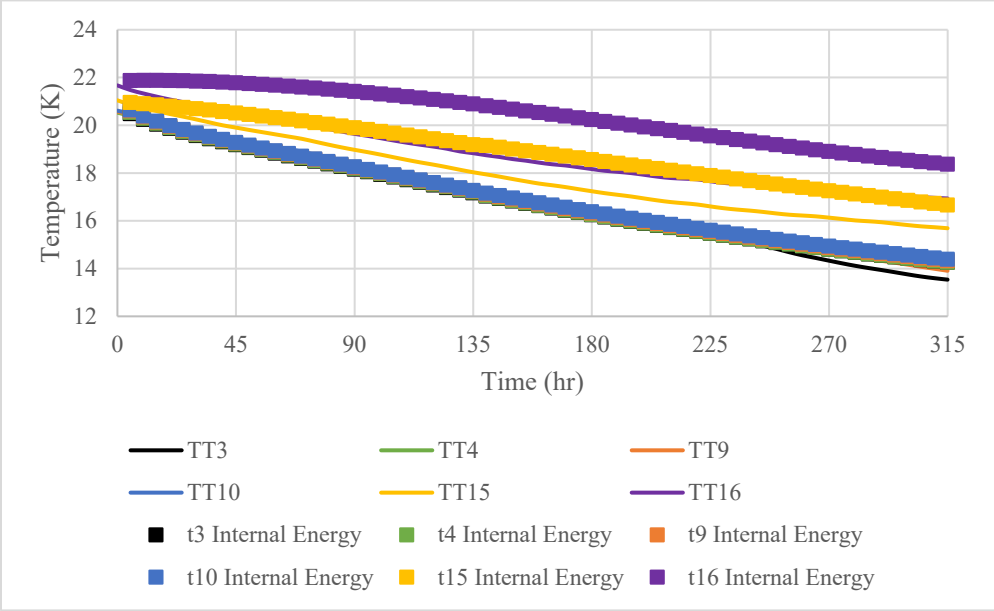

Figure A.24 660K Internal Energy Temperature Diodes

APPENDIX B

TUTORIALS FOR SIMULATION CASES

B.1 Fluent Setup for Conduction

Example Paragraph

This appendix details the setup procedure for the two Unsteady Conduction.

1) Click on ANSYS Fluent.
   a) Set Dimensions to 2D
   b) For Processing Options, select either Serial or Parallel
      i) If Parallel, use the number of processes that is less than or equal to the total number of processors on your system
      ii) If on the High Performance Computing system, use the number of processors assigned to the job
   c) Under Working Directory, change the working folder to a unique name where you want to read and write the files for your simulations
      i) Ensure your source code and mesh files are in this working directory
   d) Press OK to run Fluent.
2) Select File Read and read your mesh file
   a) If necessary your geometry may need to be scaled
      i) i.e. if geometry was created in millimeters and needs to be scaled to meters then, press the Scale option to scale the mesh to the appropriate dimensions.
3) In the Tree, Setup General. Select the Transient option under Solver Time.
4) Compile the UDF library.
   a) In the ribbon at the top in the User Defined Functions, open the Compiled UDFs dialog box.
   b) In Source Files, select and your source code and press OK.
   c) Select Build the Compiled UDFs dialog box.
      i) If there are no errors, click on Load.
5) Create the UDS.
   a) In the ribbon at the top, in the User Defined tab open the User-Defined Scalars dialog box.
   b) Set the Number of User Defined Scalars
   c) In the Flux Function, set to NONE
   d) In the Unsteady Function, set to your uds unsteady term
   e) Set your working fluid to Water
      i) In the Tree, select setup materials – can use the default – air
      ii) In the Density tab, set to your value or polynomial
      iii) In the UDS Diffusivity tab, replace the constant value with your given value.
   f) Click Change/Create to save the changes and close the Create/Edit Materials dialog box.
   6) Assign the boundary conditions.
   a) In the Tree, Setup Boundary Conditions.
      i) Open the respective Wall dialog box and go to the UDS tab.
      ii) For a temperature boundary condition, use Specified Value from the dropdown menu under User-Defined Scalar Boundary Condition.
         (1) If a heat flux boundary condition, use Specified Flux.
      iii) Set the boundary value according to the specifications given in the problem statement
      iv) For adiabatic walls, use a Specified Flux with a boundary value of 0.
7) Initialize the solution.

a) In the Tree, Select Solution Initialization.
b) Set the Initial Value of User Scalar 0 to 300 K. Click Initialize.

8) Set the transient calculation options.
9) In the Tree, Solution Run Calculation to activate the Run Calculation
   a) Choose a Time Step Size of 1 sec and set the Number of Time Steps to 600.
   b) Set the Max Iterations/Time Step to at minimum 100
   c) Set the Reporting Interval to 1
10) Run Simulation
   a) In the Tree, Select Solution Run Calculation
   b) Click Calculate to run

Fluent Setup for Conduction Phase ChangeThis appendix details the setup of the case found in the Unsteady Conduction Phase Change

B.2 Fluent Setup for Conduction Phase Change

1) Click on ANSYS Fluent.
   a) Set Dimensions to 2D
   b) For Processing Options, select either Serial or Parallel
      i) If Parallel, use the number of processes that is less than or equal to the total number of processors on your system
      ii) If on the High Performance Computing system, use the number of processors assigned to the job
   c) Under Working Directory, change the working folder to a unique name where you want to read and write the files for your simulations
      i) Ensure your source code and mesh files are in this working directory
      d) Press OK to run Fluent.
2) Select File Read and read your mesh file
   a) If necessary your geometry may need to be scaled
      i) i.e. if geometry was created in millimeters and needs to be scaled to meters then, press the Scale option to scale the mesh to the appropriate dimensions.
3) In the Tree, Setup General. Select the Transient option under Solver Time.
4) Compile the UDF library.
   a) In the ribbon at the top in the User Defined Functions, open the Compiled UDFs dialog box.
   b) In Source Files, select and your source code and press OK.
   c) Select Build the Compiled UDFs dialog box.
      i) If there are no errors, click on Load.
5) Create the UDS.
   a) In the ribbon at the top, in the User Defined tab open the User-Defined Scalars dialog box.
   b) Set the Number of User Defined Scalars
   c) In the Flux Function, set to NONE
   d) In the Unsteady Function, set to your uds unsteady term
6) Create User Defined Memory
   a) In the ribbon at the top, click User Defined to open User Defined Memory dialog box
      i) Set your number of UDMs
7) Hooking the Functions

a) In the User Defined ribbon, click to open the User Defined Function Hooks box
b) For Initialization, Adjust, and Execute at End press and add the respective function hooks.

8) Create the working fluid
   a) In the Tree, select Setup Materials Fluid – air
      i) Change Density and UDS Diffusivity in their dropdown menus to their respective property functions
      ii) Press Change/Create to save the changes and close the Create/Edit Materials dialog box.
9) Setup the Source Terms.
   a) Select the Source Terms option and go to the Source Terms tab.
   b) Click add a source term
   c) Add the corresponding number of source terms
   d) Press OK to leave the dialog boxes and go back to the main window.
10) Assign the boundary conditions
   a) In the Tree, Setup Boundary Conditions. Open the respective Wall dialog box and go to the UDS tab.
   b) Use Specified Value from the dropdown menu under User-Defined Scalar Boundary Condition.
      i) Set the boundary values of the top and bottom walls according to the specifications given in the problem statement
      ii) For adiabatic walls, use a Specified Flux with a boundary value of 0.
11) Initialize the solution.
   a) In the Tree, Solution Initialization.
   b) Set the Initial Value of User Scalar 0 to 275.15 K.
   c) Click Initialize.
12) Set Transient Calculation.
   a) In the Tree, select Solution Run Calculation to activate the Run Calculation box
   b) Choose a Time Step Size of 1 sec.
   c) Set the Number of Time Steps to 600.
   d) Set Max Iterations/Time Step to a minimum of 100.
   e) Set the Reporting Interval as 1.
13) Run the simulation.
   a) In the Tree, Solution Run Calculation.
   b) Press Calculate to run.

B.3 Fluent Setup for Convection

1) Click on ANSYS Fluent.
   a) Set Dimensions to 2D
   b) For Processing Options, select either Serial or Parallel
      i) If Parallel, use the number of processes that is less than or equal to the total number of processors on your system
      ii) If on the High Performance Computing system, use the number of processors assigned to the job
   c) Under Working Directory, change the working folder to a unique name where you want to read and write the files for your simulations

i) Ensure your source code and mesh files are in this working directory
d) Press OK to run Fluent.

2) Select File Read and read your mesh file
   a) If necessary your geometry may need to be scaled
      i) i.e. if geometry was created in millimeters and needs to be scaled to meters then, press the Scale option to scale the mesh to the appropriate dimensions.
3) In the Tree, Setup General. Select the Transient option under Solver Time.
4) Compile the UDF library.
   a) In the ribbon at the top in the User Defined Functions, open the Compiled UDFs dialog box.
   b) In Source Files, select and your source code and press OK.
   c) Select Build the Compiled UDFs dialog box.
      i) If there are no errors, click on Load.
5) Create the UDS.
   a) In the ribbon at the top, in the User Defined tab open the User-Defined Scalars dialog box.
   b) Set the Number of User Defined Scalars
   c) In the Flux Function, set to uds flux term
   d) In the Unsteady Function, set to your uds unsteady term
6) Create User Defined Memory
   a) In the ribbon at the top, click User Defined to open User Defined Memory dialog box
      i) Set your number of UDMs
7) Hooking the Functions
   a) In the User Defined ribbon, click to open the User Defined Function Hooks box
   b) For Initialization, Adjust, and Execute at End press and add the respective function hooks.
8) Create the working fluid
   a) In the Tree, select Setup Materials Fluid – air
      i) Change Density and UDS Diffusivity in their dropdown menus to their respective property functions
      ii) Press Change/Create to save the changes and close the Create/Edit Materials dialog box.
9) Setup the Source Terms.
   a) Select the Source Terms option and go to the Source Terms tab.
   b) Click add a source term
   c) Add the corresponding number of source terms
   d) Press OK to leave the dialog boxes and go back to the main window.
10) Assign the boundary conditions
   a) In the Tree, Setup Boundary Conditions. Open the respective Wall dialog box and go to the UDS tab.
      i) Set hot wall to 283 K
      ii) Set cold wall to 273 K
   b) Use Specified Value from the dropdown menu under User-Defined Scalar Boundary Condition.
      i) Set the boundary values of the top and bottom walls according to the specifications given in the problem statement

ii) For adiabatic walls, use a Specified Flux with a boundary value of 0.

11) Initialize the solution.
    a) In the Tree, Solution Initialization.
    b) Set the Initial Value of User Scalar 0 to 275.15 K.
    c) Click Initialize.
12) Set Transient Calculation.
    a) In the Tree, select Solution Run Calculation to activate the Run Calculation box
    b) Choose a Time Step Size of 0.1 sec.
    c) Set the Number of Time Steps to 20000.
    d) Set Max Iterations/Time Step to a minimum of 500.
    e) Set the Reporting Interval as 1.
13) Run the simulation.
    a) In the Tree, Solution Run Calculation.
    b) Press Calculate to run.

B.4 Fluent Setup for Convection Phase change

1) Continuing from the last item in Appendix B.4
2) Assign the boundary conditions
    a) In the Tree, Setup Boundary Conditions. Open the respective Wall dialog box and go to the UDS tab.
        i) Leave hot wall at 283 K
        ii) Set cold wall to 263 K
    b) Use Specified Value from the dropdown menu under User-Defined Scalar Boundary Condition.
        i) Set the boundary values of the top and bottom walls according to the specifications given in the problem statement
        ii) For adiabatic walls, use a Specified Flux with a boundary value of 0.
3) Set Transient Calculation.
    a) In the Tree, select Solution Run Calculation to activate the Run Calculation box
    b) Choose a Time Step Size of 0.1 sec.
    c) Set the Number of Time Steps to 30000.
    d) Set Max Iterations/Time Step to a minimum of 500.
    e) Set the Reporting Interval as 1.
4) Run the simulation.
    a) In the Tree, Solution Run Calculation.
    c) Press Calculate to run.

B.5 Fluent Setup for GODU-LH2

1) Click on ANSYS Fluent.
   a) Set Dimensions to 3D
   b) For Processing Options, select either Serial or Parallel
      i) If Parallel, use the number of processes that is less than or equal to the total number of processors on your system
      ii) If on the High Performance Computing system, use the number of processors assigned to the job
   c) Under Working Directory, change the working folder to a unique name where you want to read and write the files for your simulations
      i) Ensure your source code and mesh files are in this working directory
      d) Press OK to run Fluent.
2) Select File Read and read your mesh file
   a) If necessary your geometry may need to be scaled
      i) i.e. if geometry was created in millimeters and needs to be scaled to meters then, press the Scale option to scale the mesh to the appropriate dimensions.
3) In the Tree, Setup General. Select the Transient option under Solver Time.
4) Compile the UDF library.
   a) In the ribbon at the top in the User Defined Functions, open the Compiled UDFs dialog box.
   b) In Source Files, select and your source code and press OK.
   c) Select Build the Compiled UDFs dialog box.
      i) If there are no errors, click on Load.
5) Create the UDS.
   a) In the ribbon at the top, in the User Defined tab open the User-Defined Scalars dialog box.
   b) Set the Number of User Defined Scalars
   c) In the Flux Function, set to uds flux term
   d) In the Unsteady Function, set to your uds unsteady term
6) Create User Defined Memory
   a) In the ribbon at the top, click User Defined to open User Defined Memory dialog box
      i) Set your number of UDMs
7) Hooking the Functions
   a) In the User Defined ribbon, click to open the User Defined Function Hooks box
   b) For Initialization, Adjust, and Execute at End press and add the respective function hooks.
8) Create the working fluid – parahydrogen
   a) In the Tree, select Setup Materials Fluid – air
      i) Change Density and UDS Diffusivity in their dropdown menus to their respective property functions
      ii) Press Change/Create to save the changes and close the Create/Edit Materials dialog box.
9) Setup the Source Terms.
   a) Select the Source Terms option and go to the Source Terms tab.
   b) Click add a source term
   c) Add the corresponding number of source terms

d) Press OK to leave the dialog boxes and go back to the main window.

10) Create the report definition.
    a) Create the time step ender
        i) In the Tree, click Solution
        ii) Click Report Definitions
        iii) Select New then User Defined to open the User Defined Report Definition dialog box.
    b) Name the report definition timestep-ender and choose the appropriate definition from the Function dropdown menu.
    c) Create any other necessary report definitions
        i) In the model Tree, select Report Definitions then New and User Defined
        ii) Name the report definitions to match source code naming scheme
11) Setup the timestep convergence criteria
    a) In the Model Tree, select Solution
        i) Click Monitors
        ii) Click Residuals and select Edit to open the dialog box
    b) Uncheck the Print to Console and Plot options under Options.
    c) Uncheck the Check Convergence options for all the equations.
    d) Click Convergence Conditions to open the dialog box.
    e) Select the Time Step Convergence option to add a convergence condition.
    f) Choose the timestep-ender in the Report Definition dropdown menu.
    g) Set the Stop Criterion to a very low value, 1E-22
    h) Click OK to return to the main window
12) Assign the boundary conditions
    a) In the Tree, Setup Boundary Conditions. Open the respective Wall dialog box
    b) Use Specified Value from the dropdown menu under User-Defined Scalar Boundary Condition.
        i) Set the boundary values of the walls according to the specifications given in the problem statement
        ii) For adiabatic walls, use a Specified Flux with a boundary value of 0.
    c) Setup Front and Back walls – Periodic Repeats boundary condition
        i) In the Tree, under the Boundary Condition tab change the BC type to *Interface*
        ii) Right click to edit the boundary conditions, select periodic
        iii) Select Conformal, then select Translational
        iv) Input the distance from the front plane to the back plane in meters in the Z-axis box
        v) Click Create
13) Initialize the solution.
    a) In the Tree, Solution Initialization.
    b) Set the Initial Value of User Scalar 0 to 275.15 K.
    c) Click Initialize.
14) Set Transient Calculation.
    a) In the Tree, select Solution Run Calculation to activate the Run Calculation box
    b) Choose a Time Step Size of 0.1 sec.
    c) Set the Number of Time Steps to 20000.
    d) Set Max Iterations/Time Step to a minimum of 500.
    e) Set the Reporting Interval as 1.

15) Run the simulation.
    a) In the Tree, Solution Run Calculation.
    b) Press Calculate to run

APPENDIX C

SOURCE CODES FOR SIMULATION CASES

C.1 Source Code for Conduction and Conduction Phase Change

C.2 Source Code for Convection and Convection Phase Change

C.3 Source Code for GODU-LH2

C.4 Source Code for Parahydrogen Properties

```
/*********************************************************
        ************
PARAHYDROGEN PROPERTIES

VALUES REPORTED
Symbol          Value           Unit
T       Temperature     K
R       Density         kg/m3
P       Pressure        Pa
E       Internal Energy         J/kg
Cv      Specific Heat   J/kg-K
k       Thermal Conductivity    W/m-K
mu      Dynamic Viscosity       Pa-s or kg/m-s

LIST OF FUNCTIONS
Function        Method          Code Source     Data/Eqn Source
kfTsat          Interpolation   Winter 201      NIST
mufTsat         Interpolation   Winter 2014     NIST
compressed      Interpolation   Winter 2014     NIST
superheat       Interpolation   Winter 2014     NIST
PfTR    Curve Fit       Clark 2002      Reynolds 1979
EfTR    Integration     Clark 2002      Reynolds 1979
CvfT    Curve Fit       Clark 2002      Reynolds 1979
RfTP    Root Find       Original        Reynolds 1979
PsatfTsat       Curve Fit       Clark 2002      Reynolds 1979
TsatfPsat       Root Find       Original        Reynolds 1979
RVfTsa          Curve Fit       Original        Younglove 1982
RLfTsat         Curve Fit       Original        Younglove 1982
RfTsat          Function Hub    Original
prop            Function Hub    Original
meanof          Interpolation   Winter 2014
*********************************************************
        ***********/

#include "udf.h"

/* Index counter */
int i;

/* Sizes of property data arrays */
#define imax 41
#define jmax 25
#define kmax 1

/* Constants */
double Tcrit = 32.938;
double Pcrit = 1.28377e6;
double Tmin = 13.800;
double Pmin = 7.03734e3;
double Pmax = 1.0e6;
double Tempmax = 400.0;

/* Temperature and Pressure Axes */
double Pres[jmax] = {
```

```
        7.03734e3,    8.00000e3,    9.00000e3,    1.00000e4,
                2.00000e4,    3.00000e4,    4.00000e4,
                5.00000e4,    6.00000e4,    7.00000e4,
                8.00000e4,    9.00000e4,    1.00000e5,
                1.20000e5,    1.50000e5,    2.00000e5,
                2.50000e5,    3.00000e5,    4.00000e5,
                5.00000e5,    6.00000e5,    7.00000e5,
                8.00000e5,    9.00000e5,    1.00000e6
};
double Tsat[jmax] = {
        13.8000,        14.0237,        14.2351,        14.4292,
                15.8356,        16.7761,        17.5047,
                18.1087,        18.6293,        19.0899,
                19.5047,        19.8835,        20.2330,
                20.8627,        21.6790,        22.8117,
                23.7582,        24.5791,        25.9686,
                27.1317,        28.1411,        29.0380,
                29.8477,        30.5873,        31.2684
};
double Tem[imax] = {
        13.8000,
        14.0237,
        14.2351,
        14.4292,
        15.8356,
        16.7761,
        17.5047,
        18.1087,
        18.6293,
        19.0899,
        19.5047,
        19.8835,
        20.2330,
        20.8627,
        21.6790,
        22.8117,
        23.7582,
        24.5791,
        25.9686,
        27.1317,
        28.1411,
        29.0380,
        29.8477,
        30.5873,
        31.2684,
        35.0000,
        50.0000,
        75.0000,
        100.000,
        125.000,
        150.000,
        175.000,
        200.000,
        225.000,
        250.000,
        275.000,
        300.000,
        325.000,
        350.000,
        375.000,
        400.000
};
```

```
/* Liquid Property Data Tables */
double kL[kmax][jmax] = {
        0.075249,       0.077057,       0.078698,       0.080148,
                0.089120,       0.093744,       0.096659,
                0.098677,       0.100153,       0.101269,
                0.102133,       0.102810,       0.103347,
                0.104112,       0.104747,       0.105026,
                0.104773,       0.104220,       0.102606,
                0.100594,       0.0983187,      0.0958252,
                0.0931118,      0.0901396,      0.0868138
};
double muL[kmax][jmax] = {
        2.60351e-5,     2.52270e-5,     2.45079e-5,     2.38826e-
        5,      2.01474e-5,     1.82231e-5,     1.69550e-5,
                1.60206e-5,     1.52864e-5,     1.46846e-5,
                1.41764e-5,     1.37377e-5,     1.33524e-5,
                1.27007e-5,     1.19266e-5,     1.09614e-5,
                1.02334e-5,     9.64830e-6,     8.73485e-6,
                8.02486e-6,     7.43443e-6,     6.91914e-6,
                6.45129e-6,     6.01018e-6,     5.57593e-6
};

/* Vapor Property Data Tables */
double kV[imax][jmax] = {
        0.010454,       0.010672,       0.010878,       0.011068,
                0.012443,       0.013372,       0.014101,
                0.014714,       0.015250,       0.015731,
                0.0161710,      0.0165783,      0.0169594,
                0.0176605,      0.0186006,      0.0199757,
                0.0212025,      0.0223380,      0.0244555,
                0.0264854,      0.0285209,      0.0306383,
                0.0329208,      0.0354818,      0.0385091,
        0.010660,       0.010672,       0.010878,       0.011068,
                0.012443,       0.013372,       0.014101,
                0.014714,       0.015250,       0.015731,
                0.0161710,      0.0165783,      0.0169594,
                0.0176605,      0.0186006,      0.0199757,
                0.0212025,      0.0223380,      0.0244555,
                0.0264854,      0.0285209,      0.0306383,
                0.0329208,      0.0354818,      0.0385091,
        0.010855,       0.010866,       0.010878,       0.011068,
                0.012443,       0.013372,       0.014101,
                0.014714,       0.015250,       0.015731,
                0.0161710,      0.0165783,      0.0169594,
                0.0176605,      0.0186006,      0.0199757,
                0.0212025,      0.0223380,      0.0244555,
                0.0264854,      0.0285209,      0.0306383,
                0.0329208,      0.0354818,      0.0385091,
```

0.011032, 0.011044, 0.011056, 0.011068,
0.012443, 0.013372, 0.014101,
0.014714, 0.015250, 0.015731,
0.0161710, 0.0165783, 0.0169594,
0.0176605, 0.0186006, 0.0199757,
0.0212025, 0.0223380, 0.0244555,
0.0264854, 0.0285209, 0.0306383,
0.0329208, 0.0354818, 0.0385091,
0.012304, 0.012315, 0.012326, 0.012337,
0.012443, 0.013372, 0.014101,
0.014714, 0.015250, 0.015731,
0.0161710, 0.0165783, 0.0169594,
0.0176605, 0.0186006, 0.0199757,
0.0212025, 0.0223380, 0.0244555,
0.0264854, 0.0285209, 0.0306383,
0.0329208, 0.0354818, 0.0385091,
0.013139, 0.013150, 0.013161, 0.013171,
0.013273, 0.013372, 0.014101,
0.014714, 0.015250, 0.015731,
0.0161710, 0.0165783, 0.0169594,
0.0176605, 0.0186006, 0.0199757,
0.0212025, 0.0223380, 0.0244555,
0.0264854, 0.0285209, 0.0306383,
0.0329208, 0.0354818, 0.0385091,

0.013779, 0.013790, 0.013800, 0.013811,
0.013909, 0.014005, 0.014101,
0.014714, 0.015250, 0.015731,
0.0161710, 0.0165783, 0.0169594,
0.0176605, 0.0186006, 0.0199757,
0.0212025, 0.0223380, 0.0244555,
0.0264854, 0.0285209, 0.0306383,
0.0329208, 0.0354818, 0.0385091,
0.014306, 0.014316, 0.014327, 0.014337,
0.014433, 0.014526, 0.014619,
0.014714, 0.015250, 0.015731,
0.0161710, 0.0165783, 0.0169594,
0.0176605, 0.0186006, 0.0199757,
0.0212025, 0.0223380, 0.0244555,
0.0264854, 0.0285209, 0.0306383,
0.0329208, 0.0354818, 0.0385091,
0.014758, 0.014768, 0.014778, 0.014788,
0.014882, 0.014973, 0.015064,
0.015156, 0.015250, 0.015731,
0.0161710, 0.0165783, 0.0169594,
0.0176605, 0.0186006, 0.0199757,
0.0212025, 0.0223380, 0.0244555,
0.0264854, 0.0285209, 0.0306383,
0.0329208, 0.0354818, 0.0385091,

0.015156, 0.015166, 0.015176, 0.015185,
0.015278, 0.015367, 0.015456,
0.015546, 0.015637, 0.015732,
0.0161710, 0.0165783, 0.0169594,
0.0176605, 0.0186006, 0.0199757,
0.0212025, 0.0223380, 0.0244555,
0.0264854, 0.0285209, 0.0306383,
0.0329208, 0.0354818, 0.0385091,
0.015513, 0.015523, 0.015532, 0.015542,
0.015633, 0.015721, 0.015808,
0.015896, 0.015985, 0.016077,
0.0161710, 0.0165783, 0.0169594,
0.0176605, 0.0186006, 0.0199757,
0.0212025, 0.0223380, 0.0244555,
0.0264854, 0.0285209, 0.0306383,
0.0329208, 0.0354818, 0.0385091,
0.015838, 0.015847, 0.015857, 0.015867,
0.015956, 0.016043, 0.016128,
0.016215, 0.016302, 0.016392,
0.0164838, 0.0165783, 0.0169594,
0.0176605, 0.0186006, 0.0199757,
0.0212025, 0.0223380, 0.0244555,
0.0264854, 0.0285209, 0.0306383,
0.0329208, 0.0354818, 0.0385091,

0.016137, 0.016146, 0.016156, 0.016165,
0.016254, 0.016339, 0.016423,
0.016508, 0.016594, 0.016682,
0.0167720, 0.0168644, 0.0169594,
0.0176605, 0.0186006, 0.0199757,
0.0212025, 0.0223380, 0.0244555,
0.0264854, 0.0285209, 0.0306383,
0.0329208, 0.0354818, 0.0385091,
0.016674, 0.016683, 0.016692, 0.016701,
0.016788, 0.016871, 0.016953,
0.017035, 0.017119, 0.017204,
0.0172903, 0.0173791, 0.0174703,
0.0176605, 0.0186006, 0.0199757,
0.0212025, 0.0223380, 0.0244555,
0.0264854, 0.0285209, 0.0306383,
0.0329208, 0.0354818, 0.0385091,
0.017365, 0.017374, 0.017383, 0.017392,
0.017476, 0.017556, 0.017636,
0.017715, 0.017796, 0.017877,
0.0179600, 0.0180447, 0.0181313,
0.0183112, 0.0186006, 0.0199757,
0.0212025, 0.0223380, 0.0244555,
0.0264854, 0.0285209, 0.0306383,
0.0329208, 0.0354818, 0.0385091,

0.018318, 0.018326, 0.018335, 0.018343,
0.018424, 0.018501, 0.018577,
0.018653, 0.018729, 0.018806,
0.0188845, 0.0189642, 0.0190455,
0.0192133, 0.0194800, 0.0199757,
0.0212025, 0.0223380, 0.0244555,
0.0264854, 0.0285209, 0.0306383,
0.0329208, 0.0354818, 0.0385091,
0.019106, 0.019115, 0.019123, 0.019131,
0.019210, 0.019284, 0.019357,
0.019430, 0.019503, 0.019577,
0.0196521, 0.0197282, 0.0198055,
0.0199646, 0.0202158, 0.0206755,
0.0212025, 0.0223380, 0.0244555,
0.0264854, 0.0285209, 0.0306383,
0.0329208, 0.0354818, 0.0385091,
0.019785, 0.019793, 0.019801, 0.019809,
0.019885, 0.019958, 0.020029,
0.020099, 0.020170, 0.020241,
0.0203137, 0.0203869, 0.0204612,
0.0206136, 0.0208529, 0.0212867,
0.0217754, 0.0223380, 0.0244555,
0.0264854, 0.0285209, 0.0306383,
0.0329208, 0.0354818, 0.0385091,

0.020922, 0.020929, 0.020937, 0.020945,
0.021018, 0.021086, 0.021154,
0.021221, 0.021288, 0.021355,
0.0214235, 0.0214924, 0.0215621,
0.0217046, 0.0219268, 0.0223241,
0.0227625, 0.0232525, 0.0244555,
0.0264854, 0.0285209, 0.0306383,
0.0329208, 0.0354818, 0.0385091,
0.021860, 0.021867, 0.021875, 0.021883,
0.021953, 0.022019, 0.022084,
0.022148, 0.022212, 0.022277,
0.0223418, 0.0224075, 0.0224738,
0.0226090, 0.0228189, 0.0231911,
0.0235966, 0.0240423, 0.0250947,
0.0264854, 0.0285209, 0.0306383,
0.0329208, 0.0354818, 0.0385091,
0.022665, 0.022672, 0.022679, 0.022686,
0.022754, 0.022818, 0.022881,
0.022943, 0.023005, 0.023067,
0.0231301, 0.0231932, 0.0232569,
0.0233864, 0.0235869, 0.0239401,
0.0243216, 0.0247364, 0.0256934,
0.0268931, 0.0285209, 0.0306383,
0.0329208, 0.0354818, 0.0385091,

0.023371, 0.023378, 0.023386, 0.023393,
0.023459, 0.023521, 0.023582,
0.023642, 0.023703, 0.023763,
0.0238234, 0.0238844, 0.0239460,
0.0240709, 0.0242637, 0.0246019,
0.0249647, 0.0253563, 0.0262456,
0.0273254, 0.0287024, 0.0306383,
0.0329208, 0.0354818, 0.0385091,
0.024003, 0.024010, 0.024017, 0.024024,
0.024088, 0.024149, 0.024209,
0.024267, 0.024326, 0.024385,
0.0244435, 0.0245027, 0.0245624,
0.0246834, 0.0248698, 0.0251957,
0.0255435, 0.0259167, 0.0267545,
0.0277500, 0.0289738, 0.0305684,
0.0329208, 0.0354818, 0.0385091,
0.024574, 0.024581, 0.024588, 0.024595,
0.024658, 0.024718, 0.024776,
0.024833, 0.024890, 0.024947,
0.0250048, 0.0250625, 0.0251206,
0.0252383, 0.0254193, 0.0257347,
0.0260700, 0.0264281, 0.0272250,
0.0281572, 0.0292751, 0.0306699,
0.0325376, 0.0354818, 0.0385091,

0.025096, 0.025102, 0.025109, 0.025116,
0.025178, 0.025237, 0.025293,
0.025350, 0.025406, 0.025461,
0.0255175, 0.0255739, 0.0256306,
0.0257455, 0.0259217, 0.0262281,
0.0265528, 0.0268982, 0.0276615,
0.0284492, 0.0295831, 0.0308436,
0.0324449, 0.0346634, 0.0385091,
0.027876, 0.027882, 0.027888, 0.027894,
0.027951, 0.028004, 0.028055,
0.028105, 0.028155, 0.028205,
0.0282549, 0.0283050, 0.0283552,
0.0284564, 0.0286107, 0.0288762,
0.0291536, 0.0294442, 0.0300697,
0.0307625, 0.0315341, 0.0323998,
0.0333802, 0.0345040, 0.0358132,
0.038238, 0.038242, 0.038247, 0.038251,
0.038293, 0.038331, 0.038367,
0.038403, 0.038438, 0.0384729,
0.0385075, 0.0385419, 0.0385763,
0.0386450, 0.0387483, 0.0389223,
0.0390994, 0.0392803, 0.0396543,
0.0400458, 0.0404556, 0.0408844,
0.0413328, 0.0418013, 0.0422907,

0.056936, 0.056939, 0.056942, 0.056946,
0.056977, 0.057005, 0.057032,
0.057058, 0.057084, 0.0571095,
0.0571346, 0.0571596, 0.0571844,
0.0572336, 0.0573070, 0.0574287,
0.0575505, 0.0576727, 0.0579196,
0.0581703, 0.0584252, 0.0586845,
0.0589484, 0.0592167, 0.0594895,
0.080195, 0.080199, 0.080202, 0.080205,
0.080234, 0.080261, 0.080287,
0.080312, 0.080337, 0.080362,
0.0803860, 0.0804102, 0.0804342,
0.0804819, 0.0805527, 0.0806695,
0.0807854, 0.0809008, 0.0811307,
0.0813603, 0.0815899, 0.0818198,
0.0820503, 0.0822813, 0.0825131,
0.105987, 0.105989, 0.105992, 0.105995,
0.106019, 0.106041, 0.106063,
0.106084, 0.106104, 0.106124,
0.106144, 0.106164, 0.106183,
0.106222, 0.106279, 0.106373,
0.106466, 0.106558, 0.106741,
0.106923, 0.107105, 0.107287,
0.107468, 0.107649, 0.107831,

0.127594, 0.127596, 0.127599, 0.127601,
0.127622, 0.127642, 0.127660,
0.127678, 0.127696, 0.127713,
0.127730, 0.127747, 0.127764,
0.127796, 0.127845, 0.127925,
0.128004, 0.128082, 0.128236,
0.128390, 0.128542, 0.128694,
0.128846, 0.128998, 0.129150,
0.143561, 0.143563, 0.143566, 0.143568,
0.143587, 0.143604, 0.143621,
0.143637, 0.143652, 0.143668,
0.143683, 0.143697, 0.143712,
0.143741, 0.143783, 0.143853,
0.143922, 0.143990, 0.144124,
0.144257, 0.144389, 0.144521,
0.144652, 0.144783, 0.144914,
0.155499, 0.155501, 0.155503, 0.155505,
0.155523, 0.155539, 0.155554,
0.155568, 0.155582, 0.155596,
0.155609, 0.155623, 0.155636,
0.155662, 0.155700, 0.155762,
0.155823, 0.155883, 0.156003,
0.156120, 0.156238, 0.156354,
0.156470, 0.156586, 0.156701,

0.165054, 0.165056, 0.165058, 0.165059,
0.165076, 0.165091, 0.165105,
0.165118, 0.165131, 0.165143,
0.165155, 0.165168, 0.165180,
0.165203, 0.165238, 0.165294,
0.165349, 0.165404, 0.165511,
0.165617, 0.165723, 0.165827,
0.165932, 0.166035, 0.166139,
0.174068, 0.174070, 0.174072, 0.174073,
0.174089, 0.174103, 0.174116,
0.174128, 0.174140, 0.174152,
0.174163, 0.174174, 0.174185,
0.174207, 0.174239, 0.174290,
0.174341, 0.174391, 0.174489,
0.174586, 0.174682, 0.174777,
0.174872, 0.174966, 0.175061,
0.182988, 0.182990, 0.182992, 0.182993,
0.183008, 0.183021, 0.183033,
0.183045, 0.183056, 0.183067,
0.183078, 0.183088, 0.183098,
0.183118, 0.183148, 0.183196,
0.183243, 0.183289, 0.183380,
0.183469, 0.183557, 0.183645,
0.183732, 0.183819, 0.183905,

0.192158, 0.192160, 0.192162, 0.192163,
0.192178, 0.201854, 0.192202,
0.192213, 0.192223, 0.192233,
0.192243, 0.192253, 0.192263,
0.192282, 0.192309, 0.192354,
0.192398, 0.192441, 0.192525,
0.192608, 0.192690, 0.192772,
0.192853, 0.192933, 0.193013,
0.201823, 0.201825, 0.201827, 0.201828,
0.201842, 0.201854, 0.201865,
0.201875, 0.201885, 0.201895,
0.201905, 0.201914, 0.201923,
0.201941, 0.201967, 0.202009,
0.202050, 0.202091, 0.202170,
0.202247, 0.202324, 0.202400,
0.202476, 0.202551, 0.202625,
0.212127, 0.212129, 0.212130, 0.212132,
0.212145, 0.212157, 0.212168,
0.212178, 0.212187, 0.212196,
0.212205, 0.212214, 0.212223,
0.212240, 0.212265, 0.212305,
0.212344, 0.212382, 0.212456,
0.212529, 0.212602, 0.212673,
0.212744, 0.212815, 0.212885,

```
        0.222426,    0.222428,    0.222429,    0.222431,
                0.222444,    0.222455,    0.222465,
                0.222475,    0.222484,    0.222493,
                0.222502,    0.222510,    0.222518,
                0.222535,    0.222558,    0.222596,
                0.222633,    0.222669,    0.222740,
                0.222809,    0.222878,    0.222945,
                0.223012,    0.223079,    0.223145,
        0.232966,    0.232968,    0.232969,    0.232971,
                0.232983,    0.232994,    0.233004,
                0.233013,    0.233022,    0.233031,
                0.233039,    0.233047,    0.233055,
                0.233071,    0.233094,    0.233130,
                0.233165,    0.233200,    0.233267,
                0.233333,    0.233398,    0.233462,
                0.233525,    0.233589,    0.233651
};
double muV[imax][jmax] = {
        6.50455E-7,  6.68872E-7,  6.85697E-7,  7.00696E-
        7,      7.99843E-7,  8.60232E-7,  9.05339E-7,
                9.42143E-7,  9.73679E-7,  1.00155E-6,
                1.02671E-6,  1.04978E-6,  1.07117E-6,
                1.11007E-6,  1.16137E-6,  1.23470E-6,
                1.29841E-6,  1.35591E-6,  1.45944E-6,
                1.55453E-6,  1.64667E-6,  1.74050E-6,
                1.84132E-6,  1.95674E-6,  2.09967E-6,
        6.68554E-7,  6.68872E-7,  6.85697E-7,  7.00696E-
        7,      7.99843E-7,  8.60232E-7,  9.05339E-7,
                9.42143E-7,  9.73679E-7,  1.00155E-6,
                1.04657E-6,  1.04978E-6,  1.07117E-6,
                1.11007E-6,  1.16137E-6,  1.23470E-6,
                1.29841E-6,  1.35591E-6,  1.45944E-6,
                1.55453E-6,  1.64667E-6,  1.74050E-6,
                1.84132E-6,  1.95674E-6,  2.09967E-6,
        6.85048E-7,  6.85365E-7,  6.85697E-7,  7.00696E-
        7,      7.99843E-7,  8.60232E-7,  9.05339E-7,
                9.42143E-7,  9.73679E-7,  1.00155E-6,
                1.06480E-6,  1.06794E-6,  1.07117E-6,
                1.11007E-6,  1.16137E-6,  1.23470E-6,
                1.29841E-6,  1.35591E-6,  1.45944E-6,
                1.55453E-6,  1.64667E-6,  1.74050E-6,
                1.84132E-6,  1.95674E-6,  2.09967E-6,
        6.99719E-7,  7.00034E-7,  7.00363E-7,  7.00696E-
        7,      7.99843E-7,  8.60232E-7,  9.05339E-7,
                9.42143E-7,  9.73679E-7,  1.00155E-6,
                1.09747E-6,  1.10051E-6,  1.10361E-6,
                1.11007E-6,  1.16137E-6,  1.23470E-6,
                1.29841E-6,  1.35591E-6,  1.45944E-6,
                1.55453E-6,  1.64667E-6,  1.74050E-6,
                1.84132E-6,  1.95674E-6,  2.09967E-6,
```

7.95736E-7, 7.96035E-7, 7.96347E-7, 7.96659E-7, 7.99843E-7, 8.60232E-7, 9.05339E-7,
9.42143E-7, 9.73679E-7, 1.00155E-6,
1.13957E-6, 1.14248E-6, 1.14545E-6,
1.14849E-6, 1.16137E-6, 1.23470E-6,
1.29841E-6, 1.35591E-6, 1.45944E-6,
1.55453E-6, 1.64667E-6, 1.74050E-6,
1.84132E-6, 1.95674E-6, 2.09967E-6,
8.53105E-7, 8.53394E-7, 8.53695E-7, 8.53997E-7, 8.57064E-7, 8.60232E-7, 9.05339E-7,
9.42143E-7, 9.73679E-7, 1.00155E-6,
1.19765E-6, 1.20041E-6, 1.20322E-6,
1.20900E-6, 1.21810E-6, 1.23470E-6,
1.29841E-6, 1.35591E-6, 1.45944E-6,
1.55453E-6, 1.64667E-6, 1.74050E-6,
1.84132E-6, 1.95674E-6, 2.09967E-6,
8.95260E-7, 8.95542E-7, 8.95835E-7, 8.96129E-7, 8.99111E-7, 9.02178E-7, 9.05339E-7,
9.42143E-7, 9.73679E-7, 1.00155E-6,
1.24597E-6, 1.24862E-6, 1.25131E-6,
1.25683E-6, 1.26545E-6, 1.28098E-6,
1.29841E-6, 1.35591E-6, 1.45944E-6,
1.55453E-6, 1.64667E-6, 1.74050E-6,
1.84132E-6, 1.95674E-6, 2.09967E-6,

9.29156E-7, 9.29432E-7, 9.29719E-7, 9.30006E-7, 9.32922E-7, 9.35912E-7, 9.38984E-7,
9.42143E-7, 9.73679E-7, 1.00155E-6,
1.28774E-6, 1.29030E-6, 1.29290E-6,
1.29822E-6, 1.30649E-6, 1.32124E-6,
1.33752E-6, 1.35591E-6, 1.45944E-6,
1.55453E-6, 1.64667E-6, 1.74050E-6,
1.84132E-6, 1.95674E-6, 2.09967E-6,
9.57804E-7, 9.58075E-7, 9.58357E-7, 9.58639E-7, 9.61500E-7, 9.64428E-7, 9.67430E-7,
9.70511E-7, 9.73679E-7, 1.00155E-6,
1.35816E-6, 1.36059E-6, 1.36305E-6,
1.36807E-6, 1.37583E-6, 1.38950E-6,
1.40428E-6, 1.42048E-6, 1.45944E-6,
1.55453E-6, 1.64667E-6, 1.74050E-6,
1.84132E-6, 1.95674E-6, 2.09967E-6,
9.82811E-7, 9.83078E-7, 9.83355E-7, 9.83633E-7, 9.86447E-7, 9.89323E-7, 9.92266E-7,
9.95281E-7, 9.98375E-7, 1.00155E-6,
1.41680E-6, 1.41914E-6, 1.42150E-6,
1.42630E-6, 1.43369E-6, 1.44662E-6,
1.46042E-6, 1.47531E-6, 1.50967E-6,
1.55453E-6, 1.64667E-6, 1.74050E-6,
1.84132E-6, 1.95674E-6, 2.09967E-6,

1.00511E-6, 1.00538E-6, 1.00565E-6, 1.00592E-6, 1.00870E-6, 1.01153E-6, 1.01442E-6,
1.01738E-6, 1.02041E-6, 1.02352E-6,
1.02671E-6, 1.04978E-6, 1.07117E-6,
1.11007E-6, 1.16137E-6, 1.23470E-6,
1.29841E-6, 1.35591E-6, 1.45944E-6,
1.55453E-6, 1.64667E-6, 1.74050E-6,
1.84132E-6, 1.95674E-6, 2.09967E-6,
1.02533E-6, 1.02559E-6, 1.02586E-6, 1.02613E-6, 1.02887E-6, 1.03166E-6, 1.03451E-6,
1.03742E-6, 1.04039E-6, 1.04344E-6,
1.04657E-6, 1.04978E-6, 1.07117E-6,
1.11007E-6, 1.16137E-6, 1.23470E-6,
1.29841E-6, 1.35591E-6, 1.45944E-6,
1.55453E-6, 1.64667E-6, 1.74050E-6,
1.84132E-6, 1.95674E-6, 2.09967E-6,
1.04388E-6, 1.04414E-6, 1.04440E-6, 1.04467E-6, 1.04738E-6, 1.05013E-6, 1.05294E-6,
1.05581E-6, 1.05874E-6, 1.06173E-6,
1.06480E-6, 1.06794E-6, 1.07117E-6,
1.11007E-6, 1.16137E-6, 1.23470E-6,
1.29841E-6, 1.35591E-6, 1.45944E-6,
1.55453E-6, 1.64667E-6, 1.74050E-6,
1.84132E-6, 1.95674E-6, 2.09967E-6,
1.07709E-6, 1.07734E-6, 1.07761E-6, 1.07787E-6, 1.08052E-6, 1.08321E-6, 1.08595E-6,
1.08874E-6, 1.09159E-6, 1.09450E-6,
1.09747E-6, 1.10051E-6, 1.10361E-6,
1.11007E-6, 1.16137E-6, 1.23470E-6,
1.29841E-6, 1.35591E-6, 1.45944E-6,
1.55453E-6, 1.64667E-6, 1.74050E-6,
1.84132E-6, 1.95674E-6, 2.09967E-6,
1.11984E-6, 1.12009E-6, 1.12034E-6, 1.12060E-6, 1.12317E-6, 1.12579E-6, 1.12845E-6,
1.13116E-6, 1.13391E-6, 1.13671E-6,
1.13957E-6, 1.14248E-6, 1.14545E-6,
1.14849E-6, 1.16137E-6, 1.23470E-6,
1.29841E-6, 1.35591E-6, 1.45944E-6,
1.55453E-6, 1.64667E-6, 1.74050E-6,
1.84132E-6, 1.95674E-6, 2.09967E-6,
1.17874E-6, 1.17898E-6, 1.17923E-6, 1.17947E-6, 1.18196E-6, 1.18448E-6, 1.18703E-6,
1.18963E-6, 1.19226E-6, 1.19493E-6,
1.19765E-6, 1.20041E-6, 1.20322E-6,
1.20900E-6, 1.21810E-6, 1.23470E-6,
1.29841E-6, 1.35591E-6, 1.45944E-6,
1.55453E-6, 1.64667E-6, 1.74050E-6,
1.84132E-6, 1.95674E-6, 2.09967E-6,

1.22768E-6, 1.22792E-6, 1.22815E-6, 1.22839E-6, 1.23081E-6, 1.23325E-6, 1.23573E-6,
1.23823E-6, 1.24078E-6, 1.24335E-6,
1.24597E-6, 1.24862E-6, 1.25131E-6,
1.25683E-6, 1.26545E-6, 1.28098E-6,
1.29841E-6, 1.35591E-6, 1.45944E-6,
1.55453E-6, 1.64667E-6, 1.74050E-6,
1.84132E-6, 1.95674E-6, 2.09967E-6,
1.26996E-6, 1.27018E-6, 1.27042E-6, 1.27065E-6, 1.27301E-6, 1.27539E-6, 1.27780E-6,
1.28024E-6, 1.28270E-6, 1.28520E-6,
1.28774E-6, 1.29030E-6, 1.29290E-6,
1.29822E-6, 1.30649E-6, 1.32124E-6,
1.33752E-6, 1.35591E-6, 1.45944E-6,
1.55453E-6, 1.64667E-6, 1.74050E-6,
1.84132E-6, 1.95674E-6, 2.09967E-6,
1.34116E-6, 1.34138E-6, 1.34160E-6, 1.34183E-6, 1.34409E-6, 1.34637E-6, 1.34868E-6,
1.35101E-6, 1.35337E-6, 1.35575E-6,
1.35816E-6, 1.36059E-6, 1.36305E-6,
1.36807E-6, 1.37583E-6, 1.38950E-6,
1.40428E-6, 1.42048E-6, 1.45944E-6,
1.55453E-6, 1.64667E-6, 1.74050E-6,
1.84132E-6, 1.95674E-6, 2.09967E-6,

1.40041E-6, 1.40062E-6, 1.40083E-6, 1.40105E-6, 1.40324E-6, 1.40545E-6, 1.40768E-6,
1.40993E-6, 1.41220E-6, 1.41449E-6,
1.41680E-6, 1.41914E-6, 1.42150E-6,
1.42630E-6, 1.43369E-6, 1.44662E-6,
1.46042E-6, 1.47531E-6, 1.50967E-6,
1.55453E-6, 1.64667E-6, 1.74050E-6,
1.84132E-6, 1.95674E-6, 2.09967E-6,
1.45153E-6, 1.45174E-6, 1.45195E-6, 1.45216E-6, 1.45429E-6, 1.45644E-6, 1.45860E-6,
1.46078E-6, 1.46298E-6, 1.46520E-6,
1.46744E-6, 1.46970E-6, 1.47198E-6,
1.47661E-6, 1.48372E-6, 1.49608E-6,
1.50918E-6, 1.52316E-6, 1.55464E-6,
1.59343E-6, 1.64667E-6, 1.74050E-6,
1.84132E-6, 1.95674E-6, 2.09967E-6,
1.49671E-6, 1.49691E-6, 1.49712E-6, 1.49732E-6, 1.49940E-6, 1.50150E-6, 1.50361E-6,
1.50573E-6, 1.50788E-6, 1.51004E-6,
1.51222E-6, 1.51441E-6, 1.51663E-6,
1.52111E-6, 1.52800E-6, 1.53991E-6,
1.55246E-6, 1.56575E-6, 1.59522E-6,
1.63027E-6, 1.67502E-6, 1.74050E-6,
1.84132E-6, 1.95674E-6, 2.09967E-6,

1.53727E-6, 1.53747E-6, 1.53767E-6, 1.53788E-6, 1.53991E-6, 1.54196E-6, 1.54403E-6,
1.54610E-6, 1.54820E-6, 1.55031E-6,
1.55244E-6, 1.55458E-6, 1.55674E-6,
1.56111E-6, 1.56780E-6, 1.57935E-6,
1.59145E-6, 1.60420E-6, 1.63215E-6,
1.66461E-6, 1.70432E-6, 1.75729E-6,
1.84132E-6, 1.95674E-6, 2.09967E-6,
1.57414E-6, 1.57433E-6, 1.57453E-6, 1.57472E-6, 1.57672E-6, 1.57873E-6, 1.58076E-6,
1.58279E-6, 1.58485E-6, 1.58691E-6,
1.58899E-6, 1.59109E-6, 1.59320E-6,
1.59747E-6, 1.60400E-6, 1.61523E-6,
1.62697E-6, 1.63928E-6, 1.66602E-6,
1.69655E-6, 1.73285E-6, 1.77876E-6,
1.84331E-6, 1.95674E-6, 2.09967E-6,
1.60791E-6, 1.60810E-6, 1.60829E-6, 1.60849E-6, 1.61045E-6, 1.61243E-6, 1.61442E-6,
1.61642E-6, 1.61843E-6, 1.62046E-6,
1.62250E-6, 1.62455E-6, 1.62662E-6,
1.63080E-6, 1.63719E-6, 1.64816E-6,
1.65958E-6, 1.67152E-6, 1.69727E-6,
1.72630E-6, 1.76011E-6, 1.80140E-6,
1.85572E-6, 1.93690E-6, 2.09967E-6,
1.78972E-6, 1.78990E-6, 1.79008E-6, 1.79025E-6, 1.79205E-6, 1.79386E-6, 1.79567E-6,
1.79749E-6, 1.79932E-6, 1.80116E-6,
1.80301E-6, 1.80487E-6, 1.80674E-6,
1.81050E-6, 1.81622E-6, 1.82596E-6,
1.83599E-6, 1.84633E-6, 1.86807E-6,
1.89151E-6, 1.91712E-6, 1.94557E-6,
1.97785E-6, 2.01544E-6, 2.06071E-6,
2.45916E-6, 2.45929E-6, 2.45942E-6, 2.45956E-6, 2.46089E-6, 2.46223E-6, 2.46357E-6,
2.46492E-6, 2.46627E-6, 2.46761E-6,
2.46897E-6, 2.47032E-6, 2.47168E-6,
2.47440E-6, 2.47850E-6, 2.48539E-6,
2.49235E-6, 2.49939E-6, 2.51369E-6,
2.52834E-6, 2.54335E-6, 2.55878E-6,
2.57467E-6, 2.59106E-6, 2.60802E-6,
3.39115E-6, 3.39124E-6, 3.39133E-6, 3.39143E-6, 3.39236E-6, 3.39330E-6, 3.39424E-6,
3.39517E-6, 3.39611E-6, 3.39705E-6,
3.39799E-6, 3.39893E-6, 3.39987E-6,
3.40175E-6, 3.40457E-6, 3.40929E-6,
3.41402E-6, 3.41878E-6, 3.42830E-6,
3.43790E-6, 3.44757E-6, 3.45730E-6,
3.46711E-6, 3.47700E-6, 3.48698E-6,

4.18287E-6, 4.18294E-6, 4.18302E-6, 4.18309E-6, 4.18381E-6, 4.18453E-6, 4.18525E-6,
4.18597E-6, 4.18669E-6, 4.18741E-6,
4.18813E-6, 4.18885E-6, 4.18957E-6,
4.19101E-6, 4.19317E-6, 4.19678E-6,
4.20038E-6, 4.20400E-6, 4.21123E-6,
4.21848E-6, 4.22574E-6, 4.23302E-6,
4.24033E-6, 4.24765E-6, 4.25499E-6,
4.89502E-6, 4.89508E-6, 4.89513E-6, 4.89519E-6, 4.89577E-6, 4.89634E-6, 4.89692E-6,
4.89749E-6, 4.89807E-6, 4.89865E-6,
4.89922E-6, 4.89980E-6, 4.90037E-6,
4.90152E-6, 4.90325E-6, 4.90613E-6,
4.90900E-6, 4.91188E-6, 4.91764E-6,
4.92340E-6, 4.92916E-6, 4.93492E-6,
4.94069E-6, 4.94647E-6, 4.95225E-6,
5.55618E-6, 5.55623E-6, 5.55627E-6, 5.55632E-6, 5.55680E-6, 5.55728E-6, 5.55776E-6,
5.55824E-6, 5.55872E-6, 5.55920E-6,
5.55968E-6, 5.56016E-6, 5.56064E-6,
5.56160E-6, 5.56303E-6, 5.56543E-6,
5.56782E-6, 5.57022E-6, 5.57500E-6,
5.57979E-6, 5.58457E-6, 5.58935E-6,
5.59414E-6, 5.59892E-6, 5.60371E-6,

6.18066E-6, 6.18070E-6, 6.18074E-6, 6.18078E-6, 6.18199E-6, 6.18160E-6, 6.18202E-6,
6.18243E-6, 6.18284E-6, 6.18325E-6,
6.18366E-6, 6.18407E-6, 6.18448E-6,
6.18530E-6, 6.18653E-6, 6.18859E-6,
6.19064E-6, 6.19269E-6, 6.19679E-6,
6.20088E-6, 6.20498E-6, 6.20907E-6,
6.21316E-6, 6.21725E-6, 6.22133E-6,
6.77641E-6, 6.77645E-6, 6.77648E-6, 6.77652E-6, 6.77688E-6, 6.77724E-6, 6.77760E-6,
6.77796E-6, 6.77832E-6, 6.77868E-6,
6.77904E-6, 6.77939E-6, 6.77975E-6,
6.78047E-6, 6.78155E-6, 6.78335E-6,
6.78514E-6, 6.78693E-6, 6.79052E-6,
6.79410E-6, 6.79768E-6, 6.80126E-6,
6.80483E-6, 6.80841E-6, 6.81198E-6,
7.34835E-6, 7.34838E-6, 7.34841E-6, 7.34844E-6, 7.34876E-6, 7.34908E-6, 7.34940E-6,
7.34972E-6, 7.35004E-6, 7.35036E-6,
7.35068E-6, 7.35100E-6, 7.35132E-6,
7.35196E-6, 7.35292E-6, 7.35451E-6,
7.35611E-6, 7.35770E-6, 7.36089E-6,
7.36407E-6, 7.36725E-6, 7.37043E-6,
7.37361E-6, 7.37678E-6, 7.37996E-6,

7.89983E-6, 7.89986E-6, 7.89989E-6, 7.89992E-6, 7.90020E-6, 7.90049E-6, 7.90078E-6, 7.90107E-6, 7.90136E-6, 7.90164E-6, 7.90193E-6, 7.90222E-6, 7.90251E-6, 7.90308E-6, 7.90394E-6, 7.90538E-6, 7.90682E-6, 7.90825E-6, 7.91112E-6, 7.91398E-6, 7.91685E-6, 7.91971E-6, 7.92257E-6, 7.92542E-6, 7.92828E-6, 8.43335E-6, 8.43337E-6, 8.43340E-6, 8.43343E-6, 8.43369E-6, 8.43395E-6, 8.43421E-6, 8.43447E-6, 8.43473E-6, 8.43500E-6, 8.43526E-6, 8.43552E-6, 8.43578E-6, 8.43630E-6, 8.43709E-6, 8.43839E-6, 8.43970E-6, 8.44100E-6, 8.44361E-6, 8.44621E-6, 8.44882E-6, 8.45142E-6, 8.45402E-6, 8.45661E-6, 8.45921E-6, 8.95087E-6, 8.95089E-6, 8.95091E-6, 8.95094E-6, 8.95118E-6, 8.95142E-6, 8.95166E-6, 8.95190E-6, 8.95214E-6, 8.95238E-6, 8.95262E-6, 8.95286E-6, 8.95309E-6, 8.95357E-6, 8.95429E-6, 8.95549E-6, 8.95669E-6, 8.95788E-6, 8.96027E-6, 8.96266E-6, 8.96505E-6, 8.96743E-6, 8.96981E-6, 8.97220E-6, 8.97457E-6,

9.45401E-6, 9.45403E-6, 9.45405E-6, 9.45407E-6, 9.45430E-6, 9.45452E-6, 9.45474E-6, 9.45496E-6, 9.45518E-6, 9.45540E-6, 9.45562E-6, 9.45585E-6, 9.45607E-6, 9.45651E-6, 9.45717E-6, 9.45828E-6, 9.45938E-6, 9.46049E-6, 9.46269E-6, 9.46490E-6, 9.46710E-6, 9.46930E-6, 9.47150E-6, 9.47370E-6, 9.47590E-6, 9.94416E-6, 9.94418E-6, 9.94420E-6, 9.94422E-6, 9.94443E-6, 9.94463E-6, 9.94484E-6, 9.94504E-6, 9.94525E-6, 9.94545E-6, 9.94566E-6, 9.94586E-6, 9.94607E-6, 9.94648E-6, 9.94710E-6, 9.94812E-6, 9.94915E-6, 9.95017E-6, 9.95222E-6, 9.95427E-6, 9.95632E-6, 9.95836E-6, 9.96041E-6, 9.96245E-6, 9.96449E-6, 1.04225E-5, 1.04225E-5, 1.04226E-5, 1.04226E-5, 1.04228E-5, 1.04230E-5, 1.04231E-5, 1.04233E-5, 1.04235E-5, 1.04237E-5, 1.04239E-5, 1.04241E-5, 1.04243E-5, 1.04247E-5, 1.04253E-5, 1.04262E-5, 1.04272E-5, 1.04281E-5, 1.04300E-5, 1.04320E-5, 1.04339E-5, 1.04369E-5, 1.04378E-5, 1.04396E-5, 1.04415E-5,

```
        1.08901E-5,    1.08901E-5,    1.08902E-5,    1.08902E-
        5,        1.08904E-5,    1.08905E-5,    1.08907E-5,
                1.08909E-5,    1.08911E-5,    1.08913E-5,
                1.08914E-5,    1.08916E-5,    1.08918E-5,
                1.08922E-5,    1.08927E-5,    1.08936E-5,
                1.08945E-5,    1.08954E-5,    1.08972E-5,
                1.08990E-5,    1.09008E-5,    1.09026E-5,
                1.09043E-5,    1.09061E-5,    1.09079E-5
};

/* Saturated Thermal Conductivity
        Based on data tables recorded from NIST
        1 Input: Temperature K
        2 Outputs: Saturated Liquid Thermal Conductivity
        W/m-K, Saturated Vapor Thermal Conductivity W/m-
        K*/
void kfTsat(double fTsat, double *ykL, double *ykV)
{
        double fxubound, yubound, fxlbound, ylbound;
        int j, extrap = 0;

        if (fTsat >= Tcrit) Error("Calculted bulk temperature
        above critical temperature in Function kfTsat");

        /*For saturated vapor-Tsat[j] corresponds to P[j]*/
        for (j = 1;j < jmax;j++)
        {
                if (Tsat[j] > fTsat)
                {
                        fxubound = Tsat[j];
                        yubound = kV[j][j];
                        fxlbound = Tsat[j - 1];
                        ylbound = kV[j - 1][j - 1];
                        extrap = 0;
                        break;
                }
                else
                {
                        extrap = 1;
                }
        }

        if (extrap != 0) /*need to extropolate data based on table
        of know values*/
        {
                fxubound = Tsat[jmax - 1];
                yubound = kV[jmax - 1][jmax - 1];
                fxlbound = Tsat[jmax - 2];
                ylbound = kV[jmax - 2][jmax - 2];
        }

        *ykV = ylbound + (yubound - ylbound) / (fxubound -
        fxlbound)*(fTsat - fxlbound);

        /*For saturated liquid-Tsat[j] corresponds to P[j]*/
        for (j = 1;j < jmax;j++)
        {
                if (Tsat[j] > fTsat)
                {
                        fxubound = Tsat[j];
                        yubound = kL[0][j];
                        fxlbound = Tsat[j - 1];
```

```
                ylbound = kL[0][j - 1];
                extrap = 0;
                break;
            }
            else
            {
                extrap = 1;
            }
        }

        if (extrap != 0) /*need to extropolate data based on table
        of know values*/
        {
            fxubound = Tsat[jmax - 1];
            yubound = kL[0][jmax - 1];
            fxlbound = Tsat[jmax - 2];
            ylbound = kL[0][jmax - 2];
        }

        *ykL = ylbound + (yubound - ylbound) / (fxubound -
        fxlbound)*(fTsat - fxlbound);
}

/* Saturated Dynamic Viscosity
        Based on data tables recorded from NIST
        1 Input: Temperature K
        2 Outputs: Saturated Liquid Viscosity Pa-s, Saturated
        Vapor Viscosity Pa-s */
void mufTsat(double fTsat, double *ymuL, double *ymuV)
{
        double fxubound, yubound, fxlbound, ylbound;
        int j, extrap = 0;

        if (fTsat >= Tcrit) Error("Calculted bulk temperature
        above critical temperature in Function kfTsat");

        /*For saturated vapor-Tsat[j] corresponds to P[j]*/
        for (j = 1;j < jmax;j++)
        {
            if (Tsat[j] > fTsat)
            {
                fxubound = Tsat[j];
                yubound = muV[j][j];
                fxlbound = Tsat[j - 1];
                ylbound = muV[j - 1][j - 1];
                extrap = 0;
                break;
            }
            else
            {
                extrap = 1;
            }
        }

        if (extrap != 0) /*need to extropolate data based on table
        of know values*/
        {
            fxubound = Tsat[jmax - 1];
            yubound = muV[jmax - 1][jmax - 1];
            fxlbound = Tsat[jmax - 2];
            ylbound = muV[jmax - 2][jmax - 2];
        }
```

```
*ymuV = ylbound + (yubound - ylbound) / (fxubound -
fxlbound)*(fTsat - fxlbound);

/*For saturated liquid-Tsat[j] corresponds to P[j]*/
for (j = 1;j < jmax;j++)
{
        if (Tsat[j] > fTsat)
        {
                fxubound = Tsat[j];
                yubound = muL[0][j];
                fxlbound = Tsat[j - 1];
                ylbound = muL[0][j - 1];
                extrap = 0;
                break;
        }
        else
        {
                extrap = 1;
        }
}

if (extrap != 0) /*need to extropolate data based on table
of know values*/
{
        fxubound = Tsat[jmax - 1];
        yubound = muL[0][jmax - 1];
        fxlbound = Tsat[jmax - 2];
        ylbound = muL[0][jmax - 2];
}
        *ymuL = ylbound + (yubound - ylbound) / (fxubound -
        fxlbound)*(fTsat - fxlbound);
}

/* Compressed Liquid Properties
        Based on data tables recorded from NIST
        2 Inputs: Temperature K, Property Index (4 or 5)
        1 of 2 Outputs:
                (4) Thermal Conductivity W/m-K
                (5) Dynamic Viscosity Pa-s */
double compressed(double dfT, int retval)
{
        /*-Compressed liquid values are found using saturated
        liquid values at known T
        -A compressed liquid property value(rho(1), e(2),
        Cv(3), Cp(4), k(5), mu(6)) is returned depending on
        what integer is
         stored and passed for variable retval*/

        double yL, yV;

        /*function prototypes*/
        void kfTsat(double, double*, double*);
        void mufTsat(double, double*, double*);

        switch (retval)
        {
        case 4:
                kfTsat(dfT, &yL, &yV);
                break;
        case 5:
```

```
                mufTsat(dfT, &yL, &yV);
                break;
        default:
                Error("Invalid integer for retval in function
        compressed\n");
        }
        return (yL);
}

/* Superheated Vapor Properties
        Based on data tables recorded from NIST
        3 Inputs: Temperature K, Pressure Pa, Property Index
        (4 or 5)
        1 of 2 Outputs:
                (4) Thermal Conductivity W/m-K
                (5) Dynamic Viscosity Pa-s */
double superheat(double fT, double fP, int retval)
{
        double ll, lr, tl, tr;
        double Tubound, Pubound, Tlbound, Plbound;
        double yubound, ylbound;
        double jVl, jVr, yV;
        int i, ii, j, jj;

        /*Instead of extrapolating data, send Error if
        T>Tempmax or P>Pmax*/
        if (fT >= Tempmax) Error("Temperature exceeds
        maximum temperature table data in function
        superheat");
        if (fP >= Pmax) Error("Pressure exceeds maximum
        pressure table data in function superheat");

        /*Bracket the upper and lower bounds for P*/
        for (j = 1;j < jmax;j++)
        {
                if (Pres[j] > fP)
                {
                        Pubound = Pres[j];
                        Plbound = Pres[j - 1];
                        jj = j;
                        break;
                }
        }
        for (i = 1;i < imax;i++)
        {
                if (Tem[i] > fT)
                {
                        Tubound = Tem[i];
                        Tlbound = Tem[i - 1];
                        ii = i;
                        if (ii == jj)
                        {
                                yubound = Tsat[jj];
                                ylbound = Tsat[jj - 1];
                                Tlbound = ylbound + (yubound -
ylbound) / (Pubound - Plbound)*(fP - Plbound);
                        }
                        break;
                }
        }
        switch (retval)
        {
```

```
        case 4:
                ll = kV[ii - 1][jj - 1];
                lr = kV[ii][jj - 1];
                tl = kV[ii - 1][jj];
                tr = kV[ii][jj];
                break;
        case 5:
                ll = muV[ii - 1][jj - 1];
                lr = muV[ii][jj - 1];
                tl = muV[ii - 1][jj];
                tr = muV[ii][jj];
                break;
        default:
                Error("Invalid integer for retval in function
        superheat");
        }
        /*compute function in j direction*/
        jVl = ll + (tl - ll) / (Pubound - Plbound)*(fP - Plbound);
        jVr = lr + (tr - lr) / (Pubound - Plbound)*(fP - Plbound);
        /*using j values compute function in i direction*/
        yV = jVl + (jVr - jVl) / (Tubound - Tlbound)*(fT -
        Tlbound);

        return (yV);
}

/* Constants */
double A[32] = {
        1.150470519352900E1,
        1.055427998826072E3,
        -1.270685949968568E4,
        7.287844527295619E4,
        -7.448780703363973E5,
        2.328994151810363E-1,
        -1.635308393739296E1,
        3.730678064960389E3,
        6.299667723184813E5,
        1.210920358305697E-3,
        1.753651095884817,
        -1.367022988058101E2,
        -6.869936641299885E-3,
        3.644494201750974E-2,
        -2.559784772600182,
        -4.038855202905836E-4,
        1.485396303520942E-6,
        4.243613981060742E-4,
        -2.307910113586888E-6,
        -6.082192173879582E5,
        -1.961080967486886E6,
        -5.786932854076408E2,
        2.799129504191752E4,
        -2.381566558300913E-1,
        8.918796032452872E-1,
        -6.985739539036644E-5,
        -7.339554179182899E-3,
        -5.597033440289980E-9,
        8.842130160884514E-8,
        -2.655507264539047E-12,
        -4.544474518140164E-12,
        9.818775257001922E-11
};
double B[20] = {
```

```
        +0.916617720187E2,
        -0.179492524446,
        +0.454671158395E1,
        -0.658499589788E2,
        +0.734466804535E3,
        -0.682501045175E3,
        +0.631783674710E3,
        -0.539408873282E3,
        +0.430923811783E3,
        -0.300295738811E3,
        +0.156567165346E3,
        -0.504103608225E2,
        +0.720706926514E1,
        -0.123944440318E3,
        +0.140334800142E1,
        -0.211023804313E2,
        +0.173254622817E3,
        -0.444294580871E3,
        +0.138699365355E3,
        -0.235774161015E2
};
double D[7] = {
        4.8645813003E1,
        -3.4779278180E1,
        4.0776538192E2,
        -1.1719787304E3,
        1.6213924400E3,
        -1.1531096683E3,
        3.3825492039E2
};
double F[4] = {
        3.05300134164,
        2.80810925813,
        -6.55461216567E-1,
        1.59514439374
};
double G[17] = {
        6.1934792E3,
        2.9490437E2,
        -1.5401979E3,
        -4.9176101E3,
        6.8957165E4,
        -2.2282185E5,
        3.7990059E5,
        -3.7094216E5,
        2.1326792E5,
        -7.1519411E4,
        1.2971743E4,
        -9.8533014E2,
        1.0434776E4,
        -3.9144179E2,
        5.8277696E2,
        6.5409163E2,
        -1.8728847E2
};
double Gamma = 1.008854772E-3;
double RGC = 4124.299539;
double Rc = 31.36;
double Rtl = 77.0377;
double Rtv = 0.127454;
double Tc = 32.938;
double Tt = 13.8;
```

```
double Pt = 7042.09;
double T0 = -20.1, T1 = 35.0, T2 = 400.0;

/* Pressure
   Based on Equation of state (P-4) from Reynolds 1979
        2 Inputs: Temperature K, Density kg/m3
        1 Output: Pressure Pa */
double PfTR(double Tcell, double Rcell)
{
        double T[32];
        T[0] = Tcell;
        T[1] = sqrt(Tcell);
        T[2] = 1.0;
        T[3] = 1.0 / Tcell;
        T[4] = 1.0 / pow(Tcell, 2);
        T[5] = Tcell;
        T[6] = 1.0;
        T[7] = T[3];
        T[8] = T[4];
        T[9] = Tcell;
        T[10] = 1.0;
        T[11] = T[3];
        T[12] = 1.0;
        T[13] = T[3];
        T[14] = T[4];
        T[15] = T[3];
        T[16] = T[3];
        T[17] = T[4];
        T[18] = T[4];
        T[19] = T[4];
        T[20] = 1.0 / pow(Tcell, 3);
        T[21] = T[4];
        T[22] = 1.0 / pow(Tcell, 4);
        T[23] = T[4];
        T[24] = T[20];
        T[25] = T[4];
        T[26] = T[22];
        T[27] = T[4];
        T[28] = T[20];
        T[29] = T[4];
        T[30] = T[20];
        T[31] = T[22];

        double C[32];
        for (i = 0;i < 32;i++) C[i] = A[i] * T[i];

        double H[32];
        H[0] = pow(Rcell, 2);
        H[1] = H[0];
        H[2] = H[0];
        H[3] = H[0];
        H[4] = H[0];
        H[5] = pow(Rcell, 3);
        H[6] = H[5];
        H[7] = H[5];
        H[8] = H[5];
        H[9] = pow(Rcell, 4);
        H[10] = H[9];
        H[11] = H[9];
        H[12] = pow(Rcell, 5);
        H[13] = pow(Rcell, 6);
        H[14] = H[13];
```

```
        H[15] = pow(Rcell, 7);
        H[16] = pow(Rcell, 8);
        H[17] = H[16];
        H[18] = pow(Rcell, 9);
        H[19] = pow(Rcell, 3)*exp(-Gamma * pow(Rcell, 2));
        H[20] = H[19];
        H[21] = pow(Rcell, 5)*exp(-Gamma * pow(Rcell, 2));
        H[22] = H[21];
        H[23] = pow(Rcell, 7)*exp(-Gamma * pow(Rcell, 2));
        H[24] = H[23];
        H[25] = pow(Rcell, 9)*exp(-Gamma * pow(Rcell, 2));
        H[26] = H[25];
        H[27] = pow(Rcell, 11)*exp(-Gamma * pow(Rcell, 2));
        H[28] = H[27];
        H[29] = pow(Rcell, 13)*exp(-Gamma * pow(Rcell, 2));
        H[30] = H[29];
        H[31] = H[29];

        double P = Rcell * RGC * Tcell;
        for (i = 0;i < 32;i++) P += C[i] * H[i];

        return P;
}

/* Internal Energy
   Integration based on Equation (15) from Reynolds 1979
        2 Inputs: Temperature K, Density kg/m3
        1 Output: Internal Energy J/kg */
double EfTR(double Tcell, double Rcell)
{
        double U0 = 3.9275114E5;
        double Int_Cv0, Int_Cv01, SumCTdCI;

        double T[32];
        T[0] = Tcell;
        T[1] = sqrt(Tcell);
        T[2] = 1.0;
        T[3] = 1.0 / Tcell;
        T[4] = 1.0 / pow(Tcell, 2);
        T[5] = Tcell;
        T[6] = 1.0;
        T[7] = T[3];
        T[8] = T[4];
        T[9] = Tcell;
        T[10] = 1.0;
        T[11] = T[3];
        T[12] = 1.0;
        T[13] = T[3];
        T[14] = T[4];
        T[15] = T[3];
        T[16] = T[3];
        T[17] = T[4];
        T[18] = T[4];
        T[19] = T[4];
        T[20] = 1.0 / pow(Tcell, 3);
        T[21] = T[4];
        T[22] = 1.0 / pow(Tcell, 4);
        T[23] = T[4];
        T[24] = T[20];
        T[25] = T[4];
        T[26] = T[22];
        T[27] = T[4];
```

```
T[28] = T[20];
T[29] = T[4];
T[30] = T[20];
T[31] = T[22];

double C[32];
for (i = 0;i < 32;i++) C[i] = A[i] * T[i];

double dT[32];
dT[0] = 1.0;
dT[1] = 1.0 / (2.0*sqrt(Tcell));
dT[2] = 0.0;
dT[3] = -1.0 / pow(Tcell, 2);
dT[4] = -2.0 / pow(Tcell, 3);
dT[5] = 1.0;
dT[6] = 0.0;
dT[7] = dT[3];
dT[8] = dT[4];
dT[9] = 1.0;
dT[10] = 0.0;
dT[11] = dT[3];
dT[12] = 0.0;
dT[13] = dT[3];
dT[14] = dT[4];
dT[15] = dT[3];
dT[16] = dT[3];
dT[17] = dT[4];
dT[18] = dT[4];
dT[19] = dT[4];
dT[20] = -3.0 / pow(Tcell, 4);
dT[21] = dT[4];
dT[22] = -4.0 / pow(Tcell, 5);
dT[23] = dT[4];
dT[24] = dT[20];
dT[25] = dT[4];
dT[26] = dT[22];
dT[27] = dT[4];
dT[28] = dT[20];
dT[29] = dT[4];
dT[30] = dT[20];
dT[31] = dT[22];

double dC[32];
for (i = 0;i < 32;i++) dC[i] = A[i] * dT[i];

double I[32];
I[0] = Rcell;
I[1] = I[0];
I[2] = I[0];
I[3] = I[0];
I[4] = I[0];
I[5] = pow(Rcell, 2) / 2.0;
I[6] = I[5];
I[7] = I[5];
I[8] = I[5];
I[9] = pow(Rcell, 3) / 3.0;
I[10] = I[9];
I[11] = I[9];
I[12] = pow(Rcell, 4) / 4.0;
I[13] = pow(Rcell, 5) / 5.0;
I[14] = I[13];
I[15] = pow(Rcell, 6) / 6.0;
```

```
I[16] = pow(Rcell, 7) / 7.0;
I[17] = I[16];
I[18] = pow(Rcell, 8) / 8.0;
I[19] = (1.0 / (2.0*Gamma)*(1 - exp(-Gamma *
pow(Rcell, 2))));
I[20] = I[19];
I[21] = (-pow(Rcell, 2) / (2.0*Gamma)*exp(-Gamma *
pow(Rcell, 2)) + 1.0 / Gamma * I[19]);
I[22] = I[21];
I[23] = (-pow(Rcell, 4) / (2.0*Gamma)*exp(-Gamma *
pow(Rcell, 2)) + 2.0 / Gamma * I[21]);
I[24] = I[23];
I[25] = (-pow(Rcell, 6) / (2.0*Gamma)*exp(-Gamma *
pow(Rcell, 2)) + 3.0 / Gamma * I[23]);
I[26] = I[25];
I[27] = (-pow(Rcell, 8) / (2.0*Gamma)*exp(-Gamma *
pow(Rcell, 2)) + 4.0 / Gamma * I[25]);
I[28] = I[27];
I[29] = (-pow(Rcell, 10) / (2.0*Gamma)*exp(-Gamma
* pow(Rcell, 2)) + 5.0 / Gamma * I[27]);
I[30] = I[29];
I[31] = I[29];

if (Tcell < T0) Message0("ERROR: Cell temperature is
lower than minimum temperature %g\n", Tcell);
if (Tcell < T1) Int_Cv0 = G[0] * (Tcell - T0);
if (T1 <= Tcell && Tcell <= T2)
{
        double X = log(Tcell / T1);
        Int_Cv01 = Tcell - T1;
        Int_Cv0 = G[0] * (Tcell - T0);
        for (i = 1;i < 12;i++)
        {
                Int_Cv01 = Tcell * pow(X, i) - i *
        Int_Cv01;
                Int_Cv0 += G[i] * Int_Cv01;
        }
        }
        if (Tcell > T2)
        {
        double X = log(Tcell / T2);
        U0 += 3933318.541021109;
        Int_Cv01 = Tcell - T2;
        Int_Cv0 = G[12] * (Tcell - T2);
        for (i = 13; i < 17; i++)
        {
                Int_Cv01 = Tcell * pow(X, i - 12) - (i -
        12)*Int_Cv01;
                Int_Cv0 += G[i] * Int_Cv01;
        }
        }

        SumCTdCI = 0.0;
        for (i = 0;i < 32;i++) SumCTdCI += (C[i] - Tcell *
        dC[i])*I[i];
        double Ecell = Int_Cv0 + SumCTdCI + U0;

        return Ecell;
}

/* Specific Heat
   Based on Equation (C-5) from Reynolds 1979
```

```
        1 Input: Temperature K
        1 Output: Specific Heat J/kg-K */
double CvfT(double Tcell)
{
        double Cvcell = 0.0;

        if (Tcell < T0) Message0("ERROR: Cell temperature is
        lower than minimum temperature %g\n", Tcell);
        if (Tcell < T1) Cvcell = G[0];
        if (T1 <= Tcell && Tcell <= T2)
        {
                double X = log(Tcell / T1);
                for (i = 0;i < 12;i++) Cvcell += G[i] * pow(X,
        i);
        }
        if (Tcell > T2)
        {
                double X = log(Tcell / T2);
                for (i = 12;i < 17;i++) Cvcell += G[i] * pow(X, i
        - 12);
        }

        return Cvcell;
}

/* Density
   Root-finding method using function PfTR
        3 Inputs: Temperature K, Initial guess for Density
        kg/m3, Pressure Pa
        1 Output: Density kg/m3 */
double RfTP(double Tcell, double Rcell, double Pcell)
{
        double PfTR(double, double);
        double dR = 1e-3, dPdR;

        double tol = 1e-6, resid = 1;
        double Rcell_old, Rcell_new;

        int iter = 0;
        Rcell_new = Rcell;
        while (resid > tol && iter < 20)
        {
                Rcell_old = Rcell_new;
                dPdR = (PfTR(Tcell, Rcell_old + dR) -
        PfTR(Tcell, Rcell_old - dR)) / (2 * dR);
                Rcell_new = Rcell_old - (PfTR(Tcell,
        Rcell_old) - Pcell) / dPdR;
                resid = fabs(Rcell_old - Rcell_new) / Rcell_old;
                iter++;
        }
        if (resid > tol) Message0("Density did not
        converge!\n");
        return Rcell_new;
}

/* Saturation Pressure
   Curve fit based on Equation (S-3) from Reynolds 1979
        1 Input: Saturation Temperature K
        2 Outputs: Saturation Pressure Pa, Derivative of
        Saturation Pressure with respect to Saturation
        Temperature Pa/K */
void PsatfTsat(double Tcell, double *Pcell, double *dPdT)
```

```
{
        double alpha = 1.5814454428;
        double X = (1.0 - Tt / Tcell) / (1.0 - Tt / Tc);

        *Pcell = Pt * exp(F[0] * X + F[1] * pow(X, 2) + F[2] *
        pow(X, 3) + F[3] * X*pow(1 - X, alpha));
        *dPdT = *Pcell*(Tt / ((1.0 - Tt / Tc)*pow(Tcell,
        2)))*(F[0] + 2 * F[1] * X + 3 * F[2] * pow(X, 2) + F[3]
        * (pow(1.0 - X, alpha) - X * alpha*pow(1 - X, alpha -
        1)));
}

/* Saturation Temperature
   Root-finding method using function PsatfTsat
        2 Inputs: Saturation Pressure Pa, Initial guess for
        Saturation Temperature K
        1 Output: Saturation Temperature K */
double TsatfPsat(double Pcell, double Tcell)
{
        void PsatfTsat(double, double*, double*);
        double Psat_test, dPdT;

        double tol = 1e-6, resid = 1;
        double Tsat_old, Tsat_new;

        int iter = 0;
        Tsat_new = Tcell;
        while (resid > tol && iter < 10)
        {
                Tsat_old = Tsat_new;
                PsatfTsat(Tsat_old, &Psat_test, &dPdT);
                Tsat_new = Tsat_old - (Psat_test - Pcell) /
        dPdT;
                resid = fabs(Tsat_old - Tsat_new) / Tsat_old;
                iter++;
        }
        if (resid > tol) Message0("Saturation Temperature did
        not converge!\n");
        return Tsat_new;
}

/* Saturated Vapor Density
   Curve fit based on Equations (4,5,6) from Younglove 1982
        1 Input: Saturation Temperature K
        1 Output: Saturated Vapor Density kg/m3 */
double RVfTsat(double Tcell)
{
        double X = (Tcell - Tc) / (Tt - Tc);

        double fT = B[0] * log(X);
        for (i = 1;i <= 3;i++) fT += B[i] * (1.0 - pow(X, (i - 4.0)
        / 3.0));
        for (i = 4;i <= 12;i++) fT += B[i] * (1.0 - pow(X, (i -
        3.0) / 3.0));

        double Rcell = Rc + (Rtv - Rc)*exp(fT);
        return Rcell;
}

/* Saturated Liquid Density
        Curve fit based on Equations (6,7,8) from Younglove
        1982
```

```
        1 Input: Saturation Temperature K
        1 Output: Saturated Liquid Density kg/m3 */
double RLfTsat(double Tcell)
{
        double X = (Tcell - Tc) / (Tt - Tc);

        double fT = B[13] * log(X);
        for (i = 14;i < 17;i++) fT += B[i] * (1.0 - pow(X, (i -
        17.0) / 3.0));
        for (i = 17;i < 20;i++) fT += B[i] * (1.0 - pow(X, (i -
        16.0) / 3.0));

        double Rcell = Rc + (Rtl - Rc)*exp(fT);
        return Rcell;
}

/* Saturated Fluid Densities
   Hub for functions RVfTsat and RLfTsat
        1 Input: Saturation Temperature K
        2 Outputs: Saturated Liquid Density kg/m3, Saturated
        Vapor Density kg/m3 */
void RfTsat(double Tcell, double *rholiq, double *rhovap)
{
        double RLfTsat(double);
        double RVfTsat(double);

        *rholiq = RLfTsat(Tcell);
        *rhovap = RVfTsat(Tcell);
}

/* Property Calculator
   Hub for property functions
        4 Inputs: Temperature K, Density kg/m3, Pressure Pa,
        Property Index (1 - 5)
        1 of 5 Outputs:
          (1) Density kg/m3
                (2) Internal Energy J/kg
                (3) Specific Heat J/kg-K
                (4) Thermal Conductivity W/m-K
                (5) Dynamic Viscosity Pa-s */
double prop(double Tcell, double Rcell, double Pcell, int
        retval)
{
        double output;

        double RfTP(double, double, double);
        double RLfTsat(double);
        double EfTR(double, double);
        double CvfT(double);
        double compressed(double, int);
        double superheat(double, double, int);

        switch (retval)
        {
        case 1: /* Density */
                if (Rcell > Rc) output = RLfTsat(Tcell);
                else output = RfTP(Tcell, Rcell, Pcell);
                break;
        case 2: /* Internal Energy */
                output = EfTR(Tcell, Rcell);
                break;
        case 3: /* Specific Heat */
```

```
                output = CvfT(Tcell);
                break;
        case 4: /* Thermal Conductivity */
                if (Rcell > Rc) output = compressed(Tcell, 4);
                else output = superheat(Tcell, Pcell, 4);
                break;
        case 5: /* Dynamic Viscosity */
                if (Rcell > Rc) output = compressed(Tcell, 5);
                else output = superheat(Tcell, Pcell, 5);
                break;
        default:
                Message0("Property index %d not found\n",
        retval);
                break;
        }

        return output;
}

/* Mixed Phase Properties
   Linear interpolation of saturated properties based on the
        Vapor Phase Fraction AKA EOF
        3 Inputs: Saturated Liquid Property, Saturated Vapor
        Property, Phase Fraction/EOF
        1 Output: Mixed Phase Property */
double meanof(double A0, double A1, double EOFc)
{
        double meanA;
        meanA = EOFc * A1 + (1 - EOFc)*A0;
        return meanA;
}
```